# PET IMAGING DIAGNOSTICS OF MITOCHONDRIAL HOMEOSTASIS IN PRECISION CANCER MEDICINE

By

Matthew Roland Hight

Dissertation

Submitted to the Faculty of the

Graduate School of Vanderbilt University

in partial fulfillment of the requirements

for the degree of

DOCTOR OF PHILOSOPHY

in

Interdisciplinary Materials Science

December, 2014

Nashville, Tennessee

Approved:

H. Charles Manning, Ph.D.

Eva M. Harth, Ph.D.

Sandra J. Rosenthal, Ph.D.

Todd E. Peterson, Ph.D.

Robert J. Coffey, M.D.

M. Kay Washington, M.D., Ph.D.

To Lesha, my best friend and other half

and

To my parents, Roland and Mary, who have always supported me

## ACKNOWLEDGMENTS

The work presented in this dissertation would not have been made possible without the many efforts and contributions of family, friends, and colleagues. The support and encouragement I have received throughout my graduate career has been invaluable, and to these individuals I will always be grateful.

I thank my advisor, Charles Manning, for the knowledge and guidance he has shared with me over the years. The experiences gained in his lab have been instrumental in my development as both a scientist and professional. I also wish to acknowledge the instruction provided by the members of my committee: Todd Peterson, Bob Coffey, Kay Washington, Sandra Rosenthal, and Eva Harth. Furthermore, this work would not have been possible without the financial support of the National Institutes of Health (R01-CA140628, RC1-CA145138, K25-CA127349, P50-CA128323, P50-CA95103, U24-CA126588, S10-RR17858, R41-MH85768, 5P30-DK058404, R25-CA136440) as well as the Kleberg and Lustgarten Foundations.

The many members of the Manning group and VUIIS, past and present, have been essential to the completion of this dissertation as well as an indispensable part of my training, and in some cases survival, during my time as a graduate student. This includes, but is not limited to, Eliot McKinley, Adam Smith, Saffet Guleryuz, Allie Fu, Ping Zhao, Noor Tantawy, Clare Osborne, George Wilson, Dayo Felix, Danny Colvin, Fuxue Xin, Jarrod True, and Nancy Hagans as well as the co-authors and collaborators who have contributed to the manuscripts that comprise the bulk of this dissertation, such as Eric Dawson, Don Nolting, Frank Revetta, Dan Ayers, Emily Poulin, Michelle Beckler, Annie Powell, Galina Bogatcheva, Agnes Gorska, Harold Moses, and Chanjuan Shi.

Perhaps some of my most memorable ‘teachings’ can be attributed to Mike Nickels, who I shall forever remember standing to the side, arms crossed and sighing as

I attempt to solve a problem or fix an HPLC. I am thankful for my colleague and friend Sam Saleh, whose outings on Friday evenings served as an escape for when experiments weren't working quite as expected and have provided numerous stories and fond memories that I will always cherish. I also wish to acknowledge YY Cheung, who has not only impressed me with his infinite knowledge of popular movie quotes from the 80's and 90's, but has many times taken on the role of Yoda, teaching me that sometimes one must unlearn what has been learned. I extend my gratitude to Jason and Amanda Buck for their counsel and helpful discussions as well as to Mike Schulte, who though I have met more recently, have bonded quickly thanks to similar taste in music, love (need) for coffee, and 3 a.m. lab experiments. My experiences at Vanderbilt would not have been complete without the privilege of knowing Mrs. Paula McClain, my Tennessee Mamma.

It is only due to the support of teachers, friends, and family that I ever made it to graduate school in the first place. If it wasn't for Kenneth Caswell, my former mentor and Undergraduate Chemistry Professor, I likely would not have pursued my PhD. I want to thank my long-time friends Trent and Remy, whose countless conversations about things that don't matter have kept me imaginative and always considering the unknown. Special thanks go to my in-laws, who have forgiven my absence from certain family events *in lieu* of dissertation writing.

My parents, Roland and Mary, have always done everything in their power to provide me with the best upbringing and life possible. Their constant love and encouragement inspired me to continue my education. They are deserving of more gratitude than I will ever be capable of giving and I love them both. I have been very lucky to have such a supportive family and am eternally thankful for my grandparents (Doug, Brenda, and Joyce) and siblings (Amber and Ryan).

Finally, I owe my sincerest regards to the Vanderbilt IMS program for accepting my application to graduate school, for without the move to Nashville I would have never met my wife Lesha. Lesha is my best friend and other half. If it wasn't for her love, patience, and tolerance of my anal retentive tendencies, there is absolutely no way I would have achieved my PhD. The happiness that her presence has brought to my life, as well as that of the little monster we adopted along the way, were crucial to everything achieved during my graduate career.

**TABLE OF CONTENTS**

Page

## LIST OF TABLES

## LIST OF FIGURES

## LIST OF EQUATIONS

# CHAPTER 1

# INTRODUCTION

## 1.1. Non-Invasive Imaging

There is a critical need to develop and rigorously validate biomarkers to aid in tumor diagnosis, predict clinical outcome, and quantify response to therapeutic interventions. Conventional biomarkers in oncology typically require invasive procurement of limited quantities of tumor tissue with attendant risks and sampling errors due to heterogeneity. Furthermore, serial biopsy, as required to assess treatment response longitudinally, is clinically impractical in many instances. Non-invasive imaging circumvents these limitations and offers potential advantages over traditional biopsy-based procedures.

Imaging techniques routinely used in clinical oncology include magnetic resonance imaging (MRI), X-ray computed tomography (CT), ultrasound imaging (US), and positron emission tomography (PET). Emerging techniques also include optical imaging based approaches, however, current applications tend to be focused towards skin cancer evaluation (1) and fluorescence-guided surgery (2). The current imaging criteria used for evaluating tumor development and response to therapeutic regimens is based on the anatomically derived Response Evaluation Criteria in Solid Tumors (RECIST) guidelines (3). RECIST was originally developed to assess response to cytotoxic chemotherapeutic agents in solid state tumors by monitoring deviations in tumor size throughout the course of treatment. As this approach is solely dependent on changes in tumor size, many limitations have been observed in situations regarding molecularly targeted therapies patients with specific genomic mutations (3,4). In addition, molecular and cellular responses to therapy can precede changes in tumor size

and would be overlooked when determining therapeutic response using conventional approaches. These pitfalls, coupled with clinical rise of multiplex, combination therapies, accentuate a pressing clinical need for imaging approaches which can report and monitor early and ongoing molecular and cellular changes in tumor cells. Such techniques are needed not only for individualized response assessment but also for guiding treatment planning; so as to advance the current clinical trend to personalized medicine.

Towards fulfilling this need, molecular imaging has emerged as a non-invasive means of improving our understanding of the fundamental biological determinants of disease initiation and formation; the details of which will be discussed further in **Chapter 2**. As defined by the Molecular Imaging Center of Excellence (MICoE) in 2007, "molecular imaging is the visualization, characterization, and measurement of biological processes at the molecular and cellular levels in humans and other living systems" (5). This is distinct from traditional diagnostic imaging provides information regarding the end effects of tumor molecular abnormalities rather than the base determinants. Molecular imaging strategies can employ many of the routinely used modalities previously defined (MR, CT, US, PET, SPECT, and Optical) and are dependent on the use of molecular imaging agents, or probes, to "visualize, characterize, and measure biological processes in living systems" (5).

Of these approaches, the sensitivity and quantitative nature of positron emission tomography (PET), coupled with the ability to readily produce biologically active compounds bearing positron emitting isotopes, renders PET imaging one the most attractive techniques for detecting tumors and profiling their molecular features. The most widely used PET agent in oncology is 2-deoxy-2-($^{18}$F)fluoro-D-glucose ([$^{18}$F]FDG) and has become a mainstream tool for cancer detection and assessment. However, [$^{18}$F]FDG PET has several key limitations and efficacy gaps; the details of which will be

discussed throughout **Chapter 2** and **Chapter 4**. Despite this, the diversity of PET agents currently available for profiling tumors, and accordingly the breadth of biological questions measurable by PET, is limited.

Unmet needs in clinical oncology provide the impetus for PET agent development in order to address such clinical needs as: enabling detection of clinically important cancer precursor lesions and tumors with elevated malignancy potential; tracers that allow disambiguation of benign lesions from cancer; tracers to quantify early responses of tumors to therapy; and tracers that allow measurement of signaling pathway activity and are capable of detecting specific genetic events. Within this context, the primary molecular targets for PET agent development discussed throughout this dissertation will leverage biologically orthogonal facets of cancer cell death and metabolism, with emphasis on mitochondrial energetics and homeostasis. Within this theme, agents were developed and/or evaluated as tools for targeting molecular events associated with apoptosis, glutamine metabolism, and cholesterol metabolism.

### 1.2. Specific Aims

This dissertation seeks to develop PET imaging biomarkers that quantitatively inform mitochondrial-dependent cell processes in gastrointestinal (GI) cancers, particularly colon and pancreatic. As a nexus of cell pathways, the mitochondria serves as a prime target for cross-functional probe development (**Fig. 1.1**) and the imaging of physiologically, orthogonal metabolic processes, such as cell death (6-8), carbon and nitrogen sourcing (8-10), oxidative stress response (11), and steroidogenesis (12,13). Within this context, this dissertation focused on the study of three specific aims.

*Aim 1. To develop and evaluate a novel PET imaging agent of programmed cell death*

A known caspase inhibitor, the modified tripeptide sequence Val-Ala-Asp(OMe)-fluoromethylketone (VAD-FMK), was utilized as a scaffold for positron emission tomography (PET) probe development (14). A lead compound was identified and radiolabeled with fluorine-18. The potential for noninvasive, *in vivo* detection of caspase activity was determined in response to aurora kinase inhibition as well as a multi-drug regimen that combined an inhibitor of mutant BRAF and a dual PI3K/mTOR inhibitor in the setting of V600E colon cancer. These studies illuminate the VAD-FMK peptide as a promising scaffold for molecular imaging of caspase activity and response to molecularly targeted therapy using positron emission tomography.

*Aim 2. To evaluate glutamine metabolism PET to detect oncogenic pathway activity*

A radiolabeled analogue of glutamine, [$^{18}$F](2*S*,4*R*)4F-GLN, was explored as a PET imaging agent for reporting therapeutic response to an expansive regime of molecularly target drug therapies in *BRAF*$^{V600E}$-expressing and mutant *PI3K* colon cancers. *In vivo* comparisons were made to imaging agents of other amino acid metabolic fuel sources; mainly glucose and glutamate. Additional studies explored the relationship between mutant *Kras* expression and glutamine uptake in transgenic mouse models of colon cancer using [$^{18}$F](2*S*,4*R*)4F-GLN PET imaging. These findings not only provide a greater understanding of the role that glutaminolysis plays in CRC, but also illuminate the potential impact that glutaminolysis-derived PET could have towards guiding drug development clinical trials.

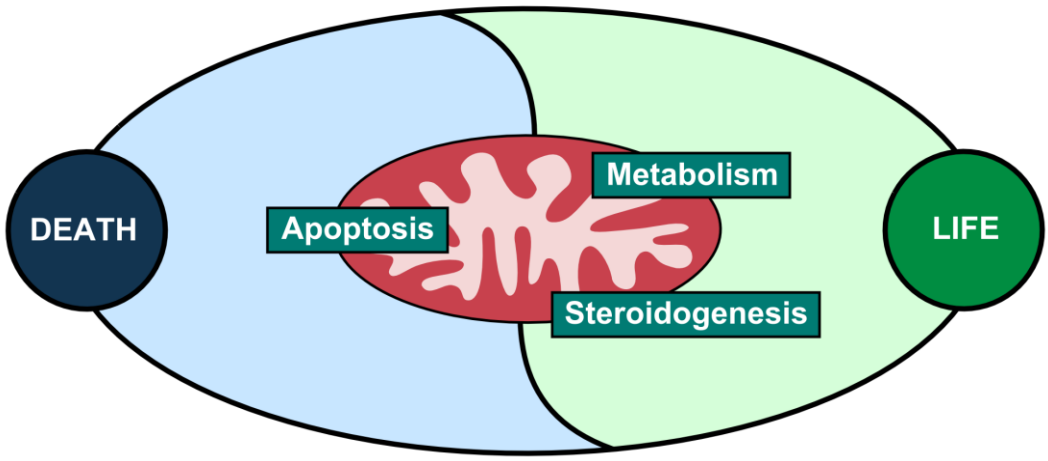


**Figure 1.1. The mitochondria is a link between cell pro-life and pro-death processes.** Many cell pathways are linked through molecular regulations occurring within the mitochondria. Relevant to this dissertation, the complex and highly regulated processes of apoptotic cell death, amino acid metabolism, oxidative stress management, and steroidogenesis are connected, and some cases dependent on one another, through mitochondrial regulated mechanisms. The specifics of these relationships will be discussed in greater detail in **Chapter 2**.

*Aim 3. To explore TSPO as an early determinant in GI cancers*

The translocator protein (TSPO) was explored as an early biomarker in the development and progression of GI cancers, mainly colorectal and pancreatic neoplasia. TSPO expression was evaluated in low- and high-grade human CRC samples as well as a diverse sampling of pre-malignant colon adenomas. Further studies elucidated the potential of TSPO as an imaging target of early pancreatic lesions in genetically engineered mice. In contrast to conventional thought, which associates elevated TSPO expression with advanced tumors, this work revealed TSPO expression to be a biomarker of early disease progression in GI cancers. This discovery could provide the basis for developing non-invasive imaging metrics for the detection and screening of patients possessing early colonic and pancreatic precursor lesions.

### 1.3. Dissertation Outline

Within the context of the specific aims, the core chapters of this dissertation will discuss PET imaging probe development, evaluation, and validation specifically relevant to: determining caspase-dependent apoptotic cell death in response to molecular targeted therapies (**Chapter 3**), exploring oncogenic determinants of glutamine metabolism (**Chapter 4**), and evaluating TSPO as an early biomarker in GI cancers (**Chapter 5**). A complete summary of conclusions, clinical relevance, and directions for future studies will be provided in **Chapter 6**. Other topics relevant broadly to molecular imaging as a field will be covered in the appendices and include discussions on: fluorescence imaging of pH heterogeneity in tumors (**Appendix 1**) (15), a comparison and evaluation of fluorescence optical imaging probes and imaging systems (**Appendix 2**), and exploration of microfluidic radiochemistry towards streamlining the PET probe radiochemical development process (**Appendix 3**). More generally, as molecular imaging is a highly interdisciplinary science, this dissertation will deal with many cross-discipline fundamentals relevant to probe development/evaluation and cover concepts which span many scientific disciplines (**Fig. 1.2**).

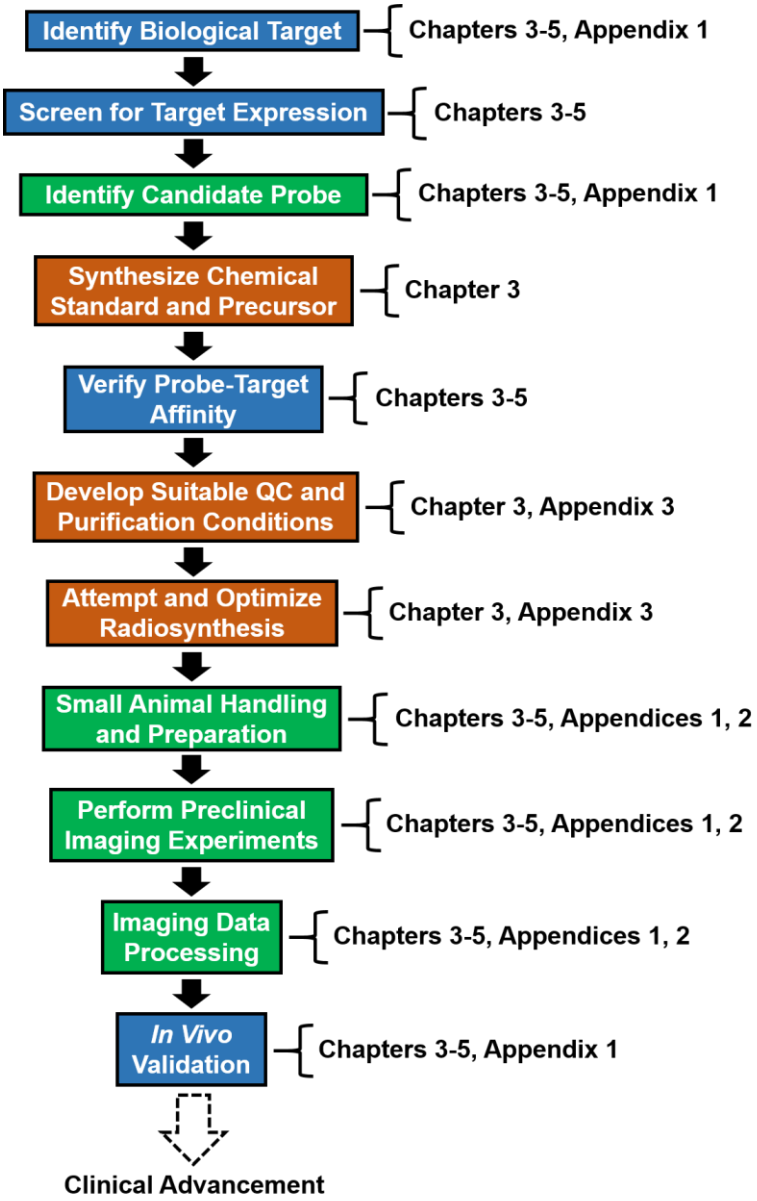


**Figure 1.2. PET probe development and molecular imaging workflow.** A general outline of the fundamental steps involved in the development and evaluation of novel and known PET imaging probes and how each dissertation chapter is integrated into this process. This process pulls from multiple scientific disciplines, including chemistry and radiochemistry (**orange**), molecular and cancer biology (**blue**), and preclinical imaging and image analysis (**green**).

### 1.4. Works Cited

1. Wassef C, Rao BK. Uses of non-invasive imaging in the diagnosis of skin cancer: an overview of the currently available modalities. Int J Dermatol 2013;52(12):1481-9.

2. Vahrmeijer AL, Hutteman M, van der Vorst JR, van de Velde CJ, Frangioni JV. Image-guided cancer surgery using near-infrared fluorescence. Nat Rev Clin Oncol 2013;10(9):507-18.

3. Tirkes T, Hollar MA, Tann M, Kohli MD, Akisik F, Sandrasegaran K. Response criteria in oncologic imaging: review of traditional and new criteria. Radiographics 2013;33(5):1323-41.

4. Nishino M, Jagannathan JP, Krajewski KM, O'Regan K, Hatabu H, Shapiro G, et al. Personalized tumor response assessment in the era of molecular medicine: cancer-specific and therapy-specific response criteria to complement pitfalls of RECIST. AJR Am J Roentgenol 2012;198(4):737-45.

5. Mankoff DA. A definition of molecular imaging. J Nucl Med 2007;48(6):18N, 21N.

6. Martinou JC, Youle RJ. Mitochondria in apoptosis: Bcl-2 family members and mitochondrial dynamics. Dev Cell 2011;21(1):92-101.

7. Boland ML, Chourasia AH, Macleod KF. Mitochondrial dysfunction in cancer. Front Oncol 2013;3:292.

8. Andersen JL, Kornbluth S. The tangled circuitry of metabolism and apoptosis. Mol Cell 2013;49(3):399-410.

9. Pochini L, Scalise M, Galluccio M, Indiveri C. Membrane transporters for the special amino acid glutamine: structure/function relationships and relevance to human health. Front Chem 2014;2:61.

10. Zhao Y, Butler EB, Tan M. Targeting cellular metabolism to improve cancer therapeutics. Cell Death Dis 2013;4:e532.

11. Ribas V, Garcia-Ruiz C, Fernandez-Checa JC. Glutathione and mitochondria. Front Pharmacol 2014;5:151.

12. Austin CJ, Kahlert J, Kassiou M, Rendina LM. The translocator protein (TSPO): a novel target for cancer chemotherapy. Int J Biochem Cell Biol 2013;45(7):1212-6.

13. Veenman L, Shandalov Y, Gavish M. VDAC activation by the 18 kDa translocator protein (TSPO), implications for apoptosis. J Bioenerg Biomembr 2008;40(3):199-205.

14. Hight MR, Cheung YY, Nickels ML, Dawson ES, Zhao P, Saleh S, et al. A peptide-based positron emission tomography probe for in vivo detection of caspase activity in apoptotic cells. Clin Cancer Res 2014;20(8):2126-35.

15. Hight MR, Nolting DD, McKinley ET, Lander AD, Wyatt SK, Gonyea M, et al. Multispectral fluorescence imaging to assess pH in biological specimens. J Biomed Opt 2011;16(1):016007.

# CHAPTER 2

# BACKGROUND AND SIGNIFICANCE

## 2.1. Molecular Imaging Modalities and Agents

Medical imaging methods have become an indispensable clinical component in the capacity of disease detection and diagnosis. Prominent medical imaging modalities, such as planar X-Ray, computed tomography (CT), magnetic resonance imaging (MRI), and ultrasound imaging, have become integrated into the standard of care for many patients. However, these methods have relied upon the detection of gross anatomy or structural anomalies, leaving the biological function and molecular determinants of the disease poorly understood. To circumvent this, molecular imaging has arisen as a promising clinical and research tool with applications towards early detection, disease diagnosis and prognosis, assessment of therapeutic efficacy and response, treatment planning, and drug development.

Broadly defined, molecular imaging is the *in vivo* visualization, characterization, and measurement of biological processes at the molecular and cellular level (1,2). In terms of application, perhaps the most defining feature of molecular imaging is the utilization of an imaging agent, or probe. Regardless of application, all molecular imaging agents possess a targeting moiety, or carrier, which is specific to a particular biological process or molecular event, and a signaling moiety, or label, which emits or produces a signal which can be detected using an appropriate imaging system (3). Common targeting moieties include small molecules, functionalized nanomaterials, peptides, proteins, and antibodies, while signaling moieties may vary between fluorophores, hyperpolarized molecules, metal chelates, nanoparticles, microbubbles, and short-lived and long-lived radionuclides, depending on the imaging modality employed. Of prevalent

imaging modalities, the following have been utilized in a molecular imaging capacity in both preclinical and clinical settings (4): nuclear imaging modalities including positron emission tomography (PET) and single-photon emission computed tomography (SPECT), magnetic resonance imaging (MRI), magnetic resonance spectroscopy (MRS), computed tomography (CT), and ultrasound (US). In addition, optical imaging modalities (fluorescence, bioluminescence, and Cerenkov luminescence imaging) have been explored in largely a preclinical research capacity (4), though clinical applications for fluorescence imaging have recently been explored in very specific circumstances. While many of these techniques measure exogenous agents, external materials which are administered to an organism, subsets of optical imaging (5), MRI (6), and MRS (7) can detect endogenous materials, which are inherent in an organism. To summarize the topics discussed throughout this section, a comparison of the performance characteristics of common molecular imaging modalities relevant to preclinical and clinical applications can be found in **Table 2.1**. Additionally, the fundamentals of molecular imaging modalities and comparisons of these approaches has been extensively reviewed in many publications (3,4,8).

| Modality | Signal | Clinical | Sensitivity | Spatial Resolution | Time | Cost |
|---|---|---|---|---|---|---|
| *PET* | $^{11}C$, $^{18}F$, $^{64}Cu$, $^{68}Ga$ | YES | $10^{-11}$ to $10^{-12}$ | 1 – 2 mm (P)<br>5 – 7 mm (C) | Min-Hours | *** |
| *SPECT* | $^{99m}Tc$, $^{123}I$, $^{111}In$, $^{177}Lu$ | YES | $10^{-10}$ to $10^{-11}$ | 1 – 2 mm (P)<br>8 – 10 mm (C) | Min-Hours | ** |
| *MRI* | Gd, SPIO, USPIO, $^{19}F$ | YES | $10^{-3}$ to $10^{-5}$ | 25 – 100 µm (P)<br>~1 mm (C) | Min-Hours | *** |
| *MRS* | $^{13}C$, $^{15}N$, $^{19}F$, $^{23}Na$, $^{31}P$, $^{1}H$ | YES | $< 10^{-3}$ | - | Min-Hours | - |
| *CT* | Iodine | YES | NA | 50 – 200 µm (P)<br>0.5 – 1 mm (C) | Min | ** |
| *US* | Microbubbles | YES | NA | 0.01 – 0.1 mm<br>1 – 2 mm (Depth) | Sec-Min | * |
| *Fluorescence* | Fluorescent Proteins, Fluorochromes | EMERGING | $10^{-8}$ to $10^{-12}$ | ~10 µm to 1 mm | Sec-Min | * |
| *BLI* | Luciferase | PRECLINICAL | $10^{-16}$ to $10^{-17}$ | 1 – 10 µm | Sec | * |

**Table 2.1. Comparison of molecular imaging modalities.** 'P' and 'C' stand for 'preclinical' and 'clinical' applications, respectively, and 'NA' for 'not applicable.' Asterisks (*) were used to indicate the relative cost of each modality, where an increasing number of asterisks corresponds to an increase in financial cost. Two value ranges are provided

for ultrasound spatial resolution as this magnitude is highest for superficial scans and decreases with tissue depth. Sensitivity values are shown in terms of mol/L (M). The contents of this table were adapted from cited works (3,4,8).

PET and SPECT imaging are the most common molecular imaging modalities in clinical use. Being nuclear based, signaling moieties include a range of radionuclides. For PET imaging, these include positron emitting isotopes [carbon-11 ($^{11}$C), oxygen-15 ($^{15}$O), nitrogen-13 ($^{13}$N), fluorine-18 ($^{18}$F), copper-64 ($^{64}$Cu), zirconium-89 ($^{89}$Zr), and gallium-68 ($^{68}$Ga)] that are typically short-lived, with radioactive half-lives being in terms of hours or days rather than days or weeks (9). Radionuclides for SPECT are longer-lived and possess half-lives spanning between several hours to days and even weeks and include gamma-emitters such as iodine-123 ($^{123}$I) and the radiometals technetium-99m ($^{99m}$Tc), indium-111 ($^{111}$In), and gallium-67 ($^{67}$Ga) (10). One of the greatest strengths of PET and SPECT imaging lies in their high sensitivity in both a preclinical and clinical settings ($10^{-11}$-$10^{-12}$ for PET and $10^{-10}$-$10^{-11}$ for SPECT) (2-4). Furthermore, the increased sensitivity of these modalities allows for relatively low quantities of imaging agents used. This is commonly referred to as the 'tracer level', meaning that concentrations of imaging agents (pmol-nmols of material) are below the threshold for elucidating a physiological response, and as such, are essentially nontoxic. While SPECT has slightly lower sensitivity, compared to PET, and lower resolution in the clinical setting (8–10 mm compared to 5–7mm with clinical PET) (11), higher resolution can be achieved with preclinical imaging due to specialized hardware. SPECT also possesses some multiplexing capabilities, which PET lacks, due to differences in gamma ray energy produced by the radioactive decay of SPECT isotopes.

While common MRI applications trend towards structural and anatomical imaging, recent years have seen the development and use of many MR specific imaging agents. Signal moieties can range from the inclusion of chelated magnetic metals to

metal nanoparticles (12) and are selected to effect either the $T_1$ or $T_2$ relaxation times of the hydrogen atoms in water, such as gadolinium (**Fig. 2.1**) or superparamagnetic iron oxide particles, respectively. Imaging strategies for detecting alterations in fluorine-19 relaxation times, rather than hydrogen, have also been developed. Compared to nuclear imaging modalities, MRI benefits from the absence of ionizing radiation and high spatial resolutions (clinical: 1 mm compared to 5–7 mm for PET, preclinical: micrometers compared to millimeter for PET) (4). However, a major limitation of MRI is its modest sensitivity. This pitfall can not only lead to extended acquisition times but may also require the use of imaging agent quantities that exceed the 'tracer level' limit. This can be problematic, as high levels of imaging agent may both alter the molecular processes being studied as well as introduce concerns for toxicity.

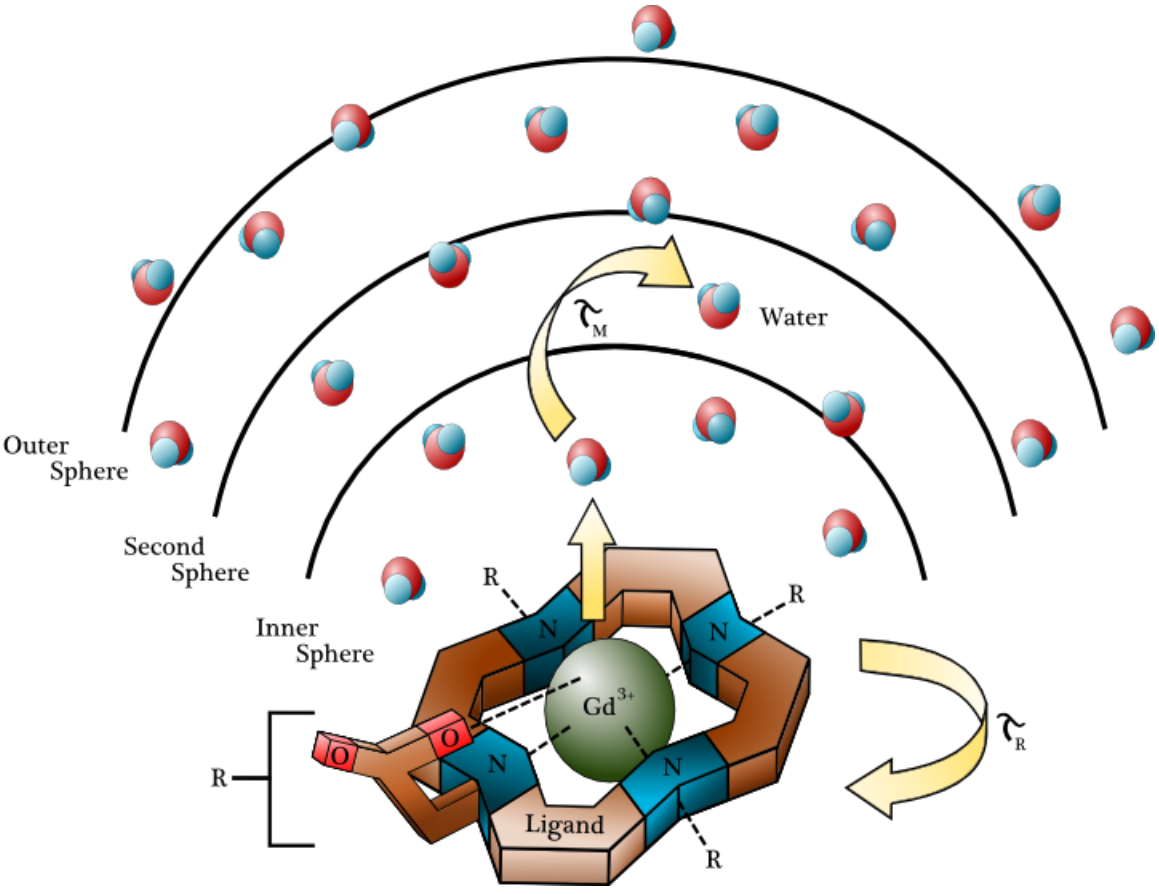


**Figure 2.1. General schematic for a gadolinium-derived $T_1$-weighted MR molecular imaging agent.** Of the eight MR contrast agents currently approved for clinical use in

the United States, seven of the eight are the product of paramagnetic metal ion chelation (shown above). For these agents, relaxation times of hydrogen atoms in water within an organism's tissues are enhanced, improving image contrast. When functionalized with targeting moieties, these agents can be used towards molecular imaging applications. This figure was modified for publication in 2011 (13).

Though commonly known as Nuclear Magnetic Resonance (NMR) spectroscopy in the fields of chemistry, in the clinical setting NMR is widely referred to as magnetic resonance spectroscopy (MRS). MRS is commonly utilized as a means to detect the spectral properties, or an induced chemical shift, of abundant endogenous molecules and metabolites such as creatine, lactate, glutamine, glutamate, alanine, lipids, and most notably choline, in which case high levels of choline-containing metabolites have been identified in nearly all types of cancer (14). Beyond hydrogen, chemical shift changes of other nuclei can also be detected using MRS, including carbon-13, fluorine-19, phosphorus-31, sodium-23, and nitrogen-15. MRS suffers from low sensitivity due to the lower concentration of endogenous molecules relative to water, but can be combined with high-resolution anatomical MRI in order to provide additional biochemical information.

Unlike traditional planar X-ray imaging techniques, CT is tomography-based and produces high-resolution, three-dimensional anatomical images of hard tissues, in contrast to MRI which benefits from high contrast in soft tissue. Iodinated contrast agents are commonly used during CT imaging to improve spatial resolution and soft tissue contrast. CT possesses limited potential as a molecular imaging modality, similar to MRI, due to the large concentrations of agents required in order to generate contrast. Despite this, the rise in nanomaterial development has produced functionalized nanoparticles that have begun to be explored for targeted CT imaging applications (15). Though molecular imaging applications are still limited, CT imaging remains a widely available, relatively cost-effective, and highly efficient morphological tool in clinical practice.

Medical US is a real-time, largely morphological imaging modality that exploits the properties and behavior of high-frequency sound waves as they travel through soft tissues. In this setting, infrared (IR) light pulses locally heat tissue causing thermoelastic expansion and subsequent production of ultrasound waves, which are then detected superficially. Common contrast agents utilized for US include gas-filled microbubbles, which are several orders of magnitude more reflective than blood. While microbubbles themselves do not enable targeted imaging of a cellular or molecular functions, the surfaces can be functionalized with peptides or antibodies for molecular imaging applications (16). While studies employing microbubbles for targeted imaging have yielded interesting results, particularly in the context of angiogenesis (17), such studies have been largely preclinical leaving clinical applications unexplored.

Optical imaging approaches benefit from high sensitivity and compared to nuclear imaging modalities, analogous to nuclear imaging modalities, but are typically more cost-effective. For fluorescence imaging, the diversity of imaging agents available, both commercially and custom, is expansive given the breadth of fluorophores available as signal moieties as well as the number of peptides, proteins, antibodies, and nanomaterials available as targeting moieties. However, fluorescence imaging possesses a number of pitfalls. These include short penetration depths (~1 cm), limited due to the scattering and absorbance of incident and fluorescent photons by biological tissues, as well as interference from tissue autofluorescence. The combination of which ultimately reduces sensitivity. These limitations have kept fluorescence imaging focused largely towards preclinical applications. However, emerging clinical techniques have begun to incorporate fluorescence imaging in applications specific towards skin cancer evaluation (18) and fluorescence guided surgery (19).

Bioluminescent imaging (BLI) is a largely preclinical optical imaging modality which utilizes reporter genes, typically expressing luciferase, that cleave injected

luciferin to biochemically produce photons of light. Due to the higher sensitivity related to enzymatic amplification of signal, compared to fluorescence imaging which requires an external excitation wavelength source, BLI possess high sensitivity and signal-to-noise ratios. As with fluorescence imaging, the most prominent limitation of BLI is related to poor tissue penetration and photon scattering.

In recent years, another luminescence modality known as Cerenkov luminescence imaging (CLI) has emerged. CLI relies on the phenomenon that radionuclides can emit visible light consistent with a form of electromagnetic radiation produced when a charged particle exceeds the speed of light while traveling in a dielectric medium (known as Cerenkov radiation) (4). Since its discovery, CLI utilizing many common nuclear imaging tracers, such as [$^{18}$F]2-fluoro-2-deoxyglucose ([$^{18}$F]FDG), have begun to be explored for optical imaging applications (20,21).

### 2.2. PET Imaging

PET is ideally suited for monitoring molecular and cellular events during the early onset of diseases, making it a powerful tool in many medical fields (e.g. oncology, neuroscience, cardiology, and pharmacology) given its capacity towards early detection, diagnosis, prognosis, and drug development (22,23). The fundamentals of PET imaging are built upon the unique decay properties of positron emitting radioactive isotopes, a process known as $\beta^+$ decay (**Fig. 2.2**). These radioisotopes are inherently unstable due to an excess of protons within the nuclei. Stability is obtained through the transformation of a proton to a neutron, positron ($e^+$), and a neutrino ($\nu$); the latter two being subsequently released from the isotope. Once ejected into surrounding tissue, the short-lived positron rapidly loses kinetic energy and eventually collides with an electron ($e^-$) resulting in matter-antimatter annihilation. This annihilation converts the mass of the two particles into two gamma rays, with energies of 511 keV, which travel opposite one

another at 180° to eventually be detected by sensors built into the PET scanner (24). The PET detectors themselves take the form of a closed ring that surrounds the object or organism being imaged and converts electrical signals created through the detection of the millions of gamma rays into sinograms that can be reconstructed through a series of algorithms into three-dimensional, tomographic images. During post-processing, corrections for dead-time, attenuation, scatter, the subtraction of random coincidences, and detector normalization are accounted for (25-27).

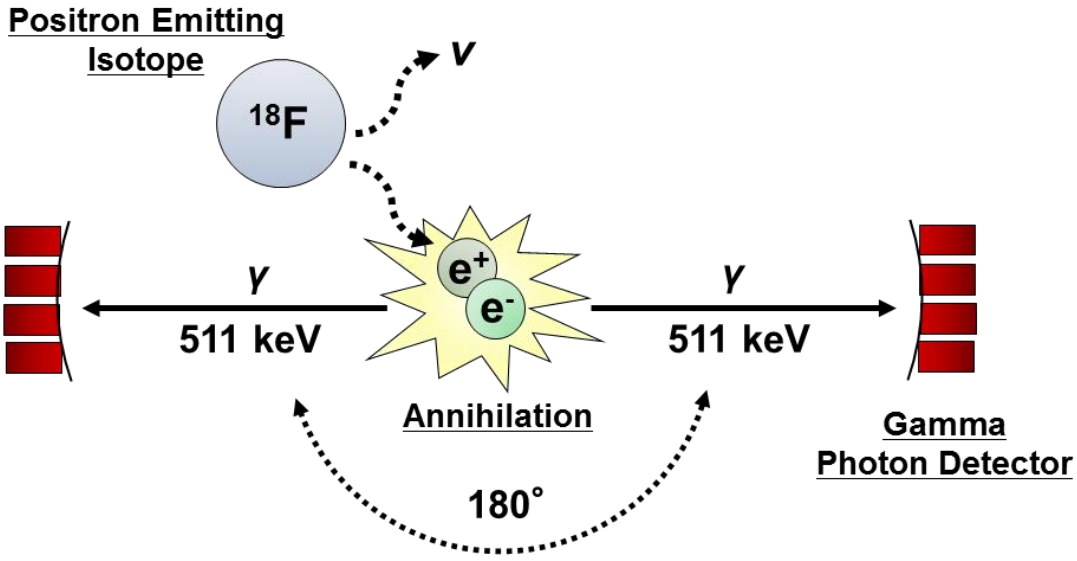


**Figure 2.2. Fundamentals of PET imaging detection.** Proton enriched radioisotopes (e.g. $^{15}$O, $^{13}$N, $^{11}$C, $^{68}$Ga, $^{18}$F, $^{64}$Cu, $^{89}$Zr) undergo $\beta^+$ radioactive decay to yield a beta particle, or positron ($e^+$), and an electron neutrino ($\nu$). This form of decay results in nuclear transmutation of the parent isotope to a new isotope with a chemical element of less than one atomic number unit (e.g. $^{18}$F to $^{18}$O). Upon positron interaction with an electron ($e^-$), an antimatter-matter annihilation occurs resulting in the release of two 511 keV gamma rays (γ) at 180° apart from one another. These particles are subsequently measured by a ring of detectors, or scintillators, built into the PET imaging scanner. This figure was adapted from cited works (24).

In its most elementary state, PET images provide a visual means for non-invasively detecting and localizing *in vivo* accumulation of imaging agents in target tissue. While this can be useful in a qualitative sense, comparison of images across subjects can be difficult due to differences in injected dose, image windowing, and

physiological variables. As the inherent quantitative nature of PET is one of its unique advantages as a molecular imaging modality, rigorous quantitative analysis can be performed. Accumulation, or specific uptake, of an imaging agent can be quantified in terms of percent injected dose per gram (%ID/g) or standardized uptake value (SUV) by normalizing the number of events, or counts, measured within a defined region of interest (ROI) to the injected dose of activity and subject's weight (28). This information can be obtained through analysis of what is commonly referred to as a 'static scan'; a PET image whose sum of frames are collected over a specific period of time, typically over the span of minutes, after the imaging agent has been delivered and allowed to reach a steady state. Kinetic properties of imaging agents can also be determined through analysis of 'dynamic scans', images where sequential frames are acquired starting immediately upon delivery of the dose and extending until steady state is achieved, using a series of techniques called compartment modeling. In compartment modeling, it is assumed that accumulation of an agent can be separated into physiologically distinct pools, or compartments. As compartment models are developed specifically for a particular imaging agent, many variants of this method exist and are reviewed in referenced work (29).

### 2.3. PET Agent Development

In clinical oncology, the most widely used PET imaging agent is 2-[$^{18}$F]fluoro-2-deoxyglucose ([$^{18}$F]FDG), a glucose analog used to imaging the abnormal dependency that cancer cells have on aerobic glycolysis for energy production, the Warburg effect. Though the first PET imaging agent to be approved by the Food and Drug Administration (FDA), [$^{18}$F]FDG bears many limitations, such as accumulation in tissues that possess increased glycolytic metabolism (e.g. brain, brown adipose tissue, fast-dividing tissues, and sites of inflammation) (30) as well as poor detection of tumors with low metabolism,

small tumors, tumors of low cell density, and [$^{18}$F]FDG indifferent cancers (e.g. bladder, prostate, and renal cancer) (31). These drawbacks have pushed the development of many novel PET imaging agents which possess alternative physiological properties and target moieties.

Novel PET agents ideally arise in response to an unmet clinical need and begins with the identification of a molecular target that is differentially expressed in the condition of interest. This leads to the selection of a targeting moiety that can serve as a scaffold for subsequent agent development (**Fig. 2.3**). Ideally, a molecular target would be expressed either uniquely or in abnormal quantities in the condition of interest, thus minimizing agent accumulation in surrounding and normal tissues. Once a targeting moiety is selected, chemical synthesis and screening can be used to synthesize, identify, and validate a lead compound for radiochemical labeling of the sensor moiety.

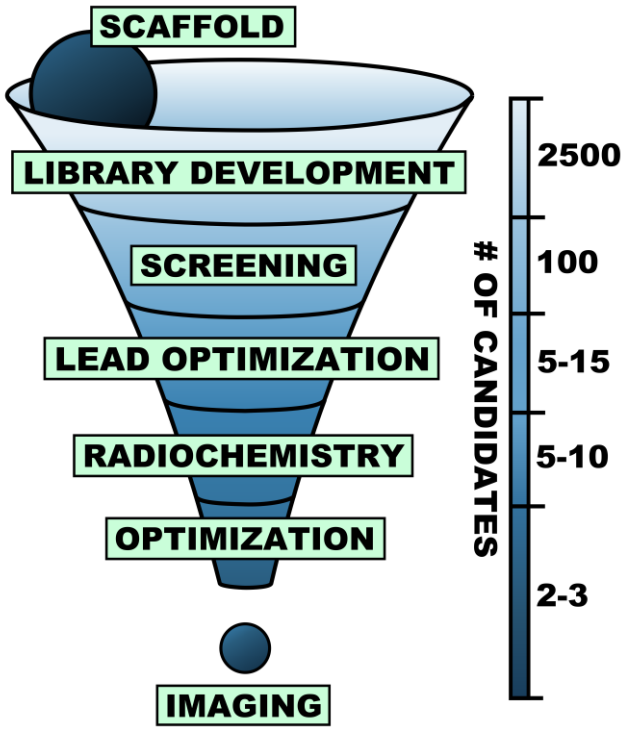


**Figure 2.3. General strategy for PET imaging agent research and development.** The advancement of a novel PET imaging agent to the clinical setting typically requires many distinct developmental steps. This process begins with the selection of a chemical scaffold which will serve as the basis of the targeting moiety. From this, a chemical

library can be developed and screened using *in vitro* techniques to evaluate biological affinity and selectivity for a molecular target. From this screening, the most promising hits will be advanced for radiochemical development and further screening and optimization. Upon successful radiolabeling, an imaging agent can then be advanced to preclinical imaging studies and *in vivo* evaluation. Eventually, these studies can lead to clinical advancement of a novel imaging agent.

Radiochemical synthetic methodologies require considerations and accommodations that differ from traditional bench-top organic synthesis (24,32,33). Many, but not all, of the signaling moieties used for PET agent development require the use of a cyclotron to generate the short-lived isotopes. Cyclotrons are particle accelerators that direct beams of protons or deuterons to a target material with sufficient energy to overcome repulsion of the positively charged nuclei in order to generate the desired isotope (24,32). For example, one of the most common PET isotopes, fluorine-18 ($t_{1/2}$ = 109.77 min), is produced through proton bombardment of an oxygen-18 target in heavy water. Other common cyclotron produced radioisotopes include carbon-11 ($t_{1/2}$ = 20.33 min), nitrogen-13 ($t_{1/2}$ = 9.97 min), oxygen-15 ($t_{1/2}$ = 2.04 min). Non-traditional radioisotopes, such as gallium-68 ($t_{1/2}$ = 67.71 min), can be produced using a generator composed of a long-lived germanium-68 ($t_{1/2}$ = 271 days) source. Radioisotope generators provide a more cost-effective alternative for facilities that cannot afford the base cost and/or upkeep required by cyclotron operation (34).

Upon production, PET radioisotopes are transferred using a stream of inert gas to a ‘hot cell’; a lead-lined fume-hood equipped with lead glass windows and robotic-manipulators all designed to reduce the radiation exposure of a user. Once transferred, the entire radiochemical synthesis is performed using a computer-controlled automated system that has been pre-equipped with reagents necessary to perform the synthesis. Many variations of these automated systems are commercially available and can be optimized for custom radiolabeling. Successful radiochemical synthesis of any PET imaging agent requires a minimum of two chemical components: a precursor, the

starting reagent and targeting moiety, and a non-radioactive, or 'cold', chemical standard of the authentic imaging agent. Due to both radiation safety restrictions as well as the relatively short periods of time allotted for synthesis involving short lived-isotopes (typically two to three half-lives), standard synthetic methods for compound validation (e.g. NMR, mass spectrometry, elemental analysis, etc.) are not feasible. Most commonly, analytical high performance liquid chromatography (HPLC) systems are used to run the authentic radiolabeled compound against the 'cold' standard in order to validate the radiolabeling and approve the product for imaging use. For clinical radiosynthesis, additional good manufacturing process (GMP) quality controls may be needed to ensure safe use in human patients.

### 2.4. Mitochondrial Cell Pathways

Within the field of cancer detection and evaluation, many PET imaging agents have been developed as tools for elucidating the molecular regulators of cancer cell reprogramming of cell metabolism, proliferation, angiogenesis, hypoxia, and apoptosis (3). Despite the ensemble of agents and targets available for PET imaging, many, if not all, possess limitations that are inherent either in the chemical and physiological characteristics of the agent or in the molecular and cellular information provided by the target detected, such as non-specificity. As such, there is a pressing need to develop novel PET imaging agents which target unique molecular events relevant to cancer research. Towards this end, mitochondrial dependent processes could serve as a prime candidate pool for selecting novel imaging targets given its critical role in many biological processes as the 'gate-keeper' of a cell's viability (35).

Though mutations in cancer cell mitochondrial genes have been recognized since the 1990's (36), conventional interest in the role that such alterations play in cancer cells began with the discovery of gene mutations in the tricarboxylic acid (TCA)

cycle, also known as the citric acid cycle or Krebs (37,38). Beyond metabolic defects, mitochondrial dysfunction in the initiation of apoptotic cell death, reactive oxygen species (ROS) regulation, and biosynthetic pathways (e.g. steroidogenesis) have also been linked to cancer cell growth and progression (35,39,40). Remarkably, these processes are connected through a complex series of molecularly controlled mechanisms that can be better understood using molecular imaging (**Fig. 2.4**).

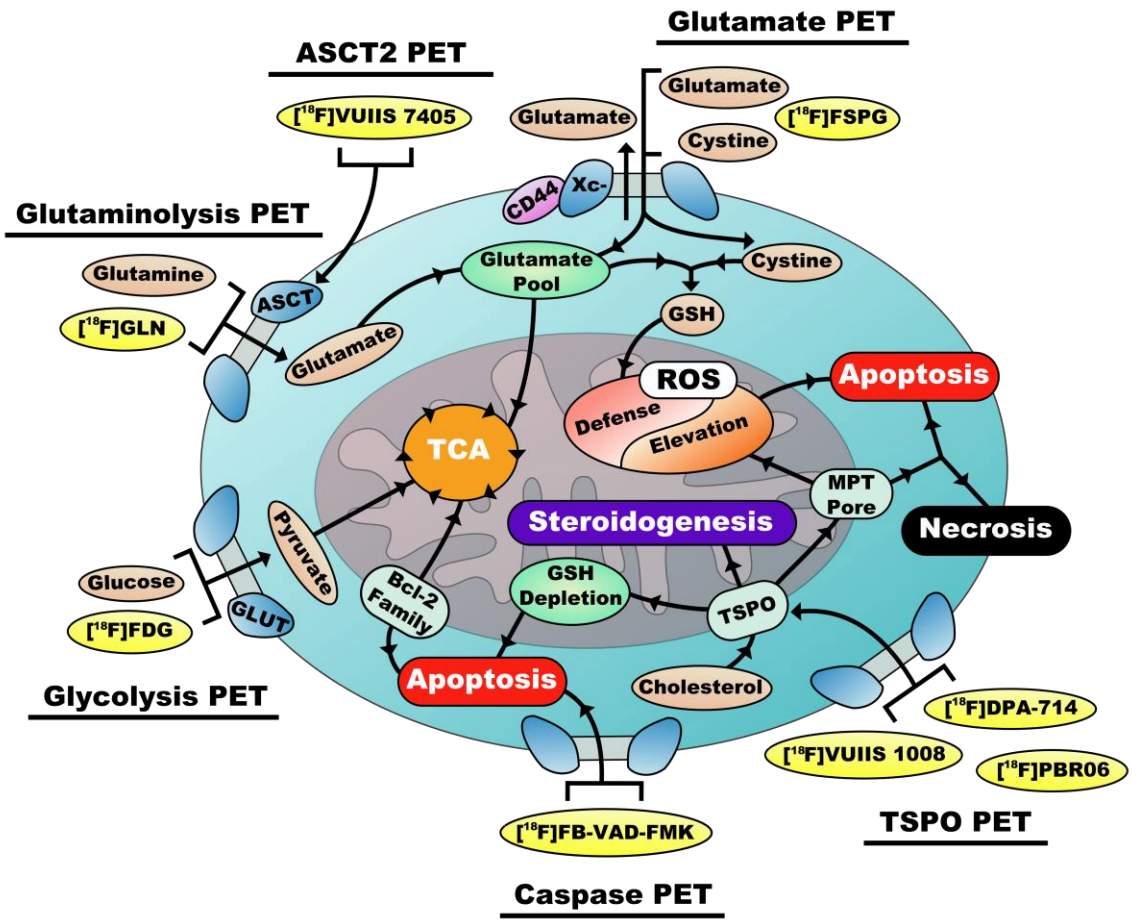


**Figure 2.4. Mechanistic rationale for targeting mitochondrial-centric cellular pathways for molecular imaging agent development.** The interplay between mitochondrial-regulated cell processes offers many molecular targets that could be highly informative towards the advancement of cancer imaging research. The connection between many of the imaging agents that will be discussed throughout this dissertation, shown in yellow, as well as the means in which they inform mitochondrial processes is illustrated above. This figure was adapted using information provided in the following cited works (35,39-43).

Alterations in the cellular consumption and carbon sourcing of glucose, glutamine, and other fuels for cancer have become well documented and are the topics for numerous review articles (44-48). Cancer cell metabolic reprogramming is characterized mainly by increases in aerobic glycolysis (48), the Warburg effect, and an increased dependency on glutamine as a fuel source (49,50). Glucose can be taken up by cells in a regulated manner using glucose transporters (GLUTs) (51) and converted to pyruvate through a series of glycolytic transformations. Pyruvate can then be transported into the mitochondria and used in the tricarboxylic acid cycle (TCA) cycle to produce two adenosine triphosphate (ATP) and six nicotinamide adenine dinucleotide (NADH) molecules per glucose. Similarly, glutamine can be transported to the cytosol by the alanine, serine, cysteine transporter (ASCT2) where it is converted to glutamate by glutaminase. Glutamate can also be taken into the cell directly using the XCT, or $X_c^-$, family of amino acid transporters. Cytosolic glutamate can be either transported into the mitochondria, where it is converted to α-ketoglutarate and used for the TCA cycle, or used in the synthesis of glutathione (GSH), a major intracellular thiol compound which serves as the main antioxidant defense against ROS. GSH can then be transported to the mitochondria (mGSH) where it regulates mitochondrial ROS levels and electrophile detoxification (40).

The ability to adapt to oxidative stress through regulation of ROS-mediated cell death is a necessary component of cancer cell survival. *In vitro* and *in vivo* studies using the natural product piperlongumine have shown that this cytotoxic agent induces cell death by decreasing GSH levels and inducing alterations in mitochondrial morphology and function (52,53). Further studies have suggested initiating the depletion of mGSH and promotion of ROS generation through administration of chemotherapeutic drugs in order to induce cancer cell death (54,55). Interestingly, as mGSH levels can be

influenced by mitochondrial cholesterol (56,57) and calcium ion levels (58), a potential link may exist between glutamate consumption and the translocator protein (TSPO).

Formerly termed peripheral benzodiazepine receptor (PBR), TSPO is an outer mitochondrial membrane (OMM) protein suggested to play a role in steroidogenesis by transporting cholesterol to the inner mitochondrial membrane (IMM) (59,60). Elevated TSPO expression has been linked with disease progression and diminished survival in patients presenting with several types of cancer, including oral (61), colorectal (62), breast (63), and brain (64). Additionally, elevated TSPO levels appear to be associated with aggressive, metastatic behavior in breast, colorectal, and prostate cancer (65). Beyond steroidogenesis, TSPO is also thought to participate in the regulation of cell death as a structural marker of the mitochondrial permeability transition (MPT) pore, the formation of which is currently believed to be controlled by the voltage-dependent anion channel (VDAC), adenine nucleotide translocase (ANT), TSPO (66), and the BCL-2 protein family (35). The MPT pore results in an increase in mitochondrial membrane permeability and can subsequently lead to apoptotic and necrotic cell death mechanisms.

Apoptosis, or programmed cell death, is a mechanism of cell death where signaling cascades are regulated largely by a family of cysteine aspartic acid-specific proteases, the caspases. Deviations from normal apoptotic programs are frequently associated with human diseases such as cancer (67) and the induction of apoptosis in cancer cells is a common goal in many anti-cancer therapies. The mitochondria is an essential component of apoptosis initiation, specifically the intrinsic pathway, through its controlled release of cytochrome c into the cytosol. Surprisingly, mitochondrial apoptosis regulators can also feedback into other cell pathways, particularly TCA dependent metabolism (42). Though major determinants of apoptosis, some of the proapoptotic Bcl-2 family of proteins (e.g. Bax, Bak, Bid, Bim, Bad, Puma, and Noxa) have recently been

shown to exhibit a dual apoptotic-metabolic nature. For example, Boohaker, *et.al.* report that Bax-deficient cells display decreased oxygen consumption, decreased ATP levels, and increased glycolysis (68). In other studies, Bad has been suggested to be a key regulator of glucose metabolism in its proposed role as a scaffold for formation of a glucokinase (GK)-derived complex necessary for normal glycolytic function (69). Conversely, metabolic dysregulation can be a factor in apoptosis induction through the BH3-only proteins Puma (70) and Noxa (71), which have been linked to glucose deprivation-induced apoptosis. Upstream apoptotic factors can also influence mitochondrial metabolism as the tumor suppressor p53, one of the most-studied proteins in cancer biology characterized as a stress-induced pro-apoptotic protein, can inhibit glycolytic flux (72) while in parallel promoting metabolic glutamine dependency (73,74).

Given the complexity of the effects that mitochondrial homeostasis has towards cancer development and progression, molecular imaging agents that illuminate mechanistic relationships between the processes of apoptosis, metabolism, ROS defense, and steroidogenesis could be highly informative towards advancing means of cancer detection, assessment of therapeutic response, and drug discovery. Subsequent chapters in this dissertation will seek to explore this potential by assessing imaging agents which specifically target key regulators in these cancer mitochondrial pathways. **Chapter 3** outlines the discovery, characterization, and validation of a novel PET imaging probe, [$^{18}$F]FB-VAD-FMK, for *in vivo* caspase activity detection (75). In **Chapter 4**, PET imaging of cancer cell nutrient uptake and metabolism will be evaluated as a measure of molecular response to targeted therapy as well as means for reporting activation of oncogenic pathways in genetically engineered mice. Exploring novel biomarkers in early stage disease, **Chapter 5** will describe the relevance of the translocator protein (TSPO) expression in early gastrointestinal (GI) neoplasia.

## 2.5. Works Cited


1. Mankoff DA. A definition of molecular imaging. J Nucl Med 2007;48(6):18N, 21N.

2. Weissleder R, Mahmood U. Molecular imaging. Radiology 2001;219(2):316-33.

3. Peterson TE, Manning HC. Molecular imaging: 18F-FDG PET and a whole lot more. J Nucl Med Technol 2009;37(3):151-61.

4. James ML, Gambhir SS. A molecular imaging primer: modalities, imaging agents, and applications. Physiol Rev 2012;92(2):897-965.

5. Georgakoudi I, Quinn KP. Optical imaging using endogenous contrast to assess metabolic state. Annu Rev Biomed Eng 2012;14:351-67.

6. Wen Z, Hu S, Huang F, Wang X, Guo L, Quan X, et al. MR imaging of high-grade brain tumors using endogenous protein and peptide-based contrast. Neuroimage 2010;51(2):616-22.

7. Celda B, Monleon D, Martinez-Bisbal MC, Esteve V, Martinez-Granados B, Pinero E, et al. MRS as endogenous molecular imaging for brain and prostate tumors: FP6 project "eTUMOR". Adv Exp Med Biol 2006;587:285-302.

8. Condeelis J, Weissleder R. In vivo imaging in cancer. Cold Spring Harb Perspect Biol 2010;2(12):a003848.

9. Ametamey SM, Honer M, Schubiger PA. Molecular imaging with PET. Chem Rev 2008;108(5):1501-16.

10. Muller C, Schibli R. Single photon emission computed tomography tracer. Recent Results Cancer Res 2013;187:65-105.

11. Blake P, Johnson B, VanMeter JW. Positron Emission Tomography (PET) and Single Photon Emission Computed Tomography (SPECT): Clinical Applications. J Neuroophthalmol 2003;23(1):34-41.

12. Yoo B, Pagel MD. An overview of responsive MRI contrast agents for molecular imaging. Front Biosci 2008;13:1733-52.

13. Buck JR, Hight, M.R., Tang, D., Manning, H.C. In: Yankeelov TE, Pickens, D.R., Price, R.R., editor. Quantitative MRI in Cancer: Taylor & Francis; 2011. p 125-33.

14. Glunde K, Artemov D, Penet MF, Jacobs MA, Bhujwalla ZM. Magnetic resonance spectroscopy in metabolic and molecular imaging and diagnosis of cancer. Chem Rev 2010;110(5):3043-59.

15. Li J, Chaudhary A, Chmura SJ, Pelizzari C, Rajh T, Wietholt C, et al. A novel functional CT contrast agent for molecular imaging of cancer. Phys Med Biol 2010;55(15):4389-97.

16. Deshpande N, Needles A, Willmann JK. Molecular ultrasound imaging: current status and future directions. Clin Radiol 2010;65(7):567-81.

17. Leong-Poi H, Christiansen J, Klibanov AL, Kaul S, Lindner JR. Noninvasive assessment of angiogenesis by ultrasound and microbubbles targeted to alpha(v)-integrins. Circulation 2003;107(3):455-60.

18. Wassef C, Rao BK. Uses of non-invasive imaging in the diagnosis of skin cancer: an overview of the currently available modalities. Int J Dermatol 2013;52(12):1481-9.

19. Vahrmeijer AL, Hutteman M, van der Vorst JR, van de Velde CJ, Frangioni JV. Image-guided cancer surgery using near-infrared fluorescence. Nat Rev Clin Oncol 2013;10(9):507-18.

20. Robertson R, Germanos MS, Li C, Mitchell GS, Cherry SR, Silva MD. Optical imaging of Cerenkov light generation from positron-emitting radiotracers. Phys Med Biol 2009;54(16):N355-65.

21. Liu H, Ren G, Miao Z, Zhang X, Tang X, Han P, et al. Molecular optical imaging with radioactive probes. PLoS One 2010;5(3):e9470.

22. Gambhir SS. Molecular imaging of cancer with positron emission tomography. Nat Rev Cancer 2002;2(9):683-93.

23. Rudin M, Weissleder R. Molecular imaging in drug discovery and development. Nat Rev Drug Discov 2003;2(2):123-31.

24. Miller PW, Long NJ, Vilar R, Gee AD. Synthesis of 11C, 18F, 15O, and 13N radiolabels for positron emission tomography. Angew Chem Int Ed Engl 2008;47(47):8998-9033.

25. Brankov JG, Yang Y, Wernick MN. Tomographic image reconstruction based on a content-adaptive mesh model. IEEE Trans Med Imaging 2004;23(2):202-12.

26. Boellaard R. Standards for PET image acquisition and quantitative data analysis. J Nucl Med 2009;50 Suppl 1:11S-20S.

27. Buckler AJ, Boellaard R. Standardization of quantitative imaging: the time is right, and 18F-FDG PET/CT is a good place to start. J Nucl Med 2011;52(2):171-2.

28. Adams MC, Turkington TG, Wilson JM, Wong TZ. A systematic review of the factors affecting accuracy of SUV measurements. AJR Am J Roentgenol 2010;195(2):310-20.

29. Watabe H, Ikoma Y, Kimura Y, Naganawa M, Shidahara M. PET kinetic analysis--compartmental model. Ann Nucl Med 2006;20(9):583-8.

30. Krasikova RN, Kuznetsova OF, Fedorova OS, Belokon YN, Maleev VI, Mu L, et al. 4-[18F]fluoroglutamic acid (BAY 85-8050), a new amino acid radiotracer for PET imaging of tumors: synthesis and in vitro characterization. J Med Chem 2011;54(1):406-10.

31. Ide M. Cancer screening with FDG-PET. Q J Nucl Med Mol Imaging 2006;50(1):23-7.

32. Mason NS, Mathis CA. Positron emission tomography radiochemistry. Neuroimaging Clin N Am 2003;13(4):671-87.

33. Wadsak W, Mitterhauser M. Basics and principles of radiopharmaceuticals for PET/CT. Eur J Radiol 2010;73(3):461-9.

34. Al-Nahhas A, Win Z, Szyszko T, Singh A, Khan S, Rubello D. What can gallium-68 PET add to receptor and molecular imaging? Eur J Nucl Med Mol Imaging 2007;34(12):1897-901.

35. Wallace DC. Mitochondria and cancer. Nat Rev Cancer 2012;12(10):685-98.

36. Horton TM, Petros JA, Heddi A, Shoffner J, Kaufman AE, Graham SD, Jr., et al. Novel mitochondrial DNA deletion found in a renal cell carcinoma. Genes Chromosomes Cancer 1996;15(2):95-101.

37. Cardaci S, Ciriolo MR. TCA Cycle Defects and Cancer: When Metabolism Tunes Redox State. Int J Cell Biol 2012;2012:161837.

38. Gaude E, Frezza C. Defects in mitochondrial metabolism and cancer. Cancer Metab 2014;2:10.

39. Boland ML, Chourasia AH, Macleod KF. Mitochondrial dysfunction in cancer. Front Oncol 2013;3:292.

40. Ribas V, Garcia-Ruiz C, Fernandez-Checa JC. Glutathione and mitochondria. Front Pharmacol 2014;5:151.

41. Koglin N, Mueller A, Berndt M, Schmitt-Willich H, Toschi L, Stephens AW, et al. Specific PET imaging of xC- transporter activity using a (1)(8)F-labeled glutamate derivative reveals a dominant pathway in tumor metabolism. Clin Cancer Res 2011;17(18):6000-11.

42. Andersen JL, Kornbluth S. The tangled circuitry of metabolism and apoptosis. Mol Cell 2013;49(3):399-410.

43. Plathow C, Weber WA. Tumor cell metabolism imaging. J Nucl Med 2008;49 Suppl 2:43S-63S.

44. Ruiz-Perez MV, Sanchez-Jimenez F, Alonso FJ, Segura JA, Marquez J, Medina MA. Glutamine, glucose and other fuels for cancer. Curr Pharm Des 2014;20(15):2557-79.

45. Andersen AP, Moreira JM, Pedersen SF. Interactions of ion transporters and channels with cancer cell metabolism and the tumour microenvironment. Philos Trans R Soc Lond B Biol Sci 2014;369(1638):20130098.

46. Icard P, Kafara P, Steyaert JM, Schwartz L, Lincet H. The metabolic cooperation between cells in solid cancer tumors. Biochim Biophys Acta 2014;1846(1):216-25.

47. Resendis-Antonio O, Gonzalez-Torres C, Jaime-Munoz G, Hernandez-Patino CE, Salgado-Munoz CF. Modeling metabolism: A window toward a comprehensive interpretation of networks in cancer. Semin Cancer Biol 2014.

48. Hsu PP, Sabatini DM. Cancer cell metabolism: Warburg and beyond. Cell 2008;134(5):703-7.

49. Zhao Y, Butler EB, Tan M. Targeting cellular metabolism to improve cancer therapeutics. Cell Death Dis 2013;4:e532.

50. Wise DR, Thompson CB. Glutamine addiction: a new therapeutic target in cancer. Trends Biochem Sci 2010;35(8):427-33.

51. Thorens B, Mueckler M. Glucose transporters in the 21st Century. Am J Physiol Endocrinol Metab 2010;298(2):E141-5.

52. Bezerra DP, Militao GC, de Castro FO, Pessoa C, de Moraes MO, Silveira ER, et al. Piplartine induces inhibition of leukemia cell proliferation triggering both apoptosis and necrosis pathways. Toxicol In Vitro 2007;21(1):1-8.

53. Raj L, Ide T, Gurkar AU, Foley M, Schenone M, Li X, et al. Selective killing of cancer cells by a small molecule targeting the stress response to ROS. Nature 2011;475(7355):231-4.

54. Schumacker PT. Reactive oxygen species in cancer cells: live by the sword, die by the sword. Cancer Cell 2006;10(3):175-6.

55. Ravindran J, Prasad S, Aggarwal BB. Curcumin and cancer cells: how many ways can curry kill tumor cells selectively? AAPS J 2009;11(3):495-510.

56. McCommis KS, McGee AM, Laughlin MH, Bowles DK, Baines CP. Hypercholesterolemia increases mitochondrial oxidative stress and enhances the MPT response in the porcine myocardium: beneficial effects of chronic exercise. Am J Physiol Regul Integr Comp Physiol 2011;301(5):R1250-8.

57. Montero J, Mari M, Colell A, Morales A, Basanez G, Garcia-Ruiz C, et al. Cholesterol and peroxidized cardiolipin in mitochondrial membrane properties, permeabilization and cell death. Biochim Biophys Acta 2010;1797(6-7):1217-24.

58. Lu C, Armstrong JS. Role of calcium and cyclophilin D in the regulation of mitochondrial permeabilization induced by glutathione depletion. Biochem Biophys Res Commun 2007;363(3):572-7.

59. Papadopoulos V, Miller WL. Role of mitochondria in steroidogenesis. Best Pract Res Clin Endocrinol Metab 2012;26(6):771-90.

60. Miller WL. Steroid hormone synthesis in mitochondria. Mol Cell Endocrinol 2013;379(1-2):62-73.

61. Nagler R, Ben-Izhak O, Savulescu D, Krayzler E, Akrish S, Leschiner S, et al. Oral cancer, cigarette smoke and mitochondrial 18kDa translocator protein (TSPO) - In vitro, in vivo, salivary analysis. Biochim Biophys Acta;1802(5):454-61.

62. Maaser K, Grabowski P, Sutter AP, Hopfner M, Foss HD, Stein H, et al. Overexpression of the peripheral benzodiazepine receptor is a relevant prognostic factor in stage III colorectal cancer. Clinical Cancer Research 2002;8(10):3205-09.

63. Galiegue S, Casellas P, Kramar A, Tinel N, Simony-Lafontaine J. Immunohistochemical assessment of the peripheral benzodiazepine receptor in breast cancer and its relationship with survival. Clin Cancer Res 2004;10(6):2058-64.

64. Miettinen H, Kononen J, Haapasalo H, Helen P, Sallinen P, Harjuntausta T, et al. Expression of Peripheral-Type Benzodiazepine Receptor and Diazepam-Binding Inhibitor in Human Astrocytomas - Relationship to Cell-Proliferation. Cancer Research 1995;55(12):2691-95.

65. Hardwick M, Fertikh D, Culty M, Li H, Vidic B, Papadopoulos V. Peripheral-type benzodiazepine receptor (PBR) in human breast cancer: Correlation of breast cancer cell aggressive phenotype with PBR expression, nuclear localization, and PBR-mediated cell proliferation and nuclear transport of cholesterol. Cancer Research 1999;59(4):831-42.

66. Veenman L, Shandalov Y, Gavish M. VDAC activation by the 18 kDa translocator protein (TSPO), implications for apoptosis. J Bioenerg Biomembr 2008;40(3):199-205.

67. Hanahan D, Weinberg RA. Hallmarks of cancer: the next generation. Cell 2011;144(5):646-74.

68. Boohaker RJ, Zhang G, Carlson AL, Nemec KN, Khaled AR. BAX supports the mitochondrial network, promoting bioenergetics in nonapoptotic cells. Am J Physiol Cell Physiol 2011;300(6):C1466-78.

69. Danial NN, Gramm CF, Scorrano L, Zhang CY, Krauss S, Ranger AM, et al. BAD and glucokinase reside in a mitochondrial complex that integrates glycolysis and apoptosis. Nature 2003;424(6951):952-6.

70. Zhao Y, Altman BJ, Coloff JL, Herman CE, Jacobs SR, Wieman HL, et al. Glycogen synthase kinase 3alpha and 3beta mediate a glucose-sensitive antiapoptotic signaling pathway to stabilize Mcl-1. Mol Cell Biol 2007;27(12):4328-39.

71. Alves NL, Derks IA, Berk E, Spijker R, van Lier RA, Eldering E. The Noxa/Mcl-1 axis regulates susceptibility to apoptosis under glucose limitation in dividing T cells. Immunity 2006;24(6):703-16.

72. Kawauchi K, Araki K, Tobiume K, Tanaka N. p53 regulates glucose metabolism through an IKK-NF-kappaB pathway and inhibits cell transformation. Nat Cell Biol 2008;10(5):611-8.

73. Hu W, Zhang C, Wu R, Sun Y, Levine A, Feng Z. Glutaminase 2, a novel p53 target gene regulating energy metabolism and antioxidant function. Proc Natl Acad Sci U S A 2010;107(16):7455-60.

74. Suzuki S, Tanaka T, Poyurovsky MV, Nagano H, Mayama T, Ohkubo S, et al. Phosphate-activated glutaminase (GLS2), a p53-inducible regulator of glutamine metabolism and reactive oxygen species. Proc Natl Acad Sci U S A 2010;107(16):7461-6.

75. Hight MR, Cheung YY, Nickels ML, Dawson ES, Zhao P, Saleh S, et al. A peptide-based positron emission tomography probe for in vivo detection of caspase activity in apoptotic cells. Clin Cancer Res 2014;20(8):2126-35.

# CHAPTER 3

# A PEPTIDE-BASED PET PROBE FOR THE DETECTION OF CASPASE ACTIVITY IN APOPTOTIC CELLS

## 3.1. Abstract

Apoptosis, or programmed cell death, can be leveraged as a surrogate measure of response to therapeutic interventions in medicine. Cysteine aspartic acid-specific proteases, or caspases, are essential determinants of apoptosis signaling cascades and represent promising targets for molecular imaging.

To this end, we reported in Clinical Cancer Research that [$^{18}$F]4-fluorobenzylcarbonyl-Val-Ala-Asp(OMe)-fluoromethylketone ([$^{18}$F]FB-VAD-FMK), a novel and potentially translatable molecular probe, enables quantification of caspase activity *in vivo* using positron emission tomography (PET) imaging. Supported by molecular modeling studies and subsequent in vitro assays suggesting probe feasibility the labeled pan-caspase inhibitory peptide, [$^{18}$F]FB-VAD-FMK, was produced in high radiochemical yield and purity using a simple two-step, radiofluorination. The biodistribution of [$^{18}$F]FB-VAD-FMK in normal tissue and its efficacy to predict response to molecularly targeted therapy in tumors was evaluated using microPET imaging of mouse models of human colorectal cancer (CRC). Accumulation of [$^{18}$F]FB-VAD-FMK was found to agree with elevated caspase-3 activity in response to Aurora B kinase inhibition as well as a multi-drug regimen that combined an inhibitor of mutant BRAF and a dual PI3K/mTOR inhibitor in $^{V600E}$BRAF colon cancer. In both scenarios, noninvasive imaging of caspase activity provided molecular insights into treatment response not previously captured by imaging phosphatidylserine externalization. [$^{18}$F]FB-VAD-FMK PET was also elevated in the tumors of cohorts that exhibited

reduction in size in response to combined inhibition of mutant BRAF and PI3K/mTOR. These studies illuminate [$^{18}$F]FB-VAD-FMK as a promising PET imaging probe to detect apoptosis in tumors and as a novel, potentially translatable biomarker for predicting response to personalized medicine.

### 3.2. Introduction

Cell death proceeds through multiple, mechanistically distinct processes that include necrosis, autophagy, mitotic catastrophe, and apoptosis (1,2). Apoptosis, or programmed cell death, is an orchestrated process that facilitates elimination of unnecessary, damaged, or compromised cells to confer an overall advantage to the host organism. As such, apoptosis is an essential component of embryonic development, tissue homeostasis, and immunological competence. Deviations from normal apoptotic programs are frequently associated with human diseases such as cancer (3). Since many anti-cancer therapies aim to selectively induce apoptosis in tumor cells (4,5), quantitative, non-invasive imaging biomarkers that reflect apoptosis represent promising tools to improve drug discovery and predict early responses in patients (6-10).

Clinically robust molecular imaging biomarkers of apoptosis have been sought after for many years, but none have yet proven optimal. Classically, molecular imaging measures of apoptosis have relied upon labeled forms of the 36 kDa protein Annexin V, which binds to externalized phosphatidylserine on the plasma membrane of cells undergoing apoptosis (7,11). Though functionalization of Annexin V for optical (9,10), single-photon emission computed tomography (SPECT) (12,13), and positron emission tomography (PET) (14,15) imaging have been reported, imaging probes based on Annexin V generally suffer from limitations that include suboptimal biodistribution and pharmacokinetics, calcium ion-dependency (16), and a lack of specificity (17-19). Another promising approach that capitalizes upon cell membrane alterations associated

with apoptosis utilizes a small molecule known as $^{18}$F-ML-10, which has been evaluated in a limited number of patients (20,21). The strengths and weaknesses of this approach are under investigation at a number of institutions. Other intracellular molecular targets within the apoptosis signaling cascade represent opportunities for molecular probe development. For example, as regulators of extrinsic and intrinsic apoptosis (**Fig. 3.1**), caspases have been suggested as promising targets for molecular imaging and for drug development (6,22).

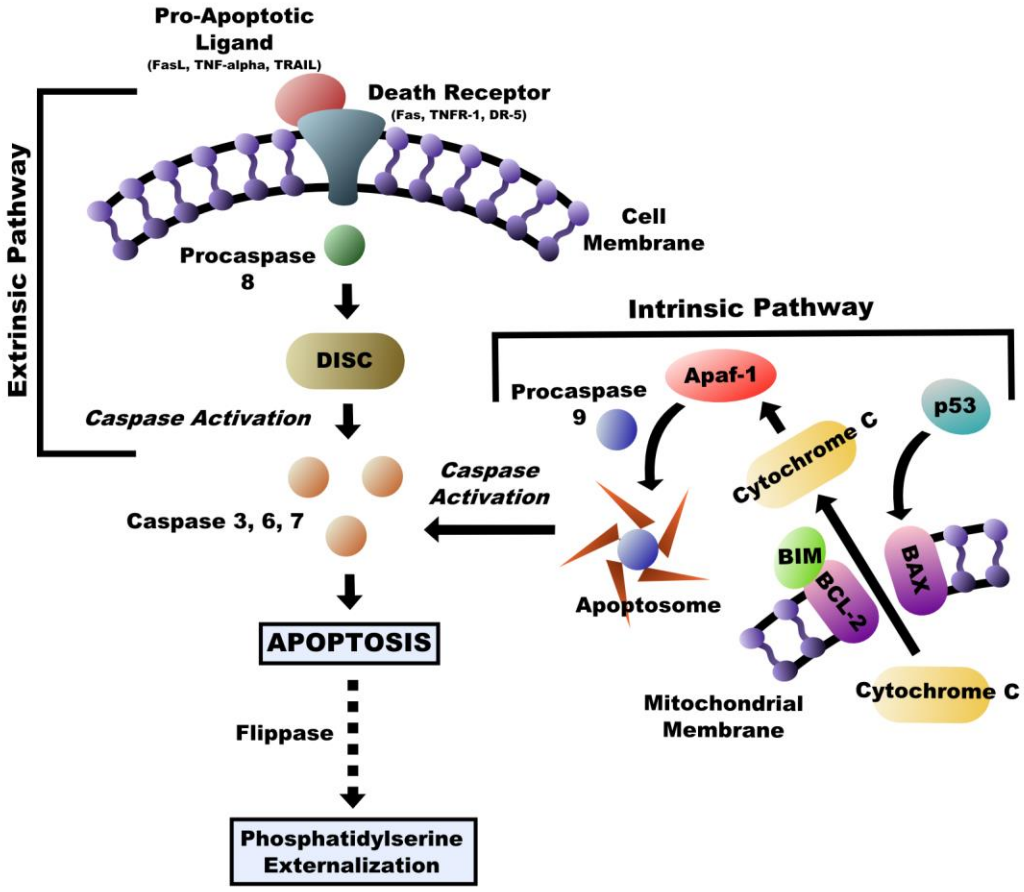


**Figure 3.1. The role of caspases in programmed cell death.** Apoptosis can proceed through two pathways; an extrinsic mechanism initiated by ligand-mediated interactions with cell-surface death receptors and an intrinsic mechanism initiated primarily through the mitochondria (2). Both pathways are highly regulated by cysteine aspartic acid specific proteases (caspases) which consist of initiators, caspase-2/8/9/10, and effectors, caspases 3/6/7. The nature of apoptosis regulation distinguishes it from other cell death mechanisms, such as necrosis and autophagy (1,2).

The goal of this study was to explore the utility of a peptide-based pan-caspase inhibitor, the modified tripeptide sequence Val-Ala-Asp(OMe)-fluoromethylketone (VAD-FMK) (23,24), to serve as the basis for developing a PET imaging probe for detecting apoptosis. Successful functionalization of VAD-FMK and similar FMK peptides with fluorescent labels (25-28) suggest the feasibility of developing PET agents based on this sequence that possess translational potential. To this end, we reported in Clinical Cancer Research that [$^{18}$F]4-fluorobenzylcarbonyl-Val-Ala-Asp(OMe)-fluoromethylketone ([$^{18}$F]FB-VAD-FMK), a novel and potentially translatable molecular probe, enables quantification of caspase activity *in vivo* using PET imaging (29). Utilizing small animal microPET imaging of multiple models of human colorectal cancer (CRC), we demonstrate that *in vivo* tumor accumulation of [$^{18}$F]FB-VAD-FMK accurately reflects elevated caspase-3 activity in response to Aurora B kinase inhibition as well as a multi-drug regimen that combined an inhibitor of mutant BRAF and a dual PI3K/mTOR inhibitor. Furthermore, though these studies illuminate [$^{18}$F]FB-VAD-FMK as a promising tool compound, more generally, these studies suggest that labeled VAD-FMK peptides warrant further development as potential scaffolds for development of translational molecular imaging probes.

### 3.3. Materials and Methods

*Chemicals*

VAD-FMK (American Peptide) and Z-VAD-FMK (TOCRIS Bioscience, #2163) were obtained commercially and used without further purification. Unless otherwise indicated, all other chemicals, reagents, and solvents were purchased from Sigma-Aldrich and used as received.

*Molecular Modeling*

Co-crystal structures for the caspase-3 protein with an aza-peptide epoxide inhibitor (PDB ID 2CNN) (30) and a covalently bound β-strand peptidomimetic inhibitor (PDB ID 3KJF) (31) were obtained from the Brookhaven Protein Data Bank and used to evaluate the potential of prosthetically labeled VAD-FMK, and deviations thereof, to be accommodated within the active caspase-3 binding domain. Structural alignment of both caspase-3 inhibitor co-crystal structures was performed using PyMOL (Molecular Graphics System, Version 1.5.0.4, Schrödinger, LLC) to reveal a minor 0.22 angstrom β-carbon protein backbone coordinate root mean squared deviation (RMSD). Both caspase-3 inhibitor-binding sites were treated as energetically equivalent and the smaller β-strand peptidomimetic inhibitor structure (PDB ID 3KJF) was chosen as the starting point for molecular docking calculations. Following removal of the co-crystallized covalent inhibitor ligand, molecular docking was performed using the high resolution, flexible SurflexDock GeomX protocol as implemented in SYBYL-X 2.0 (Tripos International, 1699 South Hanley Rd., St. Louis, Missouri, 63144, USA), with a protomol target based on the β-strand peptidomimetic inhibitor structure with the addition of a 2.0 angstrom bloat parameter. Best scoring energy-minimized docked poses were ranked using the Tripos SYBYL Surflex-Dock flexible protein scoring function, PF-score (Crash parameter) for FB-VAD-FMK, Z-VAD-FMK, IZ-VAD-FMK and VAD-FMK were determined for comparison of physically plausible, low energy minimized conformations in the bound state across the proposed peptide ligand modifications.

*Synthesis of [$^{19}$F]4-Succinimidyl-4-Fluorobenzoate ([$^{19}$F]SFB) (1)*

4-[$^{19}$F]Fluorobenzoic acid and *N*,*N*,*N'*,*N'*-tetramethyl-*O*-(*N*-succinimidyl)uronium tetrafluoroborate (1:1.5) were combined in a round bottom flask with acetonitrile for a final 4-[$^{19}$F]fluorobenzoic acid concentration of 71.4 mM. Upon reaching the final reaction

temperature, 45-50 °C, solid tetramethylammonium hydroxide (TMAH, 1.5 eq) was added to the reaction mixture. The reaction vessel was flushed with positive $N_{2(g)}$ pressure and held at this temperature overnight (16-18 h) with stirring. [$^{19}$F]SFB (**1**) formation was monitored by normal phase thin layer chromatography (TLC) (1:1, ethyl acetate:chloroform, $R_F$ = 0.76). Purification was performed by flash chromatography with SNAP silica cartridges using an hexanes:ethyl acetate gradient (100% 0-1 min, 100-70% 1-10 min, 70% 10-15 min, 70-30% 15-25 min, 30% 25-35 min; all percentiles with respect to hexanes) on a Biotage flash purification system to give the final, pure product in up to 85% yield. $^1$H-NMR characterization matched that of commercially available authentic compound purchased from Advanced Biochemical Compounds (ABX).

*Synthesis of [$^{19}$F]4-fluorobenzylcarbonyl-VAD-FMK ([$^{19}$F]FB-VAD-FMK) (3)*

Upon synthesis, (**1**) was conjugated to VAD-FMK peptide (**2**) (American Peptide Company) through the N-terminus to form the non-radioactive probe analogue, [$^{19}$F]FB-VAD-FMK (**3**) (**Fig. 3.2A**). Compounds (**1**) and (**2**) were reconstituted separately in anhydrous dimethylformamide (DMF) with equimolar amounts of *N*,*N*-diisopropylethylamine (DIPEA). Solution (**2**) was added drop-wise to solution (**1**) for a final compound (**2**) concentration of 37.5 mM and final molar equivalencies: 1:2:2 [(**1**):(**2**):DIPEA]. The reaction vessel was then flushed with positive $N_{2(g)}$ pressure, heated to 55 °C, and held at that temperature overnight (16-18 h) with stirring. Product formation was monitored by TLC [6:4, dichloromethane (DCM):(chloroform:methanol:triethylamine (TEA), 8:1.8:0.2), $R_F$ = 0.5]. Authentic compound was isolated from free peptide and unconjugated [$^{19}$F]SFB using reversed-phase high-performance liquid chromatography (HPLC) (Varian Dynamax, Microsorb C18, 8 µm, 21.4 x 250 mm, λ = 254 nm). The product eluted between 22-24 min using a phosphate buffer (1 mM):acetonitrile gradient (85% 0-2 min, 85-60% 2-10 min, 60% 10-15 min, 60-30% 15-22 min, 30% 22-40 min; all

percentiles with respect to aqueous phase) at a flow rate of 10 mL/min. The final product was rinsed with ethyl acetate and obtained in up to 65% yield.

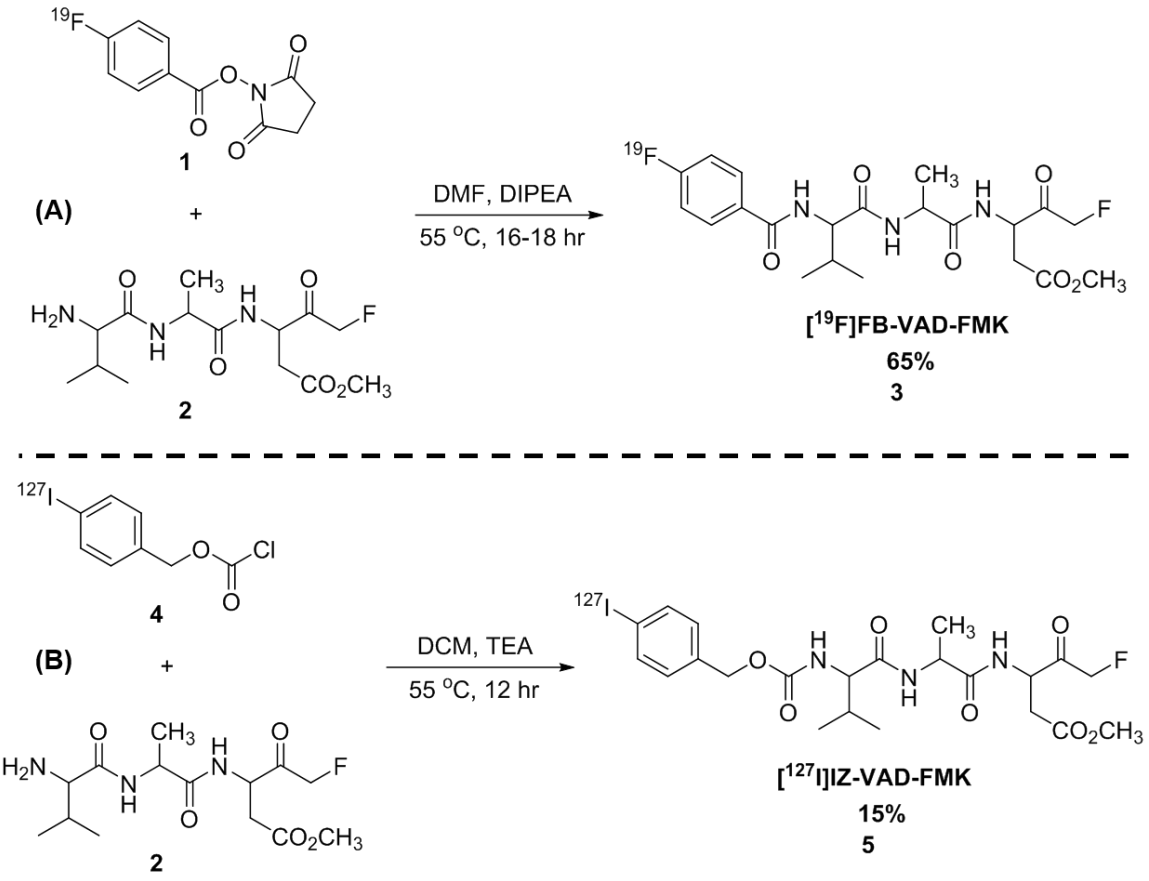


**Figure 3.2. Cold compound synthesis.** [$^{19}$F]FB-VAD-FMK (**3**) (**A**) and [$^{127}$I]IZ-VAD-FMK (**5**) (**B**) synthetic routes (29).

High-resolution mass spectroscopy (HRMS) was performed using a Waters Synapt Quadrupole Time-of-Flight high-resolution mass spectrometer equipped with a dual channel ESCI ion source. HRMS calculated for $C_{21}H_{28}F_2N_3O_6$ *m/z* = 456.1946 $(M)^+$, found 456.1945. $^1$H, $^{13}$C, and $^{19}$F nuclear magnetic resonance (NMR) spectra were recorded on a Bruker 400 MHz spectrometer. Chemical shifts are reported in ppm using residual DMSO as the internal standard (2.50 ppm for $^1$H, 39.51 ppm for $^{13}$C). The following abbreviations are used for multiplicity of NMR signals: s = singlet, d = doublet, dd = doublet of doublets, t = triplet, q = quartet, sep = septet, m = multiplet. $^1$H-NMR

($(CD_3)_2SO$, 400 MHz) δ: 8.62 (d, 1H, *J* = 7.41 Hz), 8.48 (d, 1H, *J* = 7.88 Hz), 8.35-8.27 (m, 2H), 7.94 (m, 2H), 7.28 (t, 2H, *J* = 8.45 Hz), 5.32-5.04 (m, 2H), 4.64 (q, 1H, *J* = 6.90 Hz), 4.48 (q, 1H, *J* = 6.84 Hz), 4.28 (t, 1H, *J* = 8.17 Hz), 4.22-4.12 (m, 1H), 3.59 (s, 3H), 2.86-2.79 (m, 1H), 2.67-2.58 (m, 1H), 2.09 (sep, 1H, *J* = 6.84 Hz), 1.21 (dd, 3H, *J* = 7.08 Hz, *J* = 3.73 Hz), 0.95-0.89 (m, 6H). $^{13}$C-NMR ($(CD_3)_2SO$, 400 MHz, $^1$H decoupled) δ: 197.87, 197.73, 197.52, 197.38, 168.54, 168.41, 166.63, 166.57, 166.28, 166.10, 161.07, 161.05, 160.60, 158.13, 125.73, 125.64, 110.65, 110.44, 54.27, 47.76, 47.15, 47.12, 47.01, 44.07, 43.74, 29.51, 29.23, 25.56, 14.65, 14.31, 14.28, 12.82, 12.73. $^{19}$F-NMR ($(CD_3)_2SO$, 400 MHz, $^1$H decoupled) δ: -107.36, -230.90, -231.06.

*Synthesis of [$^{127}$I]4-iodobenzyl chloroformate (4)*

[$^{127}$I]4-Iodobenzyl alcohol was solubilized in chilled anhydrous dichloromethane (DCM) (0 °C) and added drop-wise to solid triphosgene (1:1) in a reaction vessel under positive $N_{2(g)}$ pressure, with stirring, at 0 °C. Final concentration of 4-[$^{127}$I]iodobenzyl alcohol and triphosgene was 674 mM. Reaction mixture was maintained at 0 °C with stirring for 15 min, then brought to room temperature and stirred overnight (16-18 h) protected from light. [$^{127}$I]4-iodobenzyl chloroformate (**4**) formation was monitored by normal phase TLC (2:8, ethyl acetate:hexanes, $R_F$ = 0.64). The reaction solvent was removed by rotary evaporation to obtain a mixture of an off-white solid and a brown-colored liquid. The mixture was subsequently washed with hexanes and the liquid phase extracted. Hexanes were removed to obtain (**4**) as a brown-liquid that was used immediately without further purification.

*Synthesis of [$^{127}$I]4-iodobenzyloxycarbonyl-Val-Ala-Asp(OMe)-fluoromethylketone ([$^{127}$I]IZ-VAD-FMK) (5)*

[$^{127}$I]IZ-VAD-FMK was synthesized as the para-iodinated regioisomer. Here, (**4**) was conjugated to (**2**) to form (**5**) (**Fig. 3.2B**). Compounds (**4**) and (**2**) were reconstituted separately in chilled anhydrous DCM (0 °C) with TEA. Solution (**4**) was added drop-wise to (**2**) in a reaction vessel under positive $N_{2(g)}$ pressure, with stirring, at 0 °C for a final compound (**2**) concentration of 60 mM and final molar equivalencies: 4:1:2 [(**4**):(**2**):TEA]. The reaction mixture was maintained at 0 °C with stirring for 15 min, then brought to room temperature and subsequently heated at 55 °C, with stirring, for 12 h, protected from light. Product formation was monitored by TLC [6:4, DCM:(chloroform:methanol:TEA, 8:1.8:0.2), $R_F$ = 0.30]. The authentic compound was isolated from free peptide and (**4**) using HPLC (Varian Dynamax, Microsorb C18, 8 µm, 21.4 x 250 mm, λ = 254 nm). The product eluted between 22-24 min using a phosphate buffer (1 mM):acetonitrile gradient (85% 0-2 min, 85-60% 2-10 min, 60% 10-15 min, 60-30% 15-22 min, 30% 22-40 min; all percentiles with respect to the aqueous phase) at a flow rate of 10 mL/min. The final product was received in approximately 15% yield.

High-resolution mass spectroscopy (HRMS) was performed using a Waters Synapt Quadrupole Time-of-Flight high-resolution mass spectrometer equipped with a dual channel ESCI ion source. HRMS calculated for $C_{22}H_{30}FIN_3O_7$ *m/z* = 594.1113 $(M)^+$, found 594.1107. $^1$H- and $^{13}$C-NMR spectra were recorded on a Bruker 500 MHz spectrometer. Chemical shifts are reported in ppm using residual chloroform as the internal standard (7.26 ppm for $^1$H, 77.36 ppm for $^{13}$C). The following abbreviations are used for multiplicity of NMR signals: s = singlet, br s = broad singlet, d = doublet, t = triplet, m = multiplet. $^1$H-NMR ($CDCl_3$, 500 MHz) δ: 7.69 (d, 2H, *J* = 8.28 Hz), 7.10 (m, 2H), 6.48 (br s, 1H), 5.36 (m, 1H), 5.23-5.18 (m, 1H), 5.13-4.97 (m, 4H), 4.91 (m, 1H), 4.52-4.45 (m, 1H), 3.97 (t, 1H, J = 6.82 Hz), 3.68 (s, 3H), 3.13-3.08 (m, 1H), 3.03-2.98

(m, 1), 2.91-2.84 (m, 1), 2.17-2.09 (m, 1H), 1.42-1.37 (m, 4H), 1.25 (s, 2H), 0.98-0.92 (m, 7H). $^{13}$C-NMR ($CDCl_3$, 500 MHz, $^{1}$H decoupled) δ: 202.56, 172.39, 171.68, 171.62, 156.80, 138.06, 136.05, 130.32, 130.27, 94.33, 85.35, 85.26, 83.89, 83.80, 66.94, 61.00, 52.64, 52.31, 49.33, 35.17, 31.14, 30.05, 19.58, 18.31, 18.10, 8.96.

*Enzyme Selectivity Assay*

Relative enzyme inhibition of [$^{19}$F]FB-VAD-FMK was evaluated against caspase-3/6/7/8 using homogeneous caspase fluorescence assay kits (BPS Bioscience) and compared to parent peptide. Caspase inhibitor dissolved in caspase assay buffer and 1% DMSO (0.0003 – 10 μM) was combined with the caspase assay substrate and enzyme at room temperature for 30 min in accordance with the manufacturer's instructions. Fluorescence intensity was measured at an excitation of 360 nm and an emission of 460 nm using an Infinite M1000 microplate reader (Tecan).

*Analysis of Lipophilicity*

Lipophilicity characterization of compounds (**3**) and (**5**), as well as Z-VAD-FMK, was performed through log $P_{7.5}$ quantification using methodology analogous to those previously reported (32). Using reversed phase HPLC (Phenomenex Luna C18, 5 μm, 100 Å, 4.6 x 250 mm) and a (85:15) phosphate buffer (2 mM, pH 7.5) isocratic system (1 mL/min), log $P_{7.5}$ values were calculated using an average of compound retention times from three individual runs and standard curve derived linear regression. The following standards with known log *P* values were used for curve development: catechol, aniline, benzene, bromobenzene, toluene, ethylbenzene, 2-chlorobiphenyl, biphenyl, 1-chloronaphthalene, 1,2,3-trimethylbenzene, 1,2,3,4-tetrachlorobenzene, 1,2,4,5-tetrabromobenzene, and pentachlorobenzene. Log $P_{7.5}$ values were found to be 1.41, 2.38, and 2.20 for (**3**), (**5**), and Z-VAD-FMK, respectively.

*Biochemical Caspase-3 Inhibition Assay*

Caspase-Glo 3/7 (Promega) was employed as a readout of inhibition where by a caspase-cleavable protected luciferase substrate is directly sensitive to caspase-3/7 activity and quantifiable by bioluminescence (33). Caspase inhibitor dissolved in DMSO (0, 0.1, 1, 10, 100, 1000, or 10000 nM) was combined with recombinant human caspase-3 enzyme (C1224-10UG, Sigma) (100 nM) in 1X phosphate buffered saline (PBS) in microcentrifuge tubes, vortexed, and incubated at 37°C for 30 min. After incubation, Caspase-Glo 3/7 reagent (Promega) was added in accordance with the manufacturer's instructions. Solutions were vortexed, incubated for an additional 30 min, and dispensed into opaque wall/bottom 384-well plates (BD Biosciences) for measurement of caspase activity. Sample luminescence was measured using a Synergy 4 plate reader (BioTek).

*Cellular Caspase Inhibition Assay*

DiFi cells were propagated in Dulbecco's Modified Eagle's Medium (DMEM, Mediatech) and supplemented with 10% fetal bovine serum (Atlanta Biologicals) and 1 mg/mL gentamycin sulfate (Gibco) in a 95% humidity, 5% $CO_2$, 37°C atmosphere. Cells were seeded as sub-confluent monolayer cultures at a density of 1 x $10^4$ per well into 96-well, black wall/bottom plates (BD Biosciences) and allowed to adhere for 24 h at 37°C. For evaluation of caspase-3/7 inhibition concomitant with drug exposure, DiFi cells were incubated with cetuximab (0.5 µg/mL) for 24 h, based on our experience from previous work (9). Cell media was then replaced with 1X PBS containing inhibitor (0, 10, 100, 1000, 10000 nM) and incubated at 37°C for 30 min. Inhibition was assessed using Caspase-Glo 3/7 reagent in accordance with the manufacturer's instructions. Luminescence was quantified using a Synergy 4 plate reader.

*Radiochemical Production of [$^{18}$F]4-fluorobenzylcarbonyl-VAD-FMK ([$^{18}$F]FB-VAD-FMK) (11)*

[$^{18}$F]SFB was prepared using commercial GE TRACERlab-Synthesizer MX production kits (ABX) with a BIOSCAN Coincidence radiochemistry module. The automated synthetic route included flourine-18 radiolabeling of 4-[1,1-dimethylethyl ester]-*N*,*N*,*N*-trimethyl-benzenammonium triflate (**6**) to 4-[$^{18}$F]-1,1-dimethylethyl ester benzoic acid (**7**), deprotection of 4-[$^{18}$F]fluorobenzoic acid (**8**) through alcoholic saponification, and subsequent formation of the activated ester [$^{18}$F]SFB (**9**) from (**8**) (**Fig. 3.3A**). Radiochemical purity (95 ± 2%) was determined by analytical HPLC (Hitachi High Technologies LaChrom C18, 5 µm, 4.6 x 150 mm, 1 mL/min, 20-70% acetonitrile:water over 15 min, retention time (RT) = 11.5 min, λ = 254 nm). [$^{18}$F]SFB was delivered in approximately 3 mL of 4:1 acetonitrile:water, a decay-corrected radiochemical yield of 36 ± 4%, and concentrated to < 0.5 mL using positive nitrogen pressure and heating at 55 °C. Once concentrated, VAD-FMK (10 mg/mL DMF) and DIPEA (30 µmol) were added to [$^{18}$F]SFB (7.4-13.0 GBq) and heated in a sealed vessel at 55 °C for 45 min (**Fig. 3.3B**). [$^{18}$F]FB-VAD-FMK was purified using semi-prep reversed-phase HPLC (Waters Sunfire C18, 5 µm, 10 x 150 mm) and eluted between 17.7-19 min using a phosphate buffer (1 mM):acetonitrile gradient (85% 0-5 min, 85-60% 5-15 min, 60% 15-25 min, 60-30% 25-45 min; all percentiles in respect to aqueous phase) with a 4 mL/min flow rate (**Fig. 3.3C**). The product fraction was diluted 100-fold with water and passed through a C18 Sep-Pak (Waters). Labeled peptide was eluted with ethanol into a sterile flask and loaded with normal saline (0.9%). Volumes of eluent were modified as needed to ensure a final concentration of 74-185 MBq/mL (1/9, ethanol/saline) with a decay corrected radiochemical yield of 24 ± 8%. [$^{18}$F]SFB conjugation efficiency of crude product (55 ± 6%) and radiochemical purity of final post-

prep product (98 ± 1%) were determined using analytical HPLC (Phenomenex Luna C18, 5 µm, 100 Å, 4.6 x 250 mm) and the following phosphate buffer (1 mM): acetonitrile gradient: 85% 0-2 min, 85-30% 2-10 min, 30% 10-35 min; all percentiles in respect to aqueous phase (flow rate = 1 mL/min, RT = 12.3 min). Specific activities for [$^{18}$F]SFB (83 ± 56 TBq/mmol) and [$^{18}$F]FB-VAD-FMK (5 ± 3 TBq/mmol) were calculated using an HPLC-derived standard curve. Radiochemical purity, specific activity, and other synthesis results for both [$^{18}$F]SFB and [$^{18}$F]FB-VAD-FMK are summarized in **Table 3.1**.

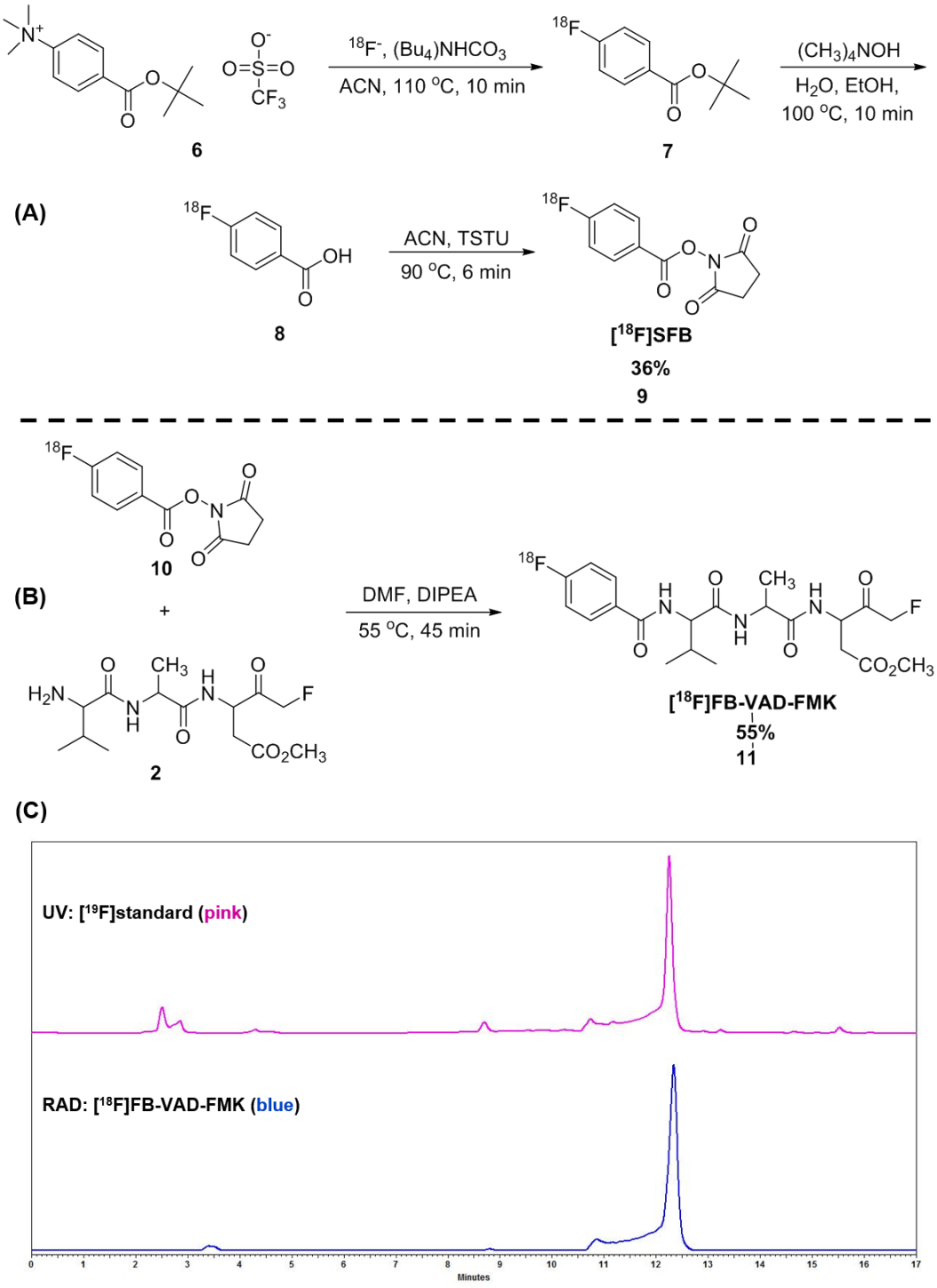


**Figure 3.3. Radiosynthesis and purification.** [$^{18}$F]SFB (**9**) (A) and [$^{18}$F]FB-VAD-FMK (**11**) (B) synthetic schemes. Compound (**9**) radiosynthesis was performed systematically using an automated radiochemistry module. HPLC radiochromatogram of post-prep (**11**) (blue, bottom) is shown overlaid with UV-chromatogram of [$^{19}$F]standard (**3**) (pink, top) (C).

| [$^{18}$F]SFB | | | [$^{18}$F]FB-VAD-FMK | | | |
|---|---|---|---|---|---|---|
| cRCY (%) | RCP (%) | SA (TBq/mmol) | Conj (%) | cRCY (%) | RCP (%) | SA (TBq/mmol) |
| 33 | 95 | 22 | 63 | 34 | 98 | 4 |
| 36 | 98 | 59 | 52 | 23 | 98 | 4 |
| 33 | 93 | 163 | 52 | 17 | 98 | 11 |
| 42 | 95 | 57 | 48 | 15 | 99 | 3 |
| 39 | 97 | 115 | 60 | 31 | 99 | 6 |
| Average ± Standard Deviation | | | | | | |
| cRCY (%) | RCP (%) | SA (TBq/mmol) | Conj (%) | cRCY (%) | RCP (%) | SA (TBq/mmol) |
| 36 ± 4 | 95 ± 2 | 83 ± 56 | 55 ± 6 | 24 ± 8 | 98 ± 1 | 5 ± 3 |

**Table 3.1. Representative summary of various radiochemical productions.** Decay corrected radiochemical yields (cRCY), radiochemical purities (RCP), and specific activities (SA) for [$^{18}$F]SFB and [$^{18}$F]FB-VAD-FMK. Percent [$^{18}$F]SFB conjugation (Conj.) to peptide is also provided.

*Synthesis of NIR800-Annexin V*

Annexin V labeled with a near-infrared dye (NIR800-Annexin V*)*, suitable for *in vivo* imaging, was prepared by fluorescently labeling Annexin V with IRDye 800CW NHS Ester (LiCor Biosciences) using methods analogous to previously reported work (9,10). In place of dialysis, labeled protein was purified from unconjugated dye using Zeba Desalting Spin Columns (Thermo Scientific).

*Radiochemical Production of [$^{99m}$Tc]HYNIC-Annexin V*

Annexin V (Sigma) conjugation with succinimidyl-HYNIC hydrochloride (ABX) and subsequent radiolabeling with technetium-99m was prepared analogously to previously reported methods (12). In place of dialysis, labeled protein was purified from unconjugated HYNIC using Zeba Desalting Spin Columns (Thermo Scientific).

*Cell Cycle Assays*

For cell cycle analysis, SW620 and DLD-1 cells were propagated to 50% confluency in 6 cm plates and treated with AZD-1152-hydroxyquinazoline pyrazol anilide

(HQPA) (Selleckchem), 0, 10, 100, 1000, or 5000 nM, for 24 or 48 hrs and prepared for flow cytometry as described (9). Propidium iodide (PI)-stained cells were analyzed by flow cytometry (FACStar PLUS, Becton-Dickinson). Data analysis was performed using CellQuest software (Becton-Dickinson) by manually gating to define and quantify sub-G0, G1, S, G2/M, and polyploidy populations. For assay of apoptosis following *in vitro* AZD-1152-HQPA exposure, SW620 and DLD-1 cells were seeded as sub-confluent monolayer cultures at a density of 1 x $10^4$ per well into 96-well, black wall/bottom plates (BD Biosciences), allowed to adhere for 24 h, and treated with AZD-1152-HQPA, 0, 10, 50, 75, 100, or 1,000 nM, for 24 or 48 hrs. Apoptosis was assessed using the Caspase-Glo 3/7 reagent, in accordance with manufacturer's instructions, and analyzed using a Synergy 4 plate reader.

*Immunoblotting*

After 24 h of drug exposure, *in vitro* cell samples were collected from 10-cm plates. Medium was removed and cell monolayers washed with 1X phosphate buffered saline (PBS) followed by addition of 450 mL of lysis buffer containing: 7 mL of CelLytic M lysis buffer (Sigma), mini protease inhibitor cocktail (Roche), and 100 mL of phosphatase inhibitor cocktail 1 and 2 (Sigma). Protein concentrations were normalized using a bicinchoninic acid assay. All samples were vortexed and centrifuged prior to final cell lysate collection.

Immunoblotting was performed by loading 20-40 µg of protein into 7.5-12% SDS PAGE gels and resolved by electrophoresis. Membranes were incubated with antibodies to cleaved PARP (Cell Signaling, 9541S), cleaved caspase-3 (Cell Signaling, 9664), or GAPDH (Millipore, MAB374) and imaged on a Xenogen IVIS 200 using Western Lightning Plus-ECL (PerkinElmer) substrate.

*Animal Models*

Studies involving animals were conducted in accordance with federal and institutional guidelines. Biodistribution studies were performed using male C57BL/6 mice. Dual xenograft-bearing mice were sequentially injected with 1 x $10^7$ SW620 and 5 x $10^6$ DLD-1 human CRC cells subcutaneously onto the left or right hind limbs (respectively) of 5- to 6-week old female, athymic nude mice (Harlan Sprague-Dawley). Palpable tumors were observed 2-3 weeks following inoculation. Animals bearing SW620 and DLD-1 xenograft tumors were treated with vehicle or AZD-1152 (25 mg/kg, DMSO) *via* intraperitoneal injection once daily for five days, analogous to previous work (34). *In vivo* PET imaging studies were performed on Day 5, approximately 4-6 h after treatment.

COLO-205 and LIM-2405 xenografts were generated by subcutaneously injecting 1 x $10^7$ cells onto the right flank of 5- to 6-week old female, athymic nude mice (Harlan Sprague-Dawley). Palpable tumors were observed within three weeks following inoculation. For BEZ-235 (Selleckchem) and PLX-4720 (synthesized using reported methods) (35) single-agent treatment, animals were administered vehicle, BEZ-235 (35 mg/kg, 0.1% Tween 80 and 0.5% methyl cellulose) or PLX-4720 (60 mg/kg, DMSO) *via* oral gavage once daily for four days. For BEZ-235 and PLX-4720 combination treatment, BEZ-235 (35 mg/kg, 0.1% Tween 80 and 0.5% methyl cellulose) and PLX-4720 (60 mg/kg, DMSO) were administered *via* oral gavage as separate doses (respectively) approximately 7-8 h apart. To monitor tumor growth, tumor volumes were measured on Days 1 and 4 of treatment using a previously established ultrasound imaging based methodology (36). *In vivo* imaging studies were performed on the $4^{th}$ day (PET), based on our previous experience with BRAF inhibition *in vivo* (37).

In Vivo *Imaging and Analysis*

For all imaging studies, mice were maintained under 2% isofluorane anesthesia in 100% oxygen at 2 L/min and kept warm *via* a circulating water heating pad for the duration of the PET scan. Small-animal PET imaging was performed using a dedicated Concorde Microsystems Focus 220 microPET scanner (Siemens Preclinical Solutions). Animals were administered 7.4-9.3 MBq of [$^{18}$F]FB-VAD-FMK *via* intravenous injection. Both static and dynamic data sets were acquired. For static scans, animals were allowed free access to food and water during a 20–40 minute uptake period, followed by anesthetization and a 20-minute image acquisition. Analogously, sixty minute dynamic acquisitions for all xenografts were initiated at the time of [$^{18}$F]FB-VAD-FMK injection.

PET data were reconstructed using a three-dimensional (3D) ordered subset expectation maximization/maximum a posteriori (OSEM3D/MAP) algorithm. Dynamic data was binned into twelve 5 s (0-1 min) and fifty-nine 60 s (2-60 min) frames. The resulting three-dimensional reconstructions had an x-y voxel size of 0.474 mm and inter-slice distance of 0.796 mm. ASIPro software (Siemens Preclinical Solutions) was used to manually draw three-dimensional regions of interest (ROI) in the tumor volume. Areas of perceived necrosis were excluded when drawing ROIs. [$^{18}$F]FB-VAD-FMK uptake was quantified as the percentage of the injected dose per gram of tissue (%ID/g); for dynamic scans, only data points collected within the time frame analyzed for analogous static scans were considered.

For optical imaging studies using NIR800-Annexin V, 1 nmol of labeled protein was administered *via* retro-orbital injection. Imaging was performed using a Pearl Impulse near-infrared fluorescence imaging system (LiCor) 24 h after probe administration (5$^{th}$ day of treatment). ROI analysis was used to assess tumor-to-normal (T/N) contrast ratios where T/N = [(tumor tissue mean pixel intensity/unit area)/(normal

tissue mean pixel intensity/unit area)]. Probe uptake in normal tissue was assessed using ROIs drawn over the scapular region.

SPECT imaging studies were performed using a NanoSPECT/CT scanner (Bioscan) with image reconstruction and co-registration carried out using HiSPECT in the corresponding InVivoScope software. Animals were administered 33.3-37.0 MBq of [$^{99m}$Tc]HYNIC-Annexin V *via* intravenous injection and imaged 3 h after probe administration. During the uptake phase, animals were allowed free access to food and water. Three-dimensional ROIs were manually drawn in the tumor volume using the free computer software, Amide. Probe uptake was quantified as %ID/g.

*Immunohistochemistry (IHC)*

Tumor tissues were harvested immediately following conclusion of imaging, fixed for 24 h in 5% buffered formalin, and blocked in paraffin. Immunohistochemistry for cleaved caspase-3 (Cell Signaling, #9664) was carried out as previously described (9). Tissues were stained using standard H&E methods and reviewed by an expert gastrointestinal pathologist (M. Kay Washington). Images displayed are representative of three randomly selected high-power fields (40x).

*Semi-Quantitative IHC Analysis*

For semi-quantitative analysis of cleaved caspase-3 IHC, the public domain image processing software ImageJ was used to selectively measure the area of positive staining of each cohort through manual threshold manipulation of hue, pixel saturation, and brightness. Analysis was performed for multiple low field (2.5x) tissue micrographs and values reported as the percent area of positive staining over total staining.

*Statistical Methods*

Unless otherwise stated, experimental replicates are reported as the arithmetic mean ± standard deviation. Statistical significance of *in vitro* and *in vivo* data sets was evaluated using an unpaired, two-tailed *t*-test. Differences were assessed within the GraphPad Prism 6.01 software package and considered statistically significant if $p < 0.05$.

## 3.4. Results

*Caspase-3 Active Site Accommodates N-Terminal Functionalization of VAD-FMK*

Imaging labels should impart minimal, if any, effects upon the biological and chemical properties of the parent molecule. Given this, we initially used a molecular modeling approach to explore multiple N-terminally functionalized analogues of VAD-FMK (**Fig. 3.4A**), two of which would result in PET/SPECT imaging probes: FB-VAD-FMK, benzyloxycarbonyl-Val-Ala-Asp(OMe)-fluoromethylketone (Z-VAD-FMK), 4-iodobenzyloxycarbonyl-Val-Ala-Asp(OMe)-fluoromethylketone (IZ-VAD-FMK) (38), and VAD-FMK. Molecular docking of each peptide into an irreversible inhibitor bound protein structure of caspase-3 (PDB ID, 3KJF) (31) enabled predictions to be drawn regarding the accommodation of modified peptides into the caspase-3 active site (**Fig. 3.4B-F**). Flexible docking calculations were performed employing post-docking energy minimization for each peptide to assess potential energetic perturbations that result from N-terminal modification. Only docked poses that positioned the C-terminal fluoro-methyl ketone moiety within 5.0 angstroms of the caspase-3 active site cysteine 163 thiol moiety were considered in our analysis. All four peptides exhibited predicted binding energy scores that fell within the micromolar to nanomolar range (Total Score) and ranked by the steric bump parameter (Crash) using SurflexDock in Tripos SYBYL-X 2.0

(**Table 3.2**). The Surflex-Dock scoring term for Polar contacts suggested that the FB-VAD-FMK peptide had greater potential to form hydrogen bonds with active caspase-3 site residues relative to other candidate structures, including the parent peptide, while displaying less internal ligand Strain scores. Of note, IZ-VAD-FMK produced docking scores that reflected a lower-scoring Polar term and demonstrated that more poses buried the larger, lipophilic iodo-moiety toward the protein active site, suggesting greater lipophilicity than FB-VAD-FMK. Though exploratory in nature, these studies suggested both tolerance to functionalization of VAD-FMK at the N-terminus with the FB prosthesis and that the resulting PET imaging probe might possess favorable physical and chemical properties relative to parent peptide and the IZ-labeled form.

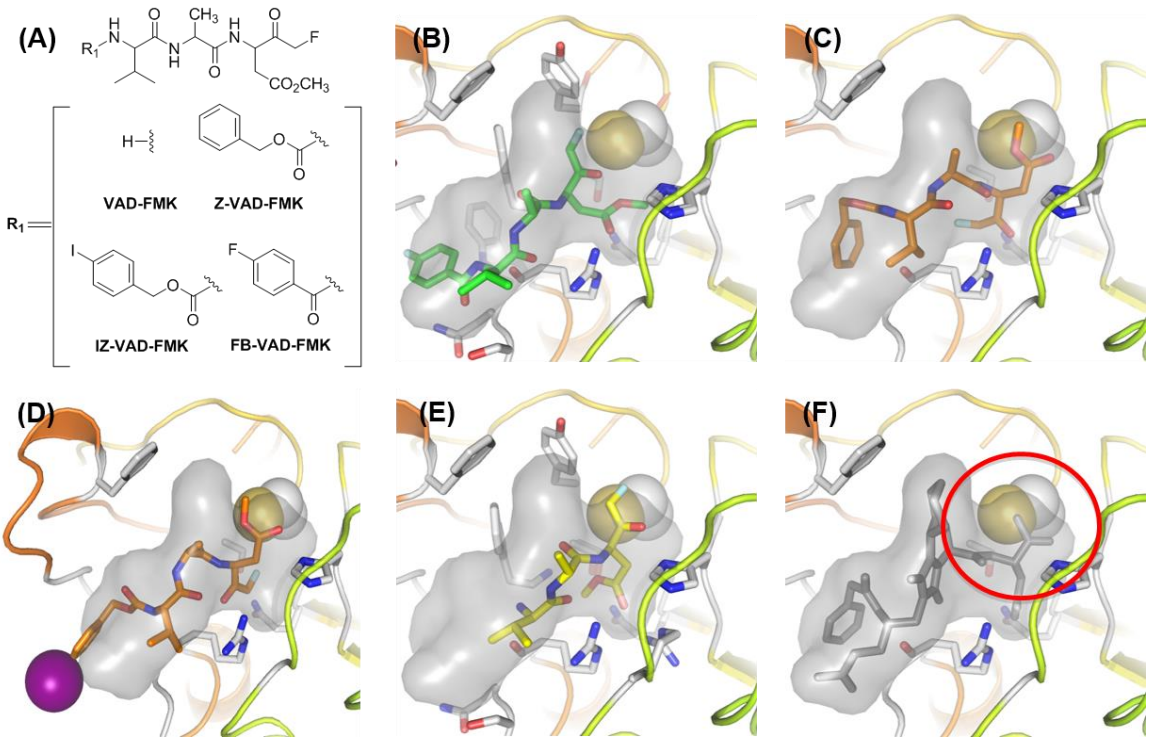


**Figure 3.4. Prioritization of FB-modified VAD-FMK peptide caspase inhibitor**. Chemical structures for R1 substitution of VAD-FMK peptide inhibitor scaffold (A). FB-VAD-FMK (green capped sticks) (B), Z-VAD-FMK (orange capped sticks) (C), IZ-VAD-FMK (orange capped sticks) (D), and VAD-FMK (yellow capped sticks) (E) shown docked into the caspase-3 protein structure (PDB ID 3KJF) (F) with covalent inhibitor removed. Covalent inhibitor protein attachment at Cys163 is shown in yellow and white VDW spheres; red circle indicates covalent inhibitor protein attachment site. Atom

colors: oxygen = red; nitrogen = blue; iodine = purple, carbon = grey. Grey VDW surfaces indicate the space-filling shape of the covalent bound inhibitor in PDB ID 3KJF.

| Compound | Total Score (-log $K_d$) | Crash | Polar | Strain | Similarity |
|---|---|---|---|---|---|
| FB-VAD-FMK | 6.2458 | 0.861 | 5.676 | 0.7802 | 0.2979 |
| Z-VAD-FMK | 8.6257 | 1.004 | 4.6776 | 3.0018 | 0.5373 |
| IZ-VAD-FMK | 9.5465 | 1.381 | 4.3824 | 1.4081 | 0.5396 |
| VAD-FMK | 6.1466 | 1.155 | 4.8703 | 2.567 | 0.4582 |

**Table 3.2. Structural effects of peptide modification on binding to caspase-3.** Docking scores are reported as ranked by the Crash (steric repulsion) score from the protein flexibility (PF-score) scoring function of the Tripos SYBYL-X v2.0 software suite that also features (among other scoring parameters) comparison with SurflexDock Total_Score (statistical estimate of binding affinity, -log $K_d$), Polar (measure of polar contacts), Strain (measure of internal ligand energetic strain) and Similarity (index of shape-based morphological similarity to reference covalent inhibitor compound) term score parameters. Proposed N-terminal modifications to the VAD-FMK peptide scaffold all scored comparably using these criteria indicating minimal predicted perturbation to interactions with the caspase-3 protein target (29).

*Enzyme Selectivity of VAD-FMK Peptide Analogues*

From the binding mechanism of VAD-FMK-type peptides (23,39), we anticipated that FB-VAD-FMK would exhibit caspase selectivity similar to that of the parent peptide. To explore this, we evaluated the relative affinity of [$^{19}$F]FB-VAD-FMK against activated caspases-3/6/7/8 (**Fig. 3.5A**). Addition of the FB-prosthesis had little impact on caspase selectivity compared to that of the parent peptide, where both peptides inhibited caspases-3/6/7 with single micro molar potency and caspase-8 with slightly greater potency. Caspase-3 was used in subsequent characterization and validation studies as a representative of other relevant caspases.

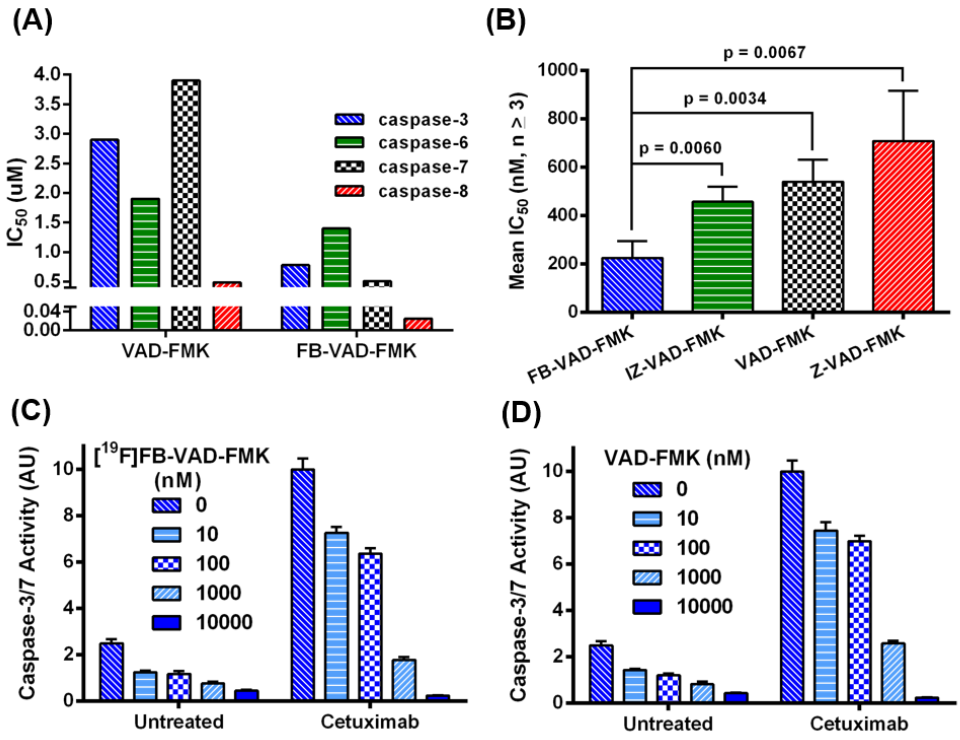


**Figure 3.5. [$^{19}$F]FB-VAD-FMK and parent peptide enzyme selectivity and activity.** Biochemistry, fluorescence measured $IC_{50}$ values, collected as duplicates, of the parent peptide, VAD-FMK, and [$^{19}$F]FB-VAD-FMK against caspases-3/6/7/8 (A). Mean $IC_{50}$ values ($n \geq 3$) of inhibition of human recombinant caspase-3 by VAD-FMK and analogues as assessed using a luminescence biochemistry assay-based method (Conc = concentration) (B). Caspase-3/7 inhibition with [$^{19}$F]FB-VAD-FMK (C) or VAD-FMK (D) in untreated or cetuximab-treated DiFi cells (n = 4).

*Lipophilicity of VAD-FMK Peptide Analogues*

To validate the predicted physical properties of the labeled VAD-FMK derivatives, lipophilicity studies were undertaken using [$^{19}$F]FB-VAD-FMK, Z-VAD-FMK, and [$^{127}$I]IZ-VAD-FMK. We determined that the FB-modified peptide ($logP_{7.5}$ = 1.41) was between 50 – 100 times less lipophilic than both Z-VAD-FMK ($logP_{7.5}$ = 2.20) and [$^{127}$I]IZ-VAD-FMK ($logP_{7.5}$ = 2.38), in support of the predicted Polar contact scores determined by molecular modeling. These findings also agree with a previous report of IZ-VAD-FMK, which suggested this compound to be too lipophilic for *in vivo* use (38).

*[$^{19}$F]FB-VAD-FMK Potently Inhibits Active Caspase Activity*

The biological activity of labeled VAD-FMK derivatives was validated with recombinant caspase-3 enzyme using a commercially available chemiluminescent caspase activity assay. Nonlinear regression analysis of the resultant inhibitory profiles yielded a mean ($n \geq 3$) fifty-percent inhibitory concentration ($IC_{50}$) of approximately 225 ± 70 nM for [$^{19}$F]FB-VAD-FMK (**Fig. 3.5B**). Though all peptides exhibited reasonable potencies that were in line with predicted affinities, [$^{19}$F]FB-VAD-FMK demonstrated the greatest potency towards caspase-3 inhibition. Similar to biochemical analysis, [$^{19}$F]FB-VAD-FMK inhibited caspase-3/7 activity at nanomolar concentrations analogously to the parent in CRC cells (DiFi) in log-phase growth (**Fig. 3.5C, D**). When apoptosis was induced in DiFi cells by exposure to the EGFR monoclonal antibody cetuximab (9), [$^{19}$F]FB-VAD-FMK inhibited caspase-3/7 activity with comparable efficacy to the parent peptide. Combined with studies demonstrating acceptable physical properties, these investigations illustrated that [$^{19}$F]FB-VAD-FMK exhibited caspase affinity similar to the parent VAD-FMK peptide and was subsequently prioritized for radiochemical development.

In Vivo *Normal Tissue Uptake and Metabolism of [$^{18}$F]FB-VAD-FMK*

The *in vivo* biodistribution of [$^{18}$F]FB-VAD-FMK was evaluated by *ex vivo* tissue counting at 60 min post-administration and correlative PET imaging up to 75 min post-administration. Upon intravenous administration, [$^{18}$F]FB-VAD-FMK was widely distributed throughout a range of normal tissues, with the greatest activity in kidneys and liver after 60 minutes of uptake (**Fig. 3.6A**). Very little radioactivity was found in brain, lung, or bone. Summed dynamic PET acquisitions following [$^{18}$F]FB-VAD-FMK administration, 0 – 75 min (**Fig. 3.6B, C**), agreed with tissue counting measurements and provided evidence of renal and hepatobiliary excretion. This was confirmed by

HPLC radiometabolite analysis, using a protocol analogous to that described for radiochemical purity analysis, which revealed largely parent compound, approximately 50% or greater, in bile and urine samples (n = 3) at 60 min post injection.

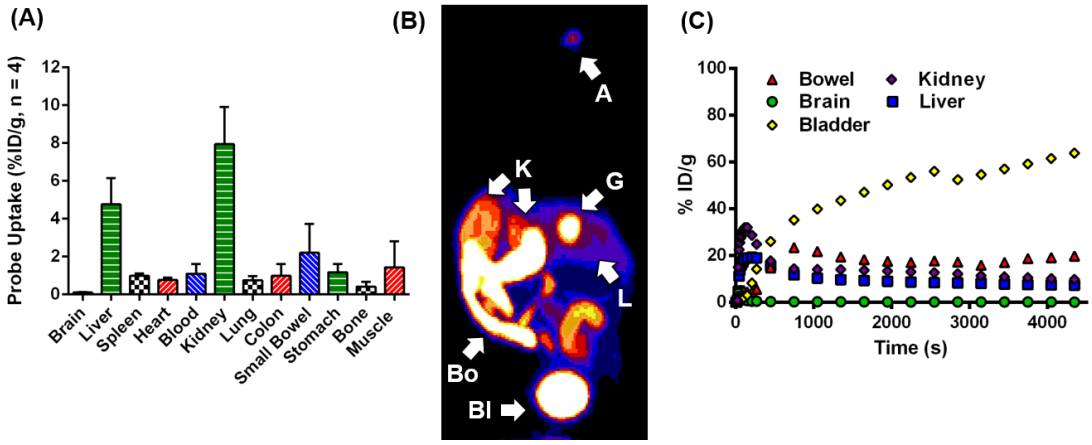


**Figure 3.6. *In vivo* biodistribution of [$^{19}$F]FB-VAD-FMK in normal tissue.** Probe biodistribution as assessed from *ex vivo* tissue count studies in male C57BL/6 mice (n = 4) (A), and a representative PET imaged maximum intensity projection (MIP) (B), A = administration site, Bl = bladder, Bo = bowel, G = gallbladder, K = kidney, L = liver, and corresponding time-activity curves (C) for normal tissues of a non-tumor bearing athymic nude mouse (29).

*[$^{18}$F]FB-VAD-FMK PET Reflects AZD-1152-dependent Caspase-3 Activity in Tumors*

*In vivo* uptake of [$^{18}$F]FB-VAD-FMK in tumor was evaluated in SW620 and DLD-1 human CRC cell line xenografts given the *in vitro* data which demonstrated, in concert with polyploidy (**Fig. 3.7A**), AZD-1152-HQPA concentration-dependent increases in cleaved PARP and cleaved caspase-3 levels (**Fig. 3.7B, C**). These results, in addition to previously reported *in vivo* findings (40), suggest that quantification of caspase activity may reflect response to Aurora B kinase inhibition in these models.

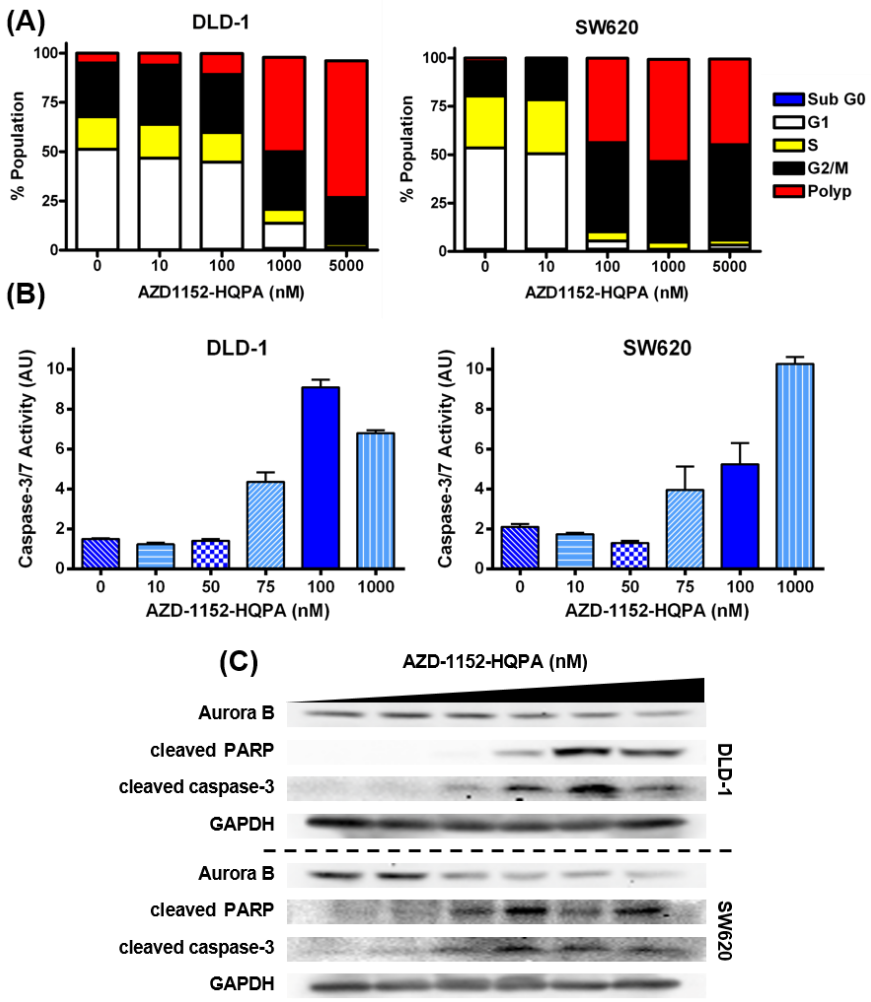


**Figure 3.7. AZD-1152-HQPA *in vitro* exposure results in cell death in DLD-1 and SW620 cell lines.** Cell cycle analysis by PI flow cytometry (A), caspase-3/7 activity (n = 5) (B), and western blot analysis of cleaved PARP and cleaved caspase-3 (C) 24 h post drug administration. Drug concentrations for western blotting were: 0, 10, 100, 500, 1000, or 5000 nM (29).

*In vivo* [$^{18}$F]FB-VAD-FMK PET was explored as a means to reflect response to AZD-1152 compared to vehicle. Animals were treated for five days and subjected to imaging after treatment on the fifth day. While vehicle treatment did not result in significant accumulation of [$^{18}$F]FB-VAD-FMK in either xenograft model, AZD-1152 treatment increased [$^{18}$F]FB-VAD-FMK uptake relative to vehicle in SW620 xenografts (0.79 ± 0.15 %ID/g and 0.42 ± 0.25 %ID/g respectively, p = 0.030) (**Fig. 3.8A-C**), which was in agreement with *in vitro* studies. Interestingly, [$^{18}$F]FB-VAD-FMK uptake was

absent in areas of central necrosis, as evident from 3D PET images (**Fig. 3.8A**). Interestingly, unlike *in vitro* studies that illustrated the sensitivity of DLD-1 cells to AZD-1152, probe accumulation was similar between AZD-1152-treated and vehicle-treated DLD-1 xenografts (0.57 ± 0.14 %ID/g and 0.49 ± 0.22 %ID/g respectively, p = 0.510).

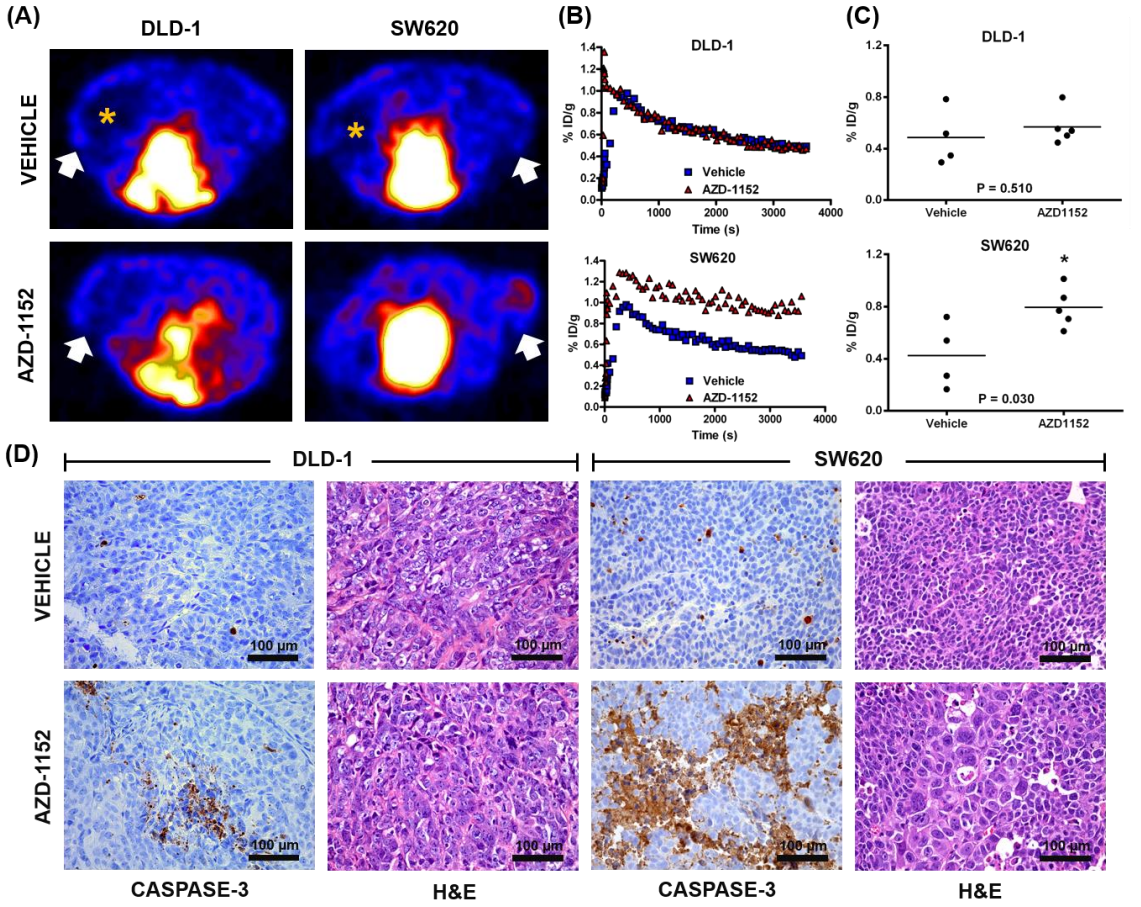


**Figure 3.8. [$^{18}$F]FB-VAD-FMK uptake reflects molecular response to Aurora B kinase inhibition *in vivo*.** Representative [$^{18}$F]FB-VAD-FMK transverse PET images of DLD-1/SW620 xenograft-bearing mice treated with vehicle or AZD-1152; tumors denoted by white arrows. Probe accumulation was absent in areas of central necrosis, as denoted by orange asterisks (A). Representative [$^{18}$F]FB-VAD-FMK time- activity curves for vehicle- and drug-treated DLD-1 and SW620 xenograft tumors. Vehicle- and drug-treated DLD-1 tumors exhibited similar washout, while greater retention in drug-*versus* vehicle-treated xenografts was observed for SW620 tumors (B). Quantification of tissue %ID/g revealed a statistical significant difference between vehicle- and drug-treated SW620 (p = 0.030) tumors but not for analogously treated DLD-1 tumors (p = 0.510) (C). Representative high- power white-light photo micrographs (40x) of caspase-3 immunohistochemical and H&E stained DLD-1 and SW620 tissues obtained from xenografts collected immediately following imaging (D) (29).

To validate imaging, xenograft tissues were harvested for histology immediately following imaging. In agreement with [$^{18}$F]FB-VAD-FMK PET, caspase-3 immunoreactivity appeared modest in both vehicle-treated SW620 and DLD-1 xenografts (**Fig. 3.8D**). Furthermore, AZD-1152 treatment led to elevated caspase-3 immunoreactivity compared to vehicle-treatment in SW620 but not DLD-1 xenografts as verified with semi-quantitative IHC analysis (**Fig. 3.9**). AZD-1152-treated SW620 xenografts demonstrated evidence of drug exposure given the presence of enlarged nuclei evident by hematoxylin and eosin (H&E) staining (40). Conversely, the lack of *in vivo* effects of AZD-1152 in DLD-1 xenografts, predicted by [$^{18}$F]FB-VAD-FMK PET, could possibly be attributed to poor drug exposure as little evidence of polyploidy was observed by H&E staining (**Fig. 3.8D**).

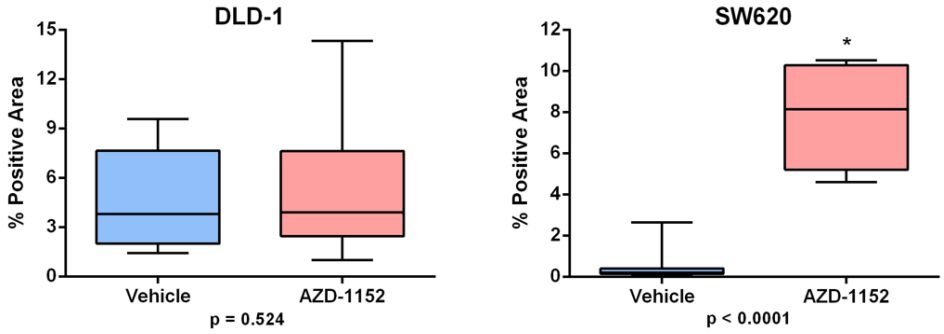


**Figure 3.9. Validation of AZD-1152 induced caspase-3 activity by IHC semi-quantification.** Semi-quantitative analysis of cleaved caspase-3 histological samples of DLD-1 and SW620 xenograft tumors treated with vehicle or AZD-1152. Evaluation of multiple low field (2.5x) micrographs revealed a statistical significant difference between vehicle- and drug-treated SW620 ($p < 0.0001$) tumors but not for analogously treated DLD-1 tumors ($p = 0.524$) (29).

*[$^{18}$F]FB-VAD-FMK PET Reflects Response to Combination Therapy*

Rational combination therapy for $^{V600E}$*BRAF* melanoma (41,42) and colon cancer (37) include an inhibitor of mutant BRAF and a PI3K family inhibitor. Leveraging this concept, [$^{18}$F]FB-VAD-FMK uptake was evaluated in $^{V600E}$*BRAF*-expressing CRC xenograft-bearing mice (COLO-205 and LIM-2405) treated with vehicle, single-agent

PI3K/mTOR inhibitor (BEZ-235), single-agent BRAF inhibitor (PLX-4720), or combination therapy (BEZ-235/PLX-4720). Animals were imaged by PET after treatment on Day 4. Elevated probe uptake in COLO-205 xenografts, relative to vehicle treatment (0.84 ± 0.16 %ID/g), was observed in the dual-agent-treated cohort (1.54 ± 0.55 %ID/g, $p = 0.007$) but not for either the BEZ-235 or PLX-4720 single agent cohorts (0.94 ± 0.09 %ID/g, $p = 0.14$ and 0.87 ± 0.13 %ID/g, $p = 0.69$, respectively) (**Fig. 3.10A, B**). Strikingly, probe uptake in LIM-2405 xenografts was non-differential, relative to vehicle treatment (0.95 ± 0.13 %ID/g), across treatment cohorts: 1.08 ± 0.25 %ID/g, $p = 0.22$ (BEZ-235), 0.92 ± 0.23 %ID/g, $p = 0.81$ (PLX-4720), and 0.78 ± 0.20 %ID/g, $p = 0.10$ (BEZ-235/PLX-4720). Representative xenograft tissue was harvested immediately following imaging. In agreement with [$^{18}$F]FB-VAD-FMK PET, caspase-3 immunoreactivity appeared modest in vehicle- and single-agent-treated COLO-205 and LIM-2405 xenografts, while combination treatment increased caspase-3 immunoreactivity in COLO-205 but not LIM-2405 xenografts (**Fig. 3.10C**). These observations were confirmed with semi-quantitative IHC analysis (**Fig. 3.11**). In concert with elevated probe uptake, after four days of treatment a significant reduction in tumor size ($p = 0.023$) was observed in COLO-205 xenografts treated with combination therapy (**Fig. 3.10D**). In contrast, statistically significant changes in tumor growth compared to vehicle were not found for single agent therapies in COLO-205 xenografts or any drug therapies in LIM-2405 cohorts.

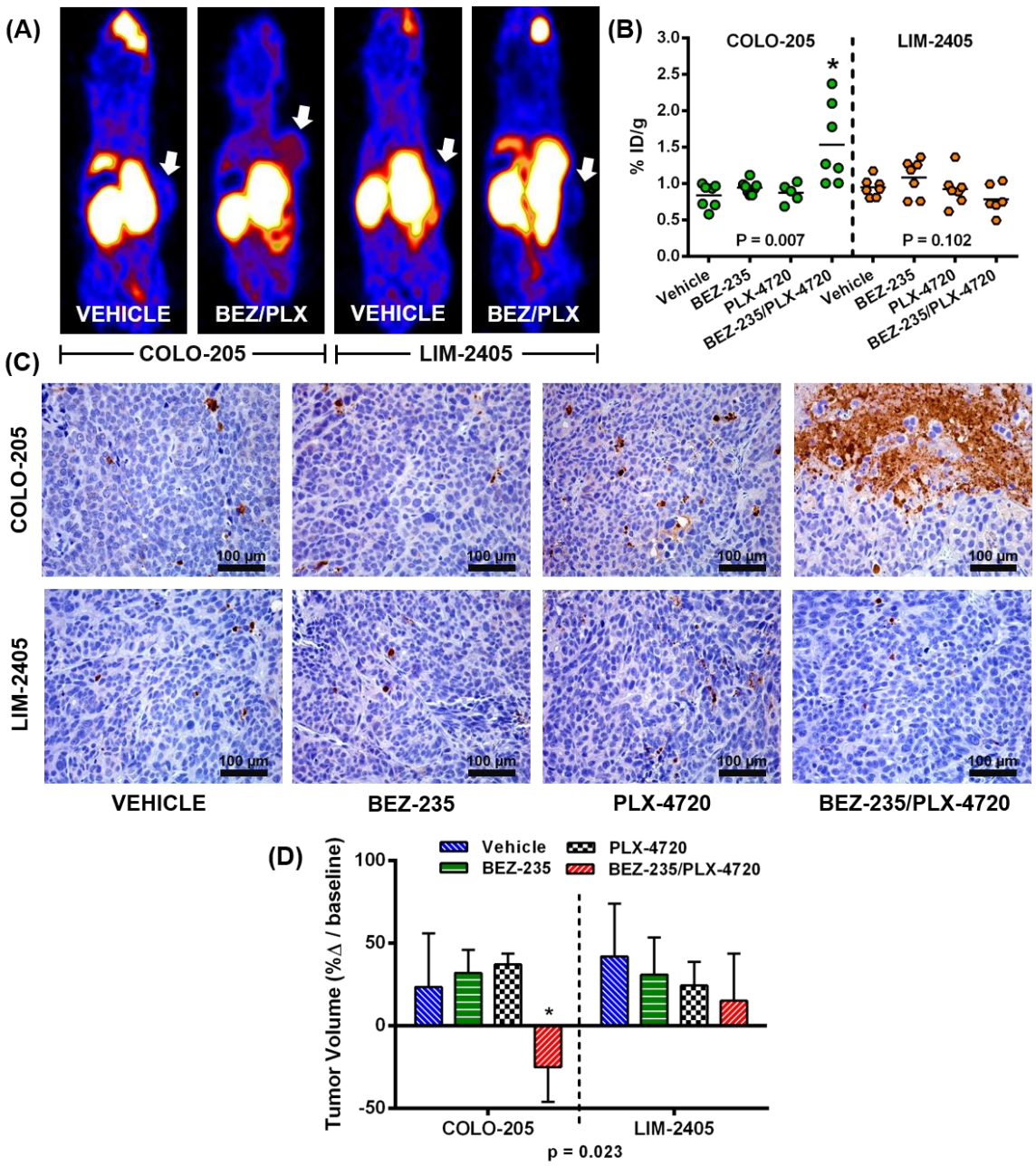


**Figure 3.10. [$^{18}$F]FB-VAD-FMK uptake reflects molecular response to combination therapy *in vivo*.** Representative [$^{18}$F]FB-VAD-FMK coronal PET images of COLO-205 and LIM-2405 xenograft tumor- bearing vehicle or BEZ-235/PLX-4720-treated mice. Tumors are denoted by white arrows (A). PET quantification of tissue %ID/g revealed a significant difference between vehicle and BEZ-235/PLX-4720- treated COLO-205 (p = 0.007) xenografts but not for analogously treated LIM-2405 xenografts (p = 0.102) (B). Representative high-power white-light photo micrographs (40x) of caspase-3 immunohistochemical stained COLO-205 and LIM-2405 tissues obtained from xenografts collected immediately following imaging (C). Changes in COLO-205 and LIM-2405 tumor volumes by Day 4 of treatment, shown as percent change from Day 1

baseline, revealed a significant difference compared to vehicle-treated mice (p = 0.023) for BEZ-235/PLX-4720-treated COLO-205 tumors only (D) (29).

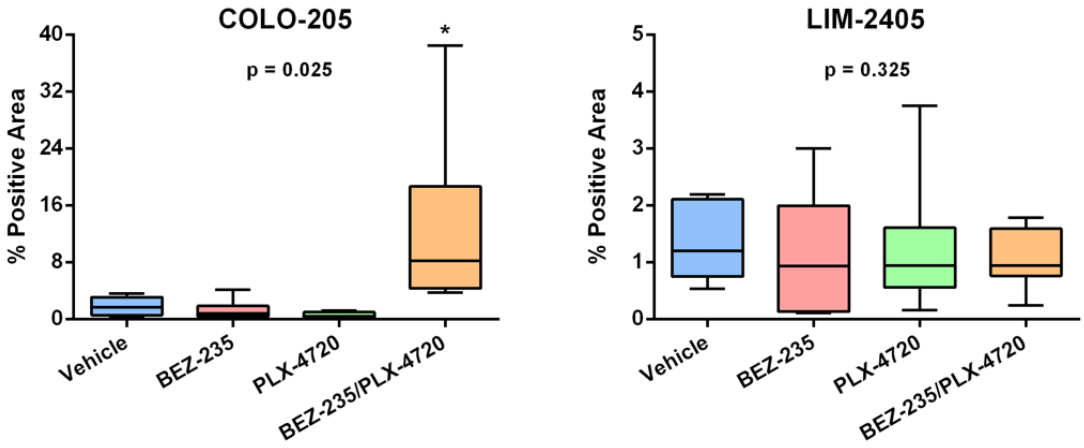


**Figure 3.11. Validation of AZD-1152 induced caspase-3 activity by IHC semi-quantification.** Semi-quantitative analysis of multiple low field (2.5x) micrographs of cleaved caspase-3 histological samples of cleaved caspase-3 histological samples of COLO-205 and LIM-2405 treatment cohorts revealed a statistical significant difference between vehicle-treated and combination-treated COLO-205 (p = 0.025) tumors but not for analogously treated LIM-2405 tumors (p = 0.325) (29).

*Phosphatidylserine Imaging to Assess Cell Death Chemotherapeutic Response*

To compare the performance of [$^{18}$F]FB-VAD-FMK PET with another imaging metric of apoptosis, we evaluated Annexin V uptake in each of the described models. Annexin V labeled with a near-infrared dye (NIR800-Annexin V) did not accumulate differentially between vehicle- and AZD-1152-treated DLD-1 xenografts (**Fig. 3.12A, B**). In SW-620 xenografts, we observed a trend towards elevated Annexin V accumulation in AZD-1152-treated xenografts compared to vehicle treatment, but unlike [$^{18}$F]FB-VAD-FMK PET, the difference between these two groups was not statistically significant (p = 0.127). Annexin V radiolabeled with technetium-99m ([$^{99m}$Tc]HYNIC-Annexin V) accumulation in dual-agent combination-treated COLO-205 xenografts did not differ from controls (p = 0.258) (**Fig. 3.12C, D**) and did not correlate with elevated caspase-3 activity, as determined by histology (**Fig. 3.10C**). Lack of probe accumulation was also

noted in single-agent-treated COLO-205 and LIM-2405 xenograft tumors. These results suggest that [$^{18}$F]FB-VAD-FMK PET may be more sensitive than NIR-dye labeled and technetium-99m radiolabeled forms of Annexin V for quantifying apoptosis in preclinical imaging studies.

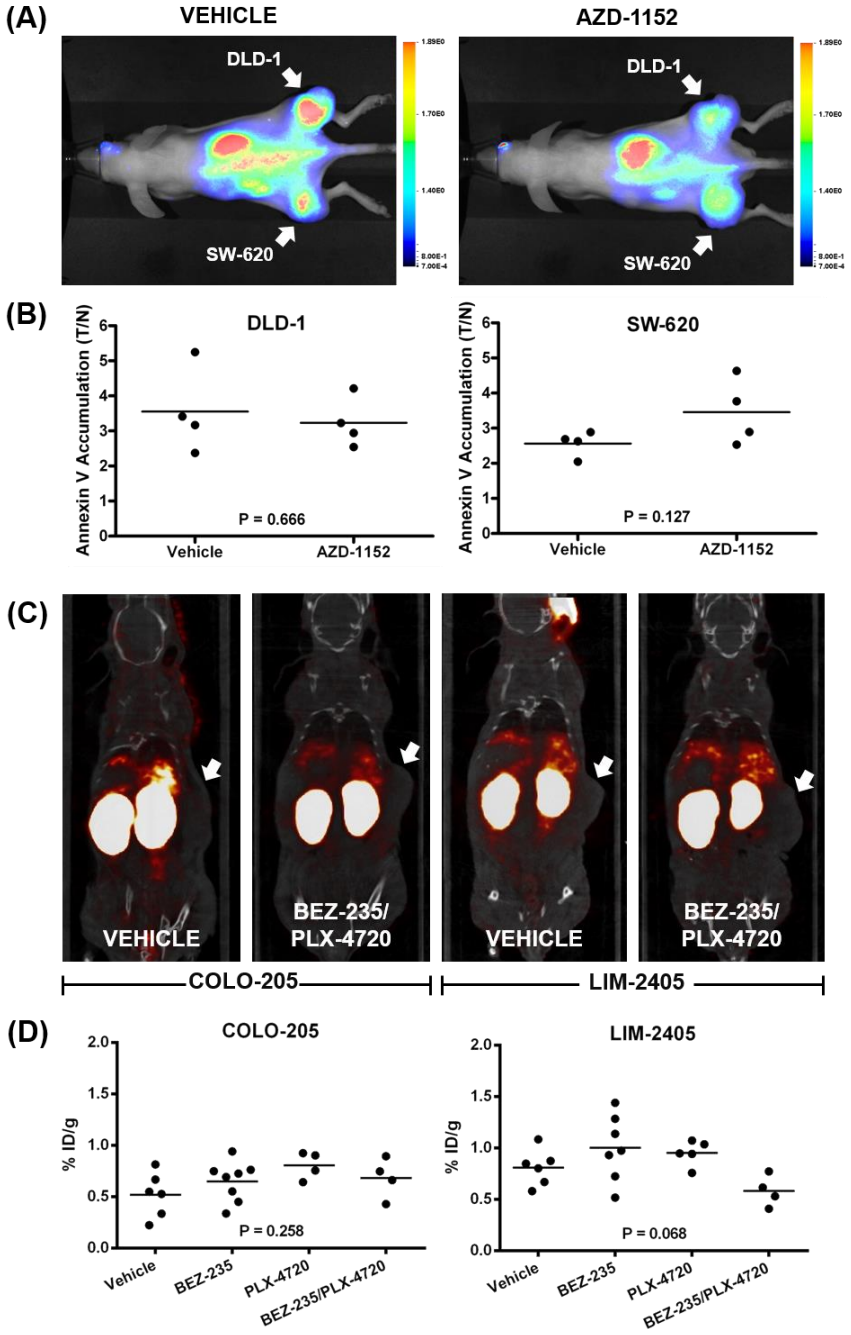


**Figure 3.12. Annexin V uptake did not reflect therapeutic response in CRC xenografts**. Near-infrared fluorescence images of NIR800-Annexin V uptake (24 hr p.i.)

in dual DLD-1 and SW-620 bearing vehicle and AZD-1152 treated mice (A). Fluorescence images are displayed as white light image overlays. Tumor accumulation was assessed through tumor-to-normal (T/N) ratio quantification and did not reflect statistically significant differences between vehicle- and AZD1152-treated mice in either DLD-1 ($p = 0.666$) or SW-620 ($p = 0.127$) xenografts (B). Co-registered SPECT/MRI images of $^{99m}$Tc-HYNIC-Annexin V uptake (3 hr p.i.) in COLO-205 or LIM-2405 bearing vehicle-, BEZ-235-, PLX-4720-, and BEZ-235/PLX-4720-treated mice (C). Quantification of tissue %ID/g did not reveal a statistically significant difference between vehicle- and BEZ-235/PLX-4720-treated COLO-205 ($p = 0.258$) and LIM-2405 ($p = 0.068$) xenograft tumors (D).

### 3.5. Discussion

Irreversible caspase binding ligands are frequently utilized as tool compound inhibitors *in vitro* and *in vivo* (23,24). Among the known inhibitors, we sought to extend the utility of VAD-FMK-type peptides to PET imaging probe development. Mechanistically, VAD-FMK peptides irreversibly bind active caspase through condensation of the fluoromethyl ketone moiety with a cysteine thiol, Cys163 for caspase-3, within the active site, permanently inactivating the enzyme (31,43). As a molecular imaging probe, irreversible binding may confer certain advantages, such as enhanced retention in apoptotic *versus* healthy cells, due to slow dissociation kinetics. We believe this study is the first to report development and *in vivo* validation of a novel PET imaging probe derived from the VAD-FMK peptide sequence. In general, the VAD-FMK sequence is known to be quite versatile and has been previously functionalized with fluorophores (25-28) and a radioisotope (38) for *in vitro* and certain preclinical applications. The probe developed here possesses all of the inherent advantages of a PET imaging agent, which include sensitivity, depth, and quantification (44,45). Furthermore, the FB derivative exhibits certain physical properties, such as improved water solubility which was a previously reported limitation of another reported labeled peptide IZ-VAD-FMK.

Inhibitor-caspase interactions have been reported (31) and provide reasonable structural templates for the design of inhibitor-based probes. The molecular modeling

approaches employed in this study were confirmed by *in vitro* biochemical studies and suggested that FB-VAD-FMK would be accommodated in the caspase-3 active site without significant perturbation of physically plausible low-energy complex structures. We interpret our results, which identified a best-scoring docked pose for FB-VAD-FMK with the FB-prosthesis pointed away from the active site and towards solvent, to suggest that further chemical modification of the N-terminus may be feasible in an effort to tune the physical properties of the peptide and optimize biodistribution in future studies. These studies suggest that the imaging prosthesis should likely be tuned to match the solvent/protein *milieu*. In support of the modeling hypothesis, *in vitro* biochemical and cell assays validated that [$^{19}$F]FB-VAD-FMK maintained similar potency against caspase-3/7 compared to the parent peptide and exhibited favorable physical properties.

Using established radiochemical methods, [$^{18}$F]FB-VAD-FMK was produced with activity and purity suitable for use in small animal PET imaging studies. [$^{18}$F]FB-VAD-FMK was initially evaluated *in vivo* in two CRC cell line models (SW620 and DLD-1) in response to prodrug (AZD-1152) treatment. Upon conversion to the active form of AZD-1152-HQPA in plasma, AZD-1152-HQPA inhibits Aurora B kinase activity (40,46) and induces 4N DNA accumulation, endoreduplication, and polyploidy (40). As demonstrated here and elsewhere (34), these events lead to apoptosis-induced cell death and elevated caspase activity in SW620 tumor cells. We demonstrated that [$^{18}$F]FB-VAD-FMK PET could be used to monitor response in this setting and that imaging accurately reflected elevated levels of apoptosis in prodrug- *versus* vehicle-treated tumors and was validated by immunohistochemistry analysis. Caspase-3 activity corresponded accordingly with evidence of drug exposure as determined by tumor polyploidic events in tissue. Interestingly, in DLD-1 xenografts, [$^{18}$F]FB-VAD-FMK uptake was not differential between drug-treated and vehicle-treated tumors. Tissues collected from these animals agreed with these findings and revealed little evidence of drug activity, as noted by the

absence of polyploidy and caspase-3 activity. We anticipate that these finding reflect poor delivery of the therapeutic agent, a common phenomenon in subcutaneous xenografts. Thus, in this model, [$^{18}$F]FB-VAD-FMK PET quantization reflected a lack of efficacy that appeared to be the result of poor therapeutic delivery.

Interestingly, using Annexin V optical imaging, we were unable to discern a correlation between AZD-1152 treatment and cell death similar to that observed in this model by *in vivo* PET imaging and IHC. A limitation of Annexin V is its tendency to accumulate in necrosis (47), which may have contributed to both the significant tumor accumulation of Annexin V in control animals as well as the overall insensitivity of Annexin V imaging to detect treatment-response in these models. [$^{18}$F]FB-VAD-FMK did not accumulate in areas of necrosis, as evident from the 3D PET images.

Next, [$^{18}$F]FB-VAD-FMK PET was used to evaluate response to a multi-drug therapeutic regimen, which included an inhibitor of mutant BRAF and a PI3K/mTOR inhibitor in $^{V600E}$*BRAF*-expressing CRC models. A non-invasive imaging metric that can be used to elucidate the basis of response to complicated therapeutic multidrug regimens would be very attractive within the setting of drug development clinical trials. [$^{18}$F]FB-VAD-FMK PET imaging demonstrated that combination therapy led to elevated apoptosis in one of two models compared to vehicle-treated or single-agent-treated CRC xenograft bearing mice. We found that changes in tumor growth closely correlated with levels of caspase activity detected by both [$^{18}$F]FB-VAD-FMK PET and IHC analysis.

To evaluate the relative sensitivity of [$^{18}$F]FB-VAD-FMK PET compared to phosphatidylserine targeted imaging metrics in the context of multi-drug therapeutic response, [$^{99m}$Tc]HYNIC-Annexin V SPECT was explored in analogous studies. Importantly, phosphatidylserine targeted imaging was unable to detect response to combination BRAF and PI3K/mTOR inhibition as observed by *in vivo* PET imaging and histology. Given the close relationship between [$^{18}$F]FB-VAD-FMK uptake, caspase

activity, and apoptosis, these studies suggest that in this setting, [$^{18}$F]FB-VAD-FMK may possess greater sensitivity than [$^{99m}$Tc]HYNIC-Annexin V SPECT.

These studies illuminate the potential for caspase-specific PET imaging probes, such as [$^{18}$F]FB-VAD-FMK, to be utilized in the assessment of early clinical response to therapeutics. A possible limitation of this probe was the relatively modest uptake observed in target tissue responding to therapy (0.8 – 2.5 %ID/g). However, other caspase-targeted PET agents reported in the literature and under clinical development are also known to exhibit modest uptake, including the promising isatin sulfonamide chemical class (48-50) and a PEG-functionalized 'DEVD-A' penta-peptide analogue, [$^{18}$F]-CP18 (51,52). From the current work (29), as well as that from previous reports (48-52), it is not clear that improvements in the overall tumor uptake, which might result in greater signal-to-noise ratio, would result in a probe that better reflects the underlying determinants of apoptosis. Future head-to-head comparisons would be beneficial towards sorting this out. Continued work should also evaluate the advantages and limitations inherent in the use of a pan-caspase targeting probe, where extrinsic and intrinsic apoptosis pathways are indistinguishable, compared with more selective compound classes.

### 3.6. Conclusions

These studies illuminate the VAD-FMK peptide as a promising scaffold for molecular imaging of caspase activity and response to molecularly targeted therapy using positron emission tomography. Among these peptides, [$^{18}$F]FB-VAD-FMK appears to be an attractive PET imaging probe for non-invasive quantification of apoptosis in tumors and may represent a potentially translatable biomarker of therapeutic efficacy in personalized medicine.

### 3.7. Works Cited


1. Bosman FT, Visser BC, van Oeveren J. Apoptosis: pathophysiology of programmed cell death. Pathol Res Pract 1996;192(7):676-83.

2. Duprez L, Wirawan E, Vanden Berghe T, Vandenabeele P. Major cell death pathways at a glance. Microbes Infect 2009;11(13):1050-62.

3. Hanahan D, Weinberg RA. Hallmarks of cancer: the next generation. Cell 2011;144(5):646-74.

4. Chang J, Ormerod M, Powles TJ, Allred DC, Ashley SE, Dowsett M. Apoptosis and proliferation as predictors of chemotherapy response in patients with breast carcinoma. Cancer 2000;89(11):2145-52.

5. Cotter TG. Apoptosis and cancer: the genesis of a research field. Nat Rev Cancer 2009;9(7):501-7.

6. Reshef A, Shirvan A, Akselrod-Ballin A, Wall A, Ziv I. Small-molecule biomarkers for clinical PET imaging of apoptosis. J Nucl Med 2010;51(6):837-40.

7. Boersma HH, Kietselaer BL, Stolk LM, Bennaghmouch A, Hofstra L, Narula J, et al. Past, present, and future of annexin A5: from protein discovery to clinical applications. J Nucl Med 2005;46(12):2035-50.

8. Nguyen QD, Challapalli A, Smith G, Fortt R, Aboagye EO. Imaging apoptosis with positron emission tomography: 'bench to bedside' development of the caspase-3/7 specific radiotracer [(18)F]ICMT-11. Eur J Cancer 2012;48(4):432-40.

9. Manning HC, Merchant NB, Foutch AC, Virostko JM, Wyatt SK, Shah C, et al. Molecular imaging of therapeutic response to epidermal growth factor receptor blockade in colorectal cancer. Clin Cancer Res 2008;14(22):7413-22.

10. Shah C, Miller TW, Wyatt SK, McKinley ET, Olivares MG, Sanchez V, et al. Imaging biomarkers predict response to anti-HER2 (ErbB2) therapy in preclinical models of breast cancer. Clin Cancer Res 2009;15(14):4712-21.

11. Schutters K, Reutelingsperger C. Phosphatidylserine targeting for diagnosis and treatment of human diseases. Apoptosis 2010;15(9):1072-82.

12. Blankenberg FG, Vanderheyden JL, Strauss HW, Tait JF. Radiolabeling of HYNIC-annexin V with technetium-99m for in vivo imaging of apoptosis. Nat Protoc 2006;1(1):108-10.

13. Ke S, Wen X, Wu QP, Wallace S, Charnsangavej C, Stachowiak AM, et al. Imaging taxane-induced tumor apoptosis using PEGylated, 111In-labeled annexin V. J Nucl Med 2004;45(1):108-15.

14. Yagle KJ, Eary JF, Tait JF, Grierson JR, Link JM, Lewellen B, et al. Evaluation of 18F-annexin V as a PET imaging agent in an animal model of apoptosis. J Nucl Med 2005;46(4):658-66.

15. Bauwens M, De Saint-Hubert M, Devos E, Deckers N, Reutelingsperger C, Mortelmans L, et al. Site-specific 68Ga-labeled Annexin A5 as a PET imaging agent for apoptosis. Nucl Med Biol 2011;38(3):381-92.

16. Balasubramanian K, Mirnikjoo B, Schroit AJ. Regulated externalization of phosphatidylserine at the cell surface: implications for apoptosis. J Biol Chem 2007;282(25):18357-64.

17. Dillon SR, Constantinescu A, Schlissel MS. Annexin V binds to positively selected B cells. J Immunol 2001;166(1):58-71.

18. Balasubramanian K, Schroit AJ. Aminophospholipid asymmetry: A matter of life and death. Annu Rev Physiol 2003;65:701-34.

19. Elliott JI, Surprenant A, Marelli-Berg FM, Cooper JC, Cassady-Cain RL, Wooding C, et al. Membrane phosphatidylserine distribution as a non-apoptotic signalling mechanism in lymphocytes. Nat Cell Biol 2005;7(8):808-16.

20. Hoglund J, Shirvan A, Antoni G, Gustavsson SA, Langstrom B, Ringheim A, et al. 18F-ML-10, a PET tracer for apoptosis: first human study. J Nucl Med 2011;52(5):720-5.

21. Allen AM, Ben-Ami M, Reshef A, Steinmetz A, Kundel Y, Inbar E, et al. Assessment of response of brain metastases to radiotherapy by PET imaging of apoptosis with (1)(8)F-ML-10. Eur J Nucl Med Mol Imaging 2012;39(9):1400-8.

22. Blankenberg FG. In vivo detection of apoptosis. J Nucl Med 2008;49 Suppl 2:81S-95S.

23. Garcia-Calvo M, Peterson EP, Leiting B, Ruel R, Nicholson DW, Thornberry NA. Inhibition of human caspases by peptide-based and macromolecular inhibitors. J Biol Chem 1998;273(49):32608-13.

24. Ekert PG, Silke J, Vaux DL. Caspase inhibitors. Cell Death Differ 1999;6(11):1081-6.

25. Bedner E, Smolewski P, Amstad P, Darzynkiewicz Z. Activation of caspases measured in situ by binding of fluorochrome-labeled inhibitors of caspases (FLICA): correlation with DNA fragmentation. Exp Cell Res 2000;259(1):308-13.

26. Amstad PA, Yu G, Johnson GL, Lee BW, Dhawan S, Phelps DJ. Detection of caspase activation in situ by fluorochrome-labeled caspase inhibitors. Biotechniques 2001;31(3):608-10, 12, 14, passim.

27. Smolewski P, Bedner E, Du L, Hsieh TC, Wu JM, Phelps DJ, et al. Detection of caspases activation by fluorochrome-labeled inhibitors: Multiparameter analysis by laser scanning cytometry. Cytometry 2001;44(1):73-82.

28. Lawson VA, Haigh CL, Roberts B, Kenche VB, Klemm HM, Masters CL, et al. Near-infrared fluorescence imaging of apoptotic neuronal cell death in a live animal model of prion disease. ACS Chem Neurosci 2010;1(11):720-7.

29. Hight MR, Cheung YY, Nickels ML, Dawson ES, Zhao P, Saleh S, et al. A peptide-based positron emission tomography probe for in vivo detection of caspase activity in apoptotic cells. Clin Cancer Res 2014;20(8):2126-35.

30. Ganesan R, Jelakovic S, Campbell AJ, Li ZZ, Asgian JL, Powers JC, et al. Exploring the S4 and S1 prime subsite specificities in caspase-3 with aza-peptide epoxide inhibitors. Biochemistry 2006;45(30):9059-67.

31. Wang Z, Watt W, Brooks NA, Harris MS, Urban J, Boatman D, et al. Kinetic and structural characterization of caspase-3 and caspase-8 inhibition by a novel class of irreversible inhibitors. Biochim Biophys Acta 2010;1804(9):1817-31.

32. Waterhouse RN, Mardon K, Giles KM, Collier TL, O'Brien JC. Halogenated 4-(phenoxymethyl)piperidines as potential radiolabeled probes for sigma-1 receptors: in vivo evaluation of [123I]-1-(iodopropen-2-yl)-4-[(4-cyanophenoxy)methyl]pip eri dine. J Med Chem 1997;40(11):1657-67.

33. Ren YG, Wagner KW, Knee DA, Aza-Blanc P, Nasoff M, Deveraux QL. Differential regulation of the TRAIL death receptors DR4 and DR5 by the signal recognition particle. Mol Biol Cell 2004;15(11):5064-74.

34. Xu J, Li K, Smith RA, Waterton JC, Zhao P, Chen H, et al. Characterizing tumor response to chemotherapy at various length scales using temporal diffusion spectroscopy. PLoS One 2012;7(7):e41714.

35. Buck JR, Saleh S, Uddin MI, Manning HC. Rapid, Microwave-Assisted Organic Synthesis of Selective (V600E)BRAF Inhibitors for Preclinical Cancer Research. Tetrahedron Lett 2012;53(32):4161-65.

36. Ayers GD, McKinley ET, Zhao P, Fritz JM, Metry RE, Deal BC, et al. Volume of preclinical xenograft tumors is more accurately assessed by ultrasound imaging than manual caliper measurements. J Ultrasound Med 2010;29(6):891-901.

37. McKinley ET, Smith RA, Zhao P, Fu A, Saleh SA, Uddin MI, et al. 3'-Deoxy-3'-18F-fluorothymidine PET predicts response to (V600E)BRAF-targeted therapy in preclinical models of colorectal cancer. J Nucl Med 2013;54(3):424-30.

38. Haberkorn U, Kinscherf R, Krammer PH, Mier W, Eisenhut M. Investigation of a potential scintigraphic marker of apoptosis: radioiodinated Z-Val-Ala-DL-Asp(O-methyl)-fluoromethyl ketone. Nucl Med Biol 2001;28(7):793-8.

39. Pereira NA, Song Z. Some commonly used caspase substrates and inhibitors lack the specificity required to monitor individual caspase activity. Biochem Biophys Res Commun 2008;377(3):873-7.

40. Wilkinson RW, Odedra R, Heaton SP, Wedge SR, Keen NJ, Crafter C, et al. AZD1152, a selective inhibitor of Aurora B kinase, inhibits human tumor xenograft growth by inducing apoptosis. Clin Cancer Res 2007;13(12):3682-8.

41. Tsai J, Lee JT, Wang W, Zhang J, Cho H, Mamo S, et al. Discovery of a selective inhibitor of oncogenic B-Raf kinase with potent antimelanoma activity. Proc Natl Acad Sci U S A 2008;105(8):3041-6.

42. Bollag G, Hirth P, Tsai J, Zhang J, Ibrahim PN, Cho H, et al. Clinical efficacy of a RAF inhibitor needs broad target blockade in BRAF-mutant melanoma. Nature 2010;467(7315):596-9.

43. Rauber P, Angliker H, Walker B, Shaw E. The synthesis of peptidylfluoromethanes and their properties as inhibitors of serine proteinases and cysteine proteinases. Biochem J 1986;239(3):633-40.

44. Peterson TE, Manning HC. Molecular imaging: 18F-FDG PET and a whole lot more. J Nucl Med Technol 2009;37(3):151-61.

45. Eckelman WC, Reba RC, Kelloff GJ. Targeted imaging: an important biomarker for understanding disease progression in the era of personalized medicine. Drug Discov Today 2008;13(17-18):748-59.

46. Mortlock AA, Foote KM, Heron NM, Jung FH, Pasquet G, Lohmann JJ, et al. Discovery, synthesis, and in vivo activity of a new class of pyrazoloquinazolines as selective inhibitors of aurora B kinase. J Med Chem 2007;50(9):2213-24.

47. Martin SJ, Reutelingsperger CP, McGahon AJ, Rader JA, van Schie RC, LaFace DM, et al. Early redistribution of plasma membrane phosphatidylserine is a general feature of apoptosis regardless of the initiating stimulus: inhibition by overexpression of Bcl-2 and Abl. J Exp Med 1995;182(5):1545-56.

48. Nguyen QD, Smith G, Glaser M, Perumal M, Arstad E, Aboagye EO. Positron emission tomography imaging of drug-induced tumor apoptosis with a caspase-3/7 specific [18F]-labeled isatin sulfonamide. Proc Natl Acad Sci U S A 2009;106(38):16375-80.

49. Chen DL, Zhou D, Chu W, Herrbrich PE, Jones LA, Rothfuss JM, et al. Comparison of radiolabeled isatin analogs for imaging apoptosis with positron emission tomography. Nucl Med Biol 2009;36(6):651-8.

50. Chen DL, Zhou D, Chu W, Herrbrich P, Engle JT, Griffin E, et al. Radiolabeled isatin binding to caspase-3 activation induced by anti-Fas antibody. Nucl Med Biol 2012;39(1):137-44.

51. Su H, Chen G, Gangadharmath U, Gomez LF, Liang Q, Mu F, et al. Evaluation of [(18)F]-CP18 as a PET imaging tracer for apoptosis. Mol Imaging Biol 2013;15(6):739-47.

52. Xia CF, Chen G, Gangadharmath U, Gomez LF, Liang Q, Mu F, et al. In vitro and in vivo evaluation of the caspase-3 substrate-based radiotracer [(18)F]-CP18 for PET imaging of apoptosis in tumors. Mol Imaging Biol 2013;15(6):748-57.

# CHAPTER 4

# GLUTAMINE METABOLISM AS A TARGET IN THE EVALUATION OF COLORECTAL CANCER DEVELOPMENT AND THERAPEUTIC RESPONSE

## 4.1. Abstract

Beyond a predilection for glycolysis, cancer cells may possess other unique metabolic characteristics, such as increased glutamine uptake. Given this, quantitative measures of glutaminolysis may reflect critical processes in oncology. The objective of these studies was to elucidate the feasibility of [$^{18}$F]4-fluoroglutamine ([$^{18}$F]4-F-GLN) PET to evaluate both molecular response to targeted drug therapies and the activation of oncogenic pathways in colorectal cancer (CRC). Given this, [$^{18}$F]4-F-GLN PET was evaluated in preclinical models of *BRAF*$^{V600E}$-expressing and mutant *PI3K* CRC as a means of detecting molecular responses to targeted therapeutics. Simulating a clinical trial proposed in Vanderbilt's GI SPORE program, the regimen included an inhibitor of mutant BRAF, a PI3K/mTOR inhibitor, and the combination thereof. For *PI3K* mutant CRC, additional therapeutic regimens included MEK and/or BCL-2 family inhibitors. Strikingly, [$^{18}$F]4-F-GLN PET was found to be sensitive to pathways of drug response, in contrast to [$^{18}$F]FDG PET, and trended with measurements obtained using the known radiolabeled glutamate amino acid derivative (4S)-4-3-[$^{18}$F]fluoropropyl)-L-glutamate ([$^{18}$F]FSPG). Further studies using a genetically engineered mouse model of colon cancer revealed [$^{18}$F]4-F-GLN to be a potential diagnostic marker of the *Kras* oncogene. We believe that these findings not only provide a greater understanding of the role that glutaminolysis plays in CRC but also illuminate the potential impact that glutaminolysis derived PET could have towards guiding drug development clinical trials as an imaging metric for detecting early therapeutic response.

## 4.2. Introduction

The metabolic properties of cancer cells diverge significantly from those of normal cells. Energy production in cancer cells is abnormally dependent on aerobic glycolysis (1,2), the Warburg effect, and is routinely analyzed by PET imaging using 2-[$^{18}$F]fluoro-2-deoxy-D-glucose ([$^{18}$F]FDG). Even though glycolysis is enhanced in many tumors, it is not necessarily a tumor-specific molecular processes (3,4). Like glucose, [$^{18}$F]FDG accumulates in other tissues that possess increased glycolytic metabolism, including the brain, brown adipose tissue, fast-dividing tissues, and sites of inflammation. Conversely, [$^{18}$F]FDG PET bears limitations in the detection of tumors with low metabolism, such as bladder, prostate, and renal cancer, in addition to small tumors, tumors of low cell density, and other [$^{18}$F]FDG-indifferent cancers. Furthermore, [$^{18}$F]FDG PET has been found to be indifferent to various therapeutics and reported to be incapable of accurately detecting response to mutant BRAF and/or PI3K/mTOR inhibition in mutant *BRAF*$^{V600E}$ tumors (5,6). Accordingly, these limitations and drawbacks necessitate alternative metabolic targets and respective PET imaging probes.

In addition to dependency on glycolysis, cancer cells have other atypical metabolic characteristics, such as increased fatty acid synthesis and increased dependency on the natural amino acid glutamine as a fuel source, a phenomenon commonly described as glutamine addiction (7). This is contrary to what is observed in normal cells where glutamine is a conditionally essential nutrient; becoming essential under conditions of cell stress. In cancer cells, both glucose and glutamine serve as key carbon sources for ATP production and biosynthesis (**Fig. 4.1**). Glutamine also participates in protein synthesis and is a nitrogen source for the production of certain amino acids and nucleotides (8).

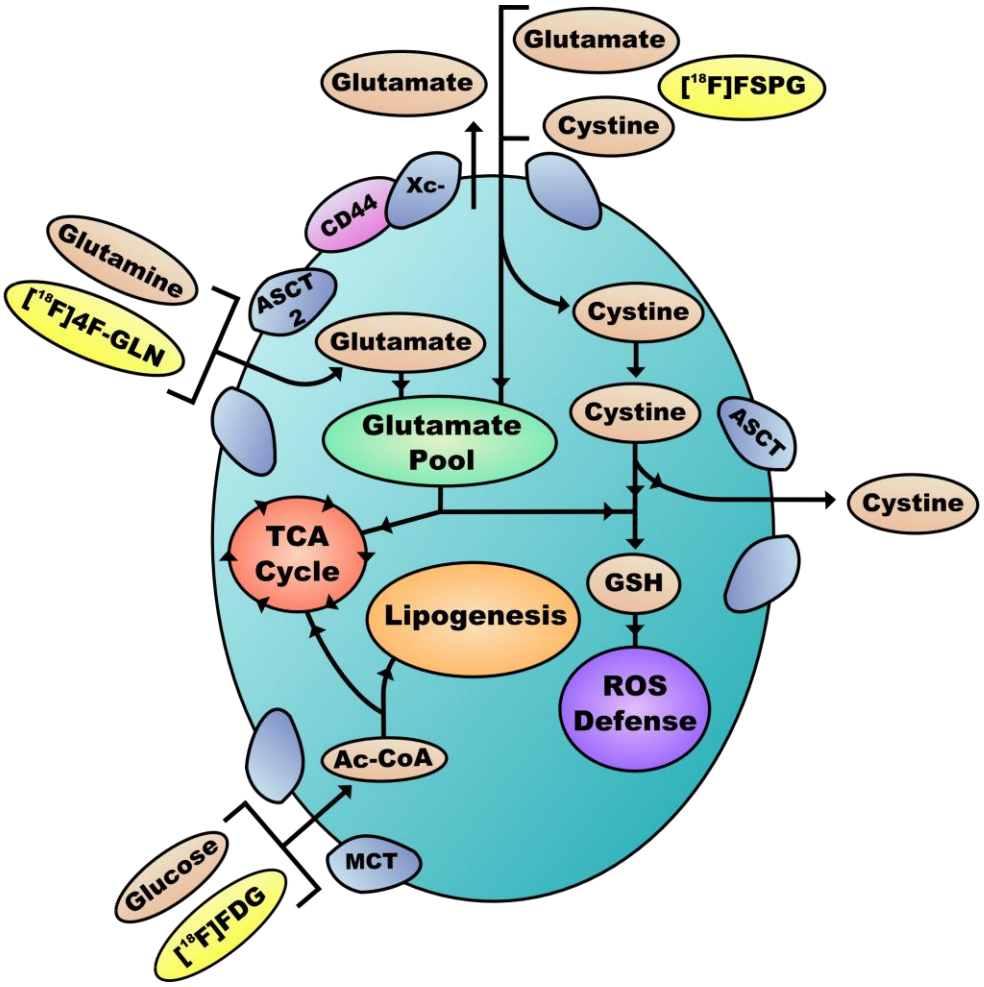


**Figure 4.1. Comparative overview of the molecular implications of [$^{18}$F]FDG, [$^{18}$F]4-F-GLN, and [$^{18}$F]FSPG.** Glucose can be taken up by cells in a regulated manner using glucose transporters (GLUTs) (9) and converted to pyruvate through a series of glycolytic transformations. Pyruvate can then be transported into the mitochondria and used in the tricarboxylic acid (TCA) cycle to produce two adenosine triphosphate (ATP) and six nicotinamide adenine dinucleotide (NADH) molecules per glucose. Similarly, glutamine can be transported to the cytosol by the alanine, serine, cysteine transporter (ASCT) family (10) where it is converted to glutamate by glutaminase. Glutamate can also be taken into the cell directly using the XCT, or $X_c^-$, family of amino acid transporters (11). Cytosolic glutamate can be either transported into the mitochondria, where it is converted to α-ketoglutarate and used for the TCA cycle, or used in the synthesis of glutathione (GSH), a major intracellular thiol compound which serves as the main antioxidant defense against reactive oxygen species (ROS).

Emerging evidence suggests that glutamine uptake in cancer cells is controlled by oncogenic signaling pathways (12-16). Given this, quantitative measures of glutamine uptake may reflect critical processes in oncology that are difficult to measure

using existing imaging metrics. For example, the role of glutamine in nucleotide synthesis suggests that measures of glutamine uptake could provide an estimate of *de novo* thymidine synthesis associated with proliferation, a process unmeasurable by 3'-deoxy-3'[($^{18}$)F]-fluorothymidine [$^{18}$F]FLT PET; a molecular marker of cellular proliferation. Using glioma cells, Wise and colleagues demonstrated that *MYC* regulates glutaminolysis and results in PI3K-independent glutamine addition (17). Other studies have revealed a role of the *KRAS* oncogene in the regulation of glutamine-derived cancer cell metabolism; a mutation found in 17-25% of all cancers (18), 30-50% of colon cancers (19-22) and up to 95% of pancreatic cancers (23,24). In pancreatic adenocarcinomas (PDAC), oncogenic *KRAS* has been shown to modulate the expression of key genes enabling the glutamine-utilizing transaminase pathway that is required for growth in PDAC, but not normal, cells (25). Accordingly, PET imaging agents targeting glutamine uptake, such as [$^{18}$F]4-fluoroglutamine ([$^{18}$F]4-F-GLN), have been reported and used in preclinical models of cancer (26,27). This agent, as well as others, have already shown potential in the context of glioblastomas and mammary tumors (26-28).

The objectives of these studies were to explore the potential of [$^{18}$F]4-F-GLN PET to monitor molecular markers of colorectal cancer (CRC) development, growth, and therapeutic response. Towards this goal, [$^{18}$F]4-F-GLN PET was evaluated as a measure of targeted therapeutic response in preclinical models of *BRAF*$^{V600E}$-expressing and mutant *PI3K* CRC. Strikingly, [$^{18}$F]4-F-GLN PET was found to be sensitive to pathways of drug response, in contrast to [$^{18}$F]FDG PET, and trended with measurements obtained using the known radiolabeled glutamate amino acid derivative (4S)-4-3-[$^{18}$F]fluoropropyl)-L-glutamate (11), also known as [$^{18}$F]FSPG or [$^{18}$F]BAY 94-9392, which follows the cysteine pathway into the cell. Additional studies in genetically

engineered mouse models of colon cancer revealed [$^{18}$F]4-F-GLN to be a potential diagnostic marker of *Kras* oncogene activation.

## 4.3. Materials and Methods

*Chemicals*

Unless otherwise indicated, all other chemicals, reagents, and solvents were purchased from Sigma-Aldrich and used as received. MLC-37-3 was applied to cells, analogously to targeted drug treatments, as a negative control in both cell lines. PLX-4720 (29) and MLC-37-3 (30) were synthesized analogously to previously reported methods.

In Vitro *Western Blots*

After 24 h of exposure with vehicle, BEZ-235 (Selleckchem), PLX-4720, AZD-6244/Selumetinib (Selleckchem), and ABT-263/Navitoclax (Ontario Chemicals Inc.) single agent or combination treatments, *in vitro* cell samples were collected from 10-cm plates. Medium was removed and cell monolayers washed with 1X phosphate buffered saline (PBS) followed by addition of 450 mL of lysis buffer containing: 7 mL of CelLytic M lysis buffer (Sigma), mini protease inhibitor cocktail (Roche), and 100 mL of phosphatase inhibitor cocktail 1 and 2 (Sigma). Protein concentrations were normalized using a bicinchoninic acid assay. All samples were vortexed and centrifuged prior to final cell lysate collection.

Immunoblotting was performed by loading 20-40 µg of protein into 7.5-12% SDS PAGE gels and resolved by electrophoresis. Membranes were incubated with antibodies to cleaved PARP (Cell Signaling, 9541S), cleaved caspase-3 (Cell Signaling, 9664), p-ERK 1/2 Thr202/Tyr204 (Cell Signaling, 4370), p-AKT Ser473 (Cell Signaling, 4060), or

GAPDH (Millipore, MAB374) and imaged on a Xenogen IVIS 200 using Western Lightning Plus-ECL (PerkinElmer) substrate.

In Vitro *[$^3$H]Glutamine Assays*

Live-cell glutamine uptake assays featuring drug treatments which mimicked proposed preclinical imaging cohorts were carried out using COLO-205 and HCT-116 cells. Cells were propagated in Dulbecco's Modified Eagle's Medium (DMEM, Mediatech) and supplemented with 10% fetal bovine serum (Atlanta Biologicals) and 1 mg/mL gentamycin sulfate (Gibco) in a 95% humidity, 5% $CO_2$, 37°C atmosphere. Upon reaching 50% confluency, cells were treated with 100 nM or 1 μM of one of the following therapeutic agents, or combination thereof, in DMSO and allowed to incubate for 24 h: vehicle, BEZ-235, PLX-4720, AZD-6244/Selumetinib, and ABT-263/Navitoclax. The novel ASCT2 (SLC1A5) inhibitor MLC-37-3 was applied to cells, analogously to targeted drug treatments, as a negative control in both cell lines. PLX-4720 was synthesized analogously to previously reported methods (29). For combination treatments, agents were delivered concomitantly at individual concentrations of 100 nM or 1 μM. Following treatment, cells were seeded as sub-confluent monolayer cultures at a density of 5 x $10^4$ cells per well into 96-well, white wall/bottom plates (CulturPlate-96, Perkin Elmer) and allowed to adhere for an additional 24 h at 37°C. Each set of conditions was carried out in at least triplicate.

Upon assay commencement, cells were washed three times with 100 uL of an assay buffer comprising of 137 mM NaCl, 5.1 mM KCl, 0.77 mM $KH_2PO_4$, 0.71 mM $MgSO_4 \cdot 7H_2O$, 1.1 mM $CaCl_2$, 10 mM D-glucose, and 10 mM HEPES at pH 6.0. Subsequently, L-[3,4-$^3$H(N)]-glutamine (Perkin Elmer), henceforth referred to as [$^3$H]glutamine or [$^3$H]GLN, in assay buffer (500 nM) was added to cells and allowed to incubate for 15 min at 37°C; after which [$^3$H]glutamine was removed and the cells

washed three times with assay buffer. Using 50 uL of NaOH (1M), cells were lysed and 150 uL of scintillation fluid (Microscint 40, Perkin Elmer) added to each well. Prepared plates were rocked, at room temperature, prior to be measured on a Topcount scintillation counter (Perkin Elmer).

*LC-MRM Proteomic Analysis*

In collaboration with Daniel Liebler and Lisa Zimmerman, liquid chromatography-multiple reaction monitoring (LC-MRM) targeted proteomic analysis has been explored to identify molecular, metabolic responses to targeted-drug therapies in CRC cells. As opposed to shotgun liquid chromatography-tandem mass spectrometry (LC-MS/MS) proteomics, LC-MRM utilizes an optimized library of protein-specific peptides to assess levels of protein expression in cell and/or tissue lysates. Using COLO-205 and HCT-116 cells, which mimicked therapeutic cohorts explored in small animal imaging studies, peptides for identification of 69 proteins were explored and represented upstream and downstream metabolic events involved in glycolysis, glutaminolysis, glutamate consumption, and the tricarboxylic acid (TCA) cycle. Though still in queue, the results from these studies could provide useful insights towards connecting *in vitro* and *in vivo* observations of therapeutic response mechanisms (**Fig. 4.2**).

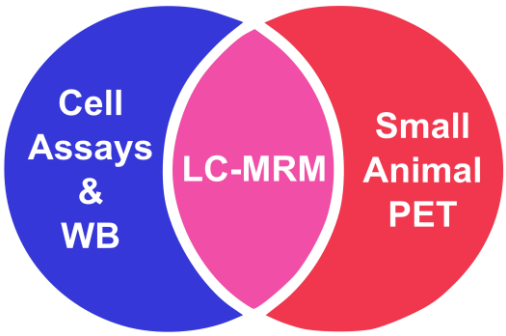


**Figure 4.2. The experimental significance of LC-MRM proteomics analysis.** A Venn diagram which illustrates the link that LC-MRM proteomics may play in furthering understanding of molecular changes observed from *in vitro* cell assay/western blot (WB) analysis and small animal PET imaging studies.

*[$^{18}$F]4-F-Gln*

[$^{18}$F]4-F-Gln and tosylate precursor were produced using methodologies analogous to those previously reported (27,31). Cyclotron-produced [$^{18}$F]fluoride ion in [$^{18}$O]water was trapped on a Waters QMA-carbonate form Sep-Pak and eluted using a solution of 18-crown-6 (10.2 mg) and potassium bicarbonate (1.8 mg) in 1.4 mL of an acetonitrile and water solution (9.3:1.7). The mixture was dried down at 99°C under a stream of helium at reduced pressure and subjected to azeotropic drying *via* iterative addition of anhydrous acetonitrile. Subsequently, tosylate precursor (6.0 mg+/-0.5 mg in 0.5 mL of anhydrous acetonitrile), provided by collaborators within the Manning group, was added directly to [$^{18}$F]fluoride and the reaction mixture heated to 80°C for 20 minutes. Following cooling to 30°C, 10 mL of a 5% acetonitrile solution was added to the mixture and passed through a preconditioned Waters HLB Plus cartridge followed by 2 mL of pure water. Activity was eluted using 2 mL of acetonitrile and the solvent removed under a gentle stream of nitrogen gas at 40°C. To the dried product was added a solution of trifluoroacetic acid (0.595 mL) and anisole (0.005 mL), which was heated to 60°C for 10 minutes. The solvent was once again removed under a gentle stream of nitrogen gas and the dried product taken up in sterile water for. The final solution was filtered through a 0.45-micron filter directly into the sterile vial and the pH adjusted to a range of 5–8 units. Overall product yields ranged from 185–5569 MBq (5.0–150.5 mCi) (n=10). Radiochemical purity and optical purity were determined by chiral HPLC (Chirex 3216 Penicillamine 150 x 4.6 mm 5uM (P/N: 00F-3126-E0) column [Phenomenex], 1.0 mM $CuSO_4$, 1.0 mL/min, ultraviolet 254-nm and γ-detector). Radiochemical purity and optical purity were greater than 90% and 95% (n=10), respectively, as determined by analytical HPLC.

*[$^{18}$F]FDG*

[$^{18}$F]FDG was purchased from PETNET with an average radiochemical purity of 98.5% and specific activity (SA) of greater than 1,000 Ci/mmol.

*[$^{18}$F]FSPG*

[$^{18}$F]FSPG and tosylate precursor were produced using methodologies analogous to those previously reported (32). Cyclotron-produced [$^{18}$F]fluoride ion in [$^{18}$O]water was trapped on a Waters QMA-carbonate form Sep-Pak and eluted using a solution of Kryptofix 2.2.2. (12.5 mg) and potassium carbonate (7 mg) in 50% acetonitrile/water (0.6 mL). The mixture was then dried down at 99°C under a stream of helium at reduced pressure, followed by azeotropic drying *via* iterative addition of anhydrous acetonitrile. Once dry, the tosylate precursor (5.0 mg+/-0.5 mg in 1.0 mL of anhydrous acetonitrile), provided by collaborators within the Manning group, and was added directly to the fluoride and the reaction mixture heated to 70°C for 5 minutes. The reaction mixture was then cooled to 30°C and a 2 M HCl solution (2 mL) was added. The reaction was then sealed, stirred and heated to 100°C for a period of 7 minutes followed by cooling to 30°C. The reaction mixture was then diluted with water to a total volume of 70 mL and passed through a preconditioned Waters MCX Plus cartridge followed by pure water (2 mL). Subsequently, activity was eluted using 5 mL of a solution comprised of 560 mg of anhydrous $Na_2HPO_4$ and 600 mg NaCl in 100 mL of deionized water. The solution was then filtered through a 0.22-micron filter directly into the final vial and the pH adjusted to a range of 5–8. Quality control on the final product solution was done by normal phase silica radio-TLC with a solvent system of n-butanol/acetic acid/water/ethanol (12/3/5/1.5) ($R_f$ of product: 0.4). Overall product yields

ranged between 1.85 – 15.43 GBq (50 – 417 mCi) (n=8) with radiochemical purities of no less than 98%.

*Human Cell Line-Bearing Mouse Models*

All studies involving small animals were conducted in accordance with both federal and institutional guidelines. COLO-205 and HCT-116 cell line xenografts were generated by subcutaneously injecting 1 x $10^7$ cells onto the right flank of 5- to 6-week old female, athymic nude mice (Harlan Sprague-Dawley). Palpable tumors were observed within one to two weeks and two to three weeks, respectively, following inoculation. For chemotherapeutic studies, BEZ-235 (Selleckchem), AZD-6244/Selumetinib (Selleckchem), and ABT-263/Navitoclax (Ontario Chemicals Inc.) were obtained commercially through indicated vendors. PLX-4720 was synthesized analogously to previously reported methods (29).

All therapeutic agents were administered *via* oral gavage for four continuous days as follows: BEZ-235 (35 mg/kg) once daily in 0.1% Tween 80 and 0.5% methyl cellulose; PLX-4720 (60 mg/kg) once daily in DMSO; AZD-6244 (25 mg/kg) twice daily in 0.1% Tween 80 and 0.5% methyl cellulose; ABT-263 once daily in a cocktail of 60% Phosal 50 PG (Lipoid), 30% PEG-400 (Rigaku), and 10% EtOH. For all combination treatments, agents were administered as separate doses. BEZ-235/PLX-4720 cohorts were treated initially with BEZ-235 followed by administration of PLX-4720 seven to eight hours later. For combinations involving MEK inhibition, the first dose of AZD-6244 was delivered one to two hours prior treatment with BEZ-235 or ABT-263. Secondary dosing with AZD-6244 was performed seven to eight hours after the initial AZD-6244 treatment and five to six hours after treatment with BEZ-235 or ABT-263. The duration between administrations of therapeutic agents was shortened to two to three hours for

combination cohorts on the fourth day of treatment in order to accommodate PET imaging acquisition.

Tumor growth rates were monitored by measuring tumor volumes on the first and fourth days of treatment using an established ultrasound imaging-based methodology (33). Dose preparation and administration, treatment duration, and imaging time-points were determined based on our previous experience in these models (5,6,34) as well as reports from similarly performed studies (35).

*Genetically Engineered Mouse Models*

Stem cell-derived colon cancer mice were provided by Dr. Robert J. Coffey, and colleagues, as part of a collaborative effort within the Vanderbilt GI SPORE program which built upon previous work where *Lrig1-CreER*$^{T2/+}$ mice (36) were crossed with *Apc*$^{fl/+}$ mice to generate the *Lrig1-CreER*$^{T2/+}$*;Apc*$^{fl/+}$ model (37). Briefly, administration of 4-hydroxytamoxifen enemas to *Lrig1-CreER*$^{T2/+}$*;Apc*$^{fl/fl}$ mice results in loss of both *APC* alleles in *Lrig1*-expressing cells, whereas administration to *Lrig1-CreER*$^{T2/+}$*;Apc*$^{fl/fl}$*;Kras*$^{G12D}$ mice results in loss of both APC alleles and activation of mutant *Kras.* Colonic tumors developed in both models. Detailed methodologies of mouse model generation will be described in future publications from the Coffey lab.

*PET Imaging and Analysis*

Animal handling methods in preparation for and during all PET imaging studies, including [$^{18}$F]FDG, [$^{18}$F]4-F-Gln and [$^{18}$F]FSPG, were derived from protocol standards established for [$^{18}$F]FDG (38-40). Prior to imaging, animals were fasted between six to eight hours and allowed to acclimate to facility environment for at least one hour in a warmed chamber at 31.5°C. Animals were administered 10.4-11.8 MBq of PET imaging agent *via* intravenous injection and imaged using a dedicated Concorde Microsystems

Focus 220 microPET scanner (Siemens Preclinical Solutions). Animals were maintained under 2% isofluorane anesthesia in 100% oxygen at 2 L/min and kept warm for the duration of the PET scan.

[$^{18}$F]4-F-Gln and [$^{18}$F]FSPG PET images in xenograft-bearing mice were acquired as 20 min static data sets following a 40 min uptake period and anesthetization. Similarly, [$^{18}$F]FDG PET images were collected as 10 min static data sets following a 50 min uptake period and anesthetization. Animals were conscious, allowed free access to water, and kept in the 31.5 °C warmed chamber for the duration of the uptake period. Imaging in models of therapeutic response was performed on the fourth day of treatment within three to four hours following single agent administration. For combination cohorts, imaging was performed approximately four to five hours and two to three hours following the first and second therapeutic treatments, respectively. [$^{18}$F]4-F-Gln PET imaging in genetically engineered mice was collected as either 20 min static acquisitions following a 40 min uptake period or 60 min dynamic acquisitions initiated upon PET agent injection. Images were acquired longitudinally starting before induction with tamoxifen and proceeding to two and four weeks after.

PET data were reconstructed using a three-dimensional (3D) ordered subset expectation maximization/maximum a posteriori (OSEM3D/MAP) algorithm. Dynamic data was binned into twelve 5 s (0-1 min) and fifty-nine 60 s (2-60 min) frames. The resulting three-dimensional reconstructions had an x-y voxel size of 0.474 mm and inter-slice distance of 0.796 mm. ASIPro software (Siemens Preclinical Solutions) was used to manually draw three-dimensional regions of interest (ROI) surrounding the entire tumor volume. PET agent uptake was quantified as the percentage of the injected dose per gram of tissue (%ID/g). For dynamic scans, only data points collected within the time frame analyzed for analogous static scans were considered.

*Immunohistochemistry and Semi-Quantitative Analysis*

Tumor tissues were harvested immediately following conclusion of imaging, fixed for 24 h in 5% buffered formalin, and blocked in paraffin. Immunohistochemistry for Ki67 (1:100, Dako M7240) activity was carried out as previously described (5). Tissues were similarly stained using standard H&E methods and reviewed by an expert gastrointestinal pathologist (M. Kay Washington). For semi-quantitative analysis of Ki67 IHC, high-resolution bright field images of whole tissue sections were obtained using a Leica SCN400 Slide Scanner. Tissue sections were scored to determine the percentage of positive cells using the accompanied Ariol Analysis software.

For immunofluorescence studies, formalin-fixed-paraffin-embedded tissues were sectioned to 4 μm thickness and stained for ASCT2. Briefly, tissue samples were de-paraffinized, rehydrated, and incubated in PBS with 0.3% Triton X-100 for 10 minutes. Antigen retrieval was performed using citrate buffer (pH = 6.0) solution for 20 minutes at 105°C followed by a 10 minute cooling period at room temperature. Samples were then treated with 3% hydrogen peroxide for 10 minutes and blocked with 3%BSA/10% donkey serum in PBS for 30 minutes. Slides were incubated with primary antibody overnight (1:500, Sigma HPA035240) at 4°C and subsequently washed with PBS. For secondary antibody detection, samples were incubated with species-specific secondary Donkey IgG conjugated to either Cy3 or Cy5 (1:100) for 1 hour at room temperature with DAPI (10 μg/mL) and subsequently washed with PBS. Slides were mounted with antifade media for imaging on an Olympus IX81 inverted fluorescent microscope at 20x magnification.

*Tissue Immunoassays*

Upon tissue collection, tumor samples that were not fixed in 5% buffered formalin were flash-frozen in liquid nitrogen and stored at -80°C. For immunoreactivity studies,

tissue samples were diluted to 100 mg/mL in lysis buffer (#7018s, Cell Signaling Technology) and subsequently homogenized, sonicated, and spun at 3.5K RPM for 1 min. Lysate samples were then screened against an array of target-specific capture antibodies using PathScan Intracellular Signaling Array Kits (#7323, Cell Signaling Technology) in accordance with the manufacturer's instructions and developed using HyBlot CL autoradiography film (#e3012, Denville Scientific Inc.). Processed films were digitized using an Epson Perfection V600 Photo scanner and the relative pixel intensities for each blot quantified using the public domain image processing software ImageJ.

Complementary western blot studies were performed by loading 20-40 µg of protein into 7.5-12% SDS PAGE gels, transferred to PVDF membranes (PerkinElmer), and resolved by electrophoresis. Membranes were blocked overnight at 4°C in tris-buffered saline 0.1% Tween-20 (TBST) containing 5% w/v nonfat dry milk powder and subsequently incubated with antibodies to p-ERK 1/2 Thr202/Tyr204 (Cell Signaling, 4370), p-AKT Ser473 (Cell Signaling, 4060), b-tubulin (Novus Biologicals, NB600-936); in which case membranes were probed for one hour in TBST with 3% bovine serum albumin (BSA) and subsequently incubated for another hour with horseradish peroxidase-conjugated secondary antibody (Jackson ImmunoResearch) diluted 1:5000 in TBST containing 3% BSA. Finally, membrane chemiluminescence was imaged on a Xenogen IVIS 200 system using Western Lightning Plus-ECL (PerkinElmer) substrate.

*Statistical Methods*

Experimental replicates are reported as the arithmetic mean ± standard deviation. The Wilcoxon Rank Sum (Mann-Whitney U) test was used to evaluate statistical significance for both *in vitro* and *in vivo* data sets. Differences were assessed within the GraphPad Prism 6.01 software package and considered statistically significant if $p < 0.05$.

## 4.4. Results

In Vitro *Evaluation of Therapeutic Cohorts*

Though many of the therapeutic agents and combinations have been reportedly previously in COLO- (5,6,34) and HCT-116 (35) cell lines, targeted drug treatment efficacy was evaluated *in vitro* by western blot. As expected from our previous work in this model, $BRAF^{V600E}$-expressing COLO-205 cells showed activation of cell death pathways with exposure to BEZ-235/PLX-4720 combination-therapy and sensitivity to inhibition of PI3K/mTOR as noted by decreases in p-AKT (473) (**Fig. 4.3A**). Mutant PI3K and wild type BRAF HCT-116 cells were resistant PLX-4720 and combination BEZ-235/PLX-4720 treatment and sensitive to BEZ-235 treatment; as noted by changes in p-AKT (473) and p-ERK (**Fig. 4.3B**). Interestingly, combined inhibition of MEK and Bcl-2/Bcl-XL/Bcl-w induced cell death in high concentrations. Changes in BIM expression in response to ABT-263 and AZD-6244 single agent and combination treatments (**Fig. 4.3C**) were in agreement with previous reports for this cell line (35).

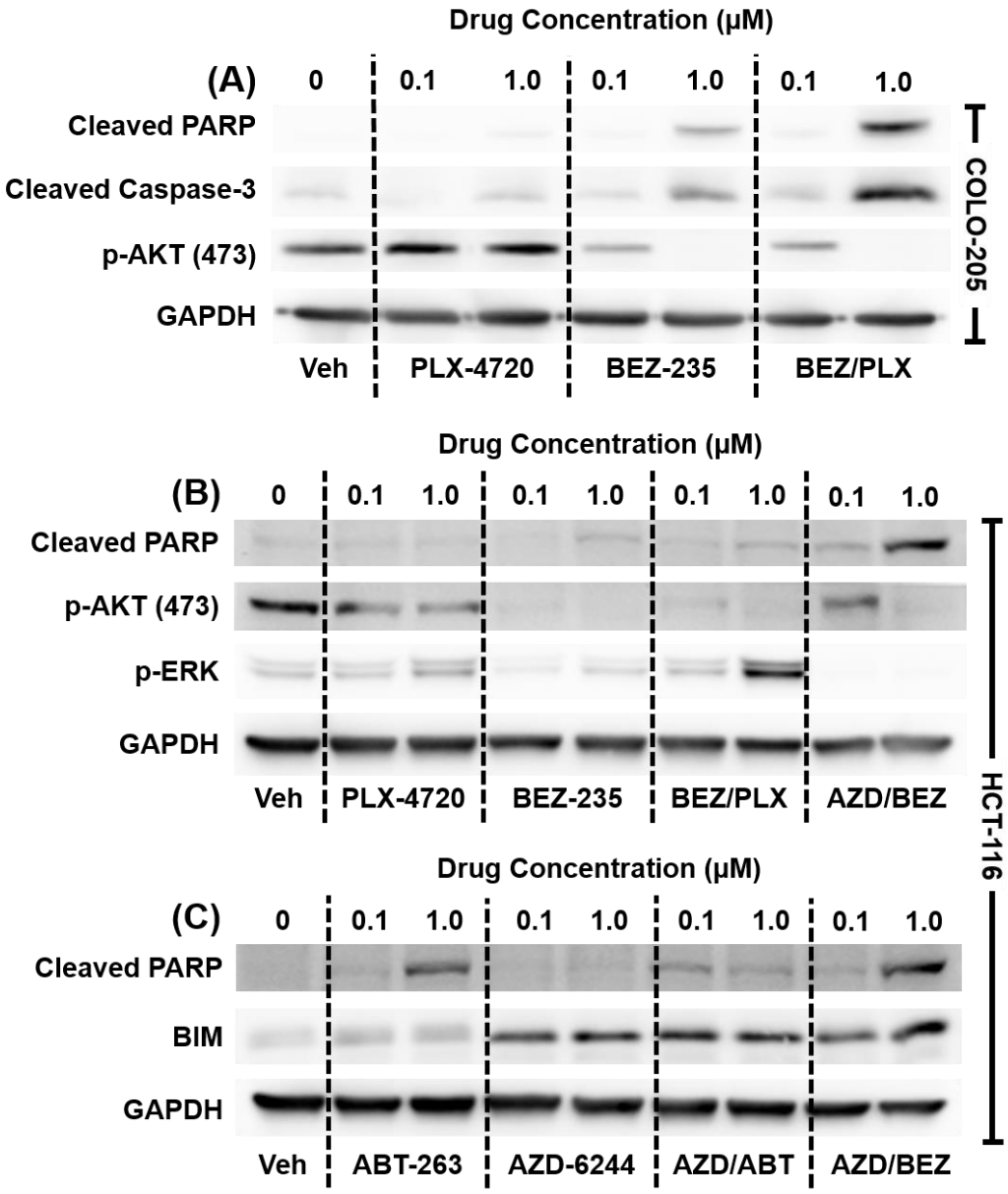


**Figure 4.3. Efficacy of targeted therapies were confirmed *in vitro*.** Western blot analysis of cleaved PARP, cleaved caspase-3 p-AKT (473), p-ERK, and BIM 24 h post-drug administration in response to a variety of targeted therapeutics in *BRAF*$^{V600E}$-expressing COLO-205 and mutant *PI3K* HCT-116 cells.

*Molecularly Targeted Therapeutics Effect* In Vitro *Glutamine Metabolism*

Initial evaluation of the effects of targeted therapies on glutamine uptake in CRC was explored *in vitro* using COLO-205 and HCT-116 cells (**Fig. 4.4**). Treatment cohorts modeled those employed for small animal imaging studies. Incorporation of

[$^{3}$H]glutamine in living COLO-205 cells revealed a reduction, compared to vehicle-treated, in 1 μM BEZ-235/PLX-4720 combination-treated cells only (p = 0.0286). In HCT-116 cells, reduction in [$^{3}$H]glutamine uptake was observed for BEZ-235 single agent-treated (p = 0.0283) as well as AZD-6244/BEZ-235 (p = 0.0081) and AZD-6244/ABT-263 (p = 0.0485) combination-treated cohorts.

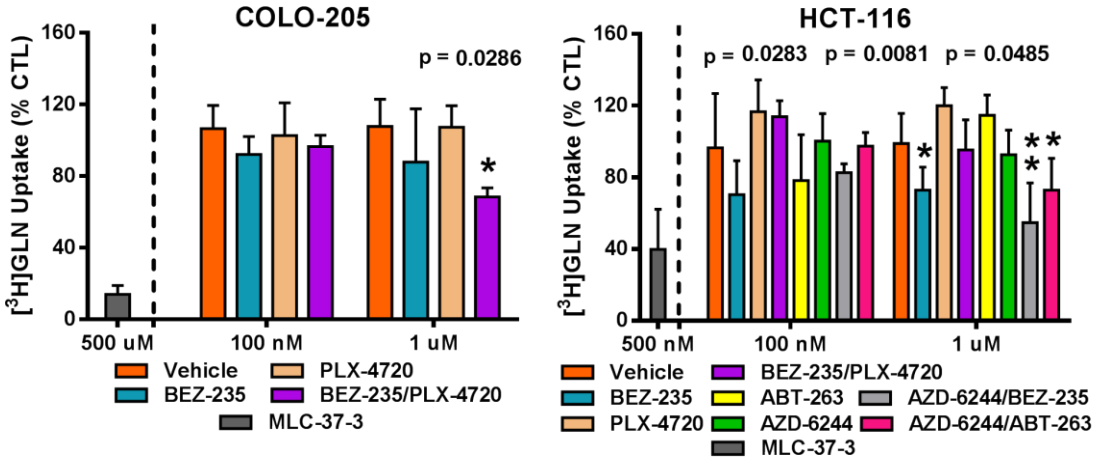


**Figure 4.4. [$^{3}$H]Glutamine in living cells reflected molecular response to targeted therapies.** Incorporation of [$^{3}$H]glutamine is reported as percent change relative to vehicle-treated cells, which was manually set as 100%. A novel ASCT2 (*SLC1A5*) inhibitor MLC-37-3 (30) was applied to cells, analogously to targeted drug treatments, as a positive control in both cell lines.

*PET Imaging of Therapeutic Response in BRAF$^{V600E}$ Colon Cancer*

*In vivo* [$^{18}$F]4-F-Gln PET was explored as a means to reflect response to targeted therapies in *BRAF$^{V600E}$* COLO-205 xenograft-bearing mice (**Fig. 4.5A**). [$^{18}$F]4-F-Gln tumor accumulation in vehicle-treated mice averaged 6.34 ± 0.93 %ID/g. When treated with a duel inhibitor of PI3K and mTOR activity (BEZ-235), PET agent accumulation in tumor tissue remained unchanged (6.07 ± 0.72 %ID/g, p = 0.5161). While a reduction in [$^{18}$F]4-F-Gln tumor uptake (5.30 ± 0.91 %ID/g) was observed in tumors treated with a mutant BRAF inhibitor (PLX-4720), this trend was not found to be significant (p = 0.0608). Strikingly, [$^{18}$F]4-F-Gln accumulation was found to be significantly reduced (4.76

± 1.07 %ID/g, p = 0.0021) when COLO-205 xenograft tumors were treated with a combination of BEZ-235 and PLX-4720.

In comparative studies, [$^{18}$F]FDG (**Fig. 4.5B**) and [$^{18}$F]FSPG (**Fig. 4.5C**) PET imaging were similarly explored. Unlike [$^{18}$F]4-F-Gln accumulation, [$^{18}$F]FDG tumor uptake was significantly reduced from vehicle (4.72 ± 0.86 %ID/g) in both single treatment cohorts (3.06 ± 0.38 %ID/g, p = 0.0006 and 3.34 ± 0.85 %ID/g, p = 0.0205 for BEZ-235 and PLX-4720, respectively) as well as for the BEZ-235/PLX-4720 combination-treated mice (2.06 ± 0.60 %ID/g, p = 0.0002). Interestingly, [$^{18}$F]FSPG trends were similar to that of [$^{18}$F]4-F-Gln as accumulation in vehicle-treated mice (1.89 ± 0.24 %ID/g) was similar to single agent BEZ-235 and PLX-4720-treated xenografts (2.06 ± 0.59 %ID/g, p = 0.3869 and 1.72 ± 0.45 %ID/g, p = 0.6031 for BEZ-235 and PLX-4720, respectively) but was reduced in BEZ-235/PLX-4720 combination-treated tumors (1.34 ± 0.28 %ID/g, p = 0.0022).

In concert with reduced [$^{18}$F]4-F-Gln uptake, after four days of treatment a significant reduction in tumor size (p < 0.0001) was observed only in COLO-205 xenografts treated with a combination of BEZ-235 and PLX-4720 (**Fig. 4.5D**) and agreed with our previous experience with this model (34). In contrast, statistically significant changes in tumor growth, compared to vehicle, were not found for single agent therapies. To further validate observations derived from PET imaging, xenograft tissues were harvested for histology immediately following imaging conclusion. In agreement with [$^{18}$F]4-F-Gln PET, [$^{18}$F]FSPG PET, and tumor growth trends, semi-quantitative analysis of Ki67 immunoreactivity revealed a reduction in proliferation (p < 0.0001), compared to vehicle-treatment, for the combination-treated cohort only (**Fig. 4.5E**).

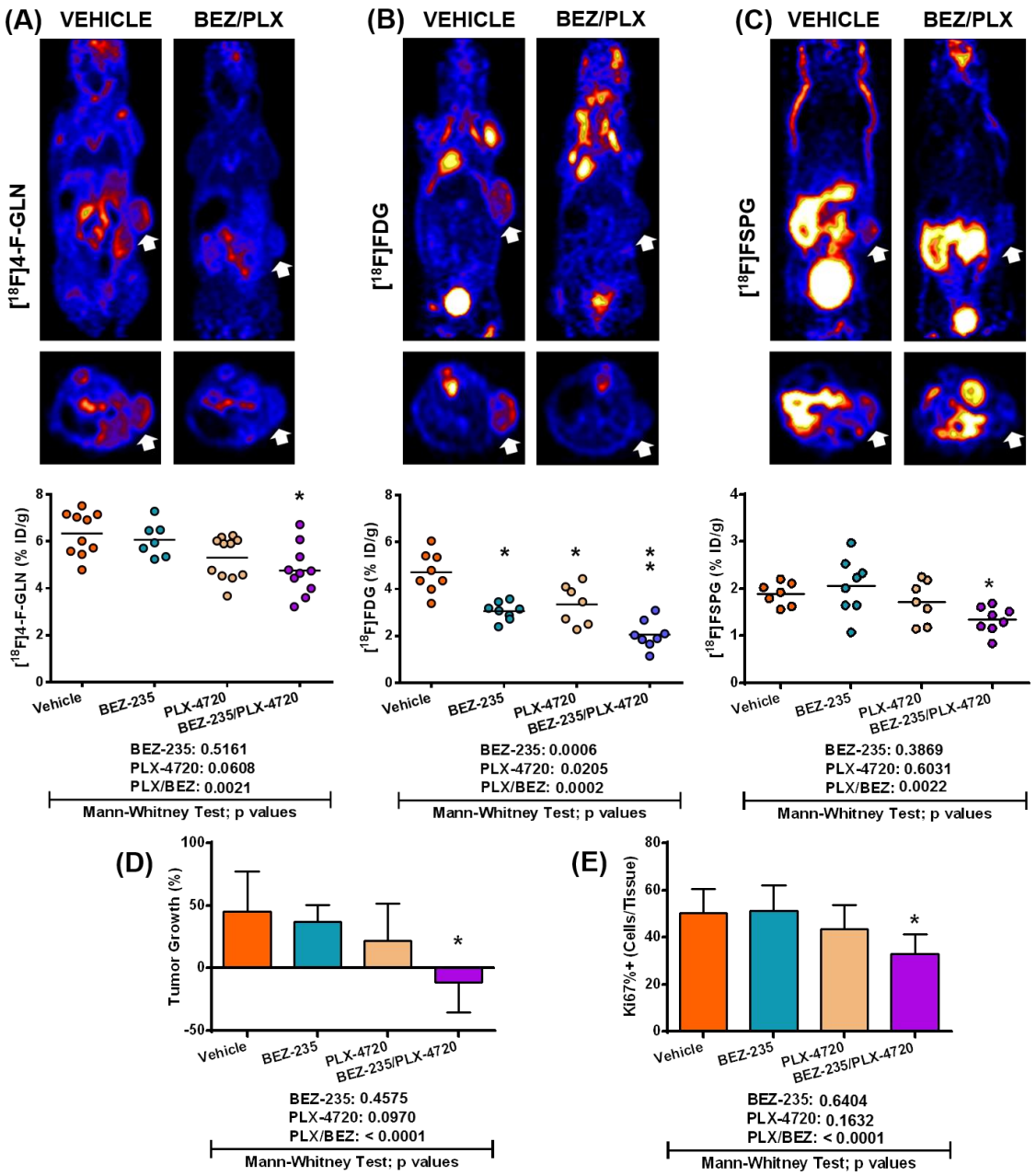


**Figure 4.5. [$^{18}$F]4-F-Gln uptake reflected molecular response to mutant *BRAF* and *PI3K/mTOR* therapy *in vivo*.** Representative transverse and coronal [$^{18}$F]4-F-Gln (A), [$^{18}$F]FDG (B), and [$^{18}$F]FSPG (C) PET images of COLO-205 xenograft tumor-bearing vehicle or BEZ-235/PLX-4720-treated mice; tumors are denoted by white arrows. PET quantification of tissue %ID/g revealed a significant difference between vehicle and BEZ-235/PLX-4720- treated xenografts for all imaging agents, however, only [$^{18}$F]4-F-Gln and [$^{18}$F]FSPG showed sensitivity to just the combination treatment. Changes in COLO-205 tumor volume by the fourth day of treatment ($N \geq 8$ for all cohorts), shown as percent change from day one baseline, revealed a significant reduction in size from vehicle-treated mice for BEZ-235/PLX-4720-treated tumors only ($p < 0.0001$) (D). Similar observations were observed by semi-quantitative analysis of Ki67 immunoreactivity

sections ($N \geq 10$ for all cohorts), where the relative percent of positively-stained cells was evaluated for an entire tumor tissue section per animal (E).

*PET Imaging of Therapeutic Response in Mutant PI3K Colon Cancer*

In parallel to imaging studies in mutant *BRAF* xenograft tumors, [$^{18}$F]4-F-Gln was also explored as a diagnostic marker of therapeutic response in *PI3K* mutant HCT-116 xenograft-bearing mice (**Fig. 4.6A, B**). [$^{18}$F]4-F-Gln tumor accumulation in vehicle treated mice was found to average 3.66 ± 0.71 %ID/g. In addition to BEZ-235 and PLX-4720, additional therapeutic inhibitors of Bcl-2/Bcl-XL/Bcl-w (ABT-263) and/or MEK (AZD-6244) were employed. [$^{18}$F]4-F-Gln uptake in most drug treated tumors was comparable to that observed in vehicle-treated tissues: 4.26 ± 0.78 %ID/g, p = 0.1783 (BEZ-235), 4.48 ± 1.56 %ID/g, p = 0.3983 (PLX-4720), 4.15 ± 0.71 %ID/g, p = 0.3337 (BEZ-235/PLX-4720), 4.25 ± 1.13 %ID/g, p = 0.4242 (ABT-263), 3.73 ± 0.84 %ID/g, p = 0.7524 (AZD-6244), and 4.42 ± 0.54 %ID/g, p = 0.1143 (AZD-6244/BEZ-235). Interestingly, imaging agent uptake was significantly reduced when using combined targeted inhibition of MEK and Bcl-2/Bcl-XL/Bcl-w activity upon administration of AZD-6244 and ABT-263 (2.39 ± 0.43 %ID/g, p = 0.0381).

In comparative studies, [$^{18}$F]FDG and [$^{18}$F]FSPG PET imaging were similarly explored (**Fig. 4.6A, B**). Unlike [$^{18}$F]4-F-Gln accumulation, [$^{18}$F]FDG tumor uptake was significantly reduced from vehicle (5.23 ± 0.68 %ID/g) in all single agent and combination-treated cohorts: 4.18 ± 0.51 %ID/g, p = 0.0070 (BEZ-235), 4.45 ± 0.58 %ID/g, p = 0.0401 (PLX-4720), 4.36 ± 0.61 %ID/g, p = 0.0093 (BEZ-235/PLX-4720), 4.34 ± 0.81 %ID/g, p = 0.0111 (ABT-263), 3.83 ± 0.85 %ID/g, p = 0.0289 (AZD-6244), 3.15 ± 1.32 %ID/g, p = 0.0262 (AZD-6244/BEZ-235), and 3.96 ± 0.99 %ID/g, p = 0.0008 (AZD-6244/ABT-263). As also observed for COLO-205 xenograft-treated tumors, [$^{18}$F]FSPG trends in drug treated HCT-116 xenografts were similar to that of [$^{18}$F]4-F-Gln. Accumulation in vehicle-treated mice (2.64 ± 0.45 %ID/g) was similar to all therapeutic

cohorts with the exception of AZD-6244/ABT-263 combination-treated mice. Uptake values were found to be: 2.45 ± 0.72 %ID/g, p = 0.4945 (BEZ-235), 2.71 ± 0.75 %ID/g, p = 0.7515 (PLX-4720), 2.19 ± 0.38 %ID/g, p = 0.1197 (BEZ-235/PLX-4720), 2.35 ± 0.43 %ID/g, p = 0.2720 (ABT-263), 2.46 ± 0.55 %ID/g, p = 0.9293 (AZD-6244), 2.16 ± 0.53 %ID/g, p = 0.1778 (AZD-6244/BEZ-235), and 2.02 ± 0.37 %ID/g, p = 0.0186 (AZD-6244/ABT-263).

After four days of treatment, a significant reduction in tumor size was observed in tumors treated with AZD-6244 (p = 0.0001), AZD-6244/BEZ-235 (p < 0.0001), and AZD-6244/ABT-263 (p < 0.0001) (**Fig. 4.6C**). These trends agreed with previously reported findings in this model (35). To explore potential imaging correlations with a marker of cell proliferation, semi-quantification of Ki67 immunohistochemistry was performed in excised tissue (**Fig. 4.6D**). Contrary to variations in tumor growth rates, significantly reduced Ki67 activity, compared to vehicle-treated tissue, was observed for AZD-6244/BEZ-235 (p = 0.0037) combination-treated tumor.

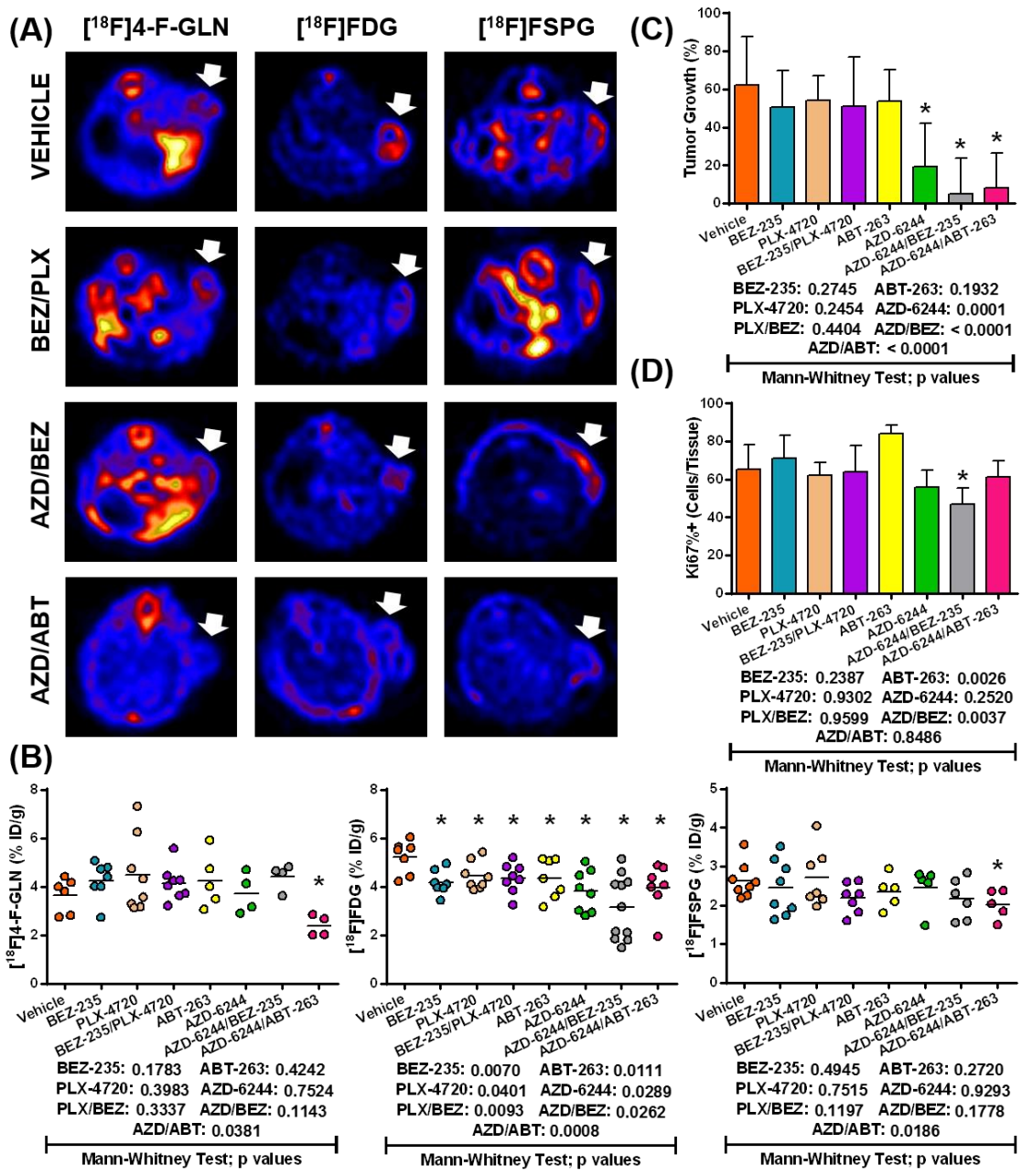


**Figure 4.6. [$^{18}$F]4-F-Gln uptake exhibited sensitivity to targeted inhibition of Bcl-2/Bcl-XL/Bcl-w and MEK *in vivo*.** Representative [$^{18}$F]4-F-Gln, [$^{18}$F]FDG, and [$^{18}$F]FSPG PET transverse images (A) of HCT-116 xenograft tumor-bearing vehicle, BEZ-235/PLX-4720, AZD-6244/BEZ-235, AZD-6244/ABT-263-treated mice; tumors are denoted by white arrows. PET quantification of tissue %ID/g (B) revealed a significant difference between vehicle and AZD-6244/ABT-263-treated xenografts for [$^{18}$F]4-F-Gln and [$^{18}$F]FSPG, however, only [$^{18}$F]FDG uptake was significantly different from vehicle-treated tumors for all treatment cohorts. Changes in HCT-116 tumor volume by the fourth day of treatment ($N \geq 9$ for all cohorts), shown as percent change from day one baseline, revealed a significant reduction in size from vehicle-treated mice for all MEK inhibitor cohorts (C). Semi-quantitative analysis of Ki67 histological samples obtained

from imaged animals ($N \geq 7$ for all cohorts), where the relative percent of positively stained cells was evaluated for an entire tumor tissue section per animal, is also shown (E).

*Molecular Response to Targeted Therapy in Xenograft Tissues*

Using flash-frozen tumor samples obtained from PET imaged CRC xenograft-bearing mice, antibody array and western blot analysis was performed to assess molecular therapeutic response in these tissues. In support of an mTOR mediated pro-survival response to targeted therapy previously reported in mutant $BRAF^{V600E}$ tumors (6), mTOR and p38 levels were elevated compared to vehicle-treated tumors ($p = 0.0382$ and $p = 0.0153$, respectively) in COLO-205 tissue lysate (**Fig. 4.7A**). Interestingly, mTOR levels were moderately down in therapeutic cohorts treated with a combination of BRAF and PI3K/mTOR inhibitors ($p = 0.0378$) or MEK and BCL-2 family inhibitors ($p = 0.0280$) and greatly decreased for treatments using a single-agent MEK inhibitor only ($p = 0.0028$) (**Fig. 4.7B**). Western blot of COLO-205 tumor tissues (**Fig. 4.7C**) revealed changes in p-AKT (ser473) and p-ERK levels and were analogous to those previously reported (6).

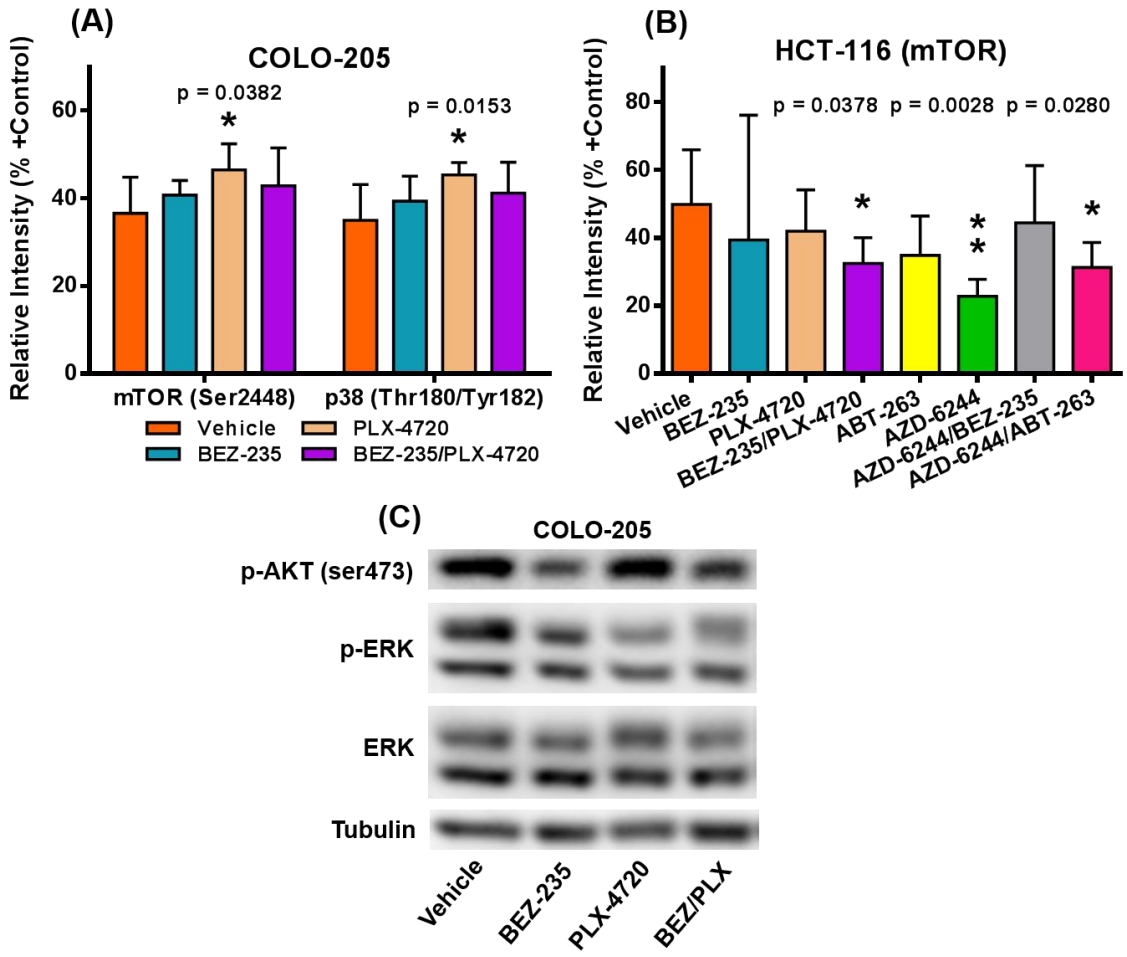


**Figure 4.7. Measures of drug response in xenograft tissues.** Chemiluminescent measured mTOR and p38 activity in COLO-205 xenograft tissue lysate (*N* = 3) illustrated elevation in PLX-4720 treated tissues only (A); similar to previously reported works (5,6). Analogously measured mTOR activity in HCT-116 xenograft tissue lysate (*N* = 3) revealed modest decreases in BEZ-235/PLX-4720 and AZD-6244/ABT-263 treated tumors while a greater decrease was observed in AZD-6244 single agent-treated tumors (B). Western blot of representative xenograft tissue lysate illustrated decreased p-ERK levels in PLX-4720 and BEZ-235/PLX-4720 combination-treated tumors (C).

*[$^{18}$F]4-F-Gln PET Detects Activation of Mutant Kras*

Using genetically engineered mice which mimicked common genetic profiles observed in human colon cancer, glutamine uptake was observed to associate with mutant *Kras* oncogene activation (**Fig. 4.8**). In collaboration with Eliot T. McKinley, histological evaluation of Asct2 expression, a sodium-dependent, neutral amino acid transporter of glutamine encoded by the gene *Slc1a5*, was explored using an

immunofluorescence methodology in tissue samples obtained from an *Lrig1-CreER$^{T2/+}$;Apc$^{fl/fl}$* and an *Lrig1-CreER$^{T2/+}$;Apc$^{fl/fl}$;Kras$^{G12D}$* mice (**Fig. 4.8A, B**). Interestingly, we observed elevated Asct2 at the tissue level when mutations in *Kras* were introduced. These results spurred further *in vivo* experiments employing [$^{18}$F]4-F-Gln PET imaging in these models. Not surprisingly, elevated uptake of [$^{18}$F]4-F-Gln was observed in tumors arising in an *Lrig1-CreER$^{T2/+}$;Apc$^{fl/fl}$;Kras$^{G12D}$* compared to an *Lrig1-CreER$^{T2/+}$;Apc$^{fl/fl}$* mice (**Fig. 4.8C-F**) as determined by image contrast between the distal colon, where *Kras* expression was induced, and normal muscle tissues (**Fig. 4.8E**). Contrast ratios, defined as C/M, were found to be longitudinally consistent over time for an *Lrig1-CreER$^{T2/+}$;Apc$^{fl/fl}$* both before and after tamoxifen induction: 1.05 ± 0.11 (pre-induction), 1.03 ± 0.15, $p > 0.9999$ (14-16 days), and 1.14 ± 0.14, $p = 0.4939$ (27-29 days). For an *Lrig1-CreER$^{T2/+}$;Apc$^{fl/fl}$;Kras$^{G12D}$* mice after induction, [$^{18}$F]4-F-Gln uptake was elevated from both the baseline time-point as well as the *Lrig1-CreER$^{T2/+}$;Apc$^{fl/fl}$* animal model: 1.05 ± 0.04 (pre-induction), 1.53 ± 0.24 (14-16 days), and 1.59 ± 0.22 (27-29 days). Analogously performed [$^{18}$F]FSPG PET did not reveal increased agent accumulation in *Lrig1-CreER$^{T2/+}$;Apc$^{fl/fl}$;Kras$^{G12D}$* mouse tissues ($p = 0.4857$) (**Fig. 4.8G**); potentially suggesting that, unlike glutaminolysis, cysteine and glutamate cellular transport may not be mediated by mutations in *Kras*. In comparison studies, [$^{18}$F]4-F-Gln PET in a single *Lrig1-CreER$^{T2/+}$;Kras$^{G12D}$* mouse revealed targeted accumulation in oral lesions (**Fig. 4.8H**). Though a sampling of one, this finding suggests that [$^{18}$F]4-F-Gln PET could be an appropriate imaging metric for evaluating amino acid metabolism and the effects of mutations in *APC*, a major initiator of CRC.

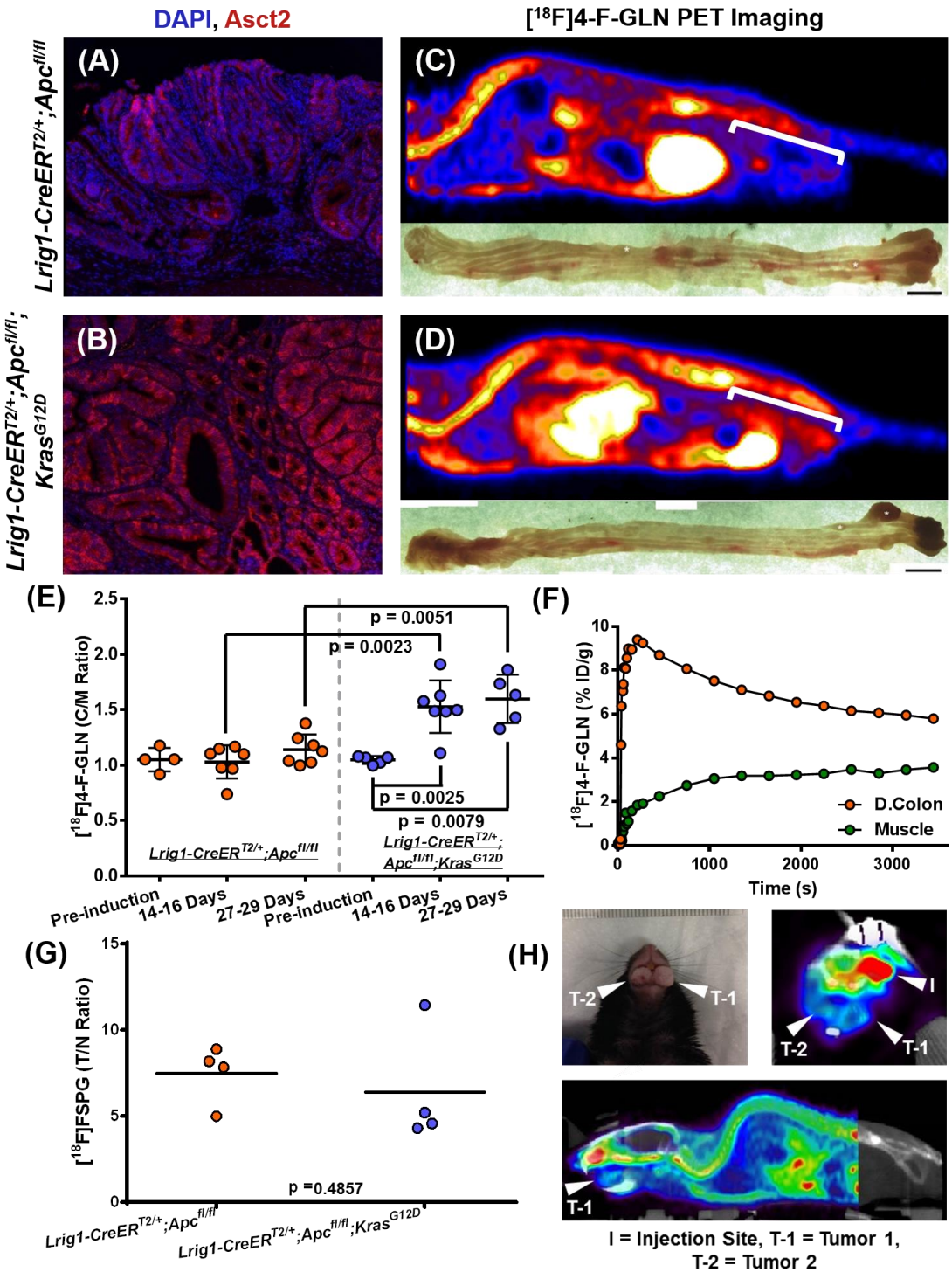


**Figure 4.8. [$^{18}$F]4-F-GLN uptake associated with expression of mutant *Kras*.** Immunofluorescence histological evaluation of Asct2 expression (red) in genetically engineered mouse tissues (A/B). Representative [$^{18}$F]4-F-Gln PET sagittal images of an *Lrig1-CreER$^{T2/+}$;Apc$^{fl/fl}$* (C) and an *Lrig1-CreER$^{T2/+}$;Apc$^{fl/fl}$;Kras$^{G12D}$* (D) mice four weeks after tamoxifen induction. White brackets denote the relative areas defined as distal colon during post-processing. PET quantification of tissue contrast (Distal

Colon/Muscle or C/M) (E) revealed a significant difference between pre- and post-induction with tamoxifen in an *Lrig1-CreER$^{T2/+}$;Apc$^{fl/fl}$;Kras$^{G12D}$* as well as between *Kras* and non-*Kras* mutant mice. A representative time activity curve (TAC) for a *Lrig1-CreER$^{T2/+}$;Apc$^{fl/fl}$;Kras$^{G12D}$* mouse (F), four weeks post-induction, revealed modest washout of glutamine imaging agent over a 60 min period with accumulation reaching equilibrium within the last 20 min. In comparative PET studies, [$^{18}$F]FSPG accumulation in was not elevated in the distal colon tissue of *Lrig1-CreER$^{T2/+}$;Apc$^{fl/fl}$;Kras$^{G12D}$* mice 20-22 day post-induction (G). Preliminary evaluations of [$^{18}$F]4-F-Gln PET in a single *Lrig1-CreER$^{T2/+}$;Kras$^{G12D}$* mouse revealed targeted accumulation in oral lesions (H).

### 4.5. Discussion

Emerging evidence has implicated oncogenic signaling with metabolic and nutrient uptake reprogramming in cancer cells (41,42). For example, cellular uptake of glucose can be controlled by activation of oncogenic pathways (43,44), such as PI3K, RAS, BRAF and MYC, while glutamine dependency has been linked to mutations in *MYC* (45-49) and *KRAS* (14,50). An observed consequence of oncogenic glutamine up-regulation has been the enhanced expression of a sodium-dependent transporter of glutamine, ASCT2 (gene symbol *SLC1A5*). ASCT2 has been suggested to play a role in metabolism, growth, and survival of lung cancer (10,51) with comparable observations being observed in clinical CRC tissue samples (52,53). Similar histological studies in clinical samples of primary colon tumors and advanced disease obtained from Vanderbilt Medical Center patients (data not shown) agree with these reports and found ASCT2 expression to be elevated in primary tumor tissue compared to metastatic disease (65% vs. 33%) and normal tissue (65% vs. 5%). Given the cellular and molecular implications of cancer metabolic reprogramming beyond glycolysis and the Warburg effect, there is a pressing need to characterize and evaluate non-invasive imaging metrics that could serve as supplementary or even alternative tools to conventional [$^{18}$F]FDG PET imaging. Towards this end, these studies sought to elucidate the feasibility of [$^{18}$F]4-F-GLN PET to report on therapeutic response and genetic mutations in CRC. To the current

knowledge of the authors, this is the first report to explore glutamine-derived PET as a means of evaluating targeted drug response *in vivo*.

A multi-drug therapeutic regimen that includes an inhibitor of mutant BRAF and a PI3K/mTOR inhibitor has been shown to be a rational therapeutic approach for $BRAF^{V600E}$ melanoma (54,55) and CRC (5,6,34). Our previous work in this setting illustrated [$^{18}$F]FDG PET to be insufficient for observing activation of pro-survival signaling pathways that were detectable by [$^{18}$F]FLT PET (6) when using BRAF/PI3K targeted therapy in $BRAF^{V600E}$ mutant CRC preclinical models. Analogously, a novel imaging agent for the detection of caspase activity *in vivo*, [$^{18}$F]FB-VAD-FMK, was capable of reflecting apoptotic cell death induced from combined inhibition of mutant BRAF and PI3K/mTOR whereas single agent therapeutics were ineffective (34). Stemming from this work, metabolic responses to targeted therapy were explored in unbiased microarray profiling of COLO-205 xenograft tumors treated with vehicle or PLX-4720, an inhibitor of mutant BRAF, revealed 267 statistically significant genes differentially expressed between these two groups (data not shown). Five solute carrier family genes were found to be up-regulated in resistant tumors. Among these, (SNAT5, gene symbol *SLC38A5*), a sodium-coupled neutral amino acid transporter of glutamine and other neutral amino acids (56), was identified as a potentially novel biomarker of resistance. Though not previously associated with carcinogenesis, SNAT5 expression has previously been observed in the kidney (56) and retina (57). The observation that SNAT5 expression is elevated in colon cancer cells that resist targeted therapy suggests an opportunity to use non-invasive imaging assays of glutamine uptake to predict resistance in this setting.

Towards this end, [$^{18}$F]4-F-Gln PET was used to evaluate response to a multi-drug therapy using PLX-4720 and BEZ-235, a PI3K/mTOR inhibitor, in $BRAF^{V600E}$-expressing COLO-205 xenograft-bearing mice. In both *in vitro* and *in vivo* studies, which

measured cellular uptake of [$^{3}$H]glutamine and [$^{18}$F]4-F-Gln respectively, decreased glutamine accumulation was observed in COLO-205 cells and tissues treated with a combination of BRAF and PI3K/mTOR inhibitors. Given the increasingly reported phenomena of MYC-regulated glutamine addiction in cancer cells (45-49), it is possible that [$^{18}$F]4-F-Gln PET acts, at least in this setting, as a measure of events downstream to PI3K/mTOR and BRAF inhibition and the subsequent loss of p-AKT and p-ERK activity; as validated by immunoblotting experiments of drug activity in both cells and resected tissue. As expected from our previous findings in COLO-205 xenografts (6), [$^{18}$F]FDG PET was incapable of discerning pro-survival feedback mechanisms against single agent PLX-4720 therapy and did not agree with evidence of drug response by immunoblotting. Interestingly, measurement of glutamate cell-dependency by [$^{18}$F]FSPG PET agreed with those observed by [$^{18}$F]4-F-Gln PET. While it is unclear from the current work which molecular responses and pathways may be involved in regulating [$^{18}$F]FSPG uptake, changes observed by PET for combination-treated animals could be related to mitochondrial stress and reactive oxygen species (ROS)-induced cell death due to the role that glutamate plays in the biosynthesis of glutathione (GSH) (32,58), a major intracellular thiol compound which serves as the main antioxidant defense against ROS. This hypothesis agrees with the apoptotic cell death response observed for BEZ-235/PLX-4720 combination-treated COLO-205 tumors in our previous work (34). Though the mechanism(s) behind these observations are still largely exploratory, greater understanding will hopefully be gained through the ongoing LC-MRM proteomic studies that have been pursued in collaboration with Daniel Liebler and Lisa Zimmerman.

When compared to other measures of therapeutic response, changes in [$^{18}$F]4-F-Gln accumulation in COLO-205 xenografts trended with measures of anti-proliferation response as tumor volumes and Ki67 IHC were found to be significantly reduced for BEZ-235/PLX-4720 combination-treated animals. Due to the role of glutamine in

nucleotide synthesis, [$^{18}$F]4-F-Gln PET may provide an estimate of de novo thymidine synthesis associated with proliferation, a process un-measurable by [$^{18}$F]-FLT PET; however, this potential correlation would need to be more rigorously explored in future work.

Given the promise of [$^{18}$F]4-F-GLN PET observed in COLO-205 treated tumors, we proceeded to explore this imaging metric as a measure of response to multi-drug therapies in wild type *BRAF*, mutant *PI3K* HCT-116 xenograft tumors. Serving as a negative control to *BRAF*$^{V600E}$ mutant COLO-205 tumors, combined inhibition of *BRAF* and *PI3K/mTOR* was found to be largely ineffective by immunoblotting, tumor growth, and Ki67 IHC analysis; as expected due to BRAF mediated resistance (5,6). Accordingly, [$^{18}$F]4-F-GLN and [$^{18}$F]FSPG PET were not sensitive to any therapeutic cohorts utilizing BEZ-235 and/or PLX-4720. Expanding these studies to drug regimens in which sensitivity has been reported in HCT-116 tumors (35), all three imaging agents were evaluated as measures of MEK and/or Bcl-2/Bcl-XL/Bcl-w inhibition using AZD-6244 and ABT-263. Initial *in vitro* studies of [$^{3}$H]glutamine uptake suggested modest sensitivity to MEK and BCL-2 family inhibition with greater response reported for MEK and PI3K/mTOR inhibition. *In vivo* PET imaging using [$^{18}$F]4-F-GLN and [$^{18}$F]FSPG disagreed with *in vitro* predictions as well as with Ki67 IHC and detected changes only in AZD-6244/ABT-263 combination-treated tumors. While these findings support previous works which claim combined MEK/BCL-XL inhibition to be a potential therapeutic approach for KRAS mutant cancers, it is presently unclear whether the observations gained from glutamine and glutamate PET imaging were a consequence of specific oncogenic regulatory pathways or the effects of cellular stress. Similar to observations in COLO-205 tumors, [$^{18}$F]FDG PET reported sensitivity to all drug cohorts and was unable to discern molecular deviations between therapeutic effects. As with the COLO-205 treatment model, determining the metabolic effects of targeted drug therapies in HCT-

116 has been the subject of exploration in ongoing collaborative LC-MRM proteomic efforts.

Expanding investigations to the detection of specifically expressed gene mutations, [$^{18}$F]4-F-GLN PET was explored in genetically engineered mouse models which recapitulate the sequence of genetic mutation and loss of function leading to colonic tumors in humans. In this setting, Asct2 expression and cellular glutamine uptake were associated with activation of mutant *Kras*. By immunofluorescence, increased Asct2 expression was observed in colon cancers arising from the *Lrig1-CreER$^{T2/+}$;Apc$^{fl/fl}$;Kras$^{G12D}$* genotype compared to *Kras* wild type mice; an expected observation given the implication of KRAS regulated glutamine dependency observed in pancreatic cancer (25). Ongoing works seek to expand the assessment of Asct2 expression levels in larger cohorts of *Lrig1-CreER$^{T2/+}$;Apc$^{fl/fl}$*, *Lrig1-CreER$^{T2/+}$;Kras$^{G12D}$*, and *Lrig1-CreER$^{T2/+}$;Apc$^{fl/fl}$;Kras$^{G12D}$* tissue samples. Concordantly, [$^{18}$F]4-F-GLN PET imaging was capable of discerning the potential expression of mutant Kras in the distal colon epithelium of these mice. Validation of Kras expression in excised mouse tissues has been actively pursued through collaborative efforts with Emily J. Poulin in the Coffey lab. Recently, the recombined *Kras* allele has been detected in gross tissue of *Lrig1-CreER$^{T2/+}$;Apc$^{fl/fl}$;Kras$^{G12D}$* mice and provides preliminary evidence, which supports the presence of mutant protein in whole tissue samples.

Given these findings, future studies could employ [$^{18}$F]4-F-GLN PET imaging to explore Wnt-induced tumor cell accumulation and CRC initiation due to the role that Myc plays as both an effector of Wnt signaling (59,60) and an inducer of glutaminolysis (45-49). As emerging evidence suggests a therapeutic role in the blockage of Wnt in the treatment of CRC (61,62), glutamine-derived molecular imaging could offer potential as a metric of predicting clinical and histopathological response to Wnt pathway-targeted

therapeutics.

### 4.6. Conclusions

We believe that these findings not only provide a greater understanding of the role that glutaminolysis plays in CRC, but also illuminates the potential impact that glutaminolysis-derived PET could have towards guiding drug development clinical trials as an imaging metric for detecting early therapeutic response. If glutamine PET imaging agents reflect Kras activity, such modalities may be useful towards the development of companion diagnostics for KRAS-targeted drugs. Future studies could also explore the relevance of ASCT2 expression in human colon adenoma samples, as a greater understanding of the clinical significance of ASCT2 expression and glutamine transport in early and advanced disease will be key for eventual translation of glutaminolysis PET imaging to clinical practice.

### 4.7. Works Cited


1. Zhao Y, Butler EB, Tan M. Targeting cellular metabolism to improve cancer therapeutics. Cell Death Dis 2013;4:e532.

2. Hsu PP, Sabatini DM. Cancer cell metabolism: Warburg and beyond. Cell 2008;134(5):703-7.

3. Ide M. Cancer screening with FDG-PET. Q J Nucl Med Mol Imaging 2006;50(1):23-7.

4. Tagliabue L, Del Sole A. Appropriate use of positron emission tomography with [(18)F]fluorodeoxyglucose for staging of oncology patients. Eur J Intern Med 2014;25(1):6-11.

5. McKinley ET, Smith RA, Zhao P, Fu A, Saleh SA, Uddin MI, et al. 3'-Deoxy-3'-18F-fluorothymidine PET predicts response to (V600E)BRAF-targeted therapy in preclinical models of colorectal cancer. J Nucl Med 2013;54(3):424-30.

6. McKinley ET, Zhao P, Coffey RJ, Washington MK, Manning HC. 3'-Deoxy-3'-[18F]-Fluorothymidine PET Imaging Reflects PI3K-mTOR-Mediated Pro-Survival Response to Targeted Therapy in Colorectal Cancer. PLoS One 2014;9(9):e108193.

7. Wise DR, Thompson CB. Glutamine addiction: a new therapeutic target in cancer. Trends Biochem Sci 2010;35(8):427-33.

8. Wellen KE, Lu C, Mancuso A, Lemons JM, Ryczko M, Dennis JW, et al. The hexosamine biosynthetic pathway couples growth factor-induced glutamine uptake to glucose metabolism. Genes Dev 2010;24(24):2784-99.

9. Thorens B, Mueckler M. Glucose transporters in the 21st Century. Am J Physiol Endocrinol Metab 2010;298(2):E141-5.

10. Hassanein M, Hoeksema MD, Shiota M, Qian J, Harris BK, Chen H, et al. SLC1A5 mediates glutamine transport required for lung cancer cell growth and survival. Clin Cancer Res 2013;19(3):560-70.

11. Krasikova RN, Kuznetsova OF, Fedorova OS, Belokon YN, Maleev VI, Mu L, et al. 4-[18F]fluoroglutamic acid (BAY 85-8050), a new amino acid radiotracer for PET imaging of tumors: synthesis and in vitro characterization. J Med Chem 2011;54(1):406-10.

12. Hensley CT, Wasti AT, DeBerardinis RJ. Glutamine and cancer: cell biology, physiology, and clinical opportunities. J Clin Invest 2013;123(9):3678-84.

13. Liu W, Le A, Hancock C, Lane AN, Dang CV, Fan TW, et al. Reprogramming of proline and glutamine metabolism contributes to the proliferative and metabolic responses regulated by oncogenic transcription factor c-MYC. Proc Natl Acad Sci U S A 2012;109(23):8983-8.

14. Gaglio D, Metallo CM, Gameiro PA, Hiller K, Danna LS, Balestrieri C, et al. Oncogenic K-Ras decouples glucose and glutamine metabolism to support cancer cell growth. Mol Syst Biol 2011;7:523.

15. Wise DR, Ward PS, Shay JE, Cross JR, Gruber JJ, Sachdeva UM, et al. Hypoxia promotes isocitrate dehydrogenase-dependent carboxylation of alpha-ketoglutarate to citrate to support cell growth and viability. Proc Natl Acad Sci U S A 2011;108(49):19611-6.

16. Wang JB, Erickson JW, Fuji R, Ramachandran S, Gao P, Dinavahi R, et al. Targeting mitochondrial glutaminase activity inhibits oncogenic transformation. Cancer Cell 2010;18(3):207-19.

17. Wise DR, DeBerardinis RJ, Mancuso A, Sayed N, Zhang XY, Pfeiffer HK, et al. Myc regulates a transcriptional program that stimulates mitochondrial glutaminolysis and leads to glutamine addiction. Proc Natl Acad Sci U S A 2008;105(48):18782-7.

18. Kranenburg O. The KRAS oncogene: past, present, and future. Biochim Biophys Acta 2005;1756(2):81-2.

19. Russo A, Bazan V, Agnese V, Rodolico V, Gebbia N. Prognostic and predictive factors in colorectal cancer: Kirsten Ras in CRC (RASCAL) and TP53CRC collaborative studies. Ann Oncol 2005;16 Suppl 4:iv44-49.

20. Nosho K, Irahara N, Shima K, Kure S, Kirkner GJ, Schernhammer ES, et al. Comprehensive biostatistical analysis of CpG island methylator phenotype in colorectal cancer using a large population-based sample. PLoS One 2008;3(11):e3698.

21. Suehiro Y, Wong CW, Chirieac LR, Kondo Y, Shen L, Webb CR, et al. Epigenetic-genetic interactions in the APC/WNT, RAS/RAF, and P53 pathways in colorectal carcinoma. Clin Cancer Res 2008;14(9):2560-9.

22. Castagnola P, Giaretti W. Mutant KRAS, chromosomal instability and prognosis in colorectal cancer. Biochim Biophys Acta 2005;1756(2):115-25.

23. Smit VT, Boot AJ, Smits AM, Fleuren GJ, Cornelisse CJ, Bos JL. KRAS codon 12 mutations occur very frequently in pancreatic adenocarcinomas. Nucleic Acids Res 1988;16(16):7773-82.

24. Almoguera C, Shibata D, Forrester K, Martin J, Arnheim N, Perucho M. Most human carcinomas of the exocrine pancreas contain mutant c-K-ras genes. Cell 1988;53(4):549-54.

25. Son J, Lyssiotis CA, Ying H, Wang X, Hua S, Ligorio M, et al. Glutamine supports pancreatic cancer growth through a KRAS-regulated metabolic pathway. Nature 2013;496(7443):101-5.

26. Lieberman BP, Ploessl K, Wang L, Qu W, Zha Z, Wise DR, et al. PET imaging of glutaminolysis in tumors by 18F-(2S,4R)4-fluoroglutamine. J Nucl Med 2011;52(12):1947-55.

27. Qu W, Zha Z, Ploessl K, Lieberman BP, Zhu L, Wise DR, et al. Synthesis of optically pure 4-fluoro-glutamines as potential metabolic imaging agents for tumors. J Am Chem Soc 2011;133(4):1122-33.

28. Wu Z, Zha Z, Li G, Lieberman BP, Choi SR, Ploessl K, et al. [F](2S,4S)-4-(3-Fluoropropyl)glutamine as a Tumor Imaging Agent. Mol Pharm 2014.

29. Buck JR, Saleh S, Uddin MI, Manning HC. Rapid, Microwave-Assisted Organic Synthesis of Selective (V600E)BRAF Inhibitors for Preclinical Cancer Research. Tetrahedron Lett 2012;53(32):4161-65.

30. Schulte MLD, E.S. Saleh, S.A. Cuthbertson, M.A. Manning, H.C. 2-Substituted Nγ-glutamylanilides as novel probes of ASCT2 with improved potency. Bioorganic & Medicinal Chemistry Letters 2014;In Press.

31. Qu W, Oya S, Lieberman BP, Ploessl K, Wang L, Wise DR, et al. Preparation and characterization of L-[5-11C]-glutamine for metabolic imaging of tumors. J Nucl Med 2012;53(1):98-105.

32. Koglin N, Mueller A, Berndt M, Schmitt-Willich H, Toschi L, Stephens AW, et al. Specific PET imaging of xC- transporter activity using a (1)(8)F-labeled glutamate derivative reveals a dominant pathway in tumor metabolism. Clin Cancer Res 2011;17(18):6000-11.

33. Ayers GD, McKinley ET, Zhao P, Fritz JM, Metry RE, Deal BC, et al. Volume of preclinical xenograft tumors is more accurately assessed by ultrasound imaging than manual caliper measurements. J Ultrasound Med 2010;29(6):891-901.

34. Hight MR, Cheung YY, Nickels ML, Dawson ES, Zhao P, Saleh S, et al. A peptide-based positron emission tomography probe for in vivo detection of caspase activity in apoptotic cells. Clin Cancer Res 2014;20(8):2126-35.

35. Corcoran RB, Cheng KA, Hata AN, Faber AC, Ebi H, Coffee EM, et al. Synthetic lethal interaction of combined BCL-XL and MEK inhibition promotes tumor regressions in KRAS mutant cancer models. Cancer Cell 2013;23(1):121-8.

36. Powell AE, Wang Y, Li Y, Poulin EJ, Means AL, Washington MK, et al. The Pan-ErbB Negative Regulator Lrig1 Is an Intestinal Stem Cell Marker that Functions as a Tumor Suppressor. Cell;149(1):146-58.

37. Powell AE, Vlacich G, Zhao ZY, McKinley ET, Washington MK, Manning HC, et al. Inducible loss of one Apc allele in Lrig1-expressing progenitor cells results in multiple distal colonic tumors with features of familial adenomatous polyposis. Am J Physiol Gastrointest Liver Physiol 2014;307(1):G16-23.

38. Fueger BJ, Czernin J, Hildebrandt I, Tran C, Halpern BS, Stout D, et al. Impact of animal handling on the results of 18F-FDG PET studies in mice. J Nucl Med 2006;47(6):999-1006.

39. Dandekar M, Tseng JR, Gambhir SS. Reproducibility of 18F-FDG microPET studies in mouse tumor xenografts. J Nucl Med 2007;48(4):602-7.

40. McKinley ET, Bugaj JE, Zhao P, Guleryuz S, Mantis C, Gokhale PC, et al. 18FDG-PET predicts pharmacodynamic response to OSI-906, a dual IGF-1R/IR inhibitor, in preclinical mouse models of lung cancer. Clin Cancer Res 2011;17(10):3332-40.

41. Levine AJ, Puzio-Kuter AM. The control of the metabolic switch in cancers by oncogenes and tumor suppressor genes. Science 2010;330(6009):1340-4.

42. Ward PS, Thompson CB. Metabolic reprogramming: a cancer hallmark even warburg did not anticipate. Cancer Cell 2012;21(3):297-308.

43. Ramsay EE, Hogg PJ, Dilda PJ. Mitochondrial metabolism inhibitors for cancer therapy. Pharm Res 2011;28(11):2731-44.

44. Galluzzi L, Kepp O, Vander Heiden MG, Kroemer G. Metabolic targets for cancer therapy. Nat Rev Drug Discov 2013;12(11):829-46.

45. Gao P, Tchernyshyov I, Chang TC, Lee YS, Kita K, Ochi T, et al. c-Myc suppression of miR-23a/b enhances mitochondrial glutaminase expression and glutamine metabolism. Nature 2009;458(7239):762-5.

46. Dang CV. Rethinking the Warburg effect with Myc micromanaging glutamine metabolism. Cancer Res 2010;70(3):859-62.

47. Dang CV, Le A, Gao P. MYC-induced cancer cell energy metabolism and therapeutic opportunities. Clin Cancer Res 2009;15(21):6479-83.

48. Gordan JD, Thompson CB, Simon MC. HIF and c-Myc: sibling rivals for control of cancer cell metabolism and proliferation. Cancer Cell 2007;12(2):108-13.

49. Qing G, Li B, Vu A, Skuli N, Walton ZE, Liu X, et al. ATF4 regulates MYC-mediated neuroblastoma cell death upon glutamine deprivation. Cancer Cell 2012;22(5):631-44.

50. Watanabe T, Kobunai T, Yamamoto Y, Matsuda K, Ishihara S, Nozawa K, et al. Differential gene expression signatures between colorectal cancers with and without KRAS mutations: crosstalk between the KRAS pathway and other signalling pathways. Eur J Cancer 2011;47(13):1946-54.

51. Kikuchi T, Hassanein M, Amann JM, Liu Q, Slebos RJ, Rahman SM, et al. In-depth proteomic analysis of nonsmall cell lung cancer to discover molecular targets and candidate biomarkers. Mol Cell Proteomics 2012;11(10):916-32.

52. Witte D, Ali N, Carlson N, Younes M. Overexpression of the neutral amino acid transporter ASCT2 in human colorectal adenocarcinoma. Anticancer Res 2002;22(5):2555-7.

53. Huang F, Zhao Y, Zhao J, Wu S, Jiang Y, Ma H, et al. Upregulated SLC1A5 promotes cell growth survival in colorectal cancer. Int J Clin Exp Pathol 2014;7(9):6006-14.

54. Tsai J, Lee JT, Wang W, Zhang J, Cho H, Mamo S, et al. Discovery of a selective inhibitor of oncogenic B-Raf kinase with potent antimelanoma activity. Proc Natl Acad Sci U S A 2008;105(8):3041-6.

55. Bollag G, Hirth P, Tsai J, Zhang J, Ibrahim PN, Cho H, et al. Clinical efficacy of a RAF inhibitor needs broad target blockade in BRAF-mutant melanoma. Nature 2010;467(7315):596-9.

56. Broer S. Amino acid transport across mammalian intestinal and renal epithelia. Physiol Rev 2008;88(1):249-86.

57. Umapathy NS, Li W, Mysona BA, Smith SB, Ganapathy V. Expression and function of glutamine transporters SN1 (SNAT3) and SN2 (SNAT5) in retinal Muller cells. Invest Ophthalmol Vis Sci 2005;46(11):3980-7.

58. Ribas V, Garcia-Ruiz C, Fernandez-Checa JC. Glutathione and mitochondria. Front Pharmacol 2014;5:151.

59. Nusse R. Wnt signaling and stem cell control. Cell Res 2008;18(5):523-7.

60. Niehrs C, Acebron SP. Mitotic and mitogenic Wnt signalling. EMBO J 2012;31(12):2705-13.

61. He B, Reguart N, You L, Mazieres J, Xu Z, Lee AY, et al. Blockade of Wnt-1 signaling induces apoptosis in human colorectal cancer cells containing downstream mutations. Oncogene 2005;24(18):3054-8.

62. Thorne CA, Hanson AJ, Schneider J, Tahinci E, Orton D, Cselenyi CS, et al. Small-molecule inhibition of Wnt signaling through activation of casein kinase 1alpha. Nat Chem Biol 2010;6(11):829-36.

# CHAPTER 5

# TSPO AS A PET BIOMARKER FOR EARLY DETECTION IN GI CANCER

## 5.1. Abstract

The outer mitochondrial membrane translocator protein (TSPO) has been associated with many cell processes and advanced cancer states. In contrast to conventional reports, the studies reported here explored the significance of TSPO expression as a biomarker of early gastrointestinal (GI) neoplasia; primarily colonic and pancreatic. Using TSPO immunohistochemistry (IHC) evaluation in clinically obtained tissue samples, TSPO expression was found to be elevated in low-grade colon cancers (G1/G2) as well as colorectal adenomas, compared to normal tissue. In clinical tissue samples of pancreatic cancer, TSPO expression was similarly elevated not only in advanced cancerous lesions, but also in pre-malignant pancreatic intraepithelial neoplasia (PanIN). PET imaging studies utilizing the TSPO ligands [$^{18}$F]VUIIS1008 and [$^{18}$F]VUIIS8310 were assessed as imaging metrics for the detection of PanIN occurrence and progression and revealed increased accumulation in lesion bearing pancreas compared to normal. Conclusively, these studies seek to expand the conception of TSPO as a cancer imaging biomarker of not only advanced disease, but of also early-stage GI neoplastic lesions.

## 5.2. Introduction

The translocator protein (TSPO), formerly termed peripheral benzodiazepine receptor (PBR), is an 18 kDa protein typically localized to the outer mitochondrial membrane and is expressed in mitochondrial-enriched tissues (*i.e.*, skeletal muscle and myocardium, renal, and other steroid-producing tissues). TSPO participates in a number

of cellular processes (**Fig. 5.1**) (1), including cholesterol metabolism, steroid biosynthesis, cellular proliferation, and apoptosis. Elevated TSPO expression is found in many disease states including neuroinflammation (2), neurological disorders (3,4), as well as cancers of the breast (5,6), prostate (7), oral cavity (8), colon (9), liver (10), and brain (11,12). Furthermore, elevated TSPO levels have been linked with disease progression and diminished survival and is conventionally associated with aggressive, metastatic behavior.

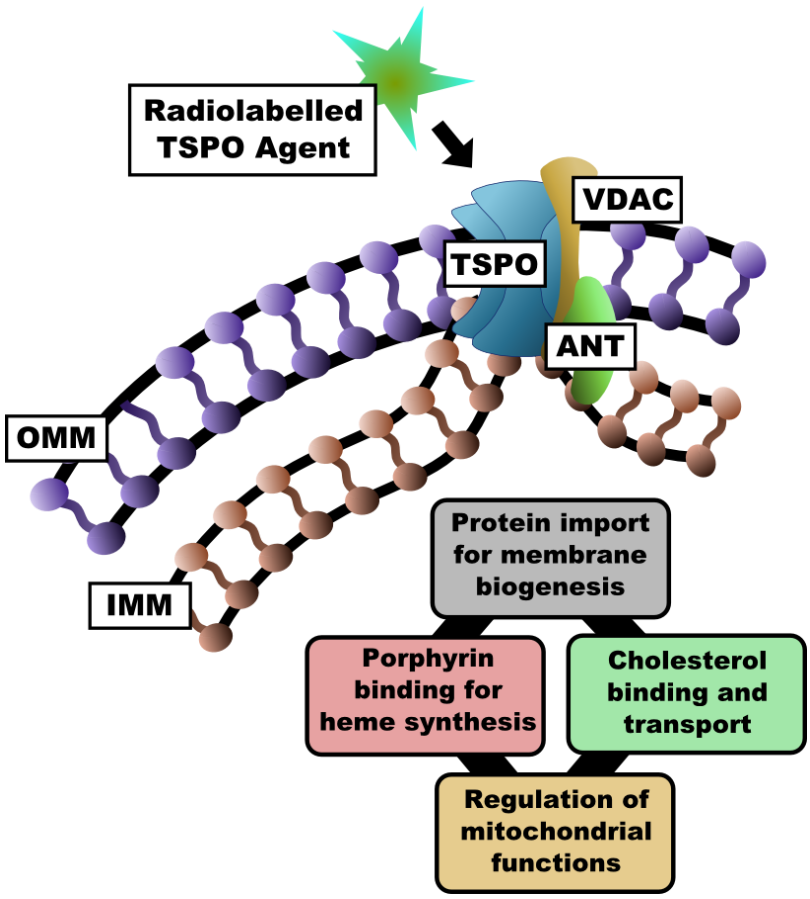


**Figure 5.1. The molecular relationship and determinants of TSPO function.** TSPO is a hetero-oligomeric, macromolecular complex which consists of the isoquinolone binding protein of 18-kDa TSPO, a voltage-dependent anion channel (VDAC) and an adenine nucleotide transporter (ANT). The transport of lipophilic molecules across the intermembrane space is facilitated by contact sites on both the outer and inner mitochondrial membranes (OMM and IMM, respectively). Combined, TSPO serves to: regulate cholesterol binding and mitochondrial transport, play a key function in steroidogenesis and bile salt synthesis, import proteins for membrane biogenesis and other cellular functions, participate in porphyrin binding and transport for heme

synthesis, and regulate a host of other mitochondrial functions. This figure was adapted from the cited work (13).

TSPO ligands were first developed and utilized as cancer imaging agents when a tritium labelled TSPO ligand, PK-11195, was shown capable of distinguishing brain tumors from normal cortex using *ex vivo* autoradiography (14). Since this initial discovery, imaging studies using PK-11195 analogues modified for positron emission tomography (PET) (15) and near infrared optical imaging (16) have revealed the potential of TSPO-targeted molecular detection as an imaging metric for cancer detection and screening. However, there are multiple shortcomings inherent to this agent class; including modest signal-to-noise ratio and low blood–brain barrier permeability. These limitations, in part, have prompted the discovery of TSPO ligands which exhibit improved *in vivo* specificity; such as the aryloxyanilides (17), indoleacetamides (18), pyrazolopyrimidines (19), and imidazolepyridines (20). Several PET imaging agents derived from these scaffolds have been developed and subsequently explored for neuroinflammation imaging (21). Towards exploring oncological applications, the aryloxyanilide [$^{18}$F]PBR06 (22) and the pyrazolopyrimidine [$^{18}$F]DPA-714 (23) have been utilized for quantitative assessment of TSPO expression in glioma. In these studies, [$^{18}$F]PBR06 and [$^{18}$F]DPA-714 were reported to be highly specific *in vivo* and found to exhibit approximately 70% displacement of the radioactive probe when challenged by the cold version of the molecule; unlike [$^{11}$C]PK-11195 which exhibited approximately 30% displacement. Beyond [$^{18}$F]PBR06 and [$^{18}$F]DPA-714, novel TSPO imaging ligands are still being developed and reported. Recently, a pyrazolopyrimidine derivative ([$^{18}$F]VUIIS1008) (24) and pyridazinoindole analogue (7-chloro-N,N,5-trimethyl-4-oxo-3(6-[$^{18}$F]fluoropyridin-2-yl)-3,5-dihydro-4H-pyridazino[4,5-b]indole-1-cetamide, henceforth referred to as [$^{18}$F]VUIIS8310) (25) were reported as possessing greater *in vivo* specificity towards TSPO than either [$^{18}$F]PBR06 or [$^{18}$F]DPA-714.

While TSPO expression in cancer is conventionally considered a biomarker of advanced tumors, emerging evidence suggests it may also be a characteristic of early neoplasia. In a recent report, PET imaging of [$^{18}$F]VUIIS1008 in a genetically engineered mouse, which recapitulated many features of familial adenomatous polyposis (ADF), revealed localized agent accumulation in distal colon tumors which expressed high levels of Tspo and β-catenin (26). Encouraged by this work, the studies reported here explored the significance of TSPO expression as a biomarker of early gastrointestinal (GI) neoplasia; primarily colonic and pancreatic. Using a tissue microarray (TMA) comprised of 89 clinically representative colon cancers from patients, we found TSPO immunohistochemistry (IHC) to be elevated in low-grade colon cancers (G1/G2). In further histological evaluations, TSPO expression was found to be elevated in colorectal adenomas, compared to normal tissue, using a pool of 56 clinically obtained samples. In tissue samples of pancreatic cancer, TSPO expression was similarly elevated not only in advanced cancerous lesions, but also in a variety of pre-malignant lesions. Molecular imaging studies using the PET imaging agents [$^{18}$F]VUIIS1008 and [$^{18}$F]VUIIS8310 were also incorporated to assess the potential of using TSPO PET as an imaging metric for the detection of early pancreatic neoplasia. Conclusively, these studies seek to expand the conception of TSPO as a cancer imaging biomarker of not only advanced disease, but of also early-stage GI neoplastic lesions.

## 5.3. Materials and Methods

*Colon Cancer Tissue Microarrays*

After institutional review board approval, primary colorectal cancer and normal colonic mucosa tissue samples were collected from 99 patients treated at Vanderbilt University Medical Center. Tissue samples were histologically verified and

representative regions, sampled in duplicate using 1 mm cores, were selected for inclusion in the TMAs. Of the original 99 patient sample pool, tissues from 84 and 89 patients, for TSPO and Ki67 respectively, were evaluable by histology. IHC biomarker expression for tumor samples were scored, in triplicate, on an ordinal intensity scale ranging from zero to three where no expression was defined as zero, weak expression as one, moderate expression as two, and strong expression as three.

*Colon Adenomas*

For evaluation of TSPO expression in early colorectal neoplasia, clinical colon adenoma samples were collected from 66 patients and selected to represent a range of cancer progression risk determinants; such as polyp size, presence of villous growth features, and degree of dysplasia (27). From the initial sampling, TSPO localization was measurable in tissue samples from 56 patients. IHC expression was assessed using an intensity scale system similar to that employed for TMA analysis.

*Tissue Microarrays of Pancreas Cancer and Pre-Malignant Lesions*

Pancreatic cancer TMAs were developed using samples collected from 155 Vanderbilt Medical Center patients and included normal pancreas, pancreatic intraepithelial neoplasia (PanIN), and invasive pancreatic ductal adenocarcinoma (PDAC). TSPO IHC expression was assessed using an intensity score-derived methodology which defined none/weak expression as one, moderate expression as two, and strong expression as three.

*[$^{18}$F]TSPO Imaging Agents*

[$^{18}$F]VUIIS1008 and [$^{18}$F]VUIIS8310 were produced using radiosynthesis methodologies analogous to those previously published (24,25). For small animal

imaging studies, radiochemical specific actives were within range of 170 ± 80 TBq/mmol for [$^{18}$F]VUIIS1008 and as high as 206 TBq/mmol for [$^{18}$F]VUIIS8310.

*Genetically Engineered Mouse Models*

All studies involving small animals were conducted in accordance with both federal and institutional guidelines. Genetically engineered mice of colon cancer were provided by Robert J. Coffey and colleagues as part of collaborative efforts through either Vanderbilt's GI SPORE program. For colon cancer models, *Lrig1-CreER$^{T2/+}$* mice (28) were crossed with *Apc$^{fl/+}$* mice (The Jackson Laboratory) to generate *Lrig1-CreER$^{T2/+}$;Apc$^{fl/+}$* mice; similarly to published works (26). Six to eight week old mice were injected with 2 mg tamoxifen intraperitoneally for three consecutive days to induce tumor formation. Mice were imaged approximately 100 days after injection of tamoxifen and then sacrificed.

Animal models of pancreatic cancer were provided by either Harold L. Moses or Robert J. Coffey, and colleagues, as part of collaborative efforts funded by the Lustgarten Foundation. Three validated genetically engineered mouse models which recapitulated genetic mutations relevant in human pancreatic cancer were generated and included: *Pft1a-Cre;Kras$^{G12D}$*, *Pft1a-Cre;Kras$^{G12D}$;Trp53$^{R172H/+}$*, and *Pft1a-Cre*;*Kras$^{G12D}$;Tgfbr2$^{+/-}$*. *Pft1a-Cre;Kras$^{G12D}$* mice progress to higher grade PanIN lesions (29) and were chosen to model pre-invasive disease. Advanced disease was modeled using and *Pft1a-Cre;Kras$^{G12D}$;Trp53$^{R172H/+}$* (30) and *Pft1a-Cre;Kras$^{G12D}$;Tgfbr2$^{+/-}$* mice (31). Animals possessing single vector (*i.e. Kras, Cre*, *Tgfbr*, or *p53* only) or wild genotypes were utilized as age-matched controls. TSPO PET imaging was evaluated at regular intervals that approached the median survival for each model. *Pft1a-Cre;Kras$^{G12D}$* mice were imaged up to twelve months of age while schedules were compressed for *Pft1a-Cre;Kras$^{G12D}$;Trp53$^{R172H/+}$* and *Pft1a-Cre;Kras$^{G12D}$;Tgfbr2$^{+/-}$* to account for the rapid

progression of tumors in these models (30-32). Animals were weighed and sacrificed for tissue collection shortly after imaging and white light photographs obtained during tissue resection to document relative location, size, and shape of the pancreas.

*PET Imaging and Analysis*

Animal handling and preparation for and during PET imaging studies were performed analogously to previously described methods (33). Upon study commencement, animals were anesthetized using 2% isofluorane anesthesia in 100% oxygen at 2 L/min and kept warm throughout the duration of the PET scan. Animals were administered 10.4-11.8 MBq of PET imaging agent *via* intravenous injection and imaged using a dedicated Concorde Microsystems Focus 220 microPET scanner (Siemens Preclinical Solutions). PET images were acquired as 60 min dynamic data sets initiated upon PET agent injection. Images were acquired at designated time points which corresponded with the age of the animal.

PET data were reconstructed using a three-dimensional (3D) ordered subset expectation maximization/maximum a posteriori (OSEM3D/MAP) algorithm. Dynamic data was binned into twelve 5 s (0-1 min) and fifty-nine 60 s (2-60 min) frames. The resulting three-dimensional reconstructions had an x-y voxel size of 0.474 mm and inter-slice distance of 0.796 mm. For quantification of PET agent uptake, ASIPro software (Siemens Preclinical Solutions) was used to manually draw three-dimensional regions of interest (ROI) around the entire tumor volume and the measured counts converted to the percentage of the injected dose per gram of tissue (%ID/g). To aid in the localization of tumor and non-tumor bearing pancreas, high field anatomical magnetic resonance images (MRI) were collected either immediately before or after PET imaging acquisitions. For initial evaluations, PET and MRI images were manually proportioned and overlaid using commercially available image processing software. Additional studies

could perform voxel-by-voxel co-registration to enable exact correlations between tracer accumulation and anatomy.

Supplementing the results presented in subsequent sections of this dissertation, a large archive of PET imaging data and tissue samples were obtained longitudinally for each of the three distinct mouse models of pancreatic cancer (**Table 5.1**). In summary, over 200 animals were imaged using TSPO PET agents (including: [$^{18}$F]VUIIS8310, [$^{18}$F]VUIIS1008, [$^{18}$F]VUIIS1009a, [$^{18}$F]VUIIS1009b, and [$^{18}$F]VUIIS1018a) in *Pft1a-Cre;Kras$^{G12D}$* (*N* = 78), *Pft1a-Cre;Kras$^{G12D}$;Tgfbr2$^{+/-}$* (*N* = 114), and *Pft1a-Cre;Kras$^{G12D}$;Trp53$^{R172H/+}$* (*N* = 25) animals. Though it is beyond the scope of this work to exhaustively explore the entirety of this data archive, further studies could rigorously evaluate the genetic implications of pancreatic cancer mutations, TSPO expression, and TSPO PET imaging as a consequence of oncogenic regulation and advancement of the disease.

| Genotype | Imaging/Sacrifice |
|---|---|
| *Pft1a-Cre;Kras$^{G12D}$* | Month 1, 3, 6, 9, 12 |
| *Pft1a-Cre;Kras$^{G12D}$;Trp53$^{R172H/+}$* | Month 1, 2, 3, 4, 5 |
| *Pft1a-Cre;Kras$^{G12D}$;Tgfbr2$^{+/-}$* | Week 4, 6, 8, 10,12 |

**Table 5.1. Summary of animal models of pancreatic cancer and imaging time points.** Animals were sacrificed at designated time points, shown above for each model, shortly following imaging studies.

*Plasma Activity and Radiometabolite*

For future determination of the arterial input function (AIF) for TSPO imaging agents, arterial blood from catheterized mice (50-80 µL) was collected every 10-15 s for the first 90 s following retro-orbital injection of 10.4-11.8 MBq. Subsequent blood samples were obtained at 2, 5, 8, 12, 20, 30, 45, and 60 min following administration. Whole blood samples were centrifuged at 14,000 rpm for 5 min in order to separate arterial plasma from whole blood. Radioactivity in isolated plasma samples (10 µL) using a NaI well counter (Capintec).

To determine the extent of arterial radiometabolism of these agents in mice, 100-200 μL of arterial blood was collected from catheterized mice at 2, 12, 30, 45, and 60 min immediately following agent administration. In some cases, the 45 min sample was eliminated dependent upon the health of the animal at that time. Arterial plasma was separated from whole blood by centrifuge. Proteins within isolated plasma (80 μL) were denatured and precipitated using a mixture of acetonitrile/water (188 μL, 7/1, v/v) and centrifugation at 14,000 rpm for 5 min. The resulting supernatant was spotted on silica/glass thin-layer chromatography (TLC) plates (GE Healthcare) and developed in a solution of 10% methanol in dichloromethane and scanned using an AR-2000 radio-TLC imaging scanner (Bioscan/TriFoil). TLC plates were evaluated by determining the ratio of the parent radioligand with respect to the total radioactivity in the plasma.

*MR Imaging and Analysis*

For MRI acquisitions, animals were secured in a prone position in a 38 mm inner diameter radiofrequency coil and placed in a 7.0T (16 cm bore) Varian small animal imaging system. Throughout scanning, animals were warmed to 37°C using heated air flow and maintained under anesthesia using 2% isofluorane anesthesia in 100% oxygen at 2 L/min. Following localization of the pancreas using multi-slice gradient echo images of all three imaging planes, T2-weighted fast-spin echo images were acquired over 22 slices in the axial and coronal planes using a 25.6 mm x 25.6 mm field of view, 1.0 mm slice thickness, and a 256 x 256 data matrix. Additional parameters included a 2 s repetition time, 36 ms effective echo time, 9 ms echo spacing, and an echo train length of 8. A pneumatic pillow was used to monitor the respiration cycle of the animals, as well as trigger the imaging acquisition to collect data at the same time point in the respiration cycle, in order to reduce motion-induced imaging artifacts.

*Immunohistochemistry*

Human colorectal cancer (CRC) TMAs, colon adenomas, and pancreatic cancer TMAs were blocked in paraffin, sectioned prior to immunostaining, and stained for TSPO expression using incubation of primary antibody (1:1000, Novus NB100-41398) for 10 min and subsequent incubation with the secondary antibody (Biocare Medical GHP516) for an additional 10 min. Additionally, human CRC TMAs were stained for β-catenin (1:1000, Transduction Labs 610154) and Ki67 (1:100, Dako M7240) for comparisons against TSPO expression. Tissues were evaluated by a group of reviewers familiar with TSPO expression patterns in oncology, including two expert GI pathologists (M. Kay Washington and Chanjuan Shi).

For mouse pancreas samples, whole tissue was harvested shortly following imaging and fixed in cold (4°C) 4% paraformaldehyde prepared fresh on the day of tissue collection. Normal and largely normal tissue samples were fixed for 1-2 h, while tumor bearing pancreas samples were fixed between 16-18 h. Duration of fixation was lengthened for tumor bearing pancreas samples due to notable increases in tissue stromal density; as observed by Masson's trichrome IHC. Following fixation, tissue samples were blocked in paraffin and stained for TSPO expression (various dilutions, Novus NB100-41398 or NBP1-95674). Tissues were similarly stained using standard H&E and Masson’s trichrome methods and reviewed by an expert gastrointestinal pathologist (Chanjuan Shi).

*Statistical Methods*

Associations among average marker expression for adenoma characteristics were estimated using the Pearson’s chi-squared and Wilcoxon signed-rank tests for statistical significance. For other determinations of statistical significance, an unpaired student t-test was applied to evaluate correlations between TSPO expression in

adenoma and PanIN/PDAC lesions compared to normal tissue. Differences were assessed within the GraphPad Prism 6.01 software package and considered statistically significant if $p < 0.05$. Unless otherwise indicated, experimental replicates are reported as the arithmetic mean ± standard error of the mean.

## 5.4. Results

*Expression of TSPO, β-Catenin, and Ki67 in Human CRC Tumors*

Initially, TSPO, β-catenin, and Ki67 protein expression were evaluated in human colorectal tumors to assess the potential utility of TSPO as a biomarker for targeted-imaging in a clinical setting. From unpublished work previously performed by Eliot T. McKinley and colleagues in the Manning group, low TSPO and β-catenin expression was observed in non-tumor colon tissue, while expression of both markers were greatly increased in grade 1, 2 and 3 tumors, compared to normal tissue. Across 84 tumors, high TSPO expression was noted in 64% (54) tumors including 82% (9/11) of grade 1 tumors (**Table 5.2**). In contrast, the widely used marker of proliferation, Ki67, showed high expression in 48% (43/89) tumors but was high in only 33% (4/12) of grade 1 tumors.

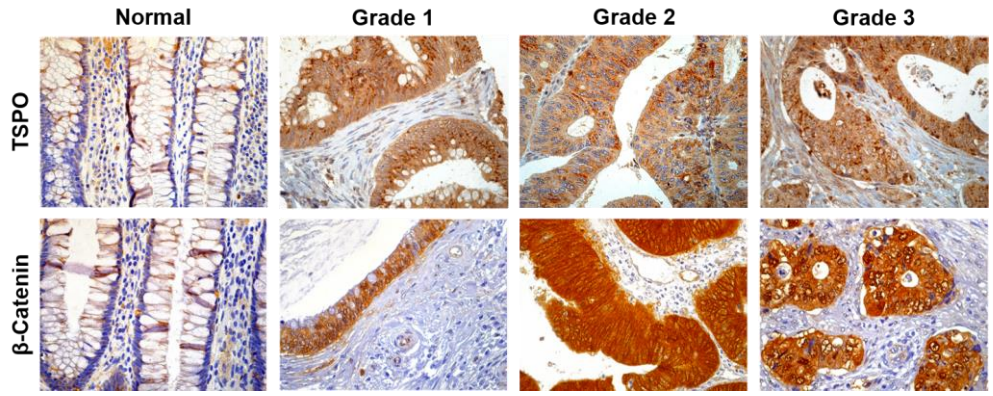


**Figure 5.2. TSPO and β-catenin expression was found elevated in human in human CRC tissues.** Representative, high-power white-light images (40x) of TSPO and

β-catenin histology in grades 1, 2, and 3 human CRC. For the images of TMA staining provided, disease grade corresponded to that of each core.

| Marker | Grade | Low | High | Total |
|---|---|---|---|---|
| TSPO | 1 | 18% (2) | 82% (9) | (13%) 11 |
| | 2 | 44% (24) | 56% (31) | (66%) 55 |
| | 3 | 22% (4) | 78% (14) | (21%) 18 |
| Total | | 36% (30) | 64% (54) | (100%) 84 |
| | | | | |
| Ki67 | 1 | 67% (8) | 33% (4) | (13%) 12 |
| | 2 | 50% (28) | 50% (28) | (63%) 56 |
| | 3 | 48% (10) | 52% (11) | (24%) 21 |
| Total | | 52% (46) | 48% (43) | (100%) 89 |

**Table 5.2. Tabulated TSPO and Ki67 IHC expression from human CRC TMAs as related to disease grade.** The average score for each biomarker was calculated and considered to by high expressing if the average IHC score exceeded 1.34.

*Distal Colon Tumors in Lrig1-CreER$^{T2/+}$;Apc$^{fl/+}$ Express High Tspo Levels and Elevated [$^{18}$F]VUIIS1008 Accumulation*

Expanding upon previous reports in the *Lrig1-CreER$^{T2/+}$;Apc$^{fl/+}$* mouse model (26), the ability of [$^{18}$F]VUIIS1008 PET to detect colon tumors in *Lrig1-CreER$^{T2/+}$;Apc$^{fl/+}$* with known tumors was explored along with wild type control mice. Wild type animals demonstrated low tracer uptake in the colon (**Fig. 5.3A, B**). *Lrig1-CreER$^{T2/+}$;Apc$^{fl/+}$* mice with colonoscopy confirmed tumors demonstrated increased focal uptake in the distal colon compared to adjacent non-tumor tissue and wild type controls. Similar uptake in the lungs, liver, and kidneys was observed across *Lrig1-CreER$^{T2/+}$;Apc$^{fl/+}$* and wild type mice. For tissue acquisition, *Lrig1-CreER$^{T2/+}$;Apc$^{fl/+}$* mice were sacrificed approximately 100 days following induction of colorectal tumors *via* tomoxifen injection. Upon sacrifice, gross examination of tissue samples revealed multiple large tumors in the distal colon with few, if any, observed in other sections of the large intestine. Histological evaluation of fixed colons illustrated robust Tspo and β-catenin expression (**Fig. 5.3C**) in the tumor

polyp, while relatively low expression of both markers in areas of normal colon. Tspo and β-catenin IHC showed similar localization in the tumor polyps with greater staining intensity observed for regions of low differentiation.

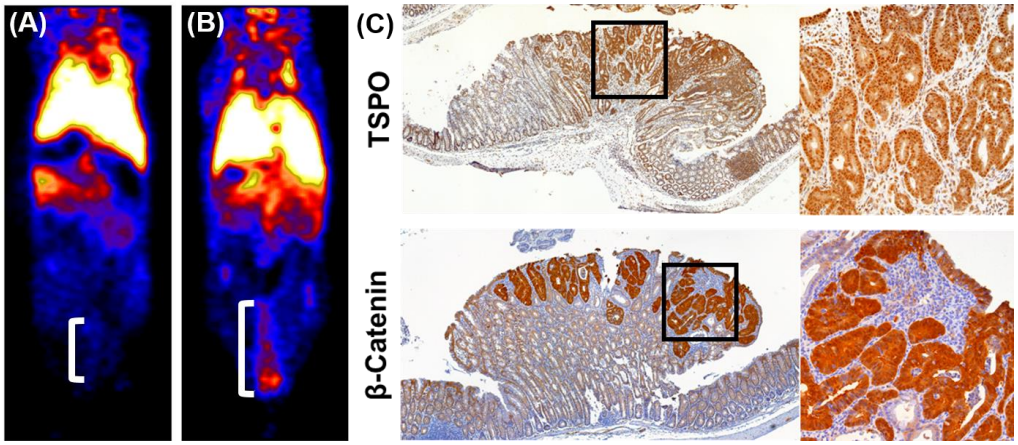


**Figure 5.3. Elevated Tspo expression was observed in *Lrig1-CreER$^{T2/+}$;Apc$^{fl/+}$* by Tspo PET and IHC.** Representative [$^{18}$F]VUIIS1008 coronal PET images of a representative wild type mouse (A) and *Lrig1-CreER$^{T2/+}$;Apc$^{fl/+}$* mouse (B) ~95 weeks after tamoxifen induction. White brackets denote the relative areas defined as distal colon during post-processing. Representative high- and low-magnification histological images (5x and 20x, respectively) of Tspo and β-catenin localization in colon lesion tissue obtained from the genetically engineered *Lrig1-CreER$^{T2/+}$;Apc$^{fl/+}$* mouse model (C).

*TSPO Expression in Human Adenoma*

Exploring TSPO as a biomarker of early CRC, TSPO expression was evaluated in 56 human adenoma samples possessing varied physical characteristics. Elevated TSPO expression was observed in sites of adenoma growth, compared to normal colon tissue within the same sample, for tubular (mean score of 1.12, $p < 0.0001$), tubulovillous (mean score of 1.74, $p < 0.0001$), and villous (mean score of 1.75, $p = 0.004$) lesions (**Fig. 5.4A, B**). Interestingly, when TSPO expression was compared against adenoma properties (*i.e.*, growth pattern, dysplasia grade, colon location, and size) (**Fig. 5.4C**) and β-catenin localization (**Fig. 5.4D**), no correlations between groups were observed. TSPO expression was found to be consistently elevated in the majority of adenomas.

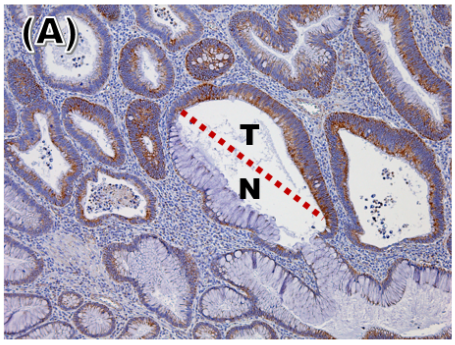


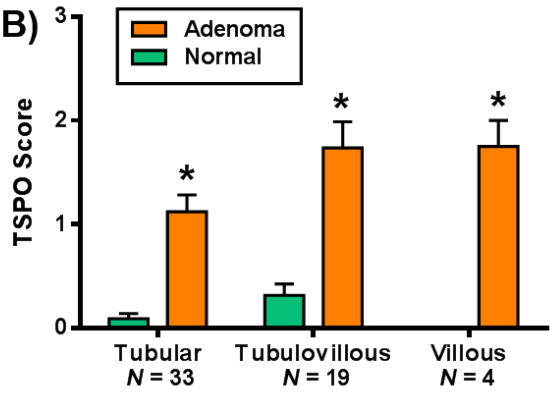


(C)

| Adenoma Properties | TSPO IHC | | | | |
|---|---|---|---|---|---|
| **Growth Patterns** | **Negative** | **Weak** | **Moderate/Strong** | **Total** | **Statistic** |
| **Tubular** | 77% (10) | 65% (11) | 46% (12) | 59% (33) | *P* = 0.368 |
| **Tubullovillous** | 23% (3) | 29% (5) | 42% (11) | 52% (29) | |
| **Villous** | 0% (0) | 6% (1) | 12% (3) | 7% (4) | |
| **Dysplasia Grade** | | | | | |
| **HGD** | 15% (2) | 12% (2) | 12% (3) | 12% (7) | *P* = 0.937 |
| **None/LGD** | 85% (11) | 88% (15) | 88% (23) | 88% (49) | |
| **Colon Location** | | | | | |
| **Left** | 38% (5) | 41% (7) | 58% (15) | 48% (27) | *P* = 0.413 |
| **Right** | 62% (8) | 59% (10) | 42% (11) | 52% (29) | |
| **Size** | | | | | |
| **Large** | 54% (7) | 59% (10) | 46% (12) | 52% (29) | *P* = 0.708 |
| **Small** | 46% (6) | 41% (7) | 54% (14) | 48% (27) | |
| **Total** | 23% (13) | 31% (17) | 46% (26) | 100% (56) | |

(D)

| β-Catenin IHC | TSPO IHC | | | | |
|---|---|---|---|---|---|
| **Surface** | **Negative** | **Weak** | **Moderate/Strong** | **Total** | **Statistic** |
| **Negative** | 69% (9) | 65% (11) | 73% (19) | 70% (39) | *P* = 0.843 |
| **Positive** | 31% (4) | 35% (6) | 27% (7) | 30% (17) | |
| **Mid** | | | | | |
| **Negative** | 69% (9) | 65% (11) | 73% (19) | 70% (39) | *P* = 0.843 |
| **Positive** | 31% (4) | 35% (6) | 27% (7) | 30% (17) | |
| **Basal** | | | | | |
| **Negative** | 54% (7) | 65% (11) | 65% (17) | 62% (35) | *P* = 0.762 |
| **Positive** | 46% (6) | 35% (6) | 35% (9) | 38% (21) | |
| **Total** | 23% (13) | 31% (17) | 46% (26) | 100% (56) | |

**Figure 5.4. TSPO expression was elevated in sites of human adenoma growth.** A representative, high-power white-light photo micrograph (10x) of a large (≥ 1 cm), tubular, human adenoma illustrates localization of TSPO staining in sites of tubular growth, 'T', as compared to normal colon tissue, 'N', within the same tissue sample (A). IHC scoring of tissue sections confirmed TSPO elevation in adenomas possessing either tubular, tubullovillous, or villous growth features (B). Values are shown as mean ± SEM and

asterisks indicate $p < 0.001$ compared to normal colon tissue. Normal tissue segments corresponding to villous adenomas (*N* = 4) were all negative for IHC expression. Tabulated TSPO IHC expression as compared to adenoma physical characteristics (C) or β-catenin expression (D) is provided. Physical characteristics evaluated included: growth features (tubular, tubullovillous, and villous), the presence of high or low grade dysplasia (HGD and LGD, respectively), colon location, or growth size (small < 1 cm, large ≥ 1 cm). Column values are displayed as the percentage of positive samples and frequency, *N*, provided in parenthesis. Test statistic values were derived using the Pearson's chi-squared test of statistical significance.

*Expression of TSPO in Early and Advanced Human Pancreatic Cancer*

In addition to human CRC, TSPO levels were evaluated in variety of early pancreatic cancer precursor lesions and pancreatic ductile adenocarcinoma compared to normal tissue and chronic pancreatitis (CP) (**Fig. 5.5**). Overall, TSPO expression was found to be very low in normal pancreas tissue with modest staining in centroascinar cells and normal ducts. Modest staining was also observed within the inflammatory infiltrate comprising chronic pancreatitis. Strikingly, both precursor lesions (PanIN1, PanIN2, and PanIN3) and invasive disease exhibited robust TSPO staining which appeared to primarily stem from ductal tissue. The mean IHC score of normal pancreas was approximately $1.025 \pm 0.104$ with CP tissue being moderately higher as $1.385 \pm 0.136$ ($p = 0.0382$). PanIN lesions were exhibited significantly higher TSPO expression with mean scores of $2.500 \pm 0.167$ ($p < 0.0001$), $2.000 \pm 0.333$ ($p = 0.0005$), and $2.000 \pm 0.548$ ($p = 0.0074$) for PanIN 1-3 lesions, respectively. Similarly, samples of PDAC exhibited high expression as noted by mean scores of $2.625 \pm 0.183$ ($p < 0.0001$), $2.576 \pm 0.156$ ($p < 0.0001$), and $1.923 \pm 0.211$ ($p = 0.0001$) for Grades 1-3, respectively.

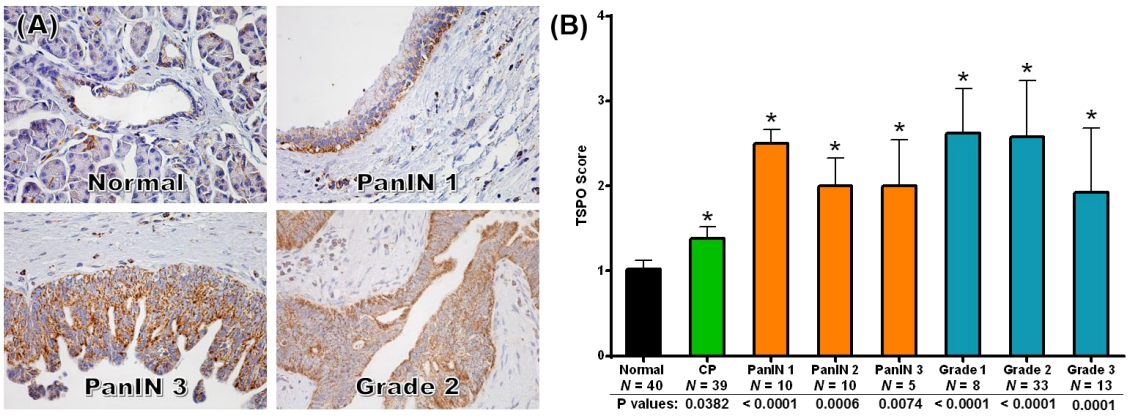


**Figure 5.5. TSPO expression was elevated in early and advanced pancreatic lesions.** Representative TSPO histological sections (40x) of Normal, PanIN 1, PanIN 3, and PDAC clinical tissue samples (A). Summary of mean ± SEM TSPO immunohistochemistry scoring of human pancreatic cancer TMA (155 patients) by three independent reviewers (B). Asterisks indicate statistical significance compared to normal pancreas. 'PanIN' comprises PanIN1-3 from this patient cohort.

*TSPO IHC in Genetically Engineered Mouse Pancreas*

All excised mouse pancreas tissue samples obtained to-date have been stained using H&E and Masson's Trichrome methodologies (**Fig. 5.6**). While current TSPO IHC methods remain un-optimized in mouse tissues, initial staining in a small cohort of samples appears promising and shows elevated protein expression, compared to normal, in PanIN lesions and invasive disease.

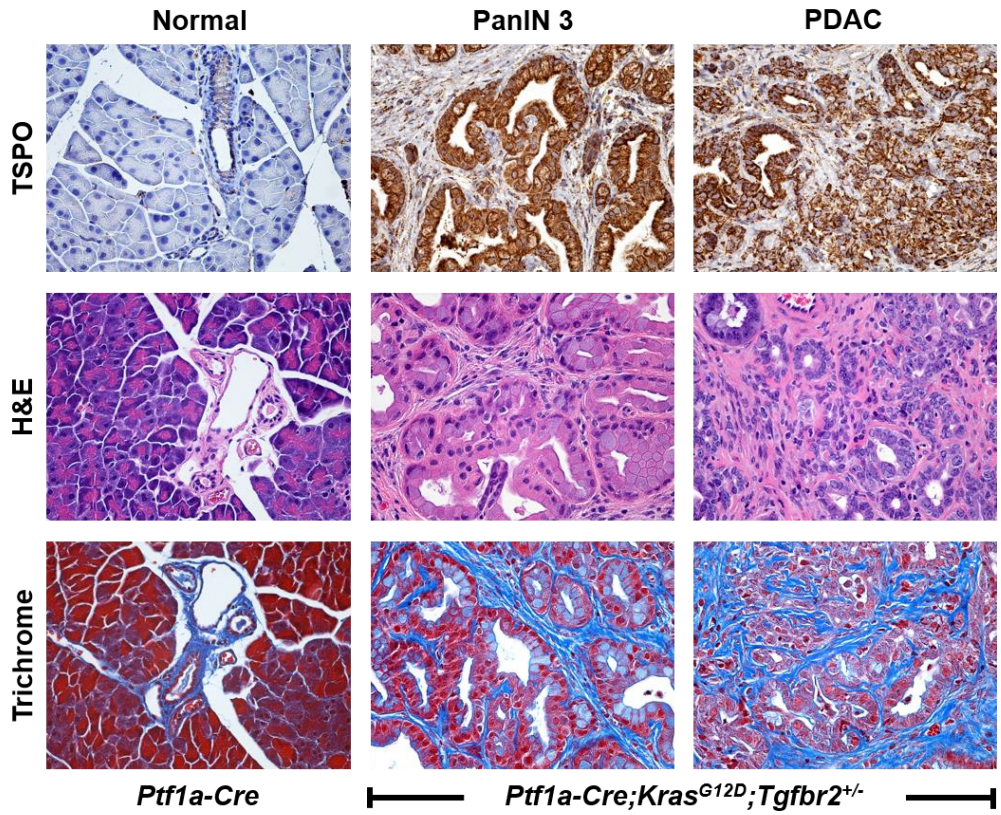


**Figure 5.6. TSPO expression in *Pft1a-Cre;Kras$^{G12D}$;Tgfbr2$^{+/-}$* pancreatic lesions.** A comparison of high-magnitude white-light images (40x) of representative TSPO (Novus NB1-95674), H&E, and Masson's Trichrome in excised tissue obtained from ≥ 12 week old mice. Images shown for *Pft1a-Cre;Kras$^{G12D}$;Tgfbr2$^{+/-}$* highlight different regions of a single tissue sample which represent high grade PanIN 3 lesions and metastatic PDAC.

*TSPO PET Imaging Detects Pancreatic Cancer Precursor Lesions*

Terminal PET imaging studies in three genetically engineered mouse models of precursor lesions and advanced pancreatic cancer (*Pft1a-Cre;Kras$^{G12D}$;Tgfbr2$^{+/-}$*, and *Pft1a-Cre;Kras$^{G12D}$;Trp53$^{R172H/+}$*) at pre-defined time-points throughout tumor development were explored with a variety imaging agents. PET imaging focused primarily on utilization of [$^{18}$F]VUIIS1008 and [$^{18}$F]VUIIS8310 and was complemented with high resolution MRI for voxel-by-voxel cross-platform registration.

Exploring [$^{18}$F]VUIIS1008 uptake in pancreatic neoplasia, three-dimensional dynamic PET data registered with high-field (7.0T) MRI data were collected. Similar to previous experience with this imaging agent in rats (24) and in the *Lrig1-CreER$^{T2/+}$;Apc$^{fl/+}$*

mouse model, accumulation of [$^{18}$F]VUIIS1008 was observed in kidney and liver as well as in myocardium and spleen. Importantly, focal uptake of [$^{18}$F]VUIIS1008 was also observed in tumor pancreas tissue of *Pft1a-Cre;Kras$^{G12D}$;Tgfbr2$^{+/-}$* mice compared to normal pancreas (**Fig. 5.7A**). Tumor morphology and structural histology confirmed the presence of predominantly low grade PanIN 1 precursor lesions in 7-8 week old *Pft1a-Cre;Kras$^{G12D}$;Tgfbr2$^{+/-}$* mice with more advanced disease being found in the tissues of 11-12 week old mice. Though increases of [$^{18}$F]VUIIS1008 uptake in tumor tissue only approached statistical significance for 11-12 week old mice ($p = 0.0466$) (**Fig. 5.7B**), which could be an indicator of lesion progression, both age cohorts exhibited trending increases in agent accumulation.

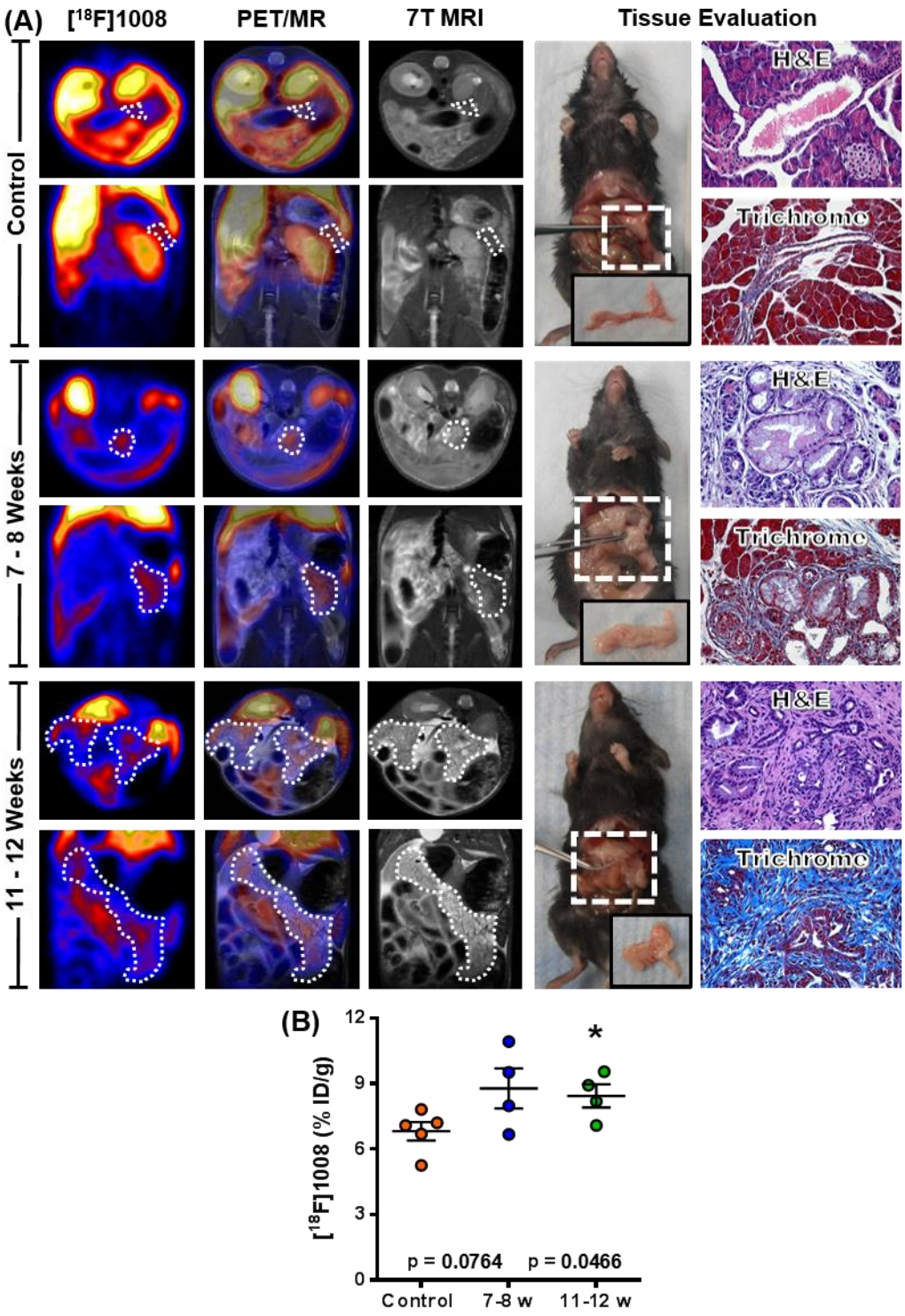


**Figure 5.7. [$^{18}$F]VUIIS1008 localization observed in *Pft1a-Cre;Kras$^{G12D}$;Tgfbr2$^{+/-}$* pancreatic lesions.** Representative [$^{18}$F]VUIIS1008 transverse and coronal PET, MR, and overlaid PET/MR images of 7-8 week old control and *Kras$^{G12D}$;Pft1a-Cre;Tgfbr2$^{+/-}$* animals (A). PET images shown are summed frames of the last 20 minutes of a 60 minute dynamic acquisition. Regions of interest for PET quantification were drawn as

indicated by white-dashed areas. High-power images of tissue resections as well as H&E and Masson's trichrome histological images (40x) from representative subjects of each animal cohort in which low-grade (PanIN1) and high-grade precursor lesions (PanIN2 and PanIN3) were observed for 7-8 and 11-12 week old mice, respectively. Quantified agent uptake (B), sown as injected dose per gram of tissue or %ID/g, of control (7-12 weeks of age) and *Pft1a-Cre;Kras$^{G12D}$;Tgfbr2$^{+/-}$* animals (7-8 weeks and 11-12 weeks of age). Asterisks indicate statistical significance compared to normal pancreas.

In other works, comparative imaging studies between [$^{18}$F]VUIIS8310 and [$^{18}$F]VUIIS1008 dynamic PET imaging in individual *Pft1a-Cre;Kras$^{G12D}$;Trp53$^{R172H/+}$* mice revealed consistent increases in [$^{18}$F]VUIIS8310 accumulation, compared to [$^{18}$F]VUIIS1008, as determined using a ratio paired t-test ($p = 0.0174$) (**Fig. 5.8**). These results coincide with the increased specificity observed for [$^{18}$F]VUIIS8310 in rat glioma reported in previous works (25).

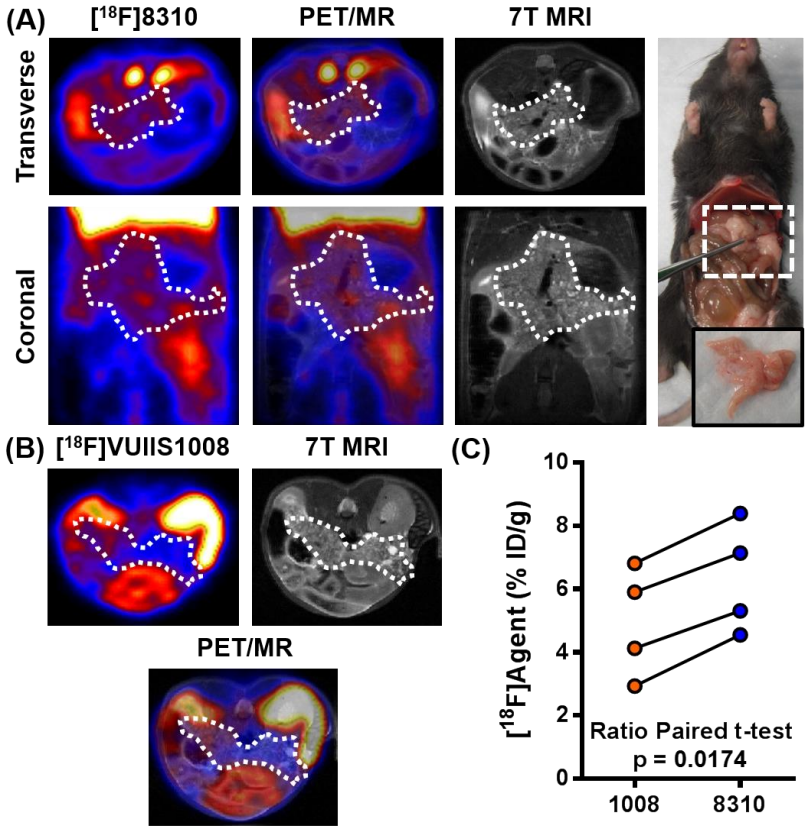


**Figure 5.8. [$^{18}$F]VUIIS8310 accumulation exceeded [$^{18}$F]VUIIS1008 in *Pft1a-Cre;Kras$^{G12D}$;Trp53$^{R172H/+}$* pancreatic lesions.** Representative [$^{18}$F]VUIIS8310 transverse and coronal PET, MR, co-registered PET/MR, and white-lite tissue resection mages

of a *Pft1a-Cre;Kras*$^{G12D}$*;Trp53*$^{R172H/+}$ animal (A). Representative [$^{18}$F]VUIIS1008 PET, MR, and co-registered PET/MR images in the same animal imaged 24 – 48 hours prior with [$^{18}$F]VUIIS8310 (B). PET images shown are summed frames of the last 20 minutes of a 60 minute dynamic acquisition. Regions of interest for PET quantification were drawn as indicated by white-dashed areas. Quantified agent uptake, sown as %ID/g, in individual animals imaged with both [$^{18}$F]VUIIS1008 and [$^{18}$F]VUIIS8310 are also shown (C).

### 5.5. Discussion

Due in part to limited detection capabilities during the early developmental stages, colorectal cancer is one of the most common causes of cancer related deaths in the Western world (34). Colonoscopy dominates the field of colorectal cancer screening with high detection success, however potentially cancerous lesions can still be overlooked with a range of miss rates reported throughout the literature (35-37). As such, there is a clinical need to determine and evaluate biomarkers of early disease progression which can serve as targets for novel, non-invasive imaging methodologies that may aid in patient screening. As high TSPO expression has been observed in a number of cancer types (5-12) and linked to cell processes commonly altered in cancer (*i.e.,* apoptosis (38,39) and reactive oxygen species generation (40,41)), TSPO is an attractive biomarker for screening by non-invasive imaging.

In contrast to being primarily associated with advanced tumors, the studies reported here revealed TSPO IHC to be elevated in a majority of low-grade colon cancers (G1/G2) compared to the gold standard clinical marker of proliferation, Ki67. Though a potential weakness of this analysis was the relatively small sampling of Grade 1 tissue samples, this finding suggests that TSPO may be a more appropriate biomarker of early disease than Ki67. Interestingly, increases in TSPO expression trended with increases in β-catenin levels, particularly in low grade colon cancers; suggesting a possible relationship between TSPO and Wnt pathway activity. Exploring this relationship in a well-controlled setting, TSPO levels were evaluated in stem cell-derived tumors arising in *Lrig1-CreER*$^{T2/+}$*;Apc*$^{fl/+}$ mice, in which one copy of *Apc* is eliminated in

Lrig1$^{+}$ progenitor cells with tamoxifen injection. In these tumors, which recapitulate many of the features of advanced human adenomas, Tspo was significantly elevated compared to the colons of wild type mice. Similarly to human tumors, Tspo levels in *Lrig1-CreER$^{T2/+}$;Apc$^{fl/+}$* tumors paralleled elevated levels of β-catenin. Taking a focused look at early disease, increases in TSPO expression, compared to normal colon, were observed in human adenomas and did not correlate with clinical risk factors for cancer; such as lesion size (≥ 1 cm), villous growth features, and evidence of high grade dysplasia. Interestingly, TSPO and β-catenin expression did not correlate in human adenoma tissues and contradicted trends observed in *Lrig1-CreER$^{T2/+}$;Apc$^{fl/+}$* and early/advanced human disease. Through western blot immunoreactivity and real time polymerase chain reaction (PCR) studies, no mechanistic dependencies between levels of TSPO and/or Wnt pathway regulators were discovered in CRC cell lines in response to TSPO inhibition or Wnt pathway activation (data not shown).

Wnt signaling activation often follows the loss of APC function, which serves as an initiating event for over 90% of CRCs (43-45). While TSPO gene expression has been observed in concordance with up-regulation of Wnt in breast cancer (42), this relationship is not completely understood. Despite the paralleling trends TSPO and β-catenin increases observed in all human CRC grade tumors, the absence of correlation between these two biomarkers in colon adenomas as well as the difficulty in identifying a mechanistic link *in vitro* makes it difficult to determine a specific relationship between TSPO expression and Wnt pathway activity. Given this, it is likely that TSPO expression in early and late stage colon cancer is modulated by other cellular and molecular determinants that will require further study to comprehend. Regardless, the tendency of TSPO expression to correlate with low- and high-risk adenoma, as well as low grade disease, reveal this biomarker to be suited for colon adenoma detection and guided tumor-resection. Given the previously reported utility of fluorescent TSPO ligands

towards detecting colonic tumors (16), TSPO could serve as an essential biomarker for the development of chromoendoscopy agents and the improvement of colonoscopy screening methodologies. Given these observations, we were encouraged to explore TSPO expression in other GI malignancies where PET imaging could play a major role in guiding patient care, such as pancreatic cancer.

Pancreatic cancer is one of the most aggressive cancers and currently retains an overall 5-year survival rate of only 5%. Despite improvements in surgery and oncologic treatments, clinical outcome has not improved over the past 25 years. In a recent report by Rahib, *et. al.*, pancreatic cancer was projected to become the second leading cause of cancer-related deaths by 2030; surpassing breast, prostate, and colorectal cancers (43). In this regard, imaging modalities capable of detecting small asymptomatic tumors or precursor lesions at a time when the disease is still in a curable stage could be imperative towards improving overall outcomes. As current diagnostic imaging methods, including [$^{18}$F]FDG PET (44), are inadequate for detecting early lesions, there remains an unmet clinical need to discover and evaluate novel imaging biomarkers which could accelerate the development of these technologies.

In clinically obtained samples of human pancreatic cancer precursor lesions and advanced disease, we evaluated TSPO levels in pancreatic ductile adenocarcinoma and a variety of pancreatic cancer precursor lesions. Though increases in TSPO expression were found elevated in a majority of PDACs, compared to normal tissue and CP, perhaps more importantly, TSPO elevation was comparable for a variety of low-grade, pre-malignant lesions. These trends suggest both a role for TSPO in the carcinogenesis of pancreatic cancer and the potential suitability of TSPO to serve as a marker of early neoplasia in this setting and a target for molecular imaging of human pancreatic cancer.

Expanding upon these findings, PET imaging studies using two second generation TSPO ligands ([$^{18}$F]VUIIS1008 and [$^{18}$F]VUIIS8310) revealed localized

accumulation in pancreas tissues bearing early and advanced pancreatic neoplasia. Interestingly, longitudinal evaluations of [$^{18}$F]VUIIS1008 accumulation in *Pft1a-Cre;Kras$^{G12D}$;Tgfbr2$^{+/-}$* lesions revealed only modest differences in uptake between early and more advanced disease states. The most substantial deviation between age cohorts was perhaps an observed decrease in uptake variance between older disease bearing animals; a phenomena which could be accounted for differences in disease growth rates between individuals. Interestingly, compartmental analysis of [$^{18}$F]VUIIS1008 TACs obtained from two *Pft1a-Cre;Kras$^{G12D}$;Tgfbr2$^{+/-}$* and two control animals revealed a stark difference in $k_3/k_4$ ratios between lesion bearing and normal pancreas tissues. This pharmacokinetic profile diverges from that previously reported in rat glioma (24) and could be a consequence of differences in blood flow properties and tissue densities, as supported by the degree of stroma observed in Masson's Trichrome stained excised tissues. As such, de-coupling blood flow properties in these models may be necessary in order to fully discern variations in TSPO agent accumulation between lesion bearing and normal pancreas. In this regard, we are poised to pursue these investigations in further works as arterial plasma activity time courses and corresponding metabolite measurements, data sets necessary for calculation of the arterial input function (AIF), have already been obtained. Alternatively, improvements in image quality may also be achieved with [$^{18}$F]VUIIS8310, in which preliminary, direct comparisons to [$^{18}$F]VUIIS1008 revealed higher uptake in pancreatic lesions and agreed with the higher specificity observed in rat glioma (25). Conclusively, these studies lay the foundation for the eventual translation of TSPO PET into the clinical setting. In fact, ongoing studies headed by colleagues within the Manning group are actively determining the suitability of TSPO PET for evaluating patients possessing intraductal papillary mucinous neoplasia (IPMN); early cystic precursor lesions to PDAC.

## 5.6. Conclusions

In contrast to conventional thought, which associates elevated TSPO expression with advanced tumors, these studies revealed TSPO expression to be a biomarker of early disease progression in GI cancers. This discovery could provide the basis for developing non-invasive imaging metrics for the detection and screening of patients possessing early colonic and pancreatic precursor lesions.

## 5.7. Works Cited


1. Papadopoulos V, Baraldi M, Guilarte TR, Knudsen TB, Lacapere JJ, Lindemann P, et al. Translocator protein (18kDa): new nomenclature for the peripheral-type benzodiazepine receptor based on its structure and molecular function. Trends Pharmacol Sci 2006;27(8):402-9.

2. Papadopoulos V, Lecanu L. Translocator protein (18 kDa) TSPO: an emerging therapeutic target in neurotrauma. Exp Neurol 2009;219(1):53-7.

3. Diorio D, Welner SA, Butterworth RF, Meaney MJ, Suranyicadotte BE. Peripheral Benzodiazepine Binding-Sites in Alzheimers-Disease Frontal and Temporal Cortex. Neurobiology of Aging 1991;12(3):255-58.

4. Messmer K, Reynolds GP. Increased peripheral benzodiazepine binding sites in the brain of patients with Huntington's disease. Neuroscience Letters 1998;241(1):53-56.

5. Hardwick M, Fertikh D, Culty M, Li H, Vidic B, Papadopoulos V. Peripheral-type benzodiazepine receptor (PBR) in human breast cancer: Correlation of breast cancer cell aggressive phenotype with PBR expression, nuclear localization, and PBR-mediated cell proliferation and nuclear transport of cholesterol. Cancer Research 1999;59(4):831-42.

6. Galiegue S, Casellas P, Kramar A, Tinel N, Simony-Lafontaine J. Immunohistochemical assessment of the peripheral benzodiazepine receptor in breast cancer and its relationship with survival. Clin Cancer Res 2004;10(6):2058-64.

7. Han Z, Slack RS, Li W, Papadopoulos V. Expression of peripheral benzodiazepine receptor (PBR) in human tumors: relationship to breast,

colorectal, and prostate tumor progression. J Recept Signal Transduct Res 2003;23(2-3):225-38.

8. Nagler R, Ben-Izhak O, Savulescu D, Krayzler E, Akrish S, Leschiner S, et al. Oral cancer, cigarette smoke and mitochondrial 18kDa translocator protein (TSPO) - In vitro, in vivo, salivary analysis. Biochim Biophys Acta;1802(5):454-61.

9. Maaser K, Grabowski P, Sutter AP, Hopfner M, Foss HD, Stein H, et al. Overexpression of the peripheral benzodiazepine receptor is a relevant prognostic factor in stage III colorectal cancer. Clinical Cancer Research 2002;8(10):3205-09.

10. Venturini I, Zeneroli ML, Corsi L, Avallone R, Farina F, Alho H, et al. Up-regulation of peripheral benzodiazepine receptor system in hepatocellular carcinoma. Life Sci 1998;63(14):1269-80.

11. Black KL, Ikezaki K, Toga AW. Imaging of Brain-Tumors Using Peripheral Benzodiazepine Receptor Ligands. Journal of Neurosurgery 1989;71(1):113-18.

12. Miettinen H, Kononen J, Haapasalo H, Helen P, Sallinen P, Harjuntausta T, et al. Expression of Peripheral-Type Benzodiazepine Receptor and Diazepam-Binding Inhibitor in Human Astrocytomas - Relationship to Cell-Proliferation. Cancer Research 1995;55(12):2691-95.

13. Ching AS, Kuhnast B, Damont A, Roeda D, Tavitian B, Dolle F. Current paradigm of the 18-kDa translocator protein (TSPO) as a molecular target for PET imaging in neuroinflammation and neurodegenerative diseases. Insights Imaging 2012;3(1):111-9.

14. Starosta-Rubinstein S, Ciliax B, Penney J, McKeever P, Young A. Imaging of a glioma using peripheral benzodiazepine receptor ligands. proceedings of the national academy of sciences of the United States of America 1987;84(3):891-5.

15. Junck L, Olson JMM, Ciliax BJ, Koeppe RA, Watkins GL, Jewett DM, et al. Pet Imaging of Human Gliomas with Ligands for the Peripheral Benzodiazepine Binding-Site. Annals of Neurology 1989;26(6):752-58.

16. Deane NG, Manning HC, Foutch AC, Washington MK, Aronow BJ, Bornhop DJ, et al. Targeted imaging of colonic tumors in smad3-/- mice discriminates cancer and inflammation. Mol Cancer Res 2007;5(4):341-9.

17. Okubo T, Yoshikawa R, Chaki S, Okuyama S, Nakazato A. Design, synthesis and structure-affinity relationships of aryloxyanilide derivatives as novel peripheral benzodiazepine receptor ligands. Bioorg Med Chem 2004;12(2):423-38.

18. Homes TP, Mattner F, Keller PA, Katsifis A. Synthesis and in vitro binding of N,N-dialkyl-2-phenylindol-3-yl-glyoxylamides for the peripheral benzodiazepine binding sites. Bioorg Med Chem 2006;14(11):3938-46.

19. Reynolds A, Hanani R, Hibbs D, Damont A, Da Pozzo E, Selleri S, et al. Pyrazolo[1,5-a]pyrimidine acetamides: 4-Phenyl alkyl ether derivatives as potent ligands for the 18 kDa translocator protein (TSPO). Bioorg Med Chem Lett;20(19):5799-802.

20. Mattner F, Mardon K, Loc'h C, Katsifis A. Pharmacological evaluation of an [(123)I] labelled imidazopyridine-3-acetamide for the study of benzodiazepine receptors. Life Sci 2006;79(3):287-94.

21. Dolle F, Luus C, Reynolds A, Kassiou M. Radiolabelled molecules for imaging the translocator protein (18 kDa) using positron emission tomography. Curr Med Chem 2009;16(22):2899-923.

22. Buck JR, McKinley ET, Hight MR, Fu A, Tang D, Smith RA, et al. Quantitative, preclinical PET of translocator protein expression in glioma using 18F-N-fluoroacetyl-N-(2,5-dimethoxybenzyl)-2-phenoxyaniline. J Nucl Med 2011;52(1):107-14.

23. Tang D, Hight MR, McKinley ET, Fu A, Buck JR, Smith RA, et al. Quantitative preclinical imaging of TSPO expression in glioma using *N*,*N*-diethyl-2-(2-(4-(2-(18F)-fluoroethoxy)phenyl)-5,7-dimethylpyrazolo[1,5-*a*]pyrimidin-3-yl)acetamide J Nucl Med 2011;*in press*.

24. Tang D, Nickels ML, Tantawy MN, Buck JR, Manning HC. Preclinical Imaging Evaluation of Novel TSPO-PET Ligand 2-(5,7-Diethyl-2-(4-(2-[F]fluoroethoxy)phenyl)pyrazolo[1,5-a]pyrimidin-3-yl)-N,N- diethylacetamide ([ F]VUIIS1008) in Glioma. Mol Imaging Biol 2014.

25. Cheung YY, Nickels ML, Tang D, Buck JR, Manning HC. Facile synthesis of SSR180575 and discovery of 7-chloro-N,N,5-trimethyl-4-oxo-3(6-[(18)F]fluoropyridin-2-yl)-3,5-dihydro-4H-pyri dazino[4,5-b]indole-1-acetamide, a potent pyridazinoindole ligand for PET imaging of TSPO in cancer. Bioorg Med Chem Lett 2014;24(18):4466-71.

26. Powell AE, Vlacich G, Zhao ZY, McKinley ET, Washington MK, Manning HC, et al. Inducible loss of one Apc allele in Lrig1-expressing progenitor cells results in multiple distal colonic tumors with features of familial adenomatous polyposis. Am J Physiol Gastrointest Liver Physiol 2014;307(1):G16-23.

27. Hassan C, Zullo A, Winn S, Eramo A, Tomao S, Rossini FP, et al. The colorectal malignant polyp: scoping a dilemma. Dig Liver Dis 2007;39(1):92-100.

28. Powell AE, Wang Y, Li Y, Poulin EJ, Means AL, Washington MK, et al. The Pan-ErbB Negative Regulator Lrig1 Is an Intestinal Stem Cell Marker that Functions as a Tumor Suppressor. Cell;149(1):146-58.

29. Hingorani SR, Petricoin EF, Maitra A, Rajapakse V, King C, Jacobetz MA, et al. Preinvasive and invasive ductal pancreatic cancer and its early detection in the mouse. Cancer Cell 2003;4(6):437-50.

30. Ijichi H, Chytil A, Gorska AE, Aakre ME, Fujitani Y, Fujitani S, et al. Aggressive pancreatic ductal adenocarcinoma in mice caused by pancreas-specific blockade of transforming growth factor-beta signaling in cooperation with active Kras expression. Genes Dev 2006;20(22):3147-60.

31. Hingorani SR, Wang L, Multani AS, Combs C, Deramaudt TB, Hruban RH, et al. Trp53R172H and KrasG12D cooperate to promote chromosomal instability and widely metastatic pancreatic ductal adenocarcinoma in mice. Cancer Cell 2005;7(5):469-83.

32. Ijichi H. Genetically-engineered mouse models for pancreatic cancer: Advances and current limitations. World J Clin Oncol 2011;2(5):195-202.

33. Hight MR, Cheung YY, Nickels ML, Dawson ES, Zhao P, Saleh S, et al. A peptide-based positron emission tomography probe for in vivo detection of caspase activity in apoptotic cells. Clin Cancer Res 2014;20(8):2126-35.

34. Grady WM. Genetic testing for high-risk colon cancer patients. Gastroenterology 2003;124(6):1574-94.

35. Rex DK, Cutler CS, Lemmel GT, Rahmani EY, Clark DW, Helper DJ, et al. Colonoscopic miss rates of adenomas determined by back-to-back colonoscopies. Gastroenterology 1997;112(1):24-8.

36. Heresbach D. Colonoscopy, tumors, and inflammatory bowel disease. Endoscopy 2008;40(2):147-51.

37. Xiang L, Zhan Q, Zhao XH, Wang YD, An SL, Xu YZ, et al. Risk factors associated with missed colorectal flat adenoma: A multicenter retrospective tandem colonoscopy study. World J Gastroenterol 2014;20(31):10927-37.

38. Veenman L, Gavish M. The role of 18 kDa mitochondrial translocator protein (TSPO) in programmed cell death, and effects of steroids on TSPO expression. Curr Mol Med 2012;12(4):398-412.

39. Veenman L, Gavish M, Kugler W. Apoptosis induction by erucylphosphohomocholine via the 18 kDa mitochondrial translocator protein: implications for cancer treatment. Anticancer Agents Med Chem 2014;14(4):559-77.

40. Gatliff J, Campanella M. The 18 kDa translocator protein (TSPO): a new perspective in mitochondrial biology. Curr Mol Med 2012;12(4):356-68.

41. Zeno S, Veenman L, Katz Y, Bode J, Gavish M, Zaaroor M. The 18 kDa mitochondrial translocator protein (TSPO) prevents accumulation of protoporphyrin IX. Involvement of reactive oxygen species (ROS). Curr Mol Med 2012;12(4):494-501.

42. Rappa G, Anzanello F, Lorico A. Imatinib mesylate enhances the malignant behavior of human breast carcinoma cells. Cancer Chemother Pharmacol 2011;67(4):919-26.

43. Rahib L, Smith BD, Aizenberg R, Rosenzweig AB, Fleshman JM, Matrisian LM. Projecting cancer incidence and deaths to 2030: the unexpected burden of thyroid, liver, and pancreas cancers in the United States. Cancer Res 2014;74(11):2913-21.

44. Rijkers AP, Valkema R, Duivenvoorden HJ, van Eijck CH. Usefulness of F-18-fluorodeoxyglucose positron emission tomography to confirm suspected pancreatic cancer: a meta-analysis. Eur J Surg Oncol 2014;40(7):794-804.

# CHAPTER 6

# CONCLUSIONS AND FUTURE DIRECTIONS

## 6.1. Summary

Studies presented in this dissertation elucidate a fraction of the molecular determents involved in cancer mitochondrial reprogramming that can serve as targets for the detection and evaluation of cancer by positron emission tomography (PET) imaging. Mitochondrial homeostasis serves as a 'gate-keeper' for a cell's viability and plays key regulatory roles in apoptotic cell death, metabolism, reactive oxygen species accumulation/defense, and various biosynthetic pathways (1-3). Given the complex intricacies between these processes in cancer, molecular imaging agents that can illuminate the interplay of mitochondrial pathway reprogramming could have implications towards improving cancer detection, drug discovery, predicting patient prognosis, and disease staging.

Working towards these objectives, **Chapter 3** outlined the discovery, characterization, and evaluation of a novel PET imaging probe, [$^{18}$F]FB-VAD-FMK, for *in vivo* caspase activity detection. These studies revealed the VAD-FMK peptide class as a promising scaffold for molecular imaging agent development for cell death detection (4). In **Chapter 4**, PET imaging of cancer cell nutrient uptake and metabolism was explored as a measure of molecular response to targeted therapy as well as means for reporting mutant gene expression in genetically engineered mice. Exploring novel biomarkers in early stage disease, **Chapter 5** described the relevance of the translocator protein (TSPO) expression in early gastrointestinal (GI) neoplasia and explored the potential of PET imaging in this setting. Conclusively, the findings reported in this dissertation

provide a basis for ultimately translating novel, non-invasive imaging metrics into clinical practice.

### 6.2. Translational Relevance

Deviations from normal cell death programs tend to promote cell survival and are frequently associated with cancer. Many anti-cancer therapies aim to selectively induce cell death in tumor cells, however, robust non-invasive biomarkers to assess such molecular events are lacking. As such, a PET imaging agent enabling quantification of apoptotic cell death could be used to predict individualized responses to therapy in patients and accelerate drug development. In the reported work, [$^{18}$F]FB-VAD-FMK was shown as a first-generation PET agent that allows non-invasive, targeted detection of caspase activation and tumor cell death following effective drug treatment. While the probe evaluated here was studied within the context of molecularly targeted therapy, the utility of this imaging agent class could be equally effective towards assessing response to conventional therapeutics.

[$^{18}$F]FDG PET has emerged as a prominent, non-invasive imaging tool in oncology for evaluating cell metabolism reprogramming and subsequent response to therapy in patients. However, as discussed primarily in **Chapters 2 and 4**, many molecular determinants involved in cancer cell metabolism remain unreported using this approach. Though further studies are required to fully understand the molecular implications of [$^{18}$F]4-F-GLN PET imaging, the work presented in **Chapter 4** suggests that this imaging metric could serve as an innovative companion diagnostic in drug development and personalized medicine. As collaborators through the Vanderbilt GI SPORE are developing novel small-molecule inhibitors of KRAS (5), glutamine-derived PET could provide the basis of an innovative platform to prioritize novel KRAS inhibitors *in vivo* when paired with the *Lrig1-CreER$^{T2}$;Apc$^{fl/fl}$;Kras$^{G12D}$* mouse model.

Ultimately, such investigations could provide quantitative measures of pharmacodynamic response in early-phase clinical trials of novel therapies in patients.

Contrary to conventional thought associating the translocator protein with advanced and malignant disease, evidence presented in this dissertation suggests TSPO to also be a biomarker of non-malignant neoplasia in gastrointestinal cancers. Colorectal cancer is a significant health problem affecting one out of 20 persons in western countries and is one of the most common malignant tumors (6). To reduce colorectal cancer-related death rates world-wide, improvements to conventional screening and detection methodologies are needed. In this setting, TSPO may be a target ideally suited for developing novel chromoendoscopy agents. Ultimately, these advancements could lead to improved colonoscopy screening methodologies for colon adenoma detection and guided polyp-resection.

The development of imaging metrics that allow for early detection of asymptomatic pancreatic tumors or precursor lesions at a time when the disease is at a curable stage is imperative to improving clinical outcomes which remains a dismal 5% overall 5-year survival rate. The initial evaluations of TSPO imaging in genetically engineered mouse models of non-cystic pancreatic intraepithelial neoplasia (PanIN) lesions have provided a foundation to explore the relevance of TSPO expression in other pancreatic cancer neoplasia, such as cystic intraductal papillary mucinous neoplasms (IPMNs). Cystic lesions of the pancreas are common incidental findings in routine cross sectional computed tomography (CT) and magnetic resonance imaging (MRI) (7). Though their incidence is relatively low (~10%), cystic lesions account for a disproportionate number of pancreatic resections (~30%). Due to the limited capability of determining the malignant potential of pancreatic cysts, treatment planning and predicting overall prognosis if lesions are left untreated can be difficult. Preliminary investigations by colleagues in the Manning group have correlated TSPO expression

with elevated malignancy potential in IPMNs. Coupled with the preclinical findings in PanIN and advanced disease bearing mice reported in this work, these results suggest that TSPO PET imaging could enable risk assessment in this setting.

### 6.3. Considerations for Advancement

Building upon the observations described in this dissertation, there are many avenues in which this work could be advanced. Leveraging VAD-FMK as a scaffold for probe development, the structure-activity elements that impart caspase selectivity should be revisited using medicinal chemistry and computational modeling in order to improve the *in vivo* pharmacokinetic properties of this probe class. Preclinical evaluations could also be expanded to include therapeutic cohorts which model apoptotic cell death induced from more conventional chemotherapeutics instead of strictly molecularly targeted therapies. Other studies could pursue head-to-head comparisons between VAD-FMK derived probes and alternative apoptotic PET imaging agents, such as the isatin sulfonamide class of caspase inhibitors (8-10) and [$^{18}$F]ML-10 (11,12). However, given the resources required to make these imaging agents available through the Vanderbilt Radiochemistry CORE facilities, the poor cost-effectiveness of these studies may preclude such pursuits. Through continued optimization of this agent class, it may be possible to translate a promising candidate to Phase 0 and Phase 1 clinical trials within 24-36 months.

While PET imaging of cell metabolism using radiolabeled analogues of glutamine may prove fruitful towards developing companion diagnostics for KRAS-targeted drugs, an alternative means of discerning increased glutamine-dependency in cancer cells may be to target the sodium dependent, neutral amino acid transporter of glutamine, ASCT2. Initial reports supporting the clinical importance of ASCT2 expression have begun to emerge and set a precedence for continued work in this field (13,14). Towards this end,

future studies could explore the relevance of ASCT2 expression in human colon adenoma samples; analogous to similar studies reported in this dissertation for TSPO. Such studies would expand upon ASCT2 histological evaluations performed in clinical samples of primary and advanced disease, which revealed elevated transporter expression in primary tumor tissue compared to metastatic disease (65% vs. 33%) and normal tissue (65% vs. 5%). Conclusively, a greater understanding of the clinical significance of ASCT2 expression and glutamine transport in early and advanced disease will be key for eventual translation of glutamine-related PET imaging into the clinic.

In lung cancer, ASCT2 has been demonstrated to play a key role in glutamine transport and controlling cancer cell metabolism, growth, and survival (15). Given this, PET agents targeting ASCT2 could meet critical needs in oncology. When screening individuals for lung cancer, the discernment of indeterminate pulmonary nodules (IPNs) which could be malignant tumors from benign lesions represents an enormous clinical challenge. PET agents targeting ASCT2 could improve the accuracy of lung cancer diagnosis, reduce the rate of unneeded, invasive surgical procedures, and reduce the overall cost of healthcare. ASCT2-specific ligands have already emerged from medicinal chemistry and screening efforts from other work in the Manning group. Therefore, radiochemical development and rigorous preclinical imaging evaluations of lead compounds is needed to advance this work. Once validated, future studies could evaluate glutamine-derived PET analogues and ASCT2-selective PET imaging agents in head-to-head preclinical imaging comparisons.

In non-cystic pancreatic precursor lesions, TSPO PET imaging has already demonstrated potential for discerning PanIN-bearing pancreas from normal tissue. While these initial reports are promising, further investigations could rigorously compare the *in vivo*, pharmacokinetic differences of TSPO PET agents in lesion bearing and normal

pancreas tissue using quantitative compartmental modeling analysis. Additionally, future studies should more closely look at the genetic implications of pancreatic cancer mutations and TSPO expression using optimized histological methodologies. Ongoing studies headed by colleagues within the Manning group are actively determining the suitability of TSPO PET advancements to patients possessing IPMNs; early cystic precursor lesions to pancreatic ductile adenocarcinoma (PDAC). In fact, efforts to prepare a Phase 1 clinical trial and an Investigational New Drug (IND) application through the Vanderbilt Medical Center are already underway. These proposed trials could explore the utility of PET imaging with [$^{18}$F]VUIIS1008 to stratify pancreatic adenocarcinoma precursor lesions in patients with cystic lesions.

### 6.4. Works Cited


1. Wallace DC. Mitochondria and cancer. Nat Rev Cancer 2012;12(10):685-98.

2. Boland ML, Chourasia AH, Macleod KF. Mitochondrial dysfunction in cancer. Front Oncol 2013;3:292.

3. Ribas V, Garcia-Ruiz C, Fernandez-Checa JC. Glutathione and mitochondria. Front Pharmacol 2014;5:151.

4. Hight MR, Cheung YY, Nickels ML, Dawson ES, Zhao P, Saleh S, et al. A peptide-based positron emission tomography probe for in vivo detection of caspase activity in apoptotic cells. Clin Cancer Res 2014;20(8):2126-35.

5. Burns MC, Sun Q, Daniels RN, Camper D, Kennedy JP, Phan J, et al. Approach for targeting Ras with small molecules that activate SOS-mediated nucleotide exchange. Proc Natl Acad Sci U S A 2014;111(9):3401-6.

6. Jemal A, Siegel R, Ward E, Hao Y, Xu J, Murray T, et al. Cancer statistics, 2008. CA Cancer J Clin 2008;58(2):71-96.

7. Xiao SY. Intraductal papillary mucinous neoplasm of the pancreas: an update. Scientifica (Cairo) 2012;2012:893632.

8. Nguyen QD, Smith G, Glaser M, Perumal M, Arstad E, Aboagye EO. Positron emission tomography imaging of drug-induced tumor apoptosis with a caspase-3/7 specific [18F]-labeled isatin sulfonamide. Proc Natl Acad Sci U S A 2009;106(38):16375-80.

9. Chen DL, Zhou D, Chu W, Herrbrich PE, Jones LA, Rothfuss JM, et al. Comparison of radiolabeled isatin analogs for imaging apoptosis with positron emission tomography. Nucl Med Biol 2009;36(6):651-8.

10. Chen DL, Zhou D, Chu W, Herrbrich P, Engle JT, Griffin E, et al. Radiolabeled isatin binding to caspase-3 activation induced by anti-Fas antibody. Nucl Med Biol 2012;39(1):137-44.

11. Hoglund J, Shirvan A, Antoni G, Gustavsson SA, Langstrom B, Ringheim A, et al. 18F-ML-10, a PET tracer for apoptosis: first human study. J Nucl Med 2011;52(5):720-5.

12. Allen AM, Ben-Ami M, Reshef A, Steinmetz A, Kundel Y, Inbar E, et al. Assessment of response of brain metastases to radiotherapy by PET imaging of apoptosis with (1)(8)F-ML-10. Eur J Nucl Med Mol Imaging 2012;39(9):1400-8.

13. Witte D, Ali N, Carlson N, Younes M. Overexpression of the neutral amino acid transporter ASCT2 in human colorectal adenocarcinoma. Anticancer Res 2002;22(5):2555-7.

14. Huang F, Zhao Y, Zhao J, Wu S, Jiang Y, Ma H, et al. Upregulated SLC1A5 promotes cell growth survival in colorectal cancer. Int J Clin Exp Pathol 2014;7(9):6006-14.

15. Hassanein M, Hoeksema MD, Shiota M, Qian J, Harris BK, Chen H, et al. SLC1A5 mediates glutamine transport required for lung cancer cell growth and survival. Clin Cancer Res 2013;19(3):560-70.

# APPENDIX 1

# MULTISPECTRAL FLUORESCENCE IMAGING TO ASSESS pH IN BIOLOGICAL SPECIMENS

## A1.1. Introduction

In normal mammalian tissues, intracellular and extracellular pH ($pH_i$ and $pH_e$, respectively) are dynamically regulated by a variety of sophisticated mechanisms (1). For example, $pH_i$ is maintained by both ion exchange mechanisms and cytosolic buffering capacity. Within this context, $pH_i$ plays important roles in numerous physiological processes such as protein synthesis and the regulation of cell cycles. Similarly, $pH_e$ is controlled by mechanisms that include vascular delivery of physiological buffers and removal of lactic acid. While the observed $pH_e$ varies across tissues of differing origin and function, deviation from normal $pH_e$ for a given tissue coincides with a variety of important pathological states (*e.g.* renal failure, ischemia, chronic pulmonary disease, cancer) (1). In highly metabolic tissues, such as tumors, reduced $pH_e$ can result from elevated production and diminished removal of lactic acid combined with the reduced capability of tumor-associated vasculature to deliver blood-based pH buffers (2). Acidic tumor $pH_e$ can impart significant consequences upon cancer cells such as increased potential for invasion and likelihood of metastasis, although further elucidation of the role of pH within this setting is needed (3). For these reasons, there is considerable interest in the development and validation of novel methods capable of measuring pH in biological specimens.

The majority of tools currently available for measurement of pH in tissues tend to be invasive (*e.g*. microelectrodes) (4) and/or provide relatively modest spatiotemporal resolution (*e.g.* magnetic resonance imaging and magnetic resonance spectroscopy)

(1,5). Limitations of the former techniques result from the inability to determine spatially resolved pH gradients without significant damage to the specimen (2). The latter methods are non-invasive but are significantly more costly and complicated to implement, limiting sample throughput and requiring highly specialized equipment and technical expertise (1,5). In contrast, optical imaging techniques offer an attractive alternative to the aforementioned techniques as they tend to be non-invasive, comparatively simple, analytically sensitive, cost-effective, and rapid (6,7). The most common optical methods rely on ratiometric fluorescence approaches. In typical assays utilizing exogenous organic dyes like fluorescein as an indicator, a pH-sensitive excitation/emission combination is compared to a pH-insensitive reference combination (2,8,9). Alternately, pH-sensitive dyes such as members of the seminaphthorhodafluor (SNARF) family can be excited at a single wavelength and emission collected at multiple wavelengths corresponding to the discrete spectra of protonated (HA) and deprotonated ($A^-$) species in solution (10-14). Though ratiometric approaches are routine for solution analysis (10) and flow cytometry (11-13), others have elegantly adapted ratiometric assays to intravital microscopy and demonstrated imaging of interstitial pH gradients in normal and neoplastic tissues in preclinical studies (2). An inherent limitation of these approaches, which is mitigated somewhat through emission filtering at the expense of signal rejection, is the difficulty of de-convolving multiple fluorescence emissions (*i.e.* signal *vs.* reference or HA vs. $A^-$) due to spectral overlap. Multispectral fluorescence imaging (MSFI) is a well-established technique that is suitable for the separation of multiple distinct, yet spectrally overlapping emissions (15). When utilized in preclinical animal studies, separation and quantification of multiple fluorescence emissions from imaging probes is feasible (16-19). Paired with pH-sensitive fluorochromes that generate unique emission spectra for HA and $A^-$ species, MSFI potentially represents an ideal paradigm for measurement of pH in solution and/or in tissue. Additionally, MSFI systems

suitable for use in preclinical animal studies or in conjunction with microscopy are now readily available and relatively inexpensive.

Here, we evaluated MSFI to quantify extracellular pH ($pH_e$) in dye-perfused, surgically-resected tumor specimens with commercially available instrumentation; as described in work published in the *Journal of Biomedical Optics* (20). Utilizing a water-soluble organic dye with pH-dependent fluorescence emission (SNARF-4F), we used standard fluorimetry to quantitatively assess the emission properties of the dye as a function of pH. By conducting these studies within the spectroscopic constraints imposed by the appropriate imaging filter set supplied with the imaging system, we determined that correction of the fluorescence emission of deprotonated dye was necessary for accurate determination of pH due to sub-optimal excitation. Subsequently, employing a fluorimetry-derived correction factor ($C_F$), MSFI data sets of aqueous dye solutions and tissue-like phantoms could be spectrally unmixed to accurately quantify equilibrium concentrations of protonated (HA) and deprotonated ($A^-$) dye and thus determine solution pH. Finally, we explored the feasibility of MSFI for high-resolution $pH_e$ mapping of human colorectal cancer (CRC) cell line xenografts.

In these studies, we illustrate a simple, rapid approach to quantitatively assess $pH_e$ in dye-perfused biological tissues utilizing MSFI and commercially available instrumentation. Using the MSFI-based approach, we demonstrate the feasibility of mapping $pH_e$ gradients pertaining to the protonation and deprotonation equilibrium of the pH-sensitive dye SNARF-4F in tissue specimens. It is anticipated that this methodology will provide valuable information regarding *ex vivo* tumor $pH_e$ and will ultimately aid in the study of the relationship between tumors and tumor microenvironments, as well as the effect of therapeutic regimens upon tumor $pH_e$.

## A1.2. Materials and Methods

*Chemicals*

All chemicals, reagents and solvents were purchased from indicated suppliers and used without further purification: SNARF-4F 5-(and-6)-carboxylic acid (Invitrogen; Carlsbad, CA), ACS grade hydrochloric acid (HCl) (EMD; Gibbstown, NJ), ACS grade sodium hydroxide (NaOH) (Fisher Scientific; Pittsburgh, PA), laboratory grade gelatin from porcine skin, type A (Sigma Aldrich; Milwaukee, WI), bovine hemoglobin (Sigma Aldrich; Milwaukee, WI), and intralipid 20% (Fresenius Kabi AB).

*Aqueous pH Solutions*

Solutions ranging from pH 3-10 in 0.5 pH increments were prepared from a 1.0 μM aqueous stock solution of SNARF-4F separated into 10 mL aliquots. The pH of each aliquot was adjusted *via* micro-additions of concentrated HCl and/or NaOH. Solution pH adjustments were monitored with a calibrated pH meter (MP220 pH Meter, Mettler Toledo) under positive nitrogen pressure with vigorous stirring. Over the course of the experiment, the solutions were wrapped in aluminum foil to minimize light exposure. Spectroscopic analysis and/or MSFI of pH-adjusted samples were performed immediately following pH adjustment and stabilization.

*Preparation of Biological Phantoms*

To validate the ability of MSFI to measure pH in biological environments, tissue-like phantoms with the approximate photon scattering and absorption properties of biological tissues were prepared (21). First, a 10% gelatin solution was prepared by adding gelatin to heated deionized water (40-50 °C) with constant stirring. The solution was then cooled to 30-40 °C, at which the desired amounts of bovine hemoglobin and

intralipid were added resulting in a 42.5 μM hemoglobin and 1% intralipid phantom mixture. Three parts buffered dye solution [acetate buffer (pH = 4.3, 5.6), phosphate buffer (pH = 6.2, 7.3), tris-HCl buffer (pH = 8.4), and carbonate buffer (pH = 9.5)] and one part phantom mixture were combined and dispensed into a chilled well plate and refrigerated at 4 °C until solid.

*Fluorimetry*

The spectroscopic characteristics of pH adjusted aqueous SNARF-4F solutions were investigated using a Photon Technology International QuantaMasterTM 50 fluorimeter (Birmingham, NJ) and a standard, 1 cm path length quartz cuvette (NSG Precision Cells 517BES10). An excitation wavelength ($\lambda_{ex}$) of 523 nm was used for single wavelength studies while an excitation range of 425-650 nm in increments of 25 nm was used for multiple wavelength studies. Emission scans were collected every nanometer over the emission wavelength ($\lambda_{em}$) range of 400-800 nm with an integration time of 0.1 s and a shutter width of 1.5 nm. Three acquisitions were averaged for each $\lambda_{ex}$. Excitation Emission Matrices of fluorescence emission as a function of excitation were generated in MATLAB (The MathWorks, Inc.; Natick, MA). Fluorimetry data were used in conjunction with **Eq. A1.1** to generate a correction factor (CF) that was later applied to the A- fluorescence intensity obtained in MSFI studies.

$$C_F = \frac{F_{\lambda 2}}{F_{\lambda 1}}, \qquad (1)$$

**Equation A1.1. Calculation of Correction Factor (CF).** Here, F refers to the fluorescence intensity at 653 nm when excited at 525 nm ($\lambda_1$) or 575 nm ($\lambda_2$).

*MSFI – Aqueous Solutions*

Aqueous SNARF-4F solutions ranging in pH from 4-8 in increments of approximately 1.0 pH unit were imaged using the Maestro™ Q FLEX In-Vivo Imaging

System from CRi, Inc. (Woburn, MA). Solutions were imaged in 1.5 mL micro-centrifuge tubes that were pre-rinsed with pH-adjusted solution prior to addition of dye solution. All images were obtained using Maestro Q Filter Set B, which features a band-pass excitation filter with transmission centered at 525 nm (full width at half max. = 47 nm) and a long-pass emission filter with 560 nm cut in. A spectral library was generated that included emission spectra for fully protonated /deprotonated dye species as well as autofluorescence from the micro-centrifuge tube plastic. This library was used throughout the solution phase experiments for spectral unmixing. Quantitative analysis of the autofluorescence signal arising from the micro-centrifuge tubes demonstrated that > 95% of the autofluorescence could be removed by spectral unmixing (data not shown). Unmixed dye fluorescence intensity data were obtained from a manually drawn region of interest (ROI) shaped and sized to include the central region of the micro-centrifuge tube. The data were fitted to a non-linear sigmoidal model and plotted against the analytically measured solution pH. Un-corrected and corrected SNARF-4F $pK_a$ values were calculated.

*MSFI – Biological Phantoms*

Using a protocol similar to that used for the solution phase experiments, dye containing tissue-like phantoms ranging in pH from 4-9.5 were imaged with the Maestro Q system. Spectral unmixing was achieved by applying the previously derived solution phase spectral library with the inclusion of autofluorescence from tissue-like phantom controls. Unmixed fluorescence intensity data were obtained from an ellipse-like manually drawn ROI sized to include the entirety of a single well. The data were fit to a non-linear sigmoidal model and plotted against the analytically measured solution pH. Un-corrected and corrected SNARF-4F $pK_a$ values were calculated.

Ex-Vivo *pH Mapping of Human Xenograft Tumor Tissue*

All studies involving the use of animal models were conducted in accordance with Vanderbilt University Institutional Animal Care and Use Committee and applicable federal guidelines. To generate the human colorectal cancer (CRC) model used for tumor imaging, 200,000 DiFi human CRC cells were subcutaneously injected on the left flank of athymic nude mice, as previously described.17 Experiments were conducted 2-3 weeks post inoculation, when tumors reached ~250 $mm^3$. For $pH_e$ mapping, 1.0 nmol of SNARF-4F in 200 µL of saline was administered to xenograft-bearing mice via intravenous injection under inhalation of anesthesia (2% isofluorane). Following dye administration, mice were allowed to briefly recover from anesthesia and given access to food and water ad libitum during a fifteen-minute uptake period. Mice were then sacrificed and tumor tissue harvested. Immediately following collection (< 2 min), tumors were macro-dissected into two equivalent hemispheres, positioned with the intratumoral facets facing toward the camera, and imaged using the Maestro Q system. Fluorescence images were collected from 560-850 nm and unmixed using the previously described spectral library (excluding autofluorescence from plastic). Unmixed fluorescence intensity data were obtained from a manually drawn ROI (~2% of the total area) that was applied to multiple areas of the tumor in order to ascertain pH heterogeneity. A gradient $pH_e$ map was generated in MATLAB from each MSFI unmixed image using **Eq. A1.2**.

$$pH = pK_a - \log\left(\frac{C_F S_{A^-}}{S_{HA}}\right) \qquad (2)$$

**Equation A1.2. Calculation of pH by MSFI.** Here, $pK_a$ is that of the dye while $S_{A^-}$ and $S_{HA}$ correspond to the observed fluorescence intensity of each species, respectively.

## A1.3. Results and Discussion

*Spectroscopy*

The fluorescence spectroscopy of the SNARF family of organic dyes is dependent upon the protonation state of the compound. Typically, the protonated and deprotonated states of the compound yield distinct, yet overlapping, emission peaks that may be separated by as much as 60 nm. For these studies, aimed at measuring pH in tissue, an important determinant was selection of a dye possessing a $pK_a$ near the anticipated pH of the specimens being assayed. These studies utilized SNARF-4F, with a known $pK_a$ of 6.4. Thus, at pH values well below its $pK_a$, the dye exists predominately in a protonated state and exhibits fluorescence emission at 580 nm when excited at 523 nm (**Fig. A1.1**). SNARF-4F exists in a predominately deprotonated state at pH values well above the $pK_a$ and exhibits fluorescence emission at 640 nm when excited at 523 nm (**Fig. A1.1**). Importantly, across the physiologically relevant pH range of 5 to 7, both HA and $A^-$ species exist in equilibrium. Due to the unique emission spectroscopy of the HA and $A^-$ species, spectral unmixing and quantitative measurement of each species facilitate determination of pH in accordance with a modified Henderson-Hasselbalch equation.

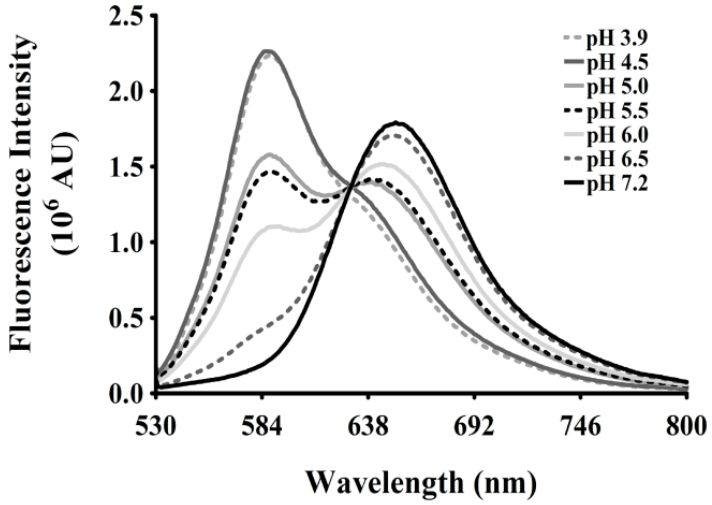


**Figure A1.1. pH dependency of SNARF-4F fluorescence emission.** Combined fluorescence emission spectra (ex. 523 nm) of aqueous SNARF-4F samples ranging in pH from approximately 4-7. The emission spectrum of pH 3.9 is representative of subsequently decreasing pH values while the emission spectrum of pH 7.2 is representative of subsequently increasing pH values (20).

Conceptually, the simplest pH imaging study coupling SNARF-4F and the Maestro system would feature utilization of a single excitation band and simultaneous collection and spectral unmixing of both the HA and $A^-$ emissions. However, an important assumption of this approach is the requirement for equivalent excitation and collection of both the HA and $A^-$ species, which may be thought of as two separate fluorophores in this experiment. Since the emission of the $A^-$ species is significantly red-shifted (ca. 60 nm) from the HA species, it follows that equivalent excitation of each species using a common excitation wavelength is unlikely. Therefore, we explored the relationships between excitation wavelength, pH, and the resulting emission spectroscopy of both the HA and $A^-$ SNARF-4F species using standard fluorimetry. We found that the HA species exhibited maximum fluorescence emission at an excitation wavelength of approximately 525 nm (emission = 590 nm), while the $A^-$ species exhibited maximum fluorescence emission at an excitation wavelength of approximately 575 nm (emission = 650 nm) (**Fig. A1.2**). Optimization of the imaging assay to utilize only a

single filter set could be accomplished using a single filter set included with the Maestro system (denoted as “B”, band-pass ex. 525/25 nm, long-pass em. 560 nm, **Fig. A1.3**). This filter set was ideally suited for exciting the HA species but was sub-optimal for exciting the $A^-$ species. We found the long-pass emission filter contained within the “B” filter set was suitable for simultaneous collection of both the HA and $A^-$ emission, with minor attenuation (~ 5 %) of the HA emission from 530-560 nm.

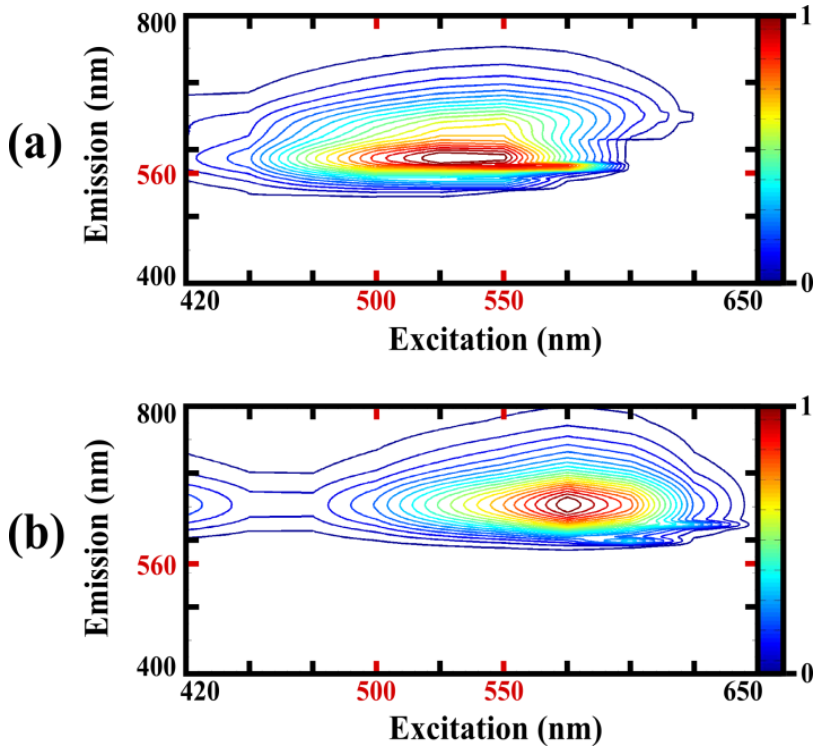


**Figure A1.2. Selection of excitation and emission filter pairing for SNARF-4F imaging.** Excitation emission matrices of SNARF-4F fluorescence emission as a function of excitation wavelength for HA (**A**, pH 4.5) and $A^-$ (**B**, pH 10.0). Red ticks located along the excitation axis show the approximate band pass transmission of the Maestro Q “B” excitation filter, while the red tick on the emission axis shows the cut on point for the longpass emission filter. The excitation-emission coordinates for the point at which maximum fluorescence emission intensity is achieved are (525, 587) for (**A**) and (575, 653) for (**B**) (20).

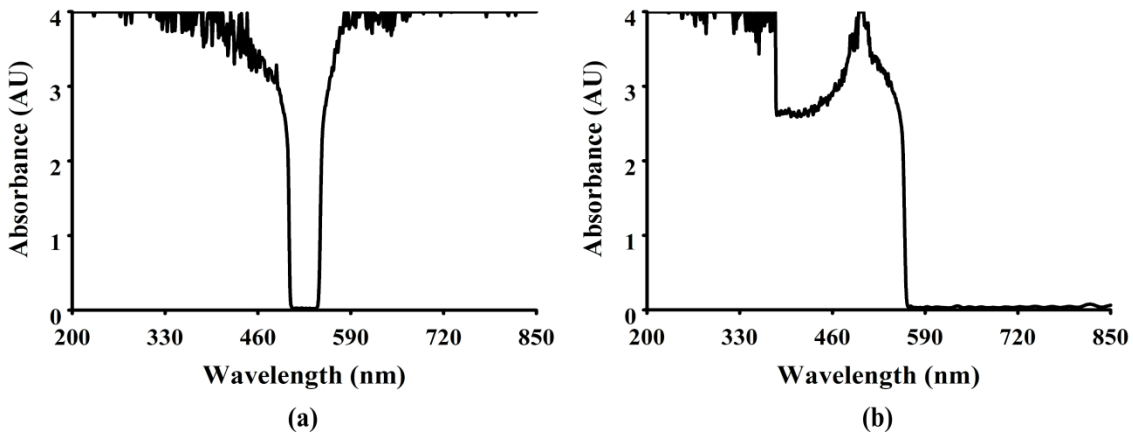


**Figure A1.3. Spectroscopic characteristics of Maestro Q imaging filters.** Transmission spectrum for (**A**) bandpass excitation filter and (**B**) longpass emission filter supplied as Filter Set "B" with the Maestro Q imaging system (20).

To compensate for the sub-optimal excitation of the $A^-$ species, a correction factor ($C_F$ = 2.1 ± 0.03) was derived from **Eq. A1.1**. This equation defines the ratio of the observed emission intensity at 650 nm for the $A^-$ species when excited at 525 nm ($\lambda_1$), the excitation wavelength in the Maestro, compared to the emission intensity at 650 nm when optimally excited at 575 nm ($\lambda_2$).

*MSFI*

To validate $C_F$ for use in MSFI assays, aqueous SNARF-4F solutions with pH values between 4 and 8 and tissue-like phantoms with pH values between 4 and 9.5 were imaged using filter set "B" and spectrally unmixed using the previously established spectral library. Following spectral unmixing, manual ROIs were drawn on unmixed images corresponding to the HA and $A^-$ species (**Fig. A1.4A, B**). Accordingly, the measured fluorescence intensities for each species were used to calculate the observed, uncorrected $pK_a$ for the dye using a modified Henderson-Hasselbalch equation, substituting the fluorescence emission intensity for each species in place of HA and $A^-$ concentration. Prior to correction of the $A^-$ intensity, fitting the unmixed HA and $A^-$

intensities to a sigmoidal curve and plotting versus pH (**Fig. A1.4C, D**) resulted in intersection between the two curves (by definition, $pK_a$) at 6.7 ± 0.3 for both the solution phase and biological phantom data (**Table A1.1**). Though these observed values are slightly higher than the known $pK_a$ of 6.4, application of the fluorimetry determined $C_F$ to the $A^-$ intensities of all data resulted in indistinguishable calculated $pK_a$ values of approximately 6.4 (**Table A1.1**) using **Eq. A1.2**; therefore validating $C_F$ derived from the fluorimetry experiments in multiple mediums.

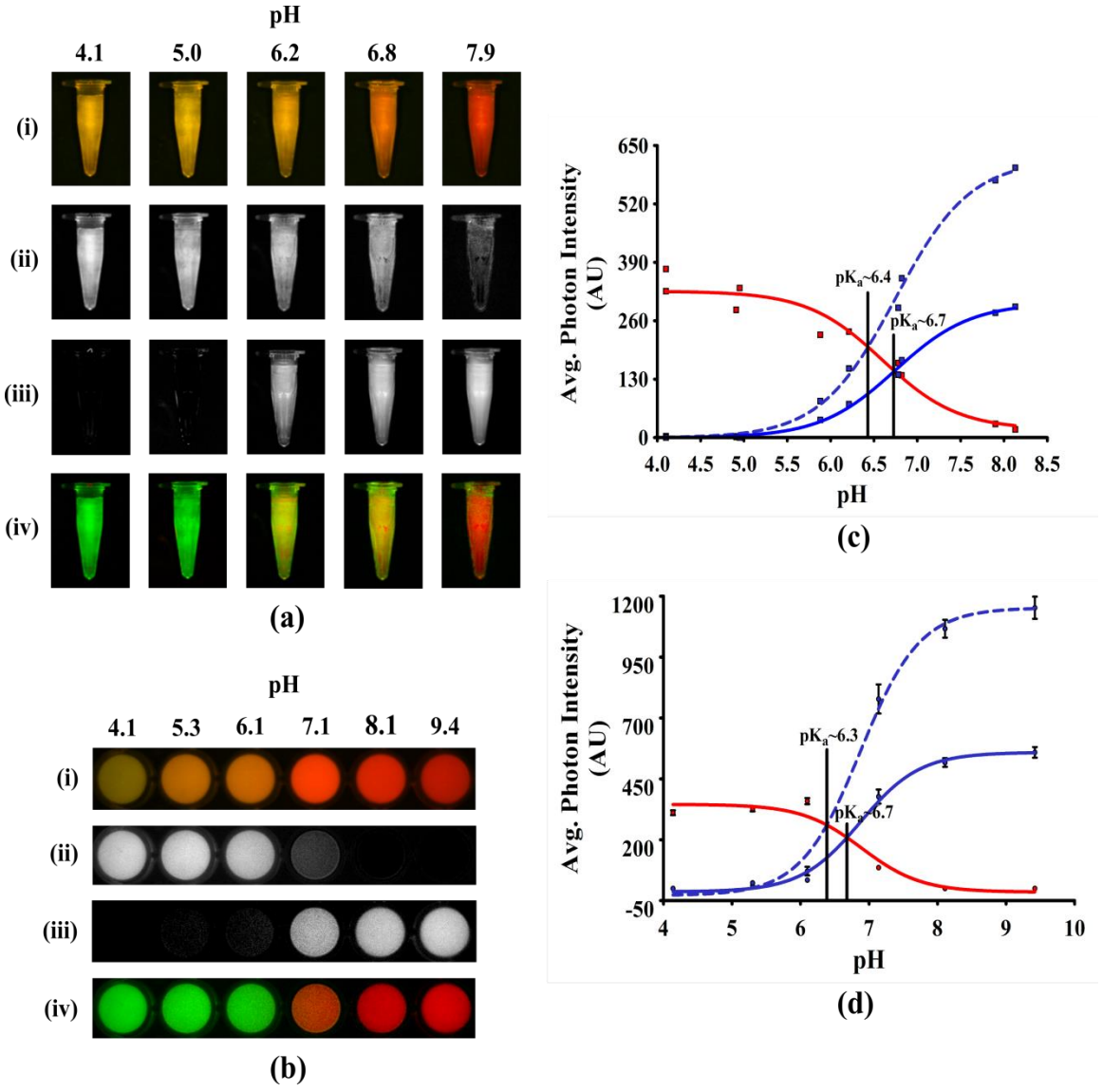


**Figure A1.4. MSFI successfully detected changes in pH dependent fluorescence.** Multi-spectral fluorescence imaging of aqueous SNARF-4F solutions ranging in pH from

approximately 4-8 (**A**) and dye containing tissue-like phantoms ranging in pH from approximately 4-9.5 (**B**). Spectrally-mixed, pseudocolor composite images are shown in (**Ai, Bi**). Spectrally-mixed composite images were unmixed to visualize emission from the HA (**Aii, Bii**) and $A^-$ (**Aiii, Biii**) species. Pseudocolor, unmixed composite images are shown in (**Aiv**, **Biv**), where the HA fluorescence emission is pseudocolorized in green and the $A^-$ fluorescence emission is pseudocolorized in red. Quantified average photon intensities from (**A**) are given in (**C**) while intensities from (**B**) are given in (**D**). HA (red) and $A^-$ (blue) species are displayed across pH as assessed by MSFI. Non-linear fits of MSFI data (solid colored lines) result in goodness of fits of 7 (**C**) and 33 (**D**) degrees of freedom. Observed $pK_a$ values (**Table A1.1**), the pH at which [HA] = [$A^-$], are noted by solid black lines. Correction of the $A^-$ intensity using $C_f$ at each point (dotted blue line) results in calculated $pK_a$ values (noted by dashed black lines) that are equivalent within one standard deviation of one another (**Table A1.1**) (20).

| *Medium* | *Observed $pK_a$* | *Calculated $pK_a$* |
|---|---|---|
| Solution | 6.7 ± 0.3 | 6.4 ± 0.2 |
| Phantom | 6.7 ± 0.3 | 6.3 ± 0.4 |

**Table A1.1. MSFI determined $pK_a$ values.** Observed (uncorrected) and calculated (corrected) $pK_a$ values for different SNARF-4F containing mediums (20).

Ex-vivo *pH mapping of xenograft tumors*

We next explored utilizing the MSFI approach for spatially resolved determination of $pH_e$ in freshly resected xenograft tumor tissue. Using the Maestro Q system we observed perfusion of SNARF-4F throughout the entire tumor, though accumulation tended to be heterogeneous (**Fig. A1.5A**). Increased levels of accumulation were noted in tissues exhibiting elevated necrosis. Non-uniform accumulation of dye in disorganized tissue such as tumors is not unexpected. It is therefore important to emphasize that the ratiometric nature of the proposed MSFI approach renders pH measurement inherently concentration independent with respect to the dye, provided that detectable quantities are present within tissues of interest. Applying the previously established spectral library for the HA and $A^-$ species to the unmixed data, fluorescence emission of the HA (**Fig. A1.5B**) and $A^-$ (**Fig. A1.5C**) species could be visualized within tumor tissue. To quantify intratumoral $pH_e$, the fluorescence intensity for the HA and $A^-$ species was measured by manual ROI analysis (**Fig. A1.5D**). The measured intensity of the $A^-$ species was

corrected using $C_F$, and tumor $pH_e$ for each ROI was calculated using **Eq. A1.2** (**Table A1.2**). We found that $pH_e$ within the tumor was heterogeneous with a mean pH of 6.9 ± 0.1. These observations are in agreement with those reported by previous studies where $pH_e$ was assessed across multiple tumor types by alternative techniques.[23-26] Expanding upon this, to generate a high-resolution pH map of tumor tissue, the HA and corrected $A^-$ pixel intensities were imported into MATLAB where the pH was calculated, fit to a color bar, and displayed across each image pixel (**Fig. A1.5E**). Although much of the tumor could be considered acidic with respect to normal tissue, we observed that tumor regions exhibiting the lowest pH tended to coincide with the highest degrees of necrosis in this model. These results suggest the feasibility of MFSI for *ex vivo* measurement of $pH_e$ in preclinical tissue specimens.

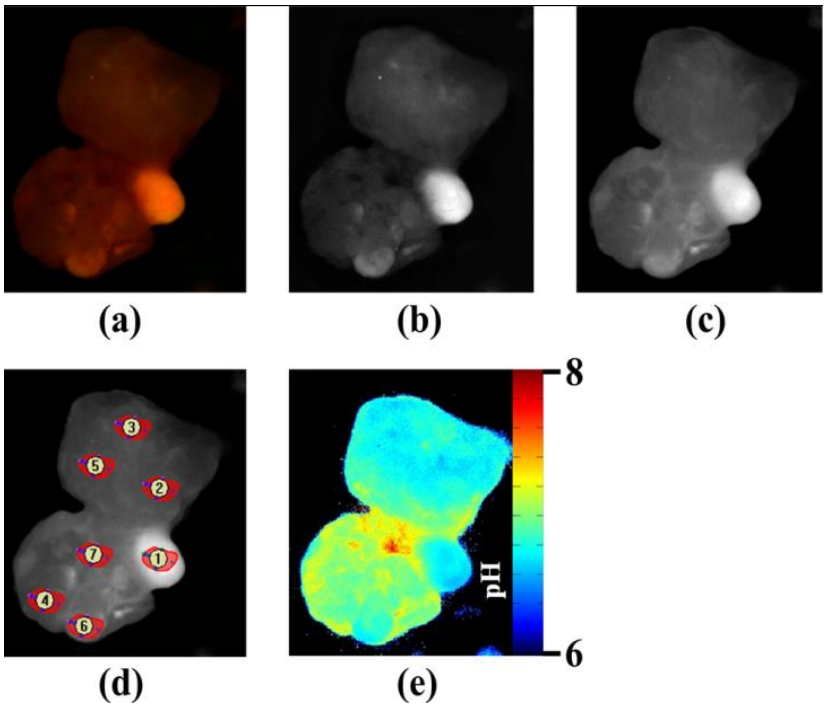


**Figure A1.5. MSFI evaluation of heterogeneous tumor tissue pH.** MSFI of dye-perfused human CRC cell line xenograft. Spectrally-mixed pseudocolor fluorescence image (**A**). Spectrally-unmixed images show HA (**B**) and $A^-$ (**C**) fluorescence emission. Map illustrating the selected ROI placement for pH measurements performed in tumor regions corresponding to the values shown in **Table A1.2** (**D**). Pixel-by-pixel $pH_e$ map generated using the HA fluorescence emission and the corrected $A^-$ emission (**E**). Colorbar corresponds to the calculated pH in each pixel (20).

| ROI | $A^-$ Photon Intensity | Corrected $A^-$ Photon Intensity | HA Photon Intensity | log($A^-$/HA) | Estimated $pH_e$ |
|---|---|---|---|---|---|
| 1 | 454 | 937 | 371 | 0.4 | 6.8 |
| 2 | 141 | 290 | 99 | 0.5 | 6.9 |
| 3 | 132 | 272 | 98 | 0.5 | 6.9 |
| 4 | 139 | 286 | 67 | 0.6 | 7.0 |
| 5 | 141 | 290 | 98 | 0.5 | 6.9 |
| 6 | 247 | 509 | 162 | 0.5 | 6.9 |
| 7 | 190 | 392 | 70 | 0.8 | 7.2 |

$pH_e$: range = 6.80-7.2, mean = 6.9 ± 0.1

**Table A1.2. Quantification of tissue pH values using MSFI.** MSFI-measured photon intensities and calculated pH values for DiFi CRC xenograft tumor. Location for each ROI is shown in **Fig. A1.5D** (20).

### A1.4. Conclusions

We report a novel method for simple, rapid measurement of $pH_e$ in biological tissue that utilizes MSFI. Given the ability to assess pH in a spatially resolved manner, this technique could be employed in preclinical research to further elucidate the relationship(s) between the pH of a tumor and its surrounding microenvironment, as well as the role of pH in other preclinical models of disease. We envision that this approach could be most useful when utilized in conjunction with other complementary molecular techniques such as immunohistochemistry and deployed immediately following tissue collection and prior to freezing or fixation.

### A1.5. Works Cited


1. Kuge Y, Zhao S, Takei T, Tamaki N. Molecular imaging of apoptosis with radio-labeled Annexin A5 focused on the evaluation of tumor response to chemotherapy. Anticancer Agents Med Chem 2009;9(9):1003-11.

2. Handl HL, Vagner J, Han H, Mash E, Hruby VJ, Gillies RJ. Hitting multiple targets with multimeric ligands. Expert Opin Ther Targets 2004;8(6):565-86.

3. Bodenheimer T, Wang MC, Rundall TG, Shortell SM, Gillies RR, Oswald N, et al. What are the facilitators and barriers in physician organizations' use of care management processes? Jt Comm J Qual Saf 2004;30(9):505-14.

4. Etyemezian V, Ahonen S, Nikolic D, Gillies J, Kuhns H, Gillette D, et al. Deposition and removal of fugitive dust in the arid southwestern United States: measurements and model results. J Air Waste Manag Assoc 2004;54(9):1099-111.

5. Li R, Simon J, Bodenheimer T, Gillies RR, Casalino L, Schmittdiel J, et al. Organizational factors affecting the adoption of diabetes care management processes in physician organizations. Diabetes Care 2004;27(10):2312-6.

6. Arino M, Barrington JP, Morrison AL, Gillies D. Management of the changeover of inotrope infusions in children. Intensive Crit Care Nurs 2004;20(5):275-80.

7. Jones TD, Hanlon M, Smith BJ, Heise CT, Nayee PD, Sanders DA, et al. The development of a modified human IFN-alpha2b linked to the Fc portion of human IgG1 as a novel potential therapeutic for the treatment of hepatitis C virus infection. J Interferon Cytokine Res 2004;24(9):560-72.

8. Willets KA, Ostroverkhova O, He M, Twieg RJ, Moerner WE. Novel fluorophores for single-molecule imaging. J Am Chem Soc 2003;125(5):1174-5.

9. Backlund MP, Lew MD, Backer AS, Sahl SJ, Moerner WE. The role of molecular dipole orientation in single-molecule fluorescence microscopy and implications for super-resolution imaging. Chemphyschem 2014;15(4):587-99.

10. Calderon CP, Thompson MA, Casolari JM, Paffenroth RC, Moerner WE. Quantifying transient 3D dynamical phenomena of single mRNA particles in live yeast cell measurements. J Phys Chem B 2013;117(49):15701-13.

11. Badieirostami M, Lew MD, Thompson MA, Moerner WE. Three-dimensional localization precision of the double-helix point spread function versus astigmatism and biplane. Appl Phys Lett 2010;97(16):161103.

12. Ptacin JL, Lee SF, Garner EC, Toro E, Eckart M, Comolli LR, et al. A spindle-like apparatus guides bacterial chromosome segregation. Nat Cell Biol 2010;12(8):791-8.

13. Goldsmith RH, Moerner WE. Watching conformational- and photo-dynamics of single fluorescent proteins in solution. Nat Chem 2010;2(3):179-86.

14. Lew MD, Thompson MA, Badieirostami M, Moerner WE. In vivo Three-Dimensional Superresolution Fluorescence Tracking using a Double-Helix Point Spread Function. Proc Soc Photo Opt Instrum Eng 2010;7571:75710Z.

15. Cohen AE, Moerner WE. Controlling Brownian motion of single protein molecules and single fluorophores in aqueous buffer. Opt Express 2008;16(10):6941-56.

16. Manning HC, Merchant NB, Foutch AC, Virostko JM, Wyatt SK, Shah C, et al. Molecular imaging of therapeutic response to epidermal growth factor receptor blockade in colorectal cancer. Clin Cancer Res 2008;14(22):7413-22.

17. Kim DY, Torruellas WE, Kang J, Bosshard C, Stegeman GI, Vidakovic P, et al. Second-order cascading as the origin of large third-order effects in organic single-crystal-core fibers. Opt Lett 1994;19(12):868-70.

18. Silence SM, Walsh CA, Scott JC, Matray TJ, Twieg RJ, Hache F, et al. Subsecond grating growth in a photorefractive polymer. Opt Lett 1992;17(16):1107-9.

19. Ducharme S, Scott JC, Twieg RJ, Moerner WE. Ducharme et al. reply. Phys Rev Lett 1991;67(18):2590.

20. Hight MR, Nolting DD, McKinley ET, Lander AD, Wyatt SK, Gonyea M, et al. Multispectral fluorescence imaging to assess pH in biological specimens. J Biomed Opt 2011;16(1):016007.

21. Ostroverkhova O, He M, Twieg RJ, Moerner WE. Role of temperature in controlling performance of photorefractive organic glasses. Chemphyschem 2003;4(7):732-44.

# APPENDIX 2

# EVALUATION OF OPTICAL IMAGING TOOLS FOR PRECLINICAL CANCER RESEARCH

## A2.1. Introduction

The scope of these studies was to carry out a broad survey of the *in vivo* performance of optical molecular imaging probes and instrumentation relevant to preclinical cancer imaging. The *in vivo* imaging characteristics of common, commercially available optical molecular imaging probes from multiple, predominantly major vendors, as of 2011, were evaluated in four optical imaging platforms. Biodistribution, approximate pharmacokinetics (PK), and tissue uptake were measured at multiple time-points using common preclinical mouse models of human cancer. Probe pharmacokinetics were estimated from optical imaging results and do not account for metabolism.

Optical imaging instruments evaluated in this study included the: Xenogen/IVIS200 (**Fig. A2.1**), Li-Cor Pearl (**Fig. A2.2**), CRI Maestro (**Fig. A2.3**), and VisEn FMT2500 (**Fig. A2.4**). All *in vivo* studies were conducted within the Vanderbilt University of Imaging Science (VUIIS) in Nashville, TN, under the authorization of the Vanderbilt University Institutional Animal Care and Use Committee (IACUC). These imaging systems differ in cost, complexity of hardware and data, thoughput, and imaging geometry but essentially aim to provide the end user with similar *in vivo* information. Quantitative and qualitative determinants were used to compare instrumentation included measurable contrast, experimental thoughput, and instrument and software usability and reliability. Though this study was performed using preclinical models of colorectal cancer (CRC), we anticipate that conclusions drawn from this study may be

useful towards guiding the future design and development of molecular probes and imaging hardware for preclinical optical imaging research.

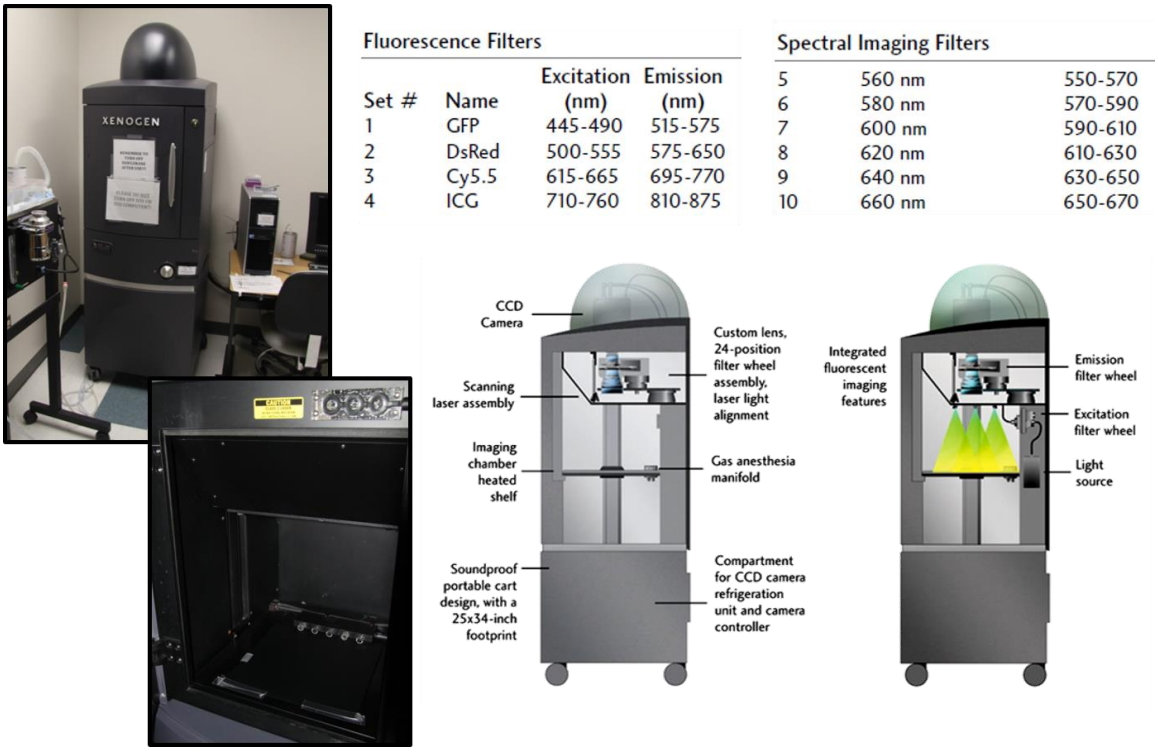


Fluorescence Filters

| Set # | Name | Excitation (nm) | Emission (nm) |
|---|---|---|---|
| 1 | GFP | 445-490 | 515-575 |
| 2 | DsRed | 500-555 | 575-650 |
| 3 | Cy5.5 | 615-665 | 695-770 |
| 4 | ICG | 710-760 | 810-875 |

Spectral Imaging Filters

| | | |
|---|---|---|
| 5 | 560 nm | 550-570 |
| 6 | 580 nm | 570-590 |
| 7 | 600 nm | 590-610 |
| 8 | 620 nm | 610-630 |
| 9 | 640 nm | 630-650 |
| 10 | 660 nm | 650-670 |

**Figure A2.1. Xenogen/IVIS200 imaging system**. Images, hardware schematic, available filter sets used for these studies. Instrument schematics and excitation/emission specs were obtained from the corresponding product literature.

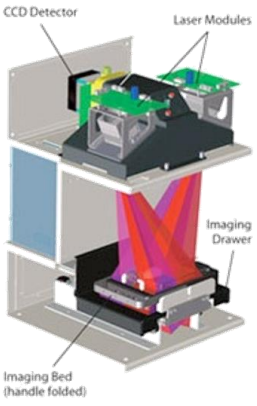



**Lasers:** 685 nm and 785 nm

**Figure A2.2. Li-Cor Pearl imaging system**. Images, hardware schematic, and laser wavelengths used for these studies. Instrument schematics and specs were obtained from the corresponding product literature.

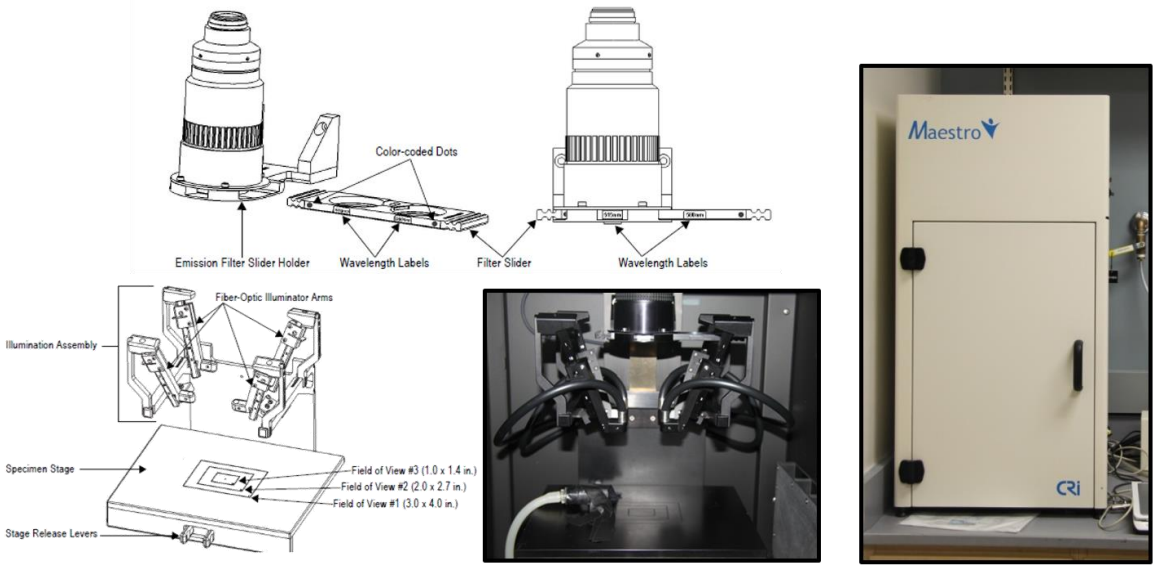


| Maestro Filter Set | Part # | Excitation Filter | Emission Filter | Acquisition Settings* |
|---|---|---|---|---|
| Blue | M-MSI-FLTR-BLUE | 445 to 490 nm | 515 nm longpass | 500 to 720 in 10 nm steps |
| Green | M-MSI-FLTR-GREEN | 503 to 555 nm | 580 nm longpass | 550 to 800 in 10 nm steps |
| Yellow | M-MSI-FLTR-YELLOW | 575 to 605 nm | 645 nm longpass | 630 to 850 in 10 nm steps |
| Red | M-MSI-FLTR-RED | 615 to 665 nm | 700 nm longpass | 680 to 950 in 10 nm steps |
| Deep Red | M-MSI-FLTR-DEEP-RED | 671 to 705 nm | 750 nm longpass | 730 to 950 in 10 nm steps |
| NIR | M-MSI-FLTR-NIR | 710 to 760 nm | 800 nm longpass | 780 to 950 in 10 nm steps |

**Figure A2.3. CRI Maestro imaging system.** Images, hardware schematic, and available filter sets used for these studies. Instrument schematics and excitation/emission filter specs were obtained from the corresponding product literature.

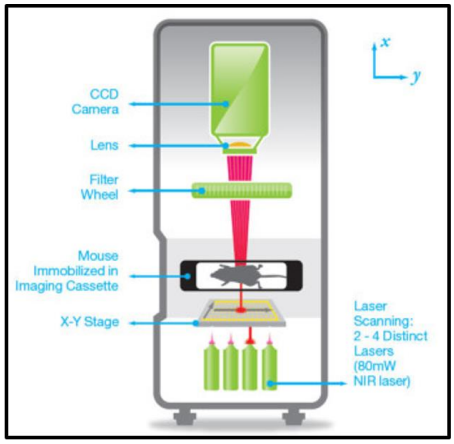



**Laser Channels**

1) ex.635nm/em. 650-670nm
2) ex.670nm/em. 690-740nm
3) ex.745nm/em. 770-800nm
4) ex.790nm/em. 805+nm

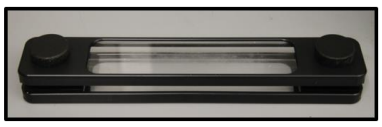

**Figure A2.4. VisEn FMT2500 imaging system.** Images, hardware schematic, and available filter sets used for these studies. Instrument schematics and

excitation/emission filter specs were obtained from the corresponding product literature.

### A2.2. Materials and Methods

*Small Animal Xenografts*

All studies involving the use of animal models were conducted in accordance with Vanderbilt University Institutional Animal Care and Use Committee and applicable federal guidelines. The DiFi model, a model of human colorectal cancer (CRC) with which we have much familiarity, was the primary model used to compare imaging probes *in vivo*. DiFi cells were isolated from a colorectal cancer patient with familial adenomatous polyposis and express very high levels of epidermal growth factor receptor (EGFR) ($2 \times 10^6$ to $2 \times 10^6$ receptors/cell) (1,2). DiFi xenografts were generated in athymic nude mice following subcutaneous injection of $2x10^6$ to $4x10^6$ cells on the right flank. As expected, tumors were visible within three to four weeks post-inoculation. *In vivo* optical imaging experiments were conducted when tumors reached 100 – 200 $mm^3$.

In some cases imaging probes were evaluated pre- and post- treatment with a chemotherapeutic agent. Probes evaluated under these conditions included 2-DG and EGF reagents. For treatment, we utilized cetuximab (C225, Erbitux) (20mg/kg) administered as monotherapy by intraperitoneal (i.p.) injection once every three days for seven days (maximum of three total injections). The monoclonal antibody cetuximab binds the ectodomain of the EGF receptor, and blocks ligand engagement and receptor activation, causing tumor size reduction, increased cellular apoptosis, and decreased cellular proliferation in DiFi xenografts. DiFi cells express wild-type *KRAS* and have *EGFR* amplification and are therefore sensitive to C225 treatment (2). In conjunction with treatment, vehicle (control) mice were prepared using i.p. saline injection. Treated and vehicle mice were administered optical probe after the third C225 administration.

*Bone Metastasis Mouse Model of Breast Cancer*

All studies involving the use of animal models were conducted in accordance with Vanderbilt University Institutional Animal Care and Use Committee and applicable federal guidelines. Optical imaging experiments investigating probes which target bone growth were performed using mice previously inoculated with GFP-labeled MDA-MB-231 tumor cells, a mouse model of bone metastasis of human breast cancer (BC). This model was prepared in athymic nude mice by infusion of MDA-MB-231 cells into the left ventricle of the heart (3,4). Prior to optical imaging with fluorescent probes, osteolytic lesions were confirmed by x-ray and GFP fluorescence imaging and subsequently used for probe evaluation studies.

*Animal Diet*

At least 24 h prior optical imaging, mice were transferred to clean cages and provided access to Harlan 2920X low fluorescence chow to reduce detectable autofluorescence. The utility of low fluorescence chow is observed when imaged in conjunction with normal chow across the IVIS, Pearl, and Maestro imaging systems using excitation/emission settings in the 650-750 nm range (**Fig. A2.5**). A 5-fold increase in detectable fluorescence for normal chow compared to Harlan 2920X low fluorescence chow was measured across the IVIS, Pearl, and Maestro. The difference in measurable counts between normal and low fluorescence chow likely stemmed from alfalfa meal. Chlorophyll in alfalfa meal can be detectable in both the deep red and near infrared spectrum, thus increasing autofluorescence in the abdominal region of an animal. We have determined in previous studies performed by our group that a minimum of 24 h on a low fluorescence diet is needed to reduce autofluorescence to levels of minimal attenuation.

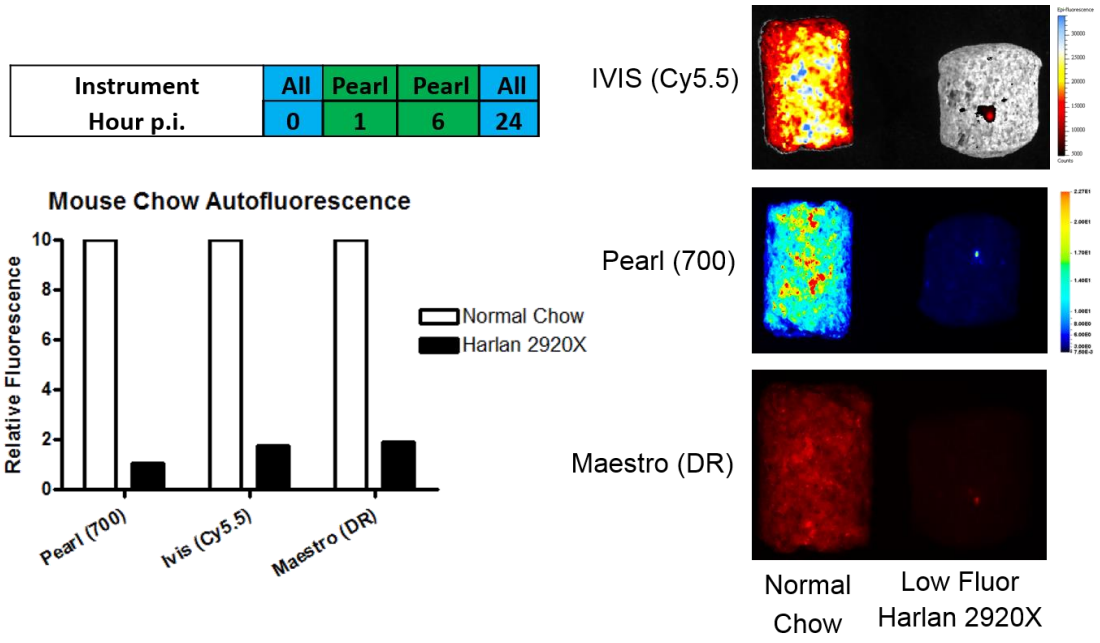


**Figure A2.5**. **Overview of imaging protocols used for subsequent optical imaging studies**. Imaging studies were carried out on all instruments immediately and 24 h post injection. Additional one and six h imaging time points were implemented in studies utilizing the Pearl imaging system. A comparison of low fluorescence animal chow (Harlan 2920X) and normal chow across the IVIS (Cy5.5 filter), Pearl (700 channel), and Maestro (DR filter) is also provided. Photon counts/area were normalized so the magnitude measured for normal chow across instruments is 10. Probe concentrations, as recommended by the product literature, was administered *via* intravenous injection.

In Vivo *Optical Imaging Protocol*

Data acquisition for all time points and imaging platforms was acquired while animals were under anesthesia (2% isoflurane in $O_2$ at 2 L/min). Animals were imaged on each platform prior probe injection to establish baseline. Optical probes were administered *via* intravenous retro-orbital injection using amounts recommended by associated product literature (**Table A2.1**). Complete dynamic imaging profiles from 0-24 h were collected at regular intervals (1, 6, and 24 h post-injection (p.i.)) using the Pearl system. Further acquisitions were collected in the IVIS, Maestro, and FMT at 24 h p.i. When collecting data across multiple platforms, data was acquired for each mouse ± 60 min. across all instruments.

| | | | Systems and Filter/Channel Settings | | | |
|---|---|---|---|---|---|---|
| **Probes** | **Probes** | **Injected (nmol)** | **Pearl** | **Maestro** | **IVIS** | **FMT (ex./em.)** |
| **LI-COR** | **IRDye 800cw 2-DG** | **10** | **800** | **NIR** | **ICG** | **790/805+** |
| | **IRDye 800cw RGD** | **1** | **800** | **NIR** | **ICG** | **790/805+** |
| | **IRDye 800cw PEG** | **1** | **800** | **NIR** | **ICG** | **790/805+** |
| | **IRDye 800cw EGF** | **2** | **800** | **NIR** | **ICG** | **790/805+** |
| | **IRDye 750 RGD** | **1** | **800** | **DR** | **ICG** | **745/770-800** |
| | **IRDye 680rd RGD** | **2** | **700** | **DR** | **Cy5.5** | **670/690-740** |
| | **IRDye 680rd EGF** | **2** | **700** | **DR** | **Cy5.5** | **670/690-740** |
| | **IRDye 680 Bone Tag** | **4** | **700** | **DR** | **Cy5.5** | **670/690-740** |
| | | | | | | |
| **Caliper** | **XenoLight 2-DG-750** | **10** | **800** | **DR** | **ICG** | **745/770-800** |
| | **XenoLight Integrin probe 750** | **2** | **800** | **DR** | **ICG** | **745/770-800** |
| | **XenoLight Bone Probe 680** | **2** | **700** | **DR** | **Cy5.5** | **670/690-740** |
| | | | | | | |
| **Perkin Elmer** | **OsteoSense 800** | **2** | **800** | **NIR** | **ICG** | **790/805+ nm** |
| | **AngioSense 750** | **2** | **800** | **DR** | **ICG** | **745/770-800** |
| | **ProSense 750** | **2** | **800** | **DR** | **ICG** | **745/770-800** |
| | **IntegriSense 750** | **2** | **800** | **DR** | **ICG** | **745/770-800** |
| | **OsteoSense 750** | **2** | **800** | **DR** | **ICG** | **745/770-800** |
| | **ProSense 680** | **2** | **700** | **DR** | **Cy5.5** | **670/690-740** |
| | **IntegriSense 680** | **2** | **700** | **DR** | **Cy5.5** | **670/690-740** |

**Table A2.1. Comprehensive listing of utilized optical probes and imaging systems.** Black text identifies probes studied using DiFi CRC xenografts while red text identifies probes studied using the MDA-231 BC model. Chosen filter settings/excitation-emission channels are provided for each instrument and probe. Settings were selected and optimized based on the spectroscopy of the dyes and the excitation/emission parameters of the chosen instrument.

*Imaging and Optical Settings*

For single animal field of view (F.O.V.), data sets were acquired on the Pearl using default settings across all three channels (700 nm, 800 nm, and white light). Maestro data sets for single animal F.O.V. were acquired using the #2 stage and light settings, 500 ms integration, and either the Blue (B) (for GFP imaging), Deep Red (DR), or Near InfraRed (NIR) excitation/emission filter settings (ex. 445-490/em. 515 nm longpass; ex. 671-705/em. 750 nm longpass; and ex. 710-760/em. 800 nm longpass respectively), as appropriate for the spectroscopy of the chosen probe. IVIS data sets for multiple animal F.O.V. were acquired using stage setting D, 5 s integration, F/stop 2, and

either the Cy5.5 or ICG excitation/emission filter settings (ex. 615-665/em. 695-770 nm and ex. 710-760/em. 810-875 nm respectively). FMT data sets for single animal F.O.V. were acquired using one of four laser channels (ex. 635/em. 650-670 nm, ex. 670/em. 690-740 nm, ex. 745/em. 770-800 nm, and ex. 790/em. 805+ nm) after calibrating using a 1 nM/mL standard solution of optical probe. Filter setting choices for data sets are indicated in **Table A2.1**.

*Data Quantification*

Imaging data was processed using the Pearl Impulse software (v2.0.16), IVIS Living Image software (v4.2), Maestro Imaging software (v3.0.1), and FMT True Quant 3D software (v3.0). For the DiFi xenograft model, data analysis was performed by manually drawing 2D ellipse regions of interest (roi's) over the tumor region and the hind limb (defined as 'normal' tissue) and used to measure fluorescence (photon counts) per pixel (area). Tumor regions were identified using corresponding white light reflectance images. Using the Pearl fluorescence data acquired at multiple time points, time activity curves (TACs) were developed and used to assess approximate probe pharmacokinetics (PK). Using fluorescence data acquired across all instruments at the 24 h time point, tumor-to-normal (T/N) ratios were developed and used to assess contrast.

Maestro image sets were spectrally unmixed using spectral libraries developed specifically for the spectroscopy of each probe and the autofluorescence measured for each animal prior to probe injection. This means of analysis was based on previously established methodologies.[5] Spectral unmixing makes it possible to achieve high levels of image contrast (T/N) that may not be readily achieved using other platforms. As such, the T/N ratios measured for Maestro data sets are likely to be higher than that measured for other instruments based largely on data analysis capabilities and not necessarily

indicative of the absolute sensitivity of the instrument. As an optical tomography system, the imaging data obtained using the FMT can provide a 3D map of probe uptake heterogeneity that may not be as discernable when using reflectance imaging techniques.

*Voxel-Wise Correlative Analysis*

This experiment was designed to correlate optical 2-DG tissue uptake with 18F-fluorodeoxyglucose ([$^{18}$F]FDG) on a voxel-wise basis across multiple imaging modalities to obtain visualization of probe characteristics. Following *in vivo* optical imaging, DiFi tumor bearing animals were intravenously injected with 700 – 800 μCi of [$^{18}$F]FDG by retro-orbital injection. Animals were fasted at least 7 h prior administration of [$^{18}$F]FDG. After an uptake period of at least one hour, animals were sacrificed by cervical dislocation, flash frozen in a 50 mL conical tube using liquid $N_2$, and subsequently imaged using a microCAT II (Imtek) to obtain whole body CT images. Approximately 1 cm of the tumor bearing mid-section was isolated by band saw and mounted on a cryomicrotome. Sequential white light images were taken every 120 μm using a Canon EOS Rebel XS Digital SLR Camera. Additionally, 40 μm thick tissue sections were preserved for autoradiography (Biospace Lab) ([$^{18}$F]FDG localization), Odyssey (LiCor) (NIR optical probe localization), and histopathological analysis. Serial images were concatenated and aligned to form a single digital image volume of the sample for each data set (*i.e*., white light, NIR, and autoradiography). These image volumes were co-registered to CT images, allowing visualization and correlation of these imaging metrics.

## A2.3. Results and Discussion

*LiCor RGD Optical Probes*

This class of imaging probe utilizes the tripeptide RGD (Arg-Gly-Asp) which binds to integrin receptors such as integrin $\alpha_v\beta_3$. RGD probes conjugated with IRDyes 680rd, 750, and 800cw were utilized using recommended doses (2 nmol, 1 nmol, and 1 nmol respectively). A comparison of Pearl images and TACs for all three RGD probes showed the fastest clearance was for RGD-680rd ($t_{1/2}$ = 13.4 hr) (**Fig. A2.6**). RGD-750 and -800cw showed slower clearance rates at $t_{1/2}$ = 20.4 hr and $t_{1/2}$ > 24 hr respectively (**Table A2.2**). Further comparison of these probes across platforms showed comparable detection of probe uptake in tumor across all four instruments; with primary fluorescence detection being localized to tumor (**Fig. A2.7**). High contrast was observed with the Maestro imaging system for RGD-680rd (T/N = 36.4) and is likely attributed to the low background noise achieved upon spectral unmixing. Analysis of the 3D images obtained using the FMT revealed whole body and tumor region fluorescence heterogeneity that was not obvious using 2D visualization. While 2D FMT images revealed non-tumor fluorescence throughout the animal, 3D visualization revealed increased measurable fluorescence in tumor region.

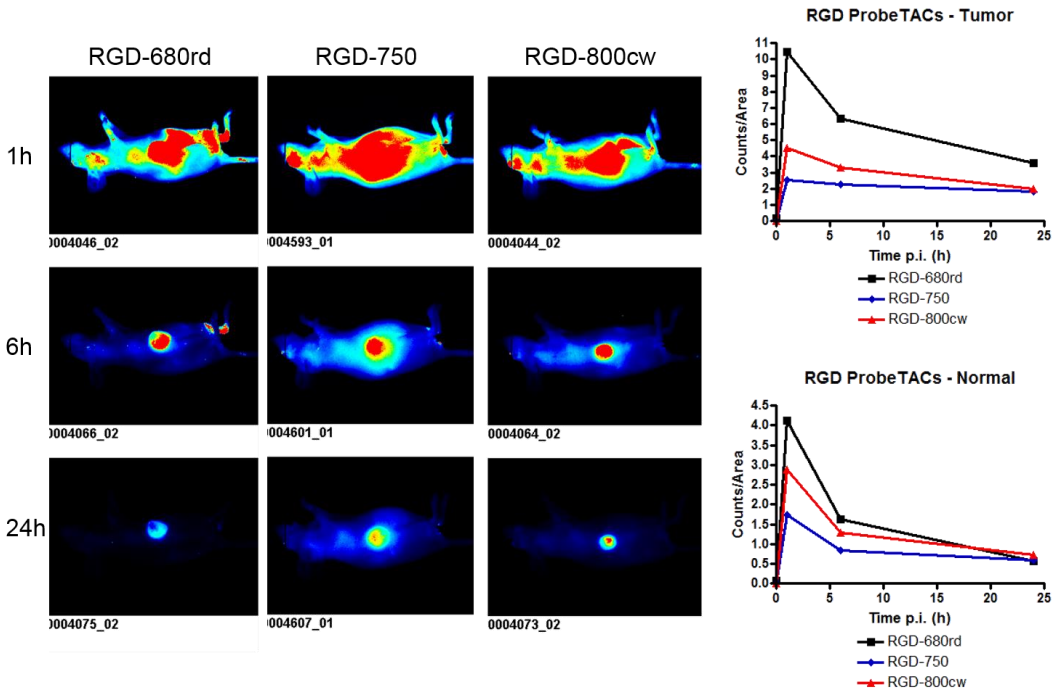


**Figure A2.6. LiCor RGD-optical probe evaluation using the Pearl imaging system**. Pearl images were acquired using protocols listed in the written report. Each column of images corresponds to a specific RGD probe and time point p.i. (as listed above). Images for an individual probe across time points are set to the same scale (ex. The 1, 6, and 24 hr images for RGD-680 are scaled the same). Time activity curves (TACs) are provided for each probe in regards to tumor and normal tissue uptake. Fluorescence measurements were normalized to counts/area to account for discrepancies in ROI size across images.

| | T/N | | | | |
|---|---|---|---|---|---|
| Probes | Pearl | Maestro | IVIS | FMT | Half-Life (hr) |
| 800cw 2-DG | 3.15 | 4.07 | 1.48 | 1.20 | 3.8 |
| 800cw RGD | 2.79 | 7.31 | 1.88 | 1.39 | 20.4 |
| 800cw PEG | 3.58 | 3.34 | 2.02 | 1.62 | >> 24 |
| 800cw EGF | 4.75 | 11.20 | 1.71 | 1.51 | 10.50 |
| 750 RGD | 3.12 | 2.67 | 1.87 | 2.15 | > 24 |
| 680rd RGD | 6.36 | 36.40 | 3.21 | 3.92 | 13.4 |
| 680rd EGF | 11.31 | 8.11 | 3.26 | 5.07 | 4.1 |
| 2-DG-750 | 3.79 | 3.39 | 2.68 | 2.80 | > 24 |
| Integrin probe 750 | 1.47 | 1.58 | 1.18 | - | 12.4 |
| AngioSense 750 | 3.27 | 2.51 | 2.56 | 2.29 | >> 24 |
| ProSense 750 | 2.37 | 1.87 | 1.17 | 1.40 | 5.4 |
| IntegriSense 750 | 4.87 | 4.17 | 2.84 | 3.69 | > 24 |
| ProSense 680 | 1.87 | 1.57 | 1.57 | 1.67 | >> 24 |
| IntegriSense 680 | 2.42 | 2.00 | 1.54 | 1.68 | > 24 |

**Table A2.2. Comparison of optical imaging probes across imaging systems**. Probe performance on each imaging system was evaluated in terms of contrast (T/N ratio) and tumor clearance rate (half-life). Half-life was determined using the Pearl developed TACs (presented throughout this report). Peak uptake was universally marked at 1 h p.i. A dash (-) mark corrupt data sets that could not be quantified.

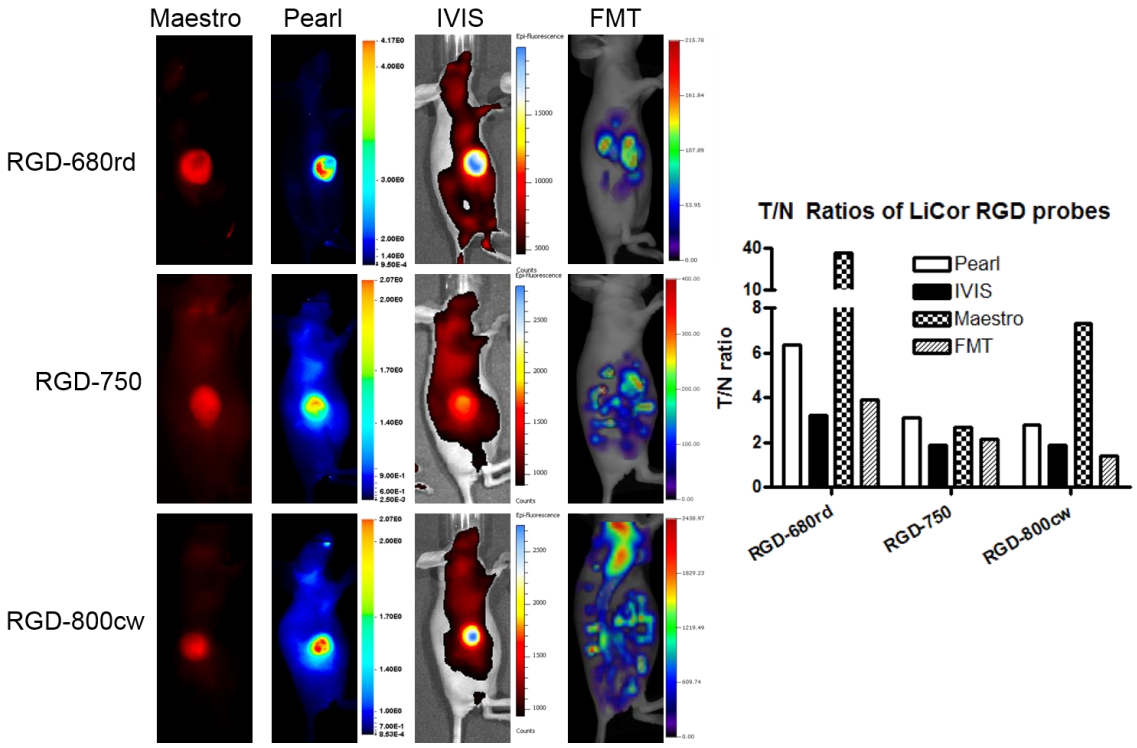


**Figure A2.7. Comparison of LiCor RGD-optical probes across imaging systems**. Images were acquired across instruments using protocols listed in the written report. Each column of images corresponds to the 24 h time point for a specific RGD probe and instrument. A comparison of tumor-normal ratios for each probe across instruments is also provided.

*Caliper and VisEn Integrin Optical Probes*

The Caliper RediJect integrin optical probe binds $\alpha_v\beta_3$ integrin expression on the cell surface. For this study, the RediJect integrin XenoLight 750 probe was used utilizing the recommended dose of 2 nmol. The VisEn IntegriSense optical probes are non-peptide small molecules which act as integrin $\alpha_v\beta_3$ and $\alpha_v\beta_5$ antagonists. For this study, the Integrisense 680 and 750 NIR fluorochromes were used utilizing the recommended doses of 2 nmol for each probe. A comparison of Pearl images and TACs for these probes showed specific uptake in tumor tissue with arguably higher uptake being observed for the IntegriSense probes based on photon counts/pixel (**Fig. A2.8**). Further comparison of these probes showed comparable detection of probe uptake in tumor across all four instruments; with primary fluorescence detection being localized to tumor

(**Fig. A2.9**). The IntegriSense probes and the Caliper RediJect probe showed similar contrast across all four instruments based on T/N ratios (**Table A2.2**). Analysis of the 3D images obtained using the FMT revealed whole body and tumor region fluorescence heterogeneity that was not obvious using 2D visualization. While 2D FMT images revealed non-tumor fluorescence throughout the animal, 3D visualization revealed increased measurable fluorescence in tumor region.

Compared to the LiCor RGD probes, the Caliper and VisEn integrin probes showed slower tissue clearance rates based on probe half-life (**Table A2.2**). RediJect integrin XenoLight 750 probe was the exception to this trend possessing the fastest clearance rate at $t_{1/2}$ = 12.4 h. T/N profiles of the LiCor, Caliper, and VisEn probes across imaging platforms were very similar, though the highest contrast was achieved with the RGD-680rd and -800cw on the Maestro imaging system.

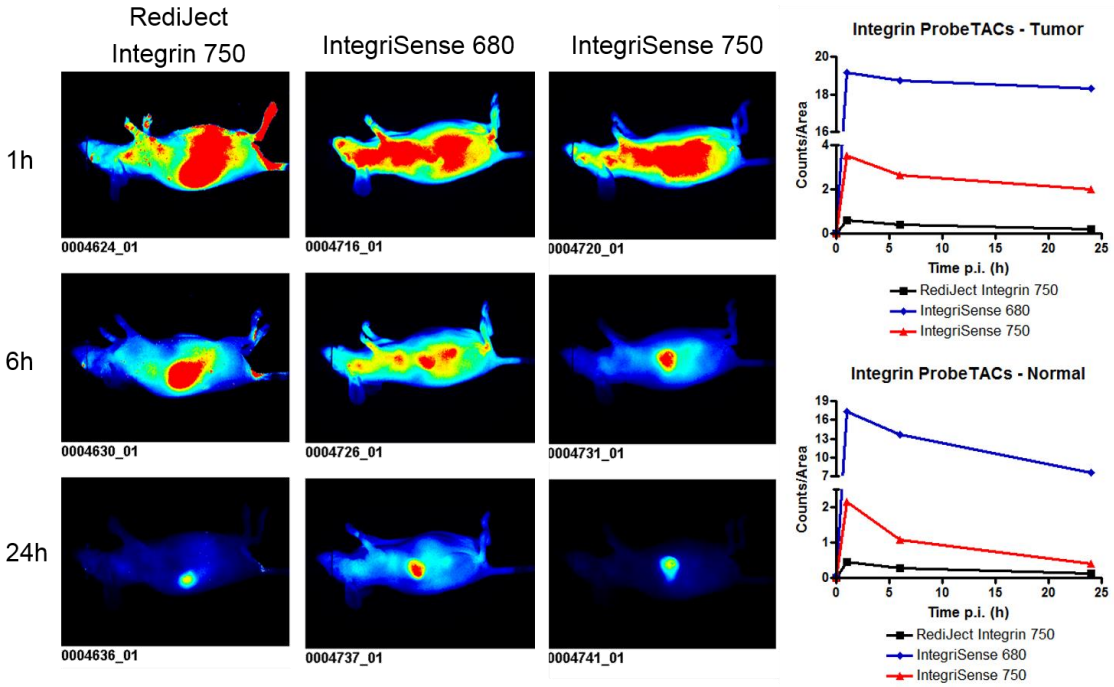


**Figure A2.8. Integrin-optical probe evaluation using the Pearl imaging system**. Pearl images were acquired using protocols listed in the written report. Each column of images corresponds to a specific probe and time point p.i. (as listed above). Images for an individual probe across time points are set to the same scale. Time activity curves (TACs) are provided for each probe in regards to tumor and normal tissue uptake.

Fluorescence measurements were normalized to counts/area to account for discrepancies in ROI size across images.

.

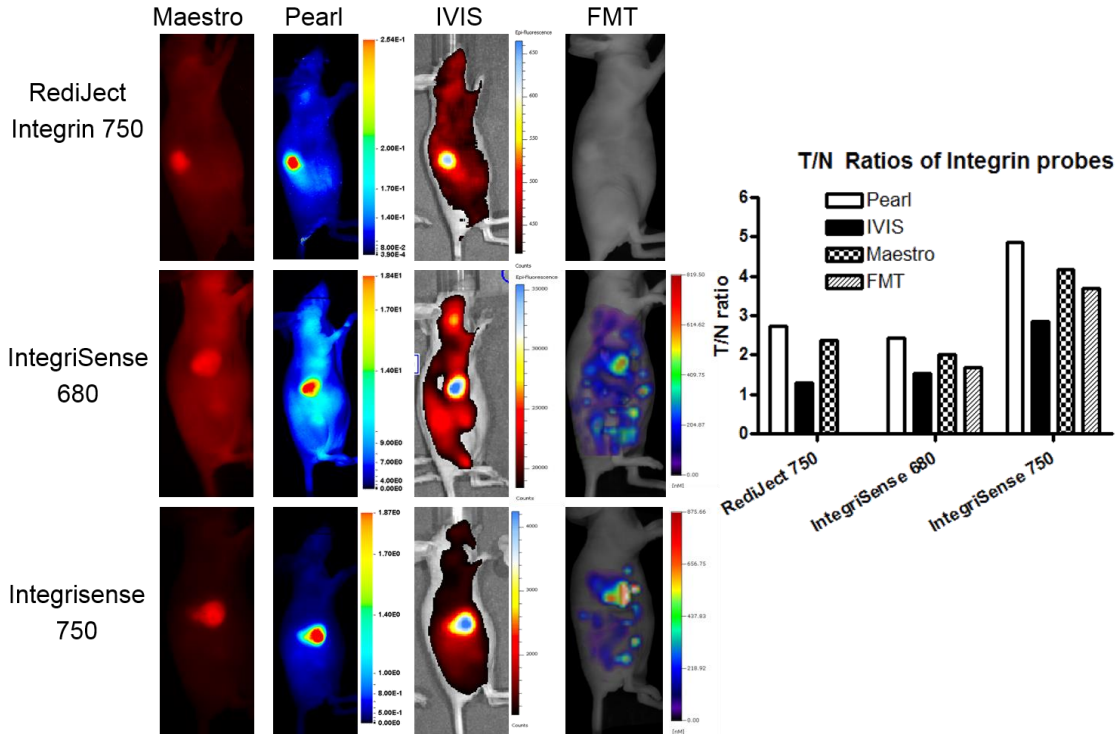


**Figure A2.9. Comparison of Integrin-specific probes across imaging systems**. Pearl images were acquired using protocols listed in the written report. Each column of images corresponds to a specific probe and time point p.i. (as listed above). Images for an individual probe across time points are set to the same scale. Time activity curves (TACs) are provided for each probe in regards to tumor and normal tissue uptake. Fluorescence measurements were normalized to counts/area to account for discrepancies in ROI size across images.

*VisEn AngioSense Optical Probe*

The VisEn AngioSense 750 optical probe acts as a blood pooling agent by accumulating in areas of vascular leakage. For this study, the recommended dose of 2 nmol was utilized. The Pearl derived TAC revealed increased measured fluorescence in tumor region that continued to increase even 24 h p.i. ($t_{1/2}$ >> 24 h); a profile typical of large biomolecules and blood pooling agents (**Fig. A2.10**). Primary fluorescence detection was localized to tumor region across platforms with limited fluorescence being detected in normal tissue based on total photon counts. T/N ratios were similar for all

four instruments; ranging between 2-3 (**Table A2.2**). Rotation of 3D FMT images revealed probe uptake heterogeneity that was not obvious across the reflectance imaging platforms.

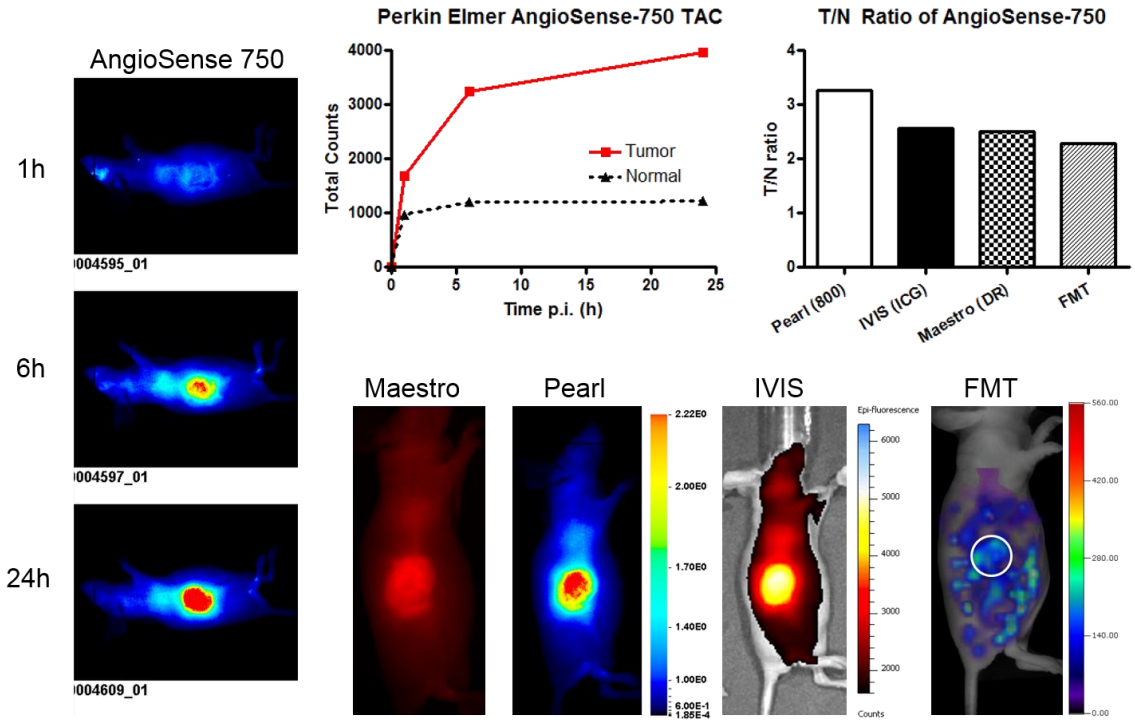


**Figure A2.10. Evaluation of AngioSense-750 across imaging systems**. Pearl images were acquired using protocols listed in the written report. All Pearl images were set to the same scale. The time activity curve (TAC) was provided in regards to tumor and normal tissue uptake. Fluorescence measurements were normalized to counts/area to account for discrepancies in ROI size across images. Images were acquired across multiple instruments using protocols listed in the written report. Each column of images corresponds to the 24 h time point. The white ellipse on the FMT image outlines the tumor area for clarity. A comparison of tumor-normal ratios for each probe across instruments is also provided.

*LiCor PEG Optical Probe*

The LiCor PEG 800cw optical probe acts as a non-specific binding agent that exploits tumor enhanced permeability and retention (EPR). For this study, the recommended dose of 2 nmol was utilized. The Pearl derived TAC revealed increased measured fluorescence in tumor region that continued to increase even 24 h p.i. ($t_{1/2}$ >> 24 h); a profile typical of large biomolecules and blood pooling agents (**Fig. A2.11**).

Primary fluorescence detection was localized to tumor region across platforms with limited fluorescence being detected in normal tissue based on total photon counts. Investigations across platforms revealed similar image contrast, with T/N ratios ranging between 1.6-3.6 for all four instruments (**Table A2.2**). Based on optical images, TACs, half-life, and T/N ratios, the LiCor PEG and VisEn AngioSense optical probes displayed similar optical and pharmacokinetic properties. Rotation of 3D FMT images revealed probe uptake heterogeneity that was not obvious across the reflectance imaging platforms.

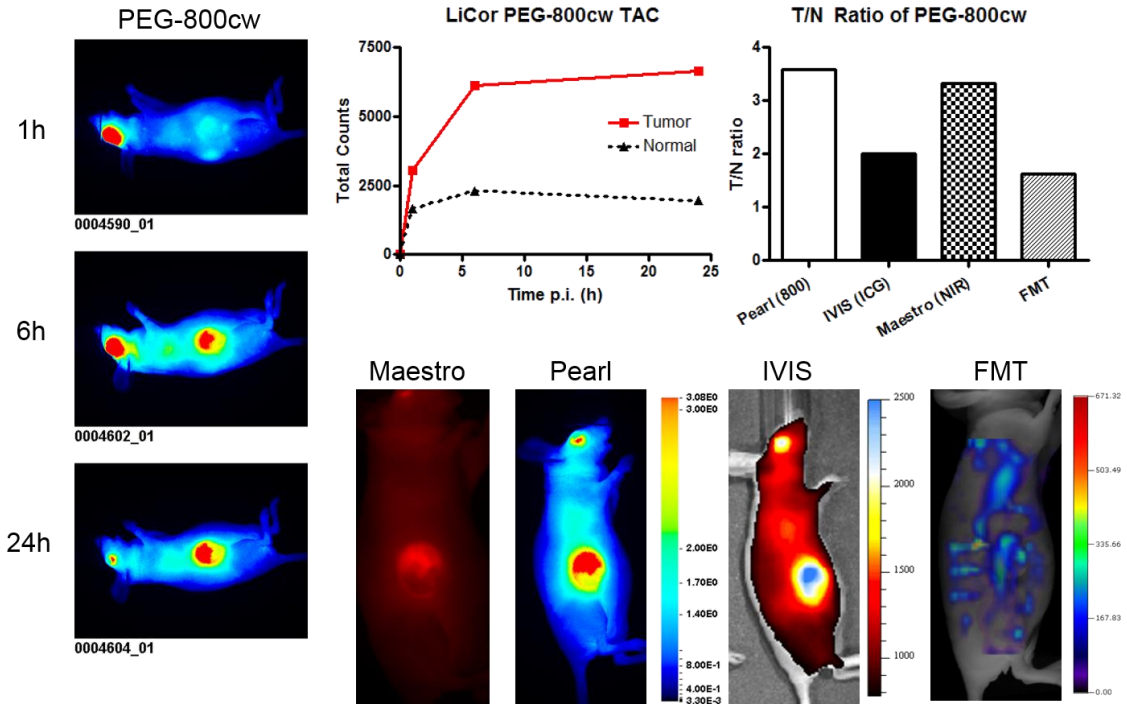


**Figure A2.11. Evaluation of PEG-800cw across imaging systems**. Pearl images were acquired using protocols listed in the written report. All Pearl images were set to the same scale. The time activity curve (TAC) was provided in regards to tumor and normal tissue uptake. Fluorescence measurements were normalized to counts/area to account for discrepancies in ROI size across images. Images were acquired across multiple instruments using protocols listed in the written report. Each column of images corresponds to the 24 h time point. The white ellipse on the FMT image outlines the tumor area for clarity. A comparison of tumor-normal ratios for each probe across instruments is also provided.

*VisEn ProSense Optical Probes*

The ProSense optical probes are activated by proteases of the cathespin family (*i.e.*, cathespin B, L, and S). According to product literature, these probes are optically silent in the inactivated state but become highly fluorescent when activated. ProSense probes conjugated with NIR fluorochromes 680 and 750were utilized using the recommended dose of 2 nmol. The Pearl derived TACs of both probes showed drastically different uptake and clearance profiles (**Fig. A2.12**). ProSense 680 showed slow tissue clearance over the 24 h uptake period ($t_{1/2}$ > 24 h) (**Table A2.2**). Due to non-specific fluorescence detection (primarily from what appears to be kidney), it is difficult to determine if counts/pixel measured by ROI placement for tumor region was the result of tumor region fluorescence or the result of adjacent non-specific kidney uptake. Unlike ProSense 680, ProSense 750 showed fast tissue clearance ($t_{1/2}$ > 5.4 h) and marginal, if any, tumor specific uptake. Images for both ProSense probes across all platforms revealed little fluorescence detection in tumor region (**Fig. A2.13**). Upon rotation of 3D FMT images, the absence of fluorescence detection in tumor was confirmed for both probes.

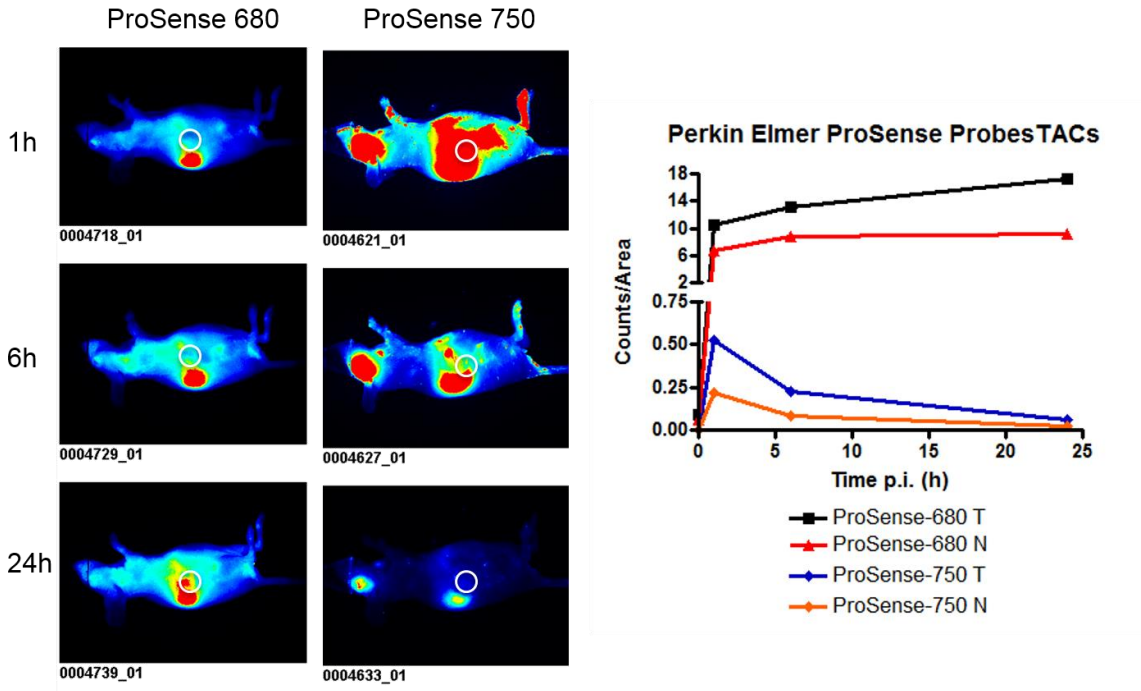


**Figure A2.12. ProSense-optical probe evaluation using the Pearl imaging system**. Pearl images were acquired using protocols listed in the written report. Each column of images corresponds to a specific probe and time point p.i. (as listed above). Images for an individual probe across time points are set to the same scale. Time activity curves (TACs) are provided for each probe in regards to tumor and normal tissue uptake. Fluorescence measurements were normalized to counts/area to account for discrepancies in ROI size across images. White ellipses were drawn across all images in order to outline tumor area for clarity.

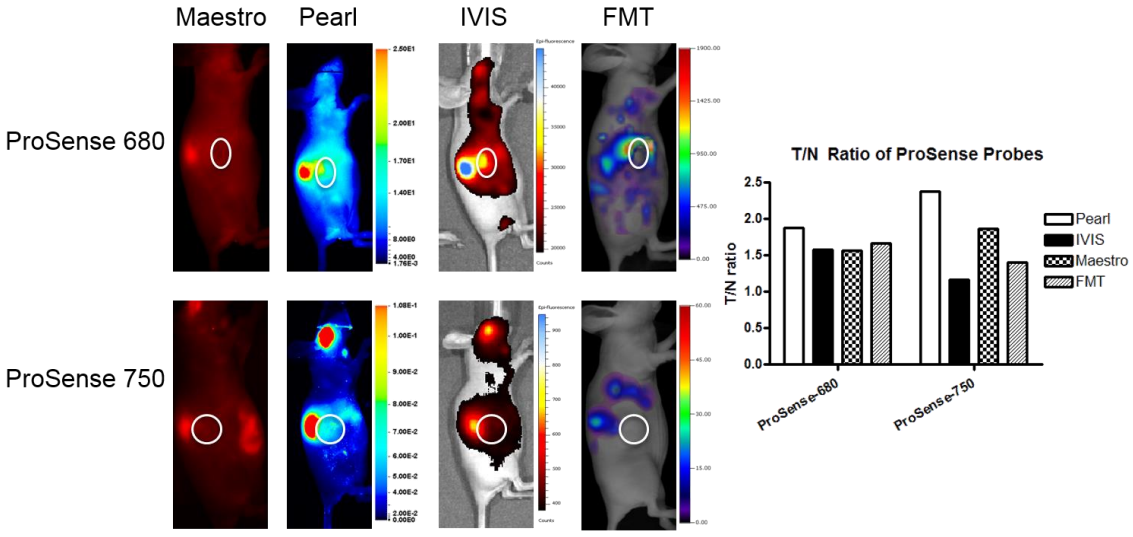


**Figure A2.13. Comparison of ProSense imaging probes across imaging systems**. Images were acquired across instruments using protocols listed in the written report. Each column of images corresponds to the 24 h time point for a specific probe and

instrument. White ellipses were drawn across all images in order to outline tumor area for clarity. A comparison of tumor-normal ratios for each probe across instruments is also provided.

*LiCor and Caliper 2-DG Optical Probes*

Both LiCor's 2-DG optical probe and Caliper's RediJect 2-DG optical probe are fluorescent analogues of 2-deoxy-D-glucose that targets elevated rates of glycolysis in tumor cells. LiCor 2-DG conjugated with IRDye 800cw and Caliper RediJect 2-DG conjugated with XenoLight 750 were utilized using the recommended doses of 10 nmol. For *in vivo* evaluation of these two probes, the protocol for optical imaging using vehicle and C225 treated DiFi mice was implemented. Pearl derived TACs for LiCor and Caliper probes showed elevated tumor fluorescence (based on counts/pixel) in both vehicle and treated mice (**Fig. A2.14-15**). Few, if any, differences between vehicle and treated tumor measurable fluorescence were observed for the LiCor and Caliper 2-DG probes across all four imaging systems (**Fig. A2.16-17**). Rotation of 3D FMT images revealed fluorescence heterogeneity for Caliper 2-DG that was not obvious across the reflectance imaging platforms. 3D FMT analysis of the LiCor 2-DG probe confirmed background detectable fluorescence for tumor region. Though unclear at the time of data collection, we anticipate that this discrepancy was due to tumor positioning in the FMT and did not reflect the FMT's inability to detect fluorescence from the LiCor 2-DG reagent. Rapid clearance was noted for the LiCor probe ($t_{1/2}$ > 3.8 h) while the Caliper probe showed much slower clearance ($t_{1/2}$ > 24 h) (**Table A2.2**).

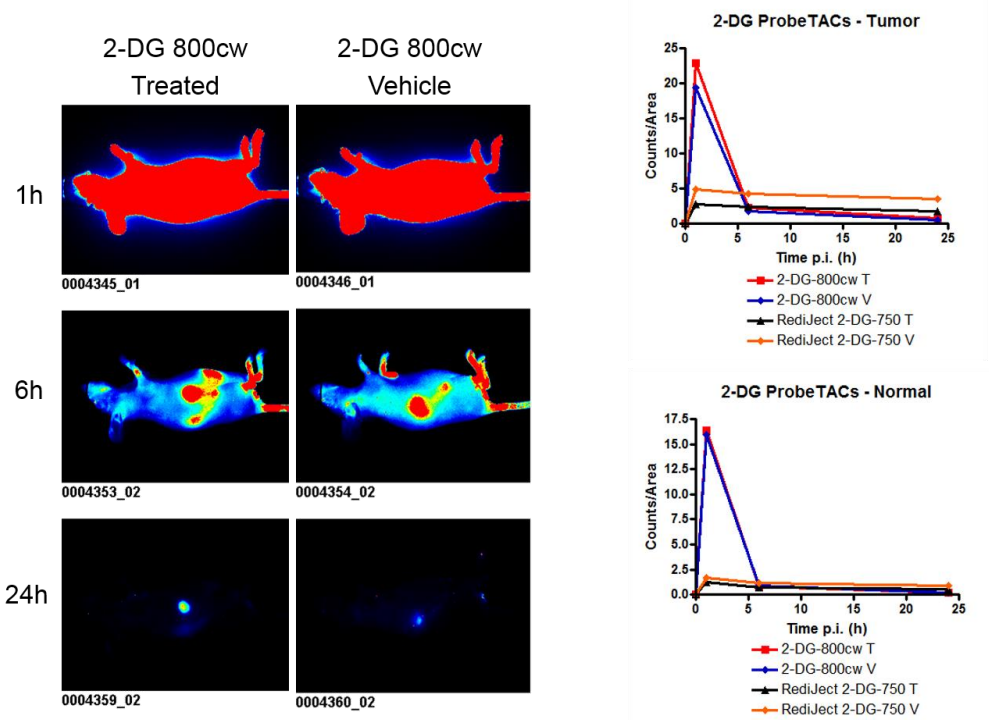


**Figure A2.14. Efficacy of 2-DG-800cw optical imaging as a measure of therapeutic response using the Pearl imaging system**. Pearl images were acquired using protocols listed in the written report. Each column of images corresponds to a specific time point p.i. (as listed above). Images across time points are set to the same scale. Time activity curves (TACs) in regards to tumor and normal tissue uptake. Fluorescence measurements were normalized to counts/area to account for discrepancies in ROI size across images.

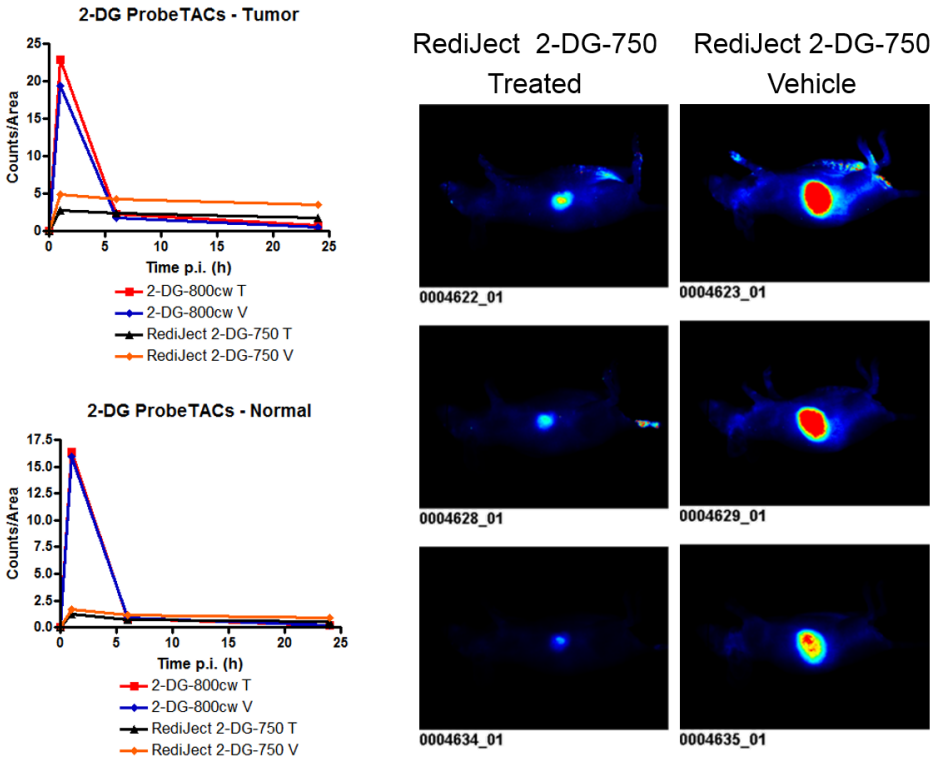


**Figure A2.15. Efficacy of RediJect 2-DG optical imaging as a measure of therapeutic response using the Pearl imaging system**. Pearl images were acquired using protocols listed in the written report. Each column of images corresponds to a specific time point p.i. (as listed above). Images across time points are set to the same scale. Time activity curves (TACs) in regards to tumor and normal tissue uptake. Fluorescence measurements were normalized to counts/area to account for discrepancies in ROI size across images.

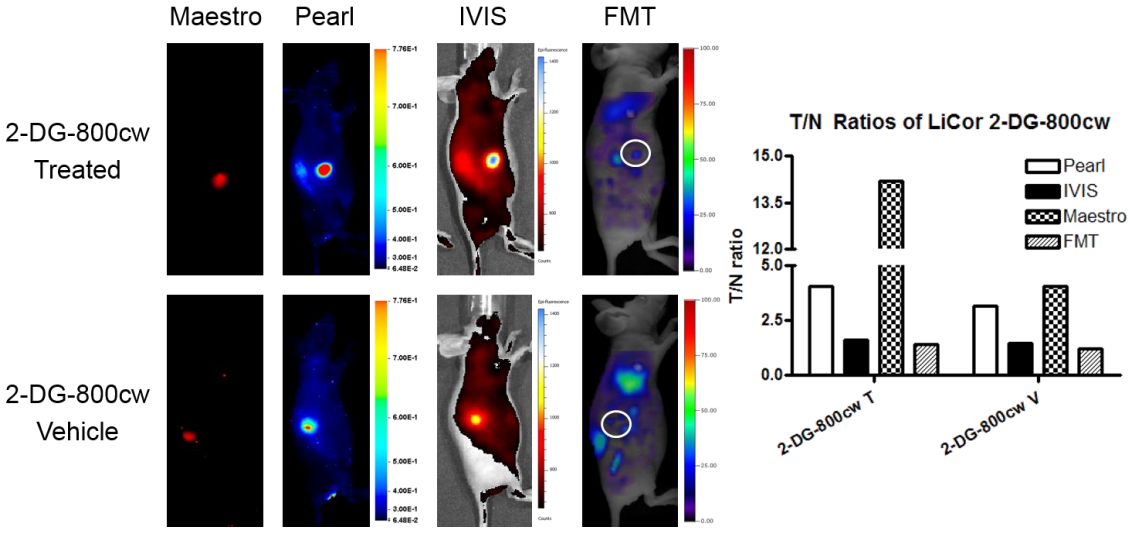


**Figure A2.16. Comparison of 2-DG-800cw optical imaging as a measure of therapeutic response across imaging systems**. Images were acquired across

instruments using protocols listed in the written report. Each column of images corresponds to the 24 h time point for a specific probe and instrument. White ellipses were drawn across FMT images in order to outline tumor area for clarity. A comparison of tumor-normal ratios for each probe across instruments is also provided.

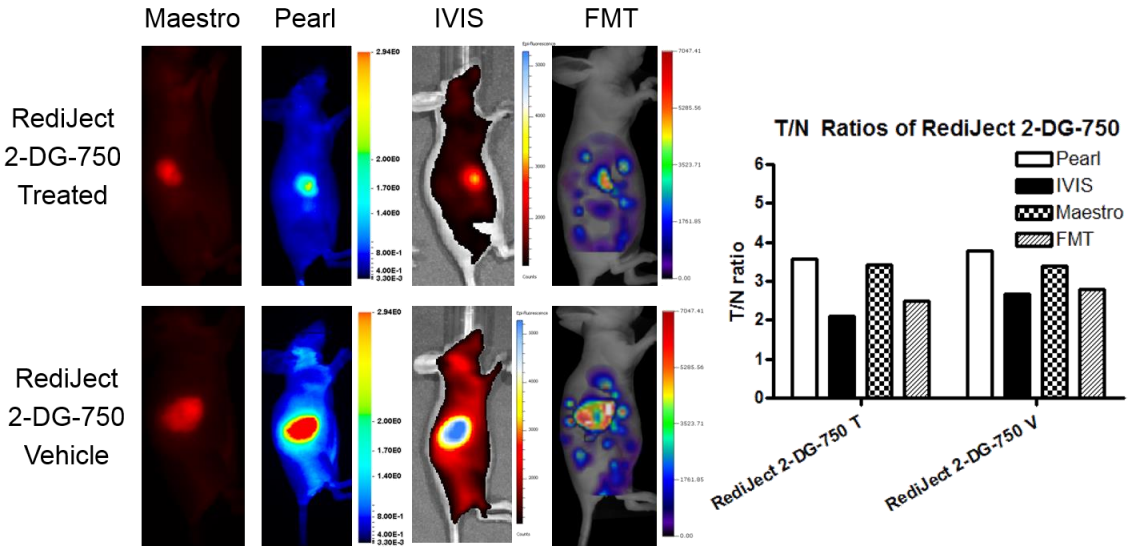


**Figure A2.17. Comparison of RediJect 2-DG optical imaging as a measure of therapeutic response across imaging systems**. Images were acquired across instruments using the protocols described. Each column of images corresponds to the 24 h time point for a specific probe and instrument. A comparison of tumor-normal ratios for each probe across instruments is also provided.

In previous studies, the inhibition of EGFR by C225 and resulting physiological effects of treatment (*i.e.,* decreased cell proliferation, increased cell apoptosis, *etc.*) were detectable by [$^{18}$F]FDG PET. Compartmental modeling showed decreased [$^{18}$F]FDG uptake in DiFi mice after C225 treatment. The optical imaging data acquired for both 2-DG probes contradict these results and disagree with the expected result of decreased tumor uptake in treated animals.

To further compare LiCor 2-DG probe with [$^{18}$F]FDG, an *ex-vivo* cross-sectional slicing experiment was performed in accordance to the protocol described previously. [$^{18}$F]FDG autoradiography of a cross sectional whole body tissue slice (40 µm thick) provided some understanding of the heterogeneous tumor tissue uptake in an untreated DiFi mouse (**Fig. A2.18**). Optical analysis using the LiCor Odyssey of the same tissue

slice showed relatively homogenous uptake of the optical 2-DG probe. 2-DG probe accumulation did not correlate with the heterogeneous distribution of [$^{18}$F]FDG, which was primarily detected within solid tumor tissue and showed peripheral accumulation around perceived areas of tissue necrosis.

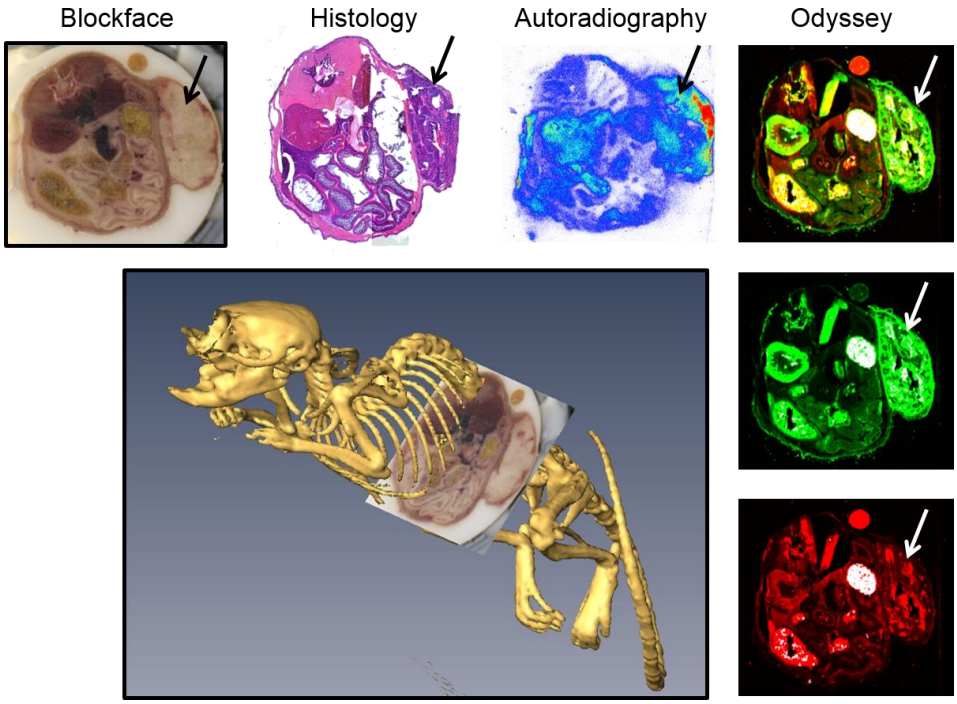


**Figure A2.18. Multi-modality comparison of measures of cellular glycolysis**. Individual registered images collected during cryosectioning of digital blockface, H&E staining, [$^{18}$F]FDG autoradiography, and optical Odessey images (top-700 (red) and 800 (green) channel overlay, middle-800 channel, and bottome-700 channel). Also shown is a coregistered image of digital blockface imaging and CT.

*LiCor EGF Optical Probes*

The EGF optical probe targets over expression of EGFR that is typically related with increased cellular proliferation and tumor cell growth. LiCor EGF probe conjugated with IRDye 680rd was utilized using the recommended dose of 2 nmol. For *in vivo* evaluation of this probe, the protocol for optical imaging using vehicle and C225 treated DiFi mice was implemented. The Pearl derived TAC showed elevated tumor specific uptake in vehicle mice and minimal tumor uptake in treated mice (**Fig. A2.19**). Similar uptake

profiles were observed across all four imaging systems and agreed with the Pearl TACs (**Fig. A2.20**). Rotation of the 3D FMT image provided a map of probe uptake heterogeneity that was not discernable when using reflectance imaging. All data acquired for the EGF-680rd agrees with previous work where optical imaging studies in C225 treated DiFi mice using EGF and Annexin-V conjugated with optical dyes showed minimal specific tumor tissue probe uptake (2).

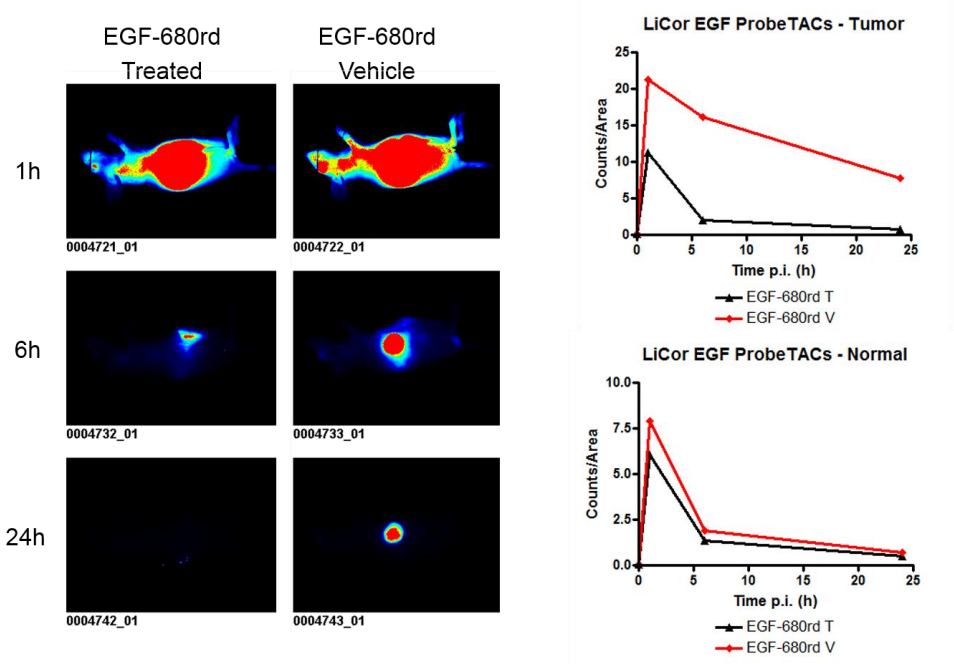


**Figure A2.19. EGF optical probe evaluation using the Pearl imaging system**. Pearl images were acquired using protocols listed in the written report. Each column of images corresponds to a specific time point p.i. (as listed above). Images across time points are set to the same scale. Time activity curves (TACs) in regards to tumor and normal tissue uptake. Fluorescence measurements were normalized to counts/area to account for discrepancies in ROI size across images.

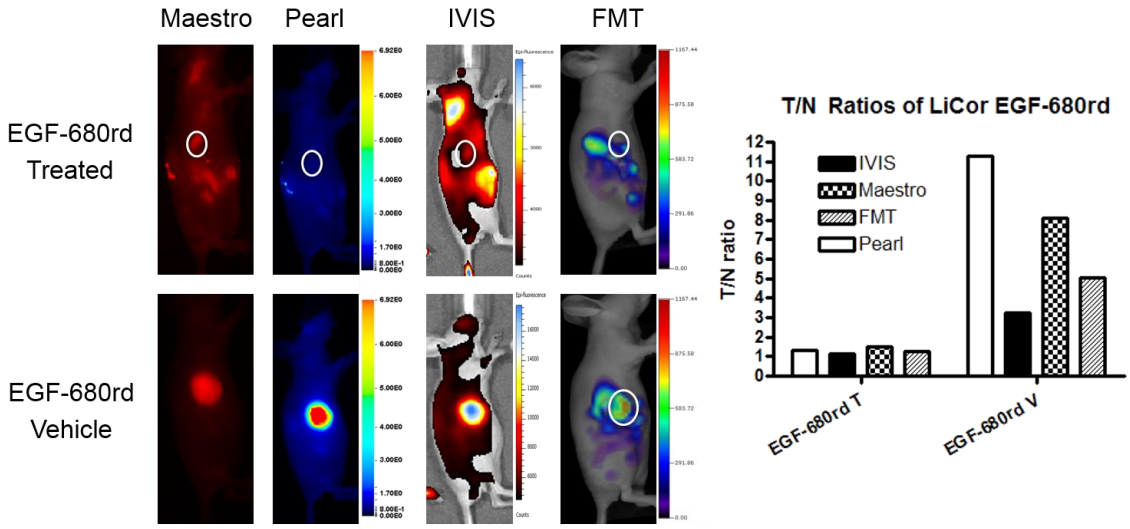


**Figure A2.20. Comparison of EGF imaging probes across imaging systems**. Images were acquired across instruments using protocols listed in the written report. Each column of images corresponds to the 24 h time point for a specific probe and instrument. White ellipses were drawn across FMT images in order to outline tumor area for clarity. A comparison of tumor-normal ratios for each probe across instruments is also provided.

*LiCor, Caliper, and Visen Bone Optical Probes*

The LiCor, Caliper, and VisEn optical bone probes target areas of active bone growth. LiCor BoneTag conjugated with IRDye 680, Caliper RediJect bone probe conjugated with XenoLight 750, and VisEn OsteoSense conjugated with NIR fluorochrome 750 were utilized using the recommended dose of 4, 2, and 2 nmol respectively. All three probes showed similar uptake profiles across instruments in the human breast cancer (BC) GFP-labeled MDA-MB-231 mouse model (**Fig. A2.21-23**). Increased fluorescence was detected in the femur, spine, and skull. In the case of Caliper's RediJect-750, non-specific probe uptake (suspected as kidney uptake) was also observed. GFP imaging with the Maestro was performed on all MDA-MB-231 animals in order to correlate GFP detection with bone probe uptake. GFP tumors were detected, bus as expected, probe accumulation did not correlate with regions of tumor detection. For the OsteoSense-750 animal set, rib cage/spine and fore/hind limb bones

were harvested after *in vivo* imaging and imaged *ex vivo* on the Maestro (Blue filter setting) and Pearl (**Fig. A2.24**). In the *ex vivo* studies using OsteoSense-750, no correlation between positive GFP detection and probe uptake was observed.

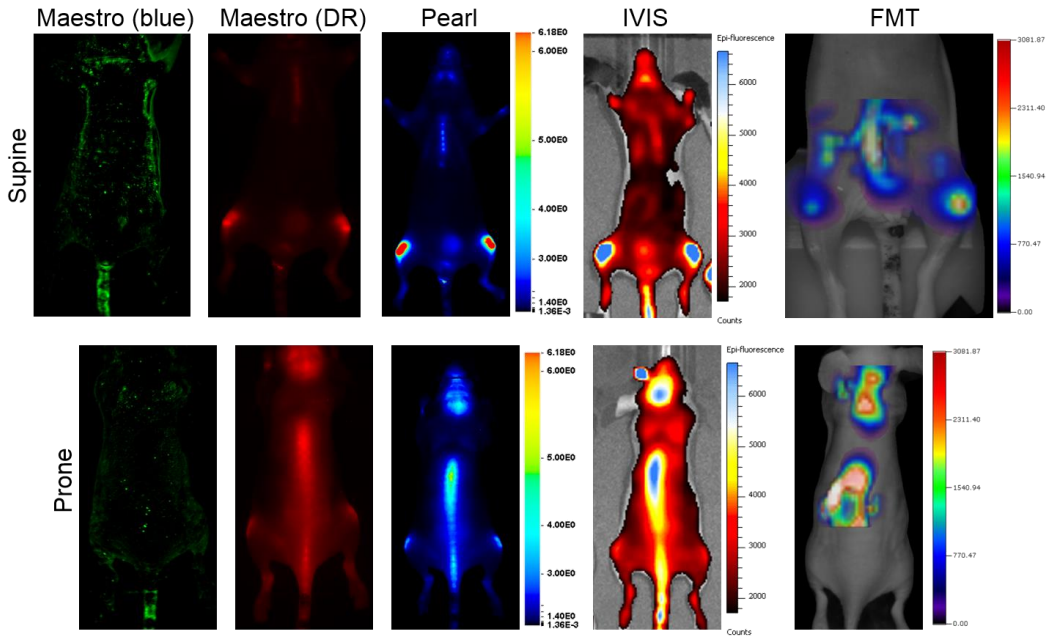


**Figure A2.21. Comparison of LiCor Bone Tag 680 imaging across imaging systems**. Images were acquired across instruments using protocols listed in the written report. Each column of images corresponds to the 24 h time point for a specific probe and instrument. Top row of images were taken with the animal in the supine position while bottom row images were taken with the animal in the prone position. GFP expression was imaged using the Maestro with the Blue filter setting (far left).

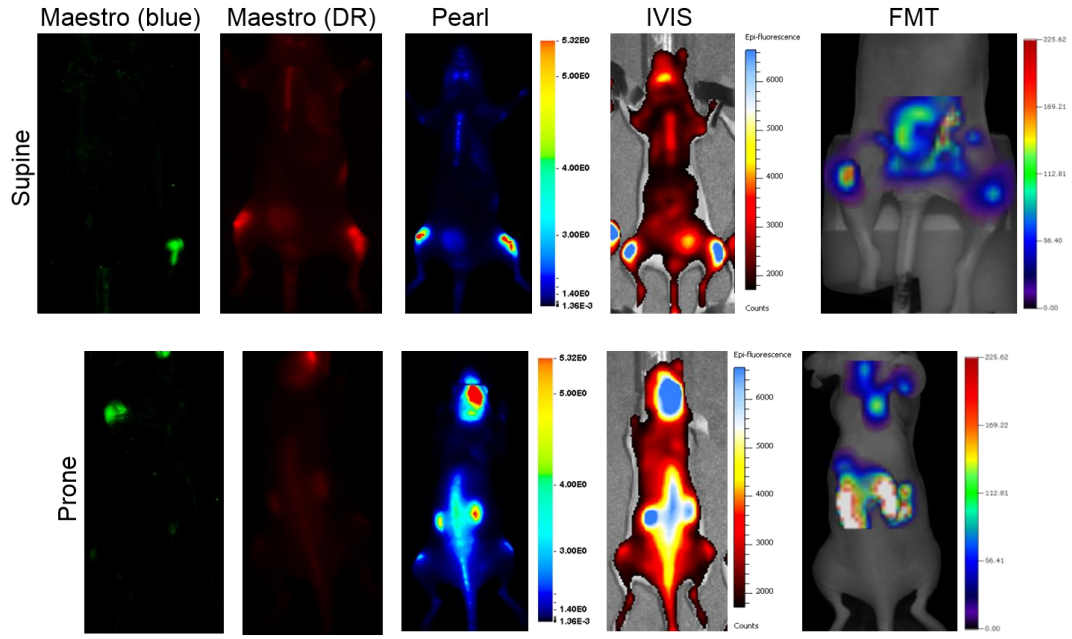


**Figure A2.22. Comparison of Caliper RediJect Bone Probe 680 imaging probe across imaging systems**. Images were acquired across instruments using protocols listed in the written report. Each column of images corresponds to the 24 h time point for a specific probe and instrument. Top row of images were taken with the animal in the supine position while bottom row images were taken with the animal in the prone position. GFP expression was imaged using the Maestro with the Blue filter setting (far left).

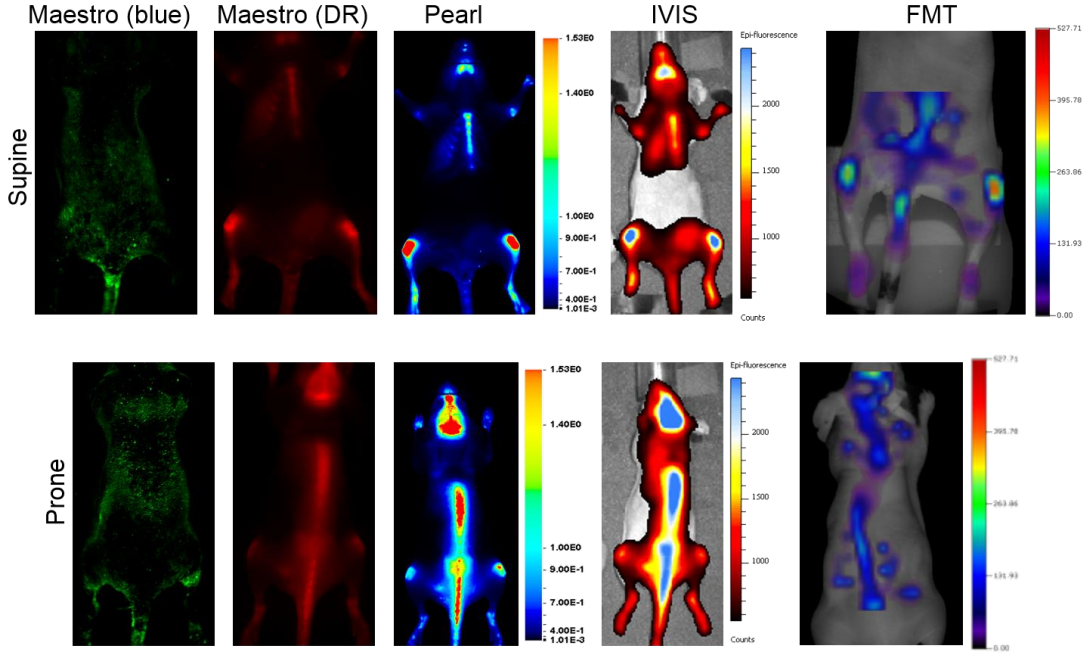


**Figure A2.23. Comparison of VisEn OsteoSense 750 imaging across imaging systems**. Images were acquired across instruments using protocols listed in the written

report. Each column of images corresponds to the 24 h time point for a specific probe and instrument. Top row of images were taken with the animal in the supine position while bottom row images were taken with the animal in the prone position. GFP expression was imaged using the Maestro with the Blue filter setting (far left).

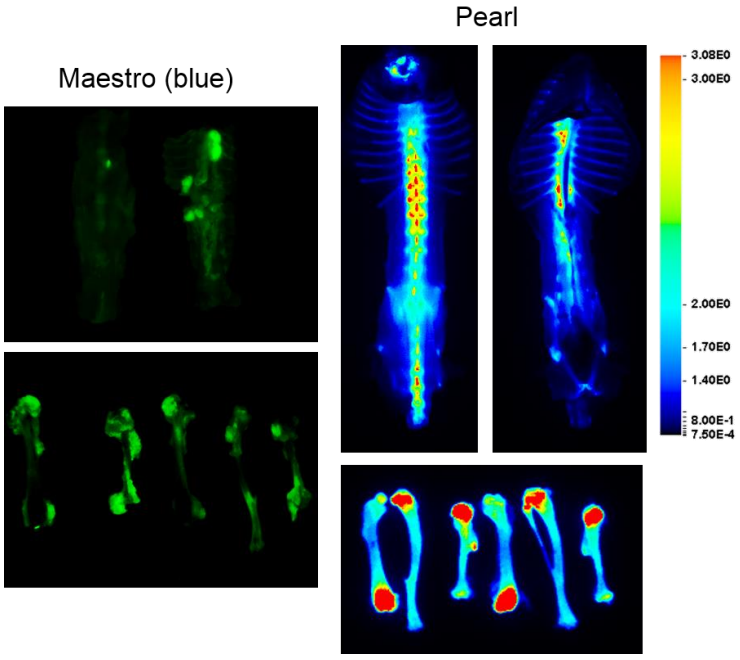


**Figure A2.24. Ex vivo imaging of bone tissue samples using VisEn OsteoSense 750 optical imaging**. Images were acquired on the Maestro and Pearl using protocols listed in the written report. Top images show rib cage and spine in two different positions (left, spine is facing camera; right, rib cage is facing camera). Bottom images show fore/hind limbs.

*Optical Imaging Instrument Comparison*

The Vandebilt IVIS system is an IVIS200 combination bioluminescence/fluorescence imaging system that was purchased new from Xenogen in approximately 2002 for ~$400,000. The Maestro imaging system was purchased new from CRi in 2006 for ~$90,000. The LiCor Pearl imaging system was purchased from LiCor in 2010 for $48,000. The FMT2500 imaging system was purchased from VisEn in 2010 for $350,000. The IVIS200, Maestro, and Pearl systems were purchased using institutional funds and the FMT2500 was purchased using funds to Dr. Manning from a NIH shared institutional grant.

Our experiences with this study have led to a group of conclusions regarding the utilization of these imaging systems. In terms of measured contrast observed in this study, the Maestro typically provided the highest T/N ratios likely due to the benefits of spectral unmixing (**Table A2.2**). The Pearl frequently demonstrated higher contrast than IVIS or FMT, though contrast did not consistently exceed that of the Maestro. The FMT showed the most variation in measured contrast, which might be the result of the transillumination geometry that this system utilizes.

| Point of Comparison | Pearl | Maestro | IVIS | FMT |
|---|---|---|---|---|
| **Throughput** | *** | ** | **** | * |
| **Reliability** | **** | ** | **** | * |
| **Ease of use (instrument)** | **** | *** | *** | ** |
| **Ease of use (software)** | **** | *** | *** | ** |

**Table A2.3. Qualitative comparisons of practical instrument usability.** Imaging systems were evaluated in terms of throughput, reliability, ease of instrument use, and ease of software use. A single asterisk (*) signifies 'fair', double asterisk (**) for 'moderate', triple asterisk (***) for 'good', and quadruple asterisk (****) for 'excellent'.

Throughout the course of this study, many practical characteristics (both positive and negative) of the four optical imaging platforms investigated became apparent. A qualitative comparison of instrument usability in terms of throughput, reliability, ease of instrument use, ease of software use is provided in **Table A2.3**. Qualitative measures of each category were made using an asterisk based system: a single asterisk (*) for fair, double asterisk (**) for moderate, triple asterisk (***) for good, and quadruple asterisk (****) for excellent. Unlike the FMT, Maestro, and Pearl, the IVIS is capable of imaging multiple mice simultaneously, thus permitting greater throughput when working with large cohorts of mice (> 25 animals). Though the Pearl is limited to one mouse per scan, the speed of acquisition and the ability to simultaneously image across the 700 nm and 800 nm channels allows the Pearl to become a fairly high-throughput instrument and comparable to the IVIS for small to moderate cohorts (1 – 25 animals). The throughput

of the Maestro is comparable to the Pearl when using short integration times (< 500 ms) and a single filter set. However, for experiments that require long integration times (> 1 s) and/or require multiple filter settings (as can be the case with co-injections of multi-wavelength probes), scan time can increase drastically and significantly impede throughput. Out of all four platforms, the FMT is the slowest in terms of animal throughput due to lengthy acquisition times. While scan times may vary depending on region size, acquisitions using a single channel routinely averaged 5 min. For any experiments which require more than five animals and/or multiple channel acquisitions, a 5 min acquisition time can cause the FMT to become a major bottle neck for multi-platform experiments and likewise hinder time point sensitive experiments (such as time course developments). For these reasons, in terms of throughput the Pearl was ranked 'good', the Maestro 'moderate', the IVIS 'excellent', and the FMT 'fair.'

The point of comparison 'reliability' was termed in regards to the frequency of technical difficulties experienced while performing extensive optical imaging experiments. Throughout the course of multiple imaging experiments, the Pearl and IVIS rarely experienced software or instrument errors that would prevent image acquisition. As such, these instruments were ranked 'excellent.' While the Maestro was frequently reliable, on occasion the software would fail to acknowledge the presence of the instrument when starting the system. Failure to collect fluorescence data due to faulty camera mechanics was another technical error occasionally encountered. These occasional disruptions typically required a complete system reset; delaying a given experiment up to 5 or 10 min. The Maestro was ranked 'moderate' for reliability. Technical difficulties were most frequent when using the FMT and associated TrueQuant software. Throughout use, a variety of instrument and software errors (such as the software freezing up, the instrument failing to initiate correctly, staging errors, *etc.*) would occur that could drastically delay or even prevent experiment completion. Frequently,

correction of the errors required repeatedly resetting the system until the instrument began functioning correctly. During the course of these studies, approximately five service calls were made to VisEn technical support to resolve these issues promptly. As such, the FMT was ranked 'fair' for reliability.

Ease of instrument/software use was defined in terms of how quickly and easily a new user could successfully learn to operate the imaging instrument without external guidance. The Pearl was the easiest and quickest instrument to use and train others how to use as operation can be achieved by the click of a button. Training a new user on the Maestro and IVIS was also easily accomplished once new users gained an understanding of what optical/acquisition settings worked best for their experiments. The FMT was perhaps the most difficult instrument to introduce to new users. Most of this difficulty stemmed from the windowing set-up implemented by the TrueQuant imaging software, which can at first be slightly confusing to new users. In addition, the need for calibrating the instrument for a specific optical probe is something many users are not accustomed to doing. While laser channel calibration is performed only the first time a new optical probe is used, it is a step in instrument operation that can sometimes be new for first time users. For these reasons, in terms of 'ease of use', the Pearl was ranked 'excellent', the Maestro 'good', the IVIS 'good', and the FMT 'moderate.'

### A2.4. Conclusions

In this study we have compared an array of small animal *in vivo* optical imaging probes from VisEn, Perkin Elmer, and LiCor across four imaging systems (IVIS, Maestro, Pearl, and FMT) to evaluate probes in animal models of cancer. Molecular imaging probes were assessed and compared based on images obtained across all four systems, Pearl derived TACs, T/N ratios, and probe half-life. Imaging instruments were compared qualitatively using a variety of practical based parameters. We feel that the

results of this study will help guide future developments of imaging technologies and optical imaging probes.

### A2.5. Works Cited


1. Ohkuma R. Congenital esophageal atresia with tracheoesophageal fistula in identical twins. J Pediatr Surg 1978;13(4):361-2.

2. Manning HC, Merchant NB, Foutch AC, Virostko JM, Wyatt SK, Shah C, et al. Molecular imaging of therapeutic response to epidermal growth factor receptor blockade in colorectal cancer. Clin Cancer Res 2008;14(22):7413-22.

3. Okinami S, Ohkuma M, Ohta M, Tsukahara I. Disruption of blood-retinal barrier at the retinal pigment epithelium after systemic urea injection. Acta Ophthalmol (Copenh) 1978;56(1):27-39.

4. Lapointe N, Parker TG, Tsoporis JN, Nguyen QT, Marcotte F, Adam A, et al. Effects of the vasopeptidase inhibitor omapatrilat on peri- and postmyocardial infarction in Zucker lean rats. Can J Cardiol 2005;21(3):291-7.

# APPENDIX 3

## MICROFLUIDIC RADIOCHEMISTRY FOR PET PROBE DISCOVERY

### A3.1. Introduction

The development and optimization of novel radiochemistries can be a bottleneck within the molecular imaging probe development paradigm as the ability to make compounds often exceeds radiolabeling capabilities. Traditional radiochemical preparations are inherently low throughput and limit the ease and efficiency at which protocol optimization and utilization can be achieved. Microfluidic radiochemistry offers a high throughput alternative approach to classical, box-based radiosyntheses (1-5) and provides: precise delivery of small isotope/precursor quantities, use of a linear, high surface-to-volume ratio reactor, laminar flow mixing of reagents, control over solvent backpressure, and rapid/sequential production of multiple tracers in relatively short periods of time. More specifically, the high-throughput nature of microfluidic approaches enables rapid optimization and evaluation of various radiochemical conditions, which may subsequently inform the feasibility of larger scale production.

In this work, utilization of the Advion NanoTek LF system (**Fig. A3.1**) and microfluidic radiochemistry were explored as a means for rapidly developing and optimizing novel and unconventional radiochemistries (**Fig. A3.2**). Leveraging previous experience involving the development of translocator protein (TSPO) specific positron emission tomography (PET) tracers, extensive focus was given towards evaluating microfluidic radiolabeling of known (i.e., [$^{18}$F]PBR06 (6,7) and [$^{18}$F]DPA714 (8,9)) and novel (10,11) TSPO ligands typically prepared using traditional means.

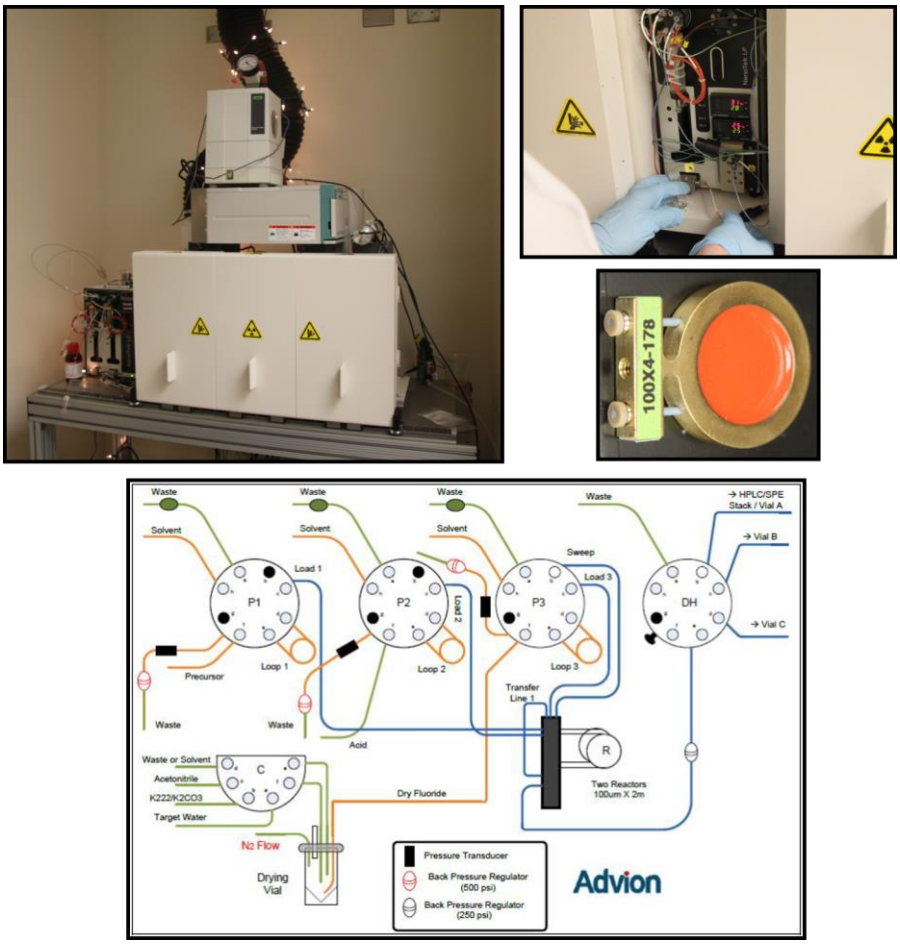


**Figure A3.1. Advion NanoTek LF radiochemistry module**. Images and hardware schematic of the microfluidic system used for these studies. Instrument schematic was obtained from the corresponding product literature.

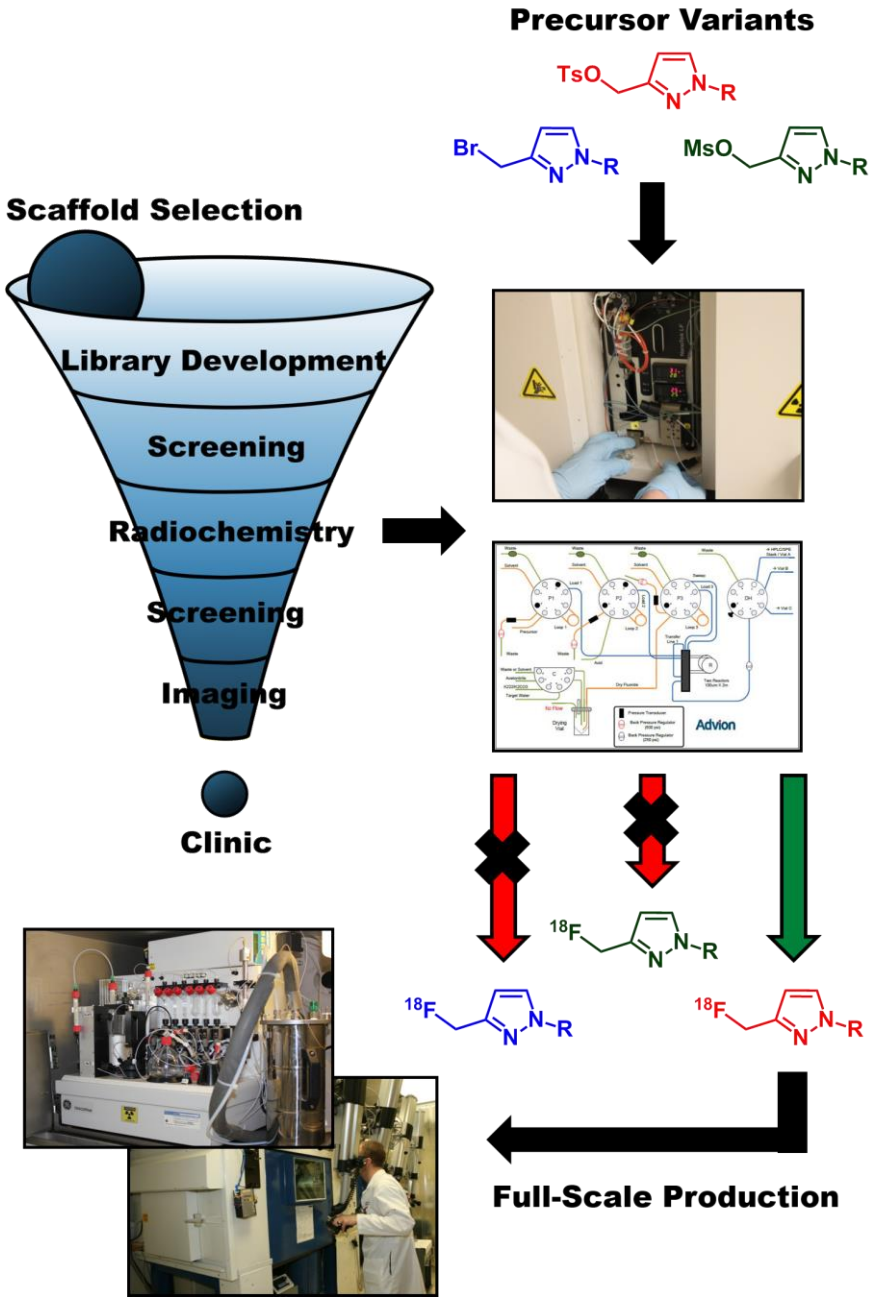


**Figure A3.2. Work-flow for microfluidic radiochemical screening**. Development paradigm for employing the NanoTek Microfluidic system towards triaging precursors and optimizing radiolabeling conditions for transition to full-scale production.

## A3.2. Materials and Methods

*Chemicals*

Unless otherwise indicated, all other chemicals, reagents, and solvents were purchased from Sigma-Aldrich and used as received. Radiochemical precursors were obtained from collaborating synthetic chemists affiliated with the Vanderbilt Institute of Imaging Science, the Vanderbilt Radiochemistry Core, and/or the Manning research group.

*Microfluidic Radiochemistry*

The Advion NanoTek$^{TM}$ LF system was used to perform microfluidic radiolabeling of a variety of aryloxyanilide and pyrazolo-pyrimidine based TSPO ligands with fluorine-18. Additional compounds, such as indomethacin and crizotinib derivatives as well as a class of small molecule BRAF inhibitors, were also explored. In the following discussions, the term *discovery* will be used to describe small volume, high-throughput microfluidic experiments where the objective was to explore, optimize, and characterize reaction conditions and properties. The term *production* will be used to describe high volume, low-throughput microfluidic experiments where the object was to synthesize a specific radiolabeled-product in sufficient yield and purity for use in small animal imaging studies.

Upon radiosynthesis, [$^{18}$F]fluoride ion (10-30 μCi) was trapped on an anion exchange cartridge and released upon complexation with K1-K1-2.2.2/$K_2CO_3$. Iterative azeotropic drying was performed at 110 °C by addition of acetonitrile. Reaction solvent was then added to the [$^{18}$F]fluoride-kryptofix solution and loaded into the pump 3 loop. Subsequently, precursor solution (4 mg/mL) was then loaded into the pump 1 loop. Prior to synthesis, transfer-lines 1 and 3 were filled with [$^{18}$F]fluoride and precursor solutions,

30 µL each, and swept through the reactor by reaction solvent *via* pump 3 at 60 µL/min. For *discovery* runs, a bolus of 10-20 µL each of [$^{18}$F]fluoride and precursor each were flushed through the reactor at a flow rate of 60 µL/min. Reaction solvents were typically acetonitrile, dimethyl sulfoxide (DMSO), or dimethylformamide (DMF). Reaction temperatures varied between 60 – 200 °C. For *production* runs, a bolus of 150 uL each of [$^{18}$F]fluoride and precursor were flushed through the reactor at a flow rate of 60 uL/min at a single temperature; as selected based on results from *discovery* experiments.

*Chromatography*

Radiochemical yield for most compounds was estimated by normal phase radio-thin layer chromatography (TLC) analysis using a BioScan radio-TLC plate reader. TLC plates were developed using an water:acetonitrile (MeCN) (10:90) mobile phase for aryloxyanilides, pyrazolo-pyrimidines, and indomethacin derivatives; where unlabeled fluorine-18 remained at the origin and [$^{18}$F]-radiolabeled compound traveled with the solvent front. For BRAF inhibitors, crizotinib derivatives, and amino acid complexes, plates were developed using a methanol (MeOH): dichloromethane (DCM) (10:90) mobile phase. Uncomplexed amino acid final product was developed using a n-butanol (n-BuOH): acetic acid: water: ethanol (EtOH) (4:1:1.6:0.5) mobile phase.

Radiochemical stability and standard curve derived specific activities (SA) were determined using a reversed-phase, high pressure liquid chromatography (HPLC) approach. Unless otherwise stated, a wavelength of 254 nm was used for acquisition of all HPLC UV-chromatograms. For aryloxyanilides, a water:MeCN (40:60) mobile phase was run at 1 mL/min on a C18 Dynamax 250·4.6 mm (Varian) column. For pyrazolo-pyrimidines, a 0.5 M aqueous ammonium acetate (NH4)OAc (pH 10):MeCN (35:65) mobile phase was run at 1 mL/min on a C18 Dynamax 250 x 4.6 mm (Varian) column. Indomethacin derivatives were analyzed using the following water:MeCN gradient at 1

mL/min on a C18 Dynamax 250 x 4.6 mm (Varian) column: 50% MeCN, 0-1 min; 50-95% MeCN, 1-15 min; 95% MeCN, 15-20 min; 95%-50% MeCN, 20-21 min. BRAF inhibitors and crizotinib derivatives were analyzed using the following water:MeCN gradient at 1 mL/min on a C18 Dynamax 250 x 4.6 mm (Varian) column: 30-90% MeCN, 0-10 min; 90% MeCN, 10-30 min. Uncomplexed amino acid final product was analyzed using a ammonium acetate:ethanol (45:55) isocratic mobile system on an Luna $NH_2$ 250 x 4.6 mm (Phenomenex) column using a flow of 1 mL/min and a UV-wavelength of 207 nm.

Low resolution mass spectra were obtained on an Agilent 1200 liquid chromatography–mass spectrometry (LC-MS) with electrospray ionization available through the Chemical Synthesis CORE at Vanderbilt.

## A3.3. Results and Discussion

*TSPO Ligands*

Initial *discovery* experiments revealed that optimizing reaction temperatures had a major impact on the radiochemical yields of aryloxyanilides ([$^{18}$F]PBR-06) and pyrazolo-pyrimidines ([$^{18}$F]DPA-714, VUIIS 7004, VUIIS 1012, VUIIS 1016) (**Fig. A3.3, Fig. A3.4**) upon substitution of a Br or tosyl-leaving group (aryloxyanilide and pyrazolo-pyrimidines, respectively) with fluorine-18. Radiolabeling Labeling efficiencies up to and greater than 90% could be achieved for all compounds when characterized at optimal temperatures. Importantly, optimized microfluidic conditions were informative towards accelerating development of high-specific activity, large-scale production methodologies developed in a GE Tracer Labs FX module.

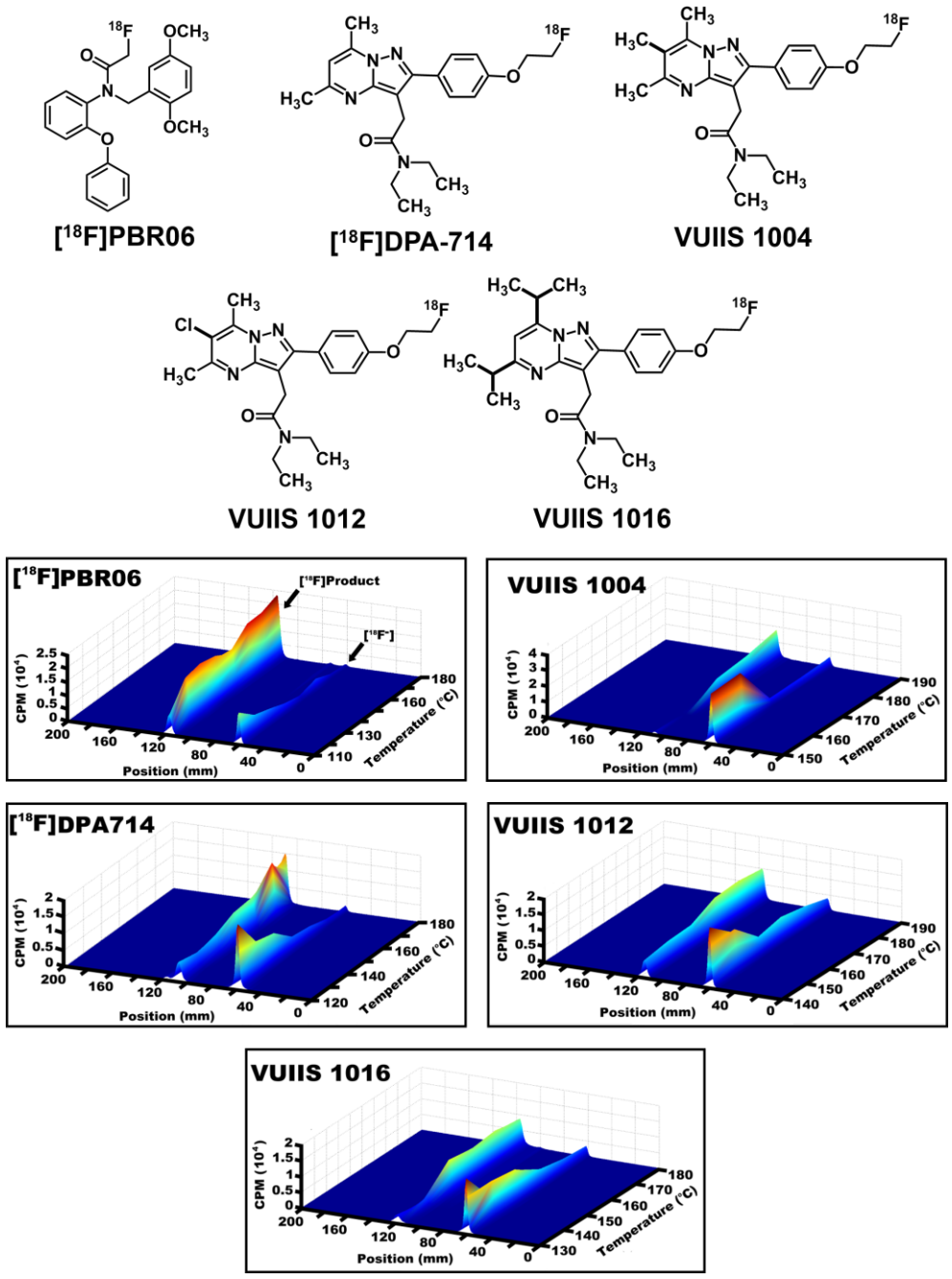


**Figure A3.3. Microfluidic *discovery* of TSPO PET ligands for the optimization of reaction temperatures.** Relative radiochemical yields, as measured by radio-TLC, of sequential microfluidic productions of TSPO ligands at different temperatures using acetonitrile as the reaction solvent. 'Position' refers to the distance traveled by compounds along the TLC-plate, where the origin is 60 mm and the solvent front is 120 mm. In all cases shown, radio-labeled product traveled with the solvent front (120 mm), while free fluorine-18 remained at the origin (60 mm).

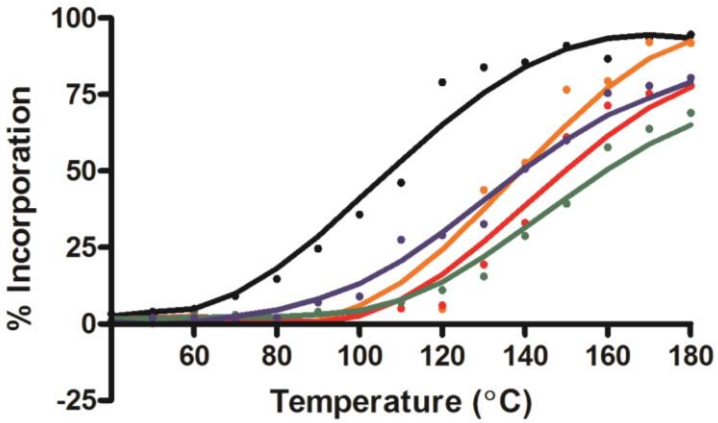


**Figure A3.4. Two-dimensional representation of fluorine-18 percent incorporation temperature dependency of TSPO ligand *discovery* radiolabelings in acetonitrile.** Compounds shown: black = [$^{18}$F]PBR06, orange = [$^{18}$F]DPA-714, red = VUIIS 1016, green = VUIIS 1012, blue/purple = VUIIS 1004.

Given the promising results of the *discovery* experiments, full-scale *production* experiments were explored to evaluate the potential of utilizing the Advion NanoTek for the synthesis of preclinical probe doses alternatively to more traditional methodologies, such as the GE Tracer Labs FX module. The bulk of these studies focused on the *production* of [$^{18}$F]PBR06 (**Table A3.1**), but radiochemical *production* of [$^{18}$F]DPA-714 (**Table A3.2**) was also explored. Interestingly, *production* runs often resulted in radiochemical yields, or percent fluorine-18 incorporation, that were significantly higher than that predicted by initial *discovery* experiments for similar reaction conditions. This difference was thought to be related to the increased conditioning of the microfluidic reactor resulting from the constant flow of fluorine-18 and precursor compound. Accordingly, the effects of reaction solvent on radiochemical incorporation were made more apparent in these experiments, as choice of reaction solvent was found to have a profound effect on radiochemical yield for pyrazolo-pyrimidines, compared to aryloxyanilides, where at least 150-160 °C was needed to reach ≥90% labeling in acetonitrile while as low as 100-110 °C was needed to achieve similar yields in dimethylformamide.

| SA (Ci/mmol) | SA (TBq/mmol) | % Labeling | Temp (°C) | Solvent |
|---|---|---|---|---|
| 22.8 | 0.8 | 70 | 160 | MeCN |
| 35.1 | 1.3 | 42 | 160 | MeCN |
| 34.2 | 1.3 | 66 | 160 | MeCN |
| 58.7 | 2.2 | 95 | 160 | MeCN |
| 22.0 | 0.8 | 58 | 160 | MeCN |
| 46.1 | 1.7 | 44 | 140 | MeCN |
| 307.0 | 11.4 | 95 | 150 | DMF |
| 81.0 | 3.0 | 98 | 150 | DMF |
| 19.1 | 0.7 | 86 | 140 | DMF |
| 2.8 | 0.1 | 90 | 140 | DMF |
| 10.3 | 0.4 | 97 | 110 | DMF |
| 8.9 | 0.3 | 89 | 100 | DMF |
| 27.2 | 1.0 | 97 | 100 | DMF |
| 110.3 | 4.1 | 99 | 110 | DMF |
| 4.5 | 0.2 | 92 | 110 | DMF |
| 5.4 | 0.2 | 35 | 110 | DMF |

**Table A3.1. Representative summary of multiple [$^{18}$F]PBR06 *productions* using the Advion NanoTek.** Specific activities (SA), Decay corrected radiochemical yields (% Labeling), reaction temperatures (Temp), and reaction solvents (acetonitrile (MeCN) or dimethylformamide (DMF)) for seven representative [$^{18}$F]PBR06 *production* runs.

| SA (Ci/mmol) | SA (TBq/mmol) | % Labeling | Temp (°C) | Solvent |
|---|---|---|---|---|
| 630.79 | 23.34 | 80.8 | 180 | MeCN |
| 175.71 | 6.50 | 58.5 | 160 | MeCN |
| 125.43 | 4.64 | 83.6 | 160 | MeCN |
| 1.6 | 0.06 | 10 | 130 | DMF |
| 3.9 | 0.15 | 24 | 130 | DMF |
| 3.6 | 0.13 | 8 | 140 | DMF |
| 15.8 | 0.59 | 31 | 140 | DMF |

**Table A3.2. Representative summary of multiple [$^{18}$F]DPA-714 *productions* using the Advion NanoTek.** Specific activities (SA), Decay corrected radiochemical yields (%

Labeling), reaction temperatures (Temp), and reaction solvents (acetonitrile (MeCN) or dimethylformamide (DMF)) for seven representative [$^{18}$F]DPA-714 *production* runs.

Despite the very promising radiochemical yields obtained in microfluidic *production* runs, a reoccurring limitation was found in the form of below average specific activities (SA). Initially, the efficiency of fluorine-18 transfer with the NanoTek system, fluoride trapping efficiency, as well as the potential introduction of fluorine-19 through precursor preparation and/or through the NanoTek system itself were all explored, and eventually eliminated, as possible causes of the low specific activity measurements. Even with assistance from Lee Collier, PhD, Advion's lead radiochemist for the NanoTek system at the time, the SA for *production* runs remained low for both [$^{18}$F]PBR06 and [$^{18}$F]DPA-714. After extensive evaluation of both the NanoTek system and subsequent *production* methodology, up to three by-products that co-eluted with radiolabeled probed were identified by LC-MS and reversed-phase HPLC analysis (**Fig. A3.5**) for [$^{18}$F]PBR06 *production* runs and were suspected as being the cause of the low SA measurements. This observation was unique to microfluidic reactions as these by-products were not found in decayed [$^{18}$F]PBR06 samples prepared using traditional radiochemistry approaches. Initially, these products were suspected to be the result of hydroxyl by-product formation. However, subsequent LC-MS studies revealed that while hydroxyl by-product formation was occurring during radiosynthesis, this by-product did not co-elute with authentic radiolabeled probe (**Fig. A3.6**). Chemical structures of the by-products were never identified as quantities sufficient for more rigorous chemical analysis (i.e. NMR and high resolution MS) were difficult to obtain due to the inherently poor chemical yields of radiochemical methodologies. Project directions changed before similar studies could be explored for [$^{18}$F]DPA-714 microfluidic productions.

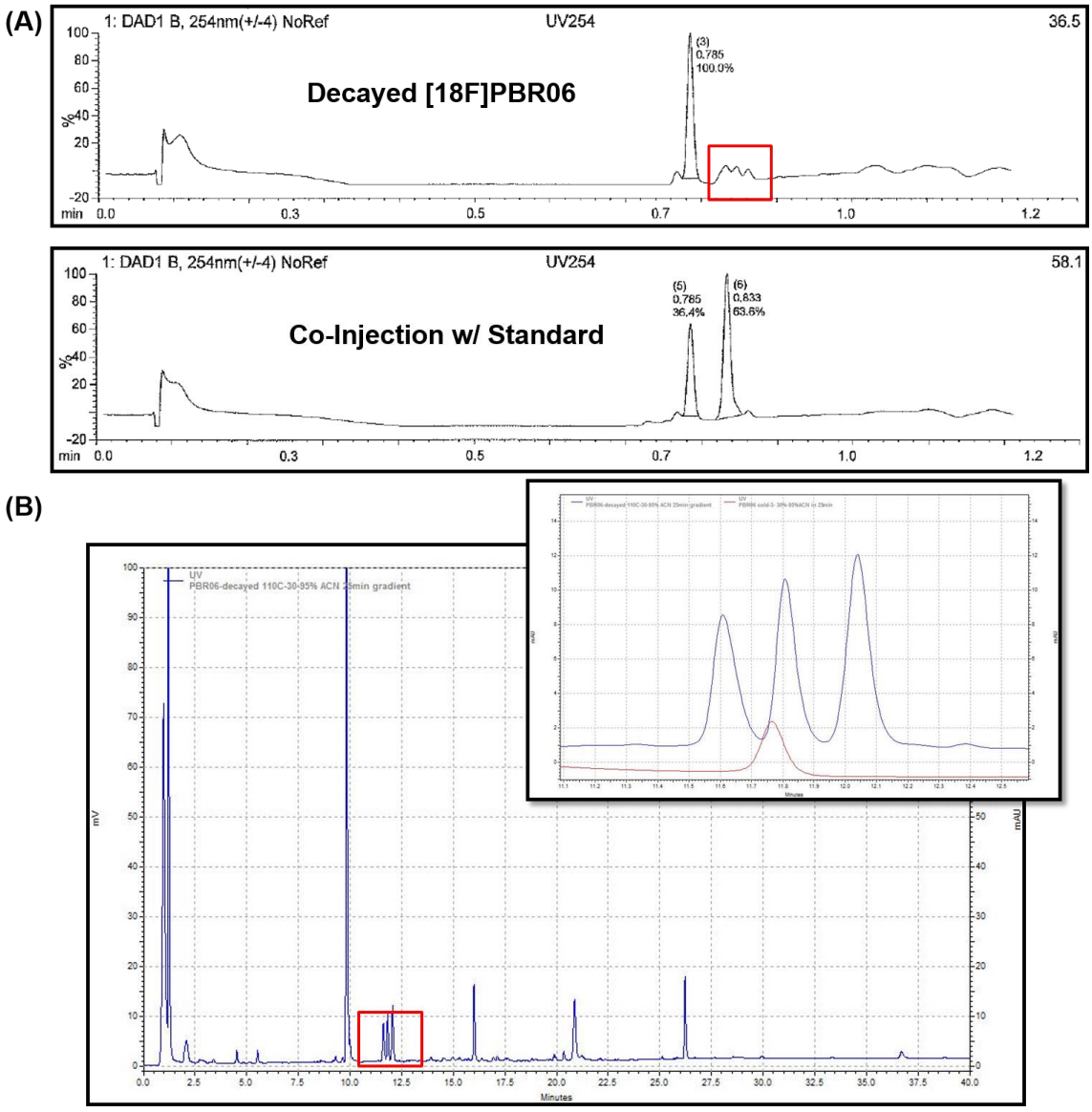


**Figure A3.5**. **LC-MS and HPLC analysis of decayed [$^{18}$F]PBR06 microfluidic radiolabeled products revealed unknown co-eluting by-products.** LC-MS analysis of a representative decayed [$^{18}$F]PBR06 sample and co-injection with [$^{19}$F]PBR06 (A) as well as a reversed-phase HPLC, UV chromatogram of a similar sample (B). A magnification of the outlined region in (B) is shown as an over-lay to a chromatogram of [$^{19}$F]PBR06 (magenta). Red squared outline the elution of the by-products.

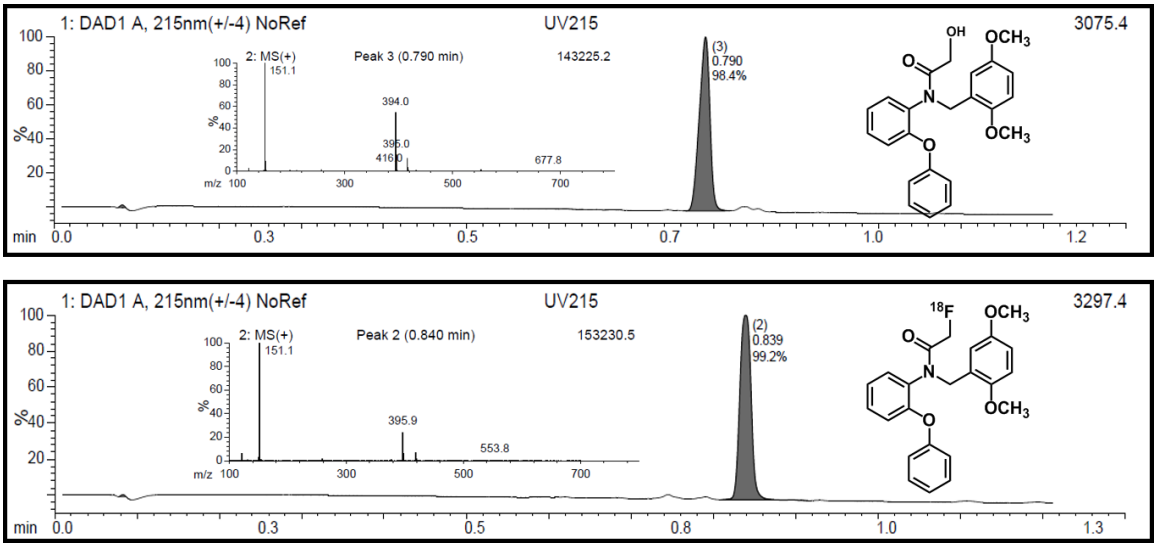


**Figure A3.6. Hydroxyl by-product did not co-elute with [$^{18}$F]PBR06**. LC-MS analysis of the hydroxyl by-product (top) and [$^{18}$F]PBR06 (bottom).

*Indomethacin Derivative*

Given the low SA limitation experienced with TSPO ligand radiolabeling, utilization of the NanoTek system was shifted to primarily *discovery* experiments and the optimization and evaluation of novel radiochemical strategies. Towards this effort, strategies for labeling a novel indomethacin derivative with fluorine-18 for PET imaging of COX2 expression was explored as part of a collaborative effort with Larry Marnett, PhD, and colleagues (**Fig. A3.7**). Using the NanoTek, it was possible to triage multiple variations of the indomethacin precursor and effectively eliminate compounds, which due to instability, were difficult to label (**Fig. A3.8, A3.9**). At a reaction temperature of 140°C, precursor **1** was found thermally unstable by HPLC analysis and exhibited no radiolabeling potential. Conversely, precursor **2** was thermally stable at 140°C, but only showed modest fluorine-18 incorporation. Similarly, precursor **3** was found stable but to possess time-dependent radiolabeling potential. Finally, a reaction temperature-based *discovery* experiment was performed using precursor **4** and revealed the highest radiolabeling potential out of the four potential compounds. However, the sample

provided was found to have impurities of compound **2**, and thus further stability studies were suspended until higher purity precursor samples could be obtained.

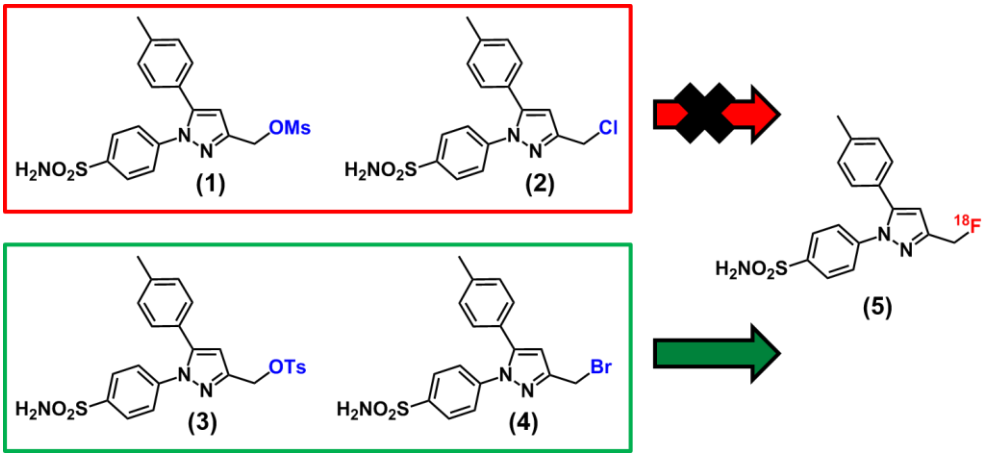


**Figure A3.7. Indomethacin precursors for radiochemical screening.** Through use of the NanoTek, it was possible to triage multiple variations of the indomethacin precursors and effectively eliminate compounds which, due to instability in common reaction solvents, were difficult to label.

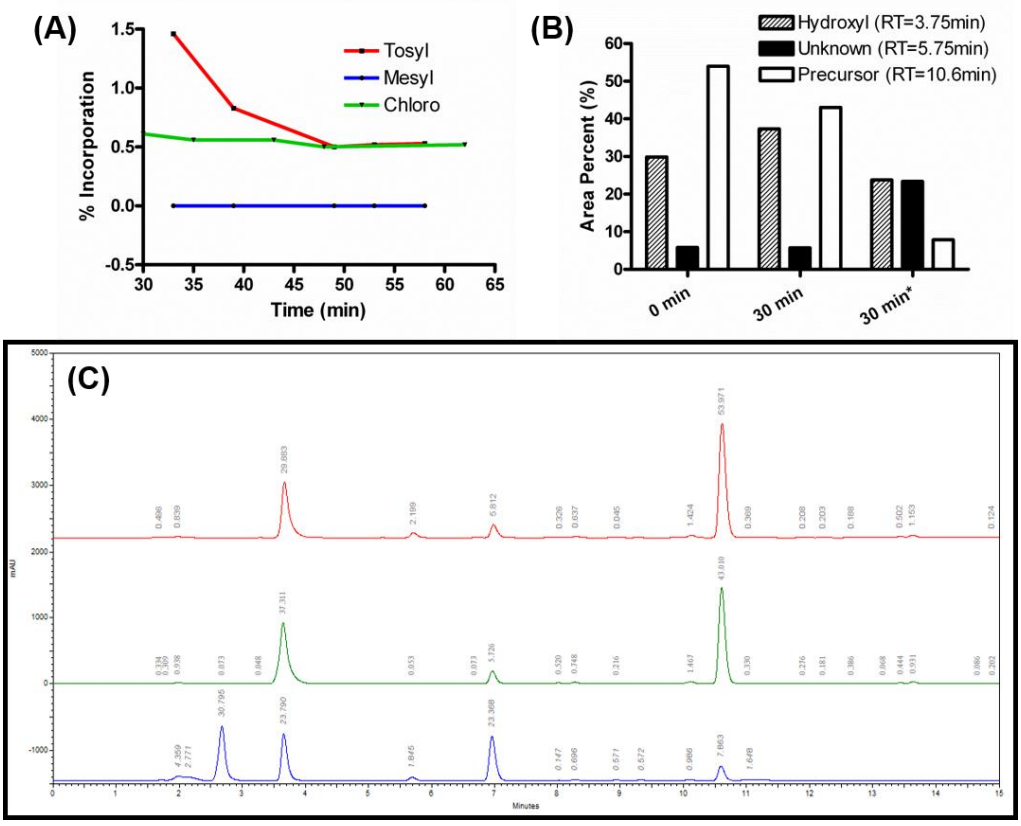


**Figure A3.8. Radiolabeling precursor stability studies for indomethacin derivatives.** TLC measured fluorine-18 incorporation for the radiolabeling precursors **1**

(mesyl), **2** (chloro), and **3** (tosyl) at 140 °C (A). Relative decomposition products, as determined by HPLC quantification (B). Representative UV-chromatograms of precursor stability, 30 min post precursor preparation in reaction solvent: red = precursor **3**, green = precursor **2**, blue = precursor **1** (C). The point at which precursor was dissolved in reaction solvent was defined as time zero. The state of precursor degradation was checked at 30 min post solution preparation both before and after radiolabeling at 140 °C ("30 min" and "30 min*" samples, respectively).

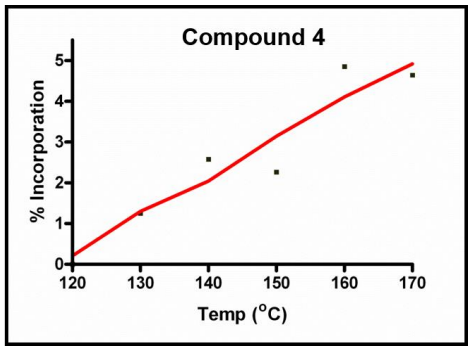


**Figure A3.9. The Br-precursor showed the greatest promise for translation to further radiochemical development.** Radiolabeling temperature-based *discovery* runs for compound 4.

*Crizotinib*

The NanoTek was used to select the optimal labeling conditions needed for the development of [$^{18}$F]crizotinib (compound **7**) (**Fig. A3.10**). Dimethyl sulfoxide (DMSO) was found to be the preferred reaction solvent at all temperatures evaluated compared to DMF. At the time of these studies, authentic [$^{19}$F]crizotinib had yet to be provided by collaborators within the Manning group. As such, HPLC validation of radiolabeled 'product', as determined by TLC, was never performed.

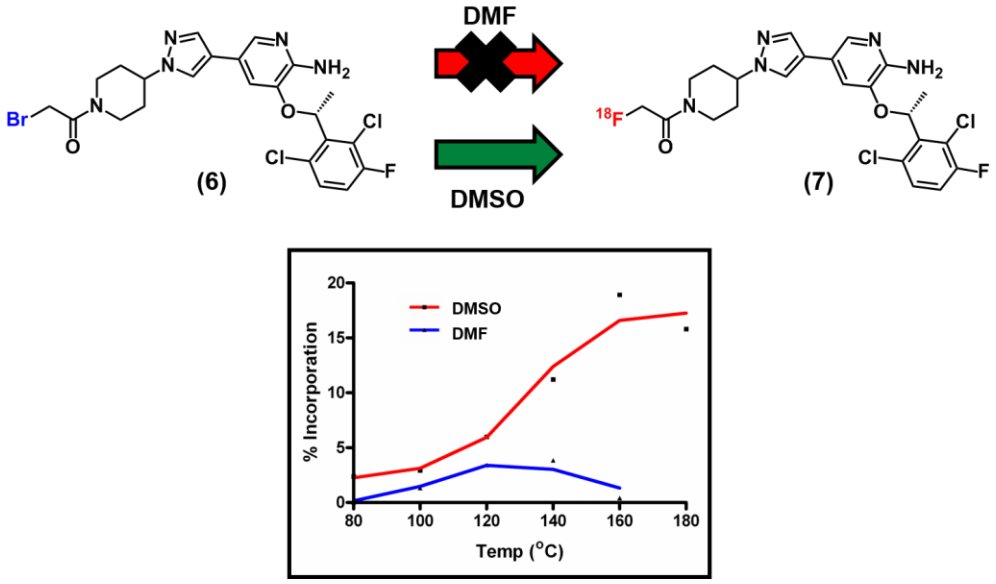


**Figure A3.10. Microfluidic fluorine-18 radiolabeling of crizotinib, bromo-precursor.** Radiolabeling temperature-based *discovery* runs for [$^{18}$F crizotinib, compound **7**.

*Inhibitors of mutant BRAF*

The NanoTek has been used to both screen and optimize the radiolabeling potential of novel derivatives of a known BRAF inhibitor from Plexxikon. Using DMF as a reaction solvent, it was found that over a range of temperatures, compound **10** showed greater feasibility towards radiolabeling than compound **8**.

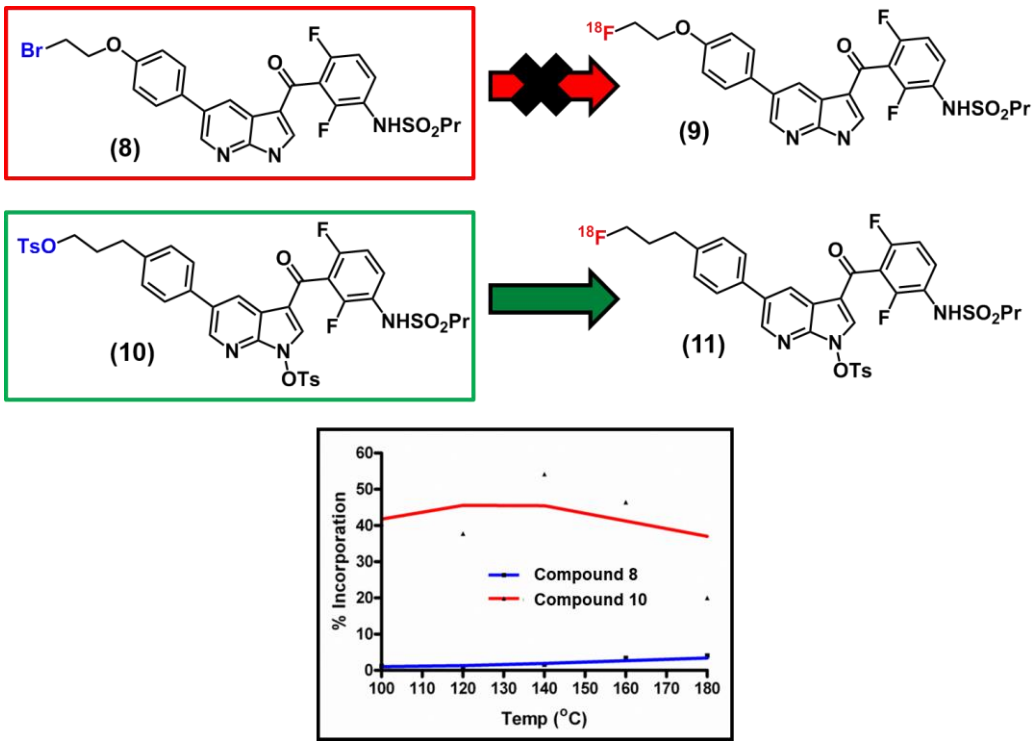


**Figure A3.11**. **Microfluidic fluorine-18 radiolabeling of inhibitors of mutant BRAF.** Radiolabeling temperature-based *discovery* runs for compounds **9** and **11**.

*Amino Acid Complexes*

Similarly, the NanoTek was instrumental towards optimizing the radiochemical production of [$^{18}$F]4-fluoro-glutamine (a complex three-step radiochemical production) due to the system's through-put, versatility, and capabilities of performing successful radiolabelings with low tracer levels (<100mCi). In this manner, this system was used to develop reaction conditions for the novel 3-step radiolabeling of [$^{18}$F]4-fluoro-glutamine (**Fig. A3.12**). These improvements aided in accelerating the development of novel probes that were actively being explored in programs such as the Vanderbilt ICMIC program, Digestive Disease Research Center (DDRC) and GI SPORE Program.

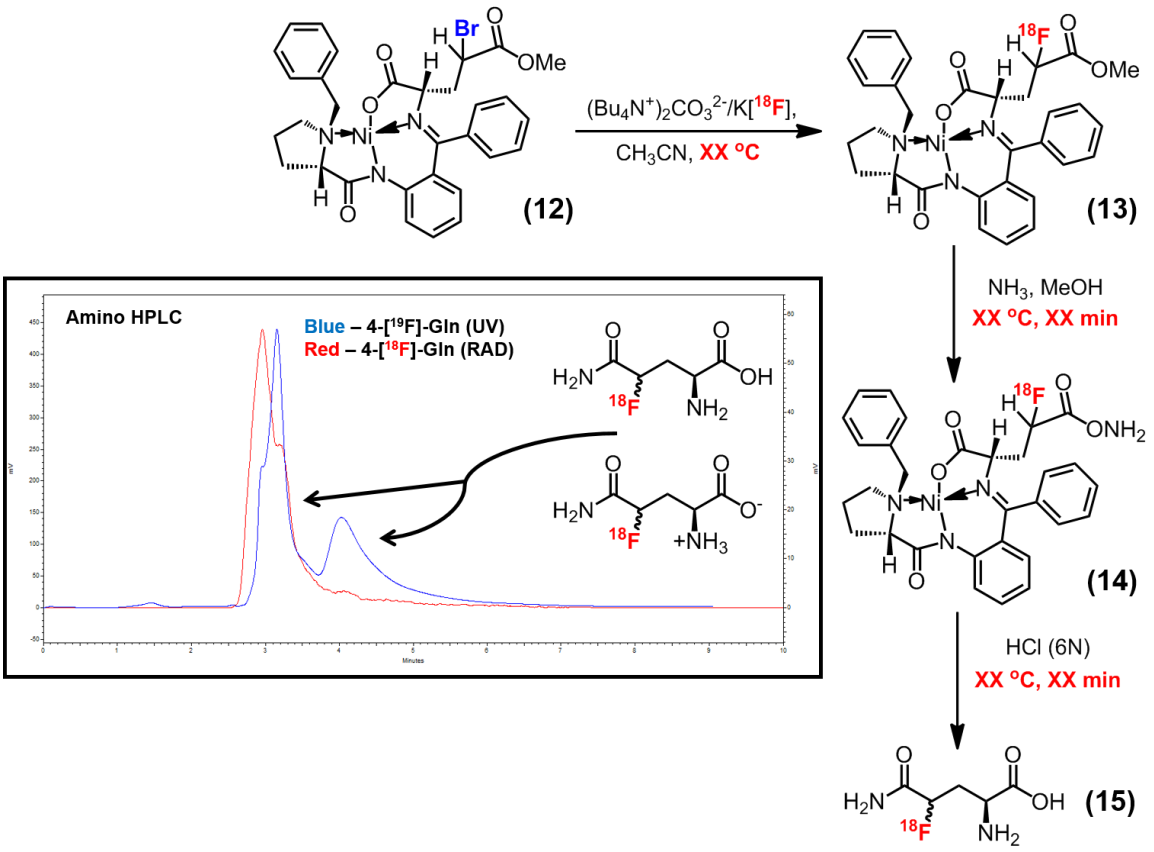


**Figure A3.12. Utilization of NanoTek for development of radiolabeling conditions for amino acid complexes.** Generalized reaction scheme for microfluidic applications towards a complex, multi-step radiolabeling of [$^{18}$F]4-fluoro-glutamine (HPLC chromatography shown above).

### A3.4. Conclusions

While preliminary data suggested the feasibility of [$^{18}$F]PBR06 *production*, the improved labeling efficiency of the system came at a cost in the form of accelerated production of by-products. Despite certain limitations, the improved throughput NanoTek system has demonstrated utility towards determining labeling feasibility, probe stability, and optimal reaction conditions prior to transitioning to full-scale hot-cell based production. Pre-production method optimization could streamline probe development capabilities achievable by traditional radiochemistries. Given this, microfluidic radiochemistry and the Advion NanoTek system could be a useful component of PET

probe development in a *discovery* capacity and offers potential towards better understanding and optimizing radiochemical productions.

### A3.5. Works Cited


1. Date SV, Marcotte EM. Protein function prediction using the Protein Link EXplorer (PLEX). Bioinformatics 2005;21(10):2558-9.

2. Strain MC, Letendre S, Pillai SK, Russell T, Ignacio CC, Gunthard HF, et al. Genetic composition of human immunodeficiency virus type 1 in cerebrospinal fluid and blood without treatment and during failing antiretroviral therapy. J Virol 2005;79(3):1772-88.

3. Kang S, Zhao J, Liu Q, Zhou R, Wang N, Li Y. Vascular endothelial growth factor gene polymorphisms are associated with the risk of developing adenomyosis. Environ Mol Mutagen 2009;50(5):361-6.

4. Jia J, Yang Z, Li G, Liu C, Lei M, Zhang T, et al. Isolation and chromosomal distribution of a novel Ty1-copia-like sequence from Secale, which enables identification of wheat-Secale africanum introgression lines. J Appl Genet 2009;50(1):25-8.

5. Zhou L, Beuerman RW, Ang LP, Chan CM, Li SF, Chew FT, et al. Elevation of human alpha-defensins and S100 calcium-binding proteins A8 and A9 in tear fluid of patients with pterygium. Invest Ophthalmol Vis Sci 2009;50(5):2077-86.

6. Buck JR, McKinley ET, Hight MR, Fu A, Tang D, Smith RA, et al. Quantitative, preclinical PET of translocator protein expression in glioma using 18F-N-fluoroacetyl-N-(2,5-dimethoxybenzyl)-2-phenoxyaniline. J Nucl Med 2011;52(1):107-14.

7. Zhou L, Long R, Pu X, Qi J, Zhang W. Studies of a naturally occurring sulfur-induced copper deficiency in Przewalski's gazelles. Can Vet J 2009;50(12):1269-72.

8. Zhou JL, Liu SQ, Qiu B, Hu QJ, Ming JH, Peng H. The protective effect of sodium hyaluronate on the cartilage of rabbit osteoarthritis by inhibiting peroxisome proliferator-activated receptor-gamma messenger RNA expression. Yonsei Med J 2009;50(6):832-7.

9. Tang D, Hight MR, McKinley ET, Fu A, Buck JR, Smith RA, et al. Quantitative preclinical imaging of TSPO expression in glioma using N,N-diethyl-2-(2-(4-(2-18F-fluoroethoxy)phenyl)-5,7-dimethylpyrazolo[1,5-a]pyrimi din-3-yl)acetamide. J Nucl Med 2012;53(2):287-94.

10. Tang D, McKinley ET, Hight MR, Uddin MI, Harp JM, Fu A, et al. Synthesis and Structure-Activity Relationships of 5,6,7-Substituted Pyrazolopyrimidines: Discovery of a Novel TSPO PET Ligand for Cancer Imaging. J Med Chem 2013.

11. Wang Z, Zhao C, Yu L, Zhou W, Li K. Regional metabolic changes in the hippocampus and posterior cingulate area detected with 3-Tesla magnetic resonance spectroscopy in patients with mild cognitive impairment and Alzheimer disease. Acta Radiol 2009;50(3):312-9.